Development of a GridPix-based X-ray Polarimeter

Dissertation
zur
Erlangung des Doktorgrades (Dr. rer. nat.)
der
Mathematisch-Naturwissenschaftlichen Fakultät
der
Rheinischen Friedrich-Wilhelms-Universität Bonn

von
Markus Gruber
aus
Bonn

Bonn, March 2025

Angefertigt mit Genehmigung der Mathematisch-Naturwissenschaftlichen Fakultät der Rheinischen Friedrich-Wilhelms-Universität Bonn

Gutachter/Betreuer:	Prof. Dr. Klaus Desch
Gutachter:	Prof. Dr. Jochen Dingfelder
Tag der Promotion:	03.07.2025
Erscheinungsjahr:	2025

Contents

CHAPTER 1

Introduction

Foils as polarisation filter for the optical part of the electromagnetic spectrum are quite common and used for example in sunglasses or to separate the pictures for the left and the right eye in a 3D cinema. Unfortunately, such easy polarisation filters do not exist in the X-ray part of the electromagnetic spectrum. Unfortunately, because measuring the polarisation of an X-ray beam has several interesting applications for example in X-ray astronomy or in material science. In the former, it can be used to study the X-ray emission characteristics of astronomical objects and thus deepen our understanding of them. In the latter, it can be used to study the structure of materials and thus help in the development and the improvement of new materials. One possibility to measure the polarisation of an X-ray beam is via so called Bragg crystals. A beam which interacts with such a crystal interacts with its atomic lattice and only the polarisation component that is in direction of the crystal structure is reflected while the orthogonal component is absorbed. The energy band for which this works is very narrow and depends on the lattice step of the crystal. Therefore, for a measurement in a broader energy band multiple crystals with different lattice steps are needed. Furthermore, such a device can only analyse the polarisation in a single plane, based on the working principle. Based on the limitations of Bragg crystals it would be helpful to have a detector that works in a broader energy band and can analyse multiple polarisation planes simultaneously. Such a detector was developed and tested in the scope of this thesis.

It is a gaseous detector which uses the photoelectric effect via which soft X-ray photons interact with a medium. The emission direction of the photo electron is correlated with the polarisation direction of the X-ray beam. Due to the usage of a gas as interaction medium the photo electrons have a sufficient length before they lose all their energy in further interactions with the medium which makes tracking of the electrons possible. To get to the needed spatial resolution and electron detection efficiency a GridPix is used. It is a combination of a pixelised readout ASIC with an integrated gas amplification stage built directly on top of it via photolithography. This enables the tracking of the photo electrons and thus the reconstruction of the polarisation of the X-ray beam.

In this thesis, first the theoretical aspects of polarisation of electromagnetic waves and then aspects of polarised X-rays will be explained in Chapter 2. This is followed by an insight into applications for an X-ray polarimeter in Chapter 3. In Chapter 4 the theoretical aspects of a gaseous detector with a focus on relevant processes for an X-ray polarimeter will be described. The next two chapters will first introduce the two readout ASICs (Chapter 5) that were used for detectors that were operated as X-ray polarimeter. This is followed by a detailed description of the readout system that was developed during this thesis for one of them: the Timepix3 (Chapter 6). Based on the description of the two ASICs Chapter 7 will introduce the GridPix and the detectors that were using it. For these detectors, an end-to-end simulation was implemented that starts with detector and beam parameters and produces the same data as the readout systems of the detectors. This simulation will be introduced in Chapter 8. In the following Chapter 9 the reconstruction of first the events and then the X-ray polarisation will be described. In Chapter 10 the simulation will be used to evaluate the reconstruction approaches and find the optimal reconstruction parameters. Chapter 11 presents X-ray polarisation measurements with two different detectors. In this chapter the data of these measurements are analysed, the results are presented and discussed.

CHAPTER 2

X-ray Polarisation

This chapter presents the main fundamentals for X-ray polarisation and its measurement. Section 2.1 will introduce the term "polarisation" and what it means for electromagnetic waves. Section 2.2 will continue with the mathematical description of the polarisation and typical parameters used by polarimeters. Afterwards, Section 2.3 will discuss the statistics of measuring polarisation and its influence on polarimetry. Sections 2.1 to 2.3 are based on [1] if not stated differently. In the last Section 2.4, a possibility to generate polarised X-rays with an X-ray tube and via Bragg diffraction will be explained.

2.1 Polarisation of Electromagnetic Waves

In an electromagnetic wave the electric field vector can be expressed as a function of time [1]:

$$\vec{E}\,(t) = \left(\hat{x}E_1 + \hat{y}E_2\right) \mathrm{e}^{i\omega t} \,. \tag{2.1}$$

The $\hat{x}$ and $\hat{y}$ are orthogonal axes that are additionally orthogonal to the propagation direction of the wave. ω is the angular frequency of the wave. E_1 and E_2 are complex components and independent of time. These components can be expressed as [1]:

$$E_1 = \left(E_a\right)_1 \mathrm{e}^{i\phi_1} \tag{2.2}$$

$$E_2 = \left(E_a\right)_2 \mathrm{e}^{i\phi_2} \,, \tag{2.3}$$

with the amplitudes $\left(E_a\right)_1$ and $\left(E_a\right)_2$ and the phases ϕ_1 and ϕ_2. Based on this, the electric field vector can be decomposed into the components for the two axes [1]:

$$E_x\,(t) = \left(E_a\right)_1 \cos\left(\omega t + \phi_1\right) \tag{2.4}$$

$$E_y\,(t) = \left(E_a\right)_2 \cos\left(\omega t + \phi_2\right) \,. \tag{2.5}$$

Here, the real part of the electric field vector was taken to show the physical components along the axes. With some calculations (see [1]) and the definition $\delta = \phi_2 - \phi_1$ it can be shown that the polarisation ellipse is given by:

$$\frac{E_x^2}{(E_a)_1^2} - 2\frac{E_x E_y}{(E_a)_1 (E_a)_2}\cos\delta + \frac{E_y^2}{(E_a)_2^2} = \sin^2\delta\,. \tag{2.6}$$

For this, the angle ϕ_0 between the axis of the coordinate system and the semi-major axis of the ellipse can be expressed as [1]:

$$\tan 2\phi_0 = \frac{2\,(E_a)_1\,(E_a)_2 \cos\delta}{(E_a)_1^2 - (E_a)_2^2}\,. \tag{2.7}$$

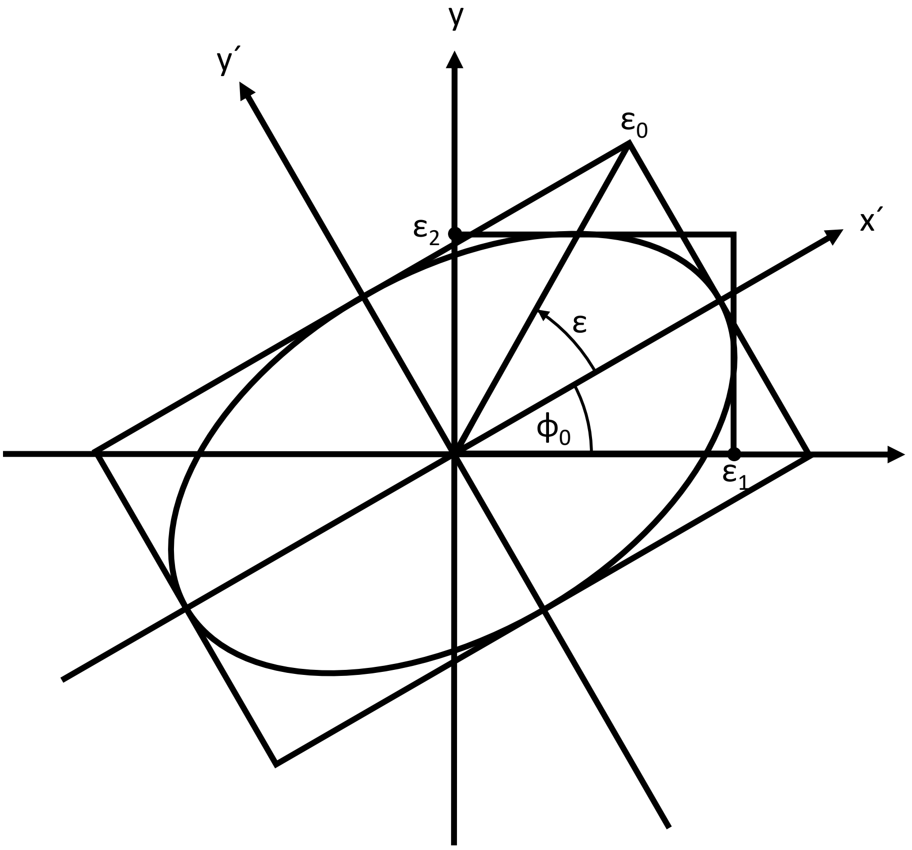

Figure 2.1: Sketch of the polarisation ellipse. The angle ϕ_0 describes the rotation of the coordinate system of the polarised beam with respect to the reference coordinate system. The angle ϵ describes the angle between the rotated coordinate system of the polarised beam with respect to the virtual diagonal of a rectangle that encloses the polarisation ellipse. Based on [1].

Furthermore, the angle ϵ between the semi-axis and a diagonal of a virtual rectangle (see Figure 2.1) enclosing the ellipse can be expressed as [1]:

$$\sin 2\epsilon = \frac{2\left(E_a\right)_1\left(E_a\right)_2 \sin\delta}{\left(E_a\right)_1^2 - \left(E_a\right)_2^2} \,. \tag{2.8}$$

With some further calculations [1] one arrives at the equation:

$$\left(\left(E_a\right)_1^2 + \left(E_a\right)_2^2\right)^2 - \left(\left(E_a\right)_1^2 - \left(E_a\right)_2^2\right)^2 - \left(2\left(E_a\right)_1\left(E_a\right)_2 \cos\delta\right)^2 = \left(2\left(E_a\right)_1\left(E_a\right)_2 \sin\delta\right)^2 \,. \tag{2.9}$$

Based on the relation $I^2 = U^2 + Q^2 + V^2$ for the Stokes parameters for completely polarised radiation, this gives the individual Stokes parameters [1]:

$$I = \left(E_a\right)_1^2 + \left(E_a\right)_2^2 \tag{2.10}$$

$$Q = \left(E_a\right)_1^2 - \left(E_a\right)_2^2 \tag{2.11}$$

$$U = 2\left(E_a\right)_1\left(E_a\right)_2 \cos\delta \tag{2.12}$$

$$V = 2\left(E_a\right)_1\left(E_a\right)_2 \sin\delta \,. \tag{2.13}$$

The Stokes parameters describe the total intensity I of the beam, the intensity Q of the linearly polarised part of the beam along the axes x and y, the intensity U of the linearly polarised part of the beam in a ±45° rotated axis and the circularly polarised intensity V. With the Stokes parameters the angles of the polarisation ellipse can be rewritten as [1]:

$$\tan 2\phi_0 = \frac{U}{Q} \tag{2.14}$$

$$\sin 2\epsilon = \frac{V}{I} \,. \tag{2.15}$$

In case of a quasi-monochromatic wave, that is completely polarised in a time span of $\Delta t = \frac{1}{\omega}$ and a frequency spread of $\Delta\omega > \frac{1}{\Delta t}$ so that $\Delta\omega \ll \omega$, a time average of the electric field on the observation time leads to the following definitions for the Stokes parameters [1]:

$$I = \left\langle E_1 E_1^* \right\rangle + \left\langle E_2 E_2^* \right\rangle = \left\langle \left(E_a\right)_1^2 + \left(E_a\right)_2^2 \right\rangle \tag{2.16}$$

$$Q = \left\langle E_1 E_1^* \right\rangle - \left\langle E_2 E_2^* \right\rangle = \left\langle \left(E_a\right)_1^2 - \left(E_a\right)_2^2 \right\rangle \tag{2.17}$$

$$U = \left\langle E_1 E_2^* \right\rangle + \left\langle E_2 E_1^* \right\rangle = 2\left\langle \left(E_a\right)_1\left(E_a\right)_2 \cos\delta \right\rangle \tag{2.18}$$

$$V = \frac{1}{i}\left(\left\langle E_1 E_2^* \right\rangle - \left\langle E_2 E_1^* \right\rangle\right) = 2\left\langle \left(E_a\right)_1\left(E_a\right)_2 \sin\delta \right\rangle \,. \tag{2.19}$$

Using the Cauchy-Schwartz inequality $\left\langle E_1 E_1^* \right\rangle \left\langle E_2 E_2^* \right\rangle \geq \left\langle E_1 E_2^* \right\rangle \left\langle E_2 E_1^* \right\rangle$ the Stokes parameters can be related with [1]:

$$I^2 \geq U^2 + Q^2 + V^2 \,, \tag{2.20}$$

where the equality holds only for a completely polarised beam. In a beam that is a composition of a polarised and an unpolarised one can write:

$$I_{\text{tot}} = \sqrt{U^2 + Q^2 + V^2} + \left(I_{\text{tot}} - \sqrt{U^2 + Q^2 + V^2}\right) . \tag{2.21}$$

Because the Stokes parameters are additive for a superimposition of independent waves here the intensity of the polarised part is represented by $I_{\text{pol}} = \sqrt{U^2 + Q^2 + V^2}$ and the intensity of the unpolarised part is represented by $I_{\text{tot}} - \sqrt{U^2 + Q^2 + V^2}$. With this, the degree of polarisation P can be written as [1]:

$$P = \frac{I_{\text{pol}}}{I_{\text{tot}}} = \frac{\sqrt{U^2 + Q^2 + V^2}}{I_{\text{tot}}} , \tag{2.22}$$

and thus [1]:

$$\left(P I_{\text{tot}}\right)^2 = U^2 + Q^2 + V^2 . \tag{2.23}$$

In case of a beam that is a composition of a linear polarisation ($V = 0$) and an unpolarised part, a polarimeter that analyses orthogonal to the polarisation axis finds the intensity $I_{\text{min}} = \frac{1}{2} I_{\text{unpol}}$. If it analyses parallel to the polarisation axis, it finds the intensity $I_{\text{max}} = \frac{1}{2} I_{\text{unpol}} + I_{\text{pol}}$. With this, the degree of polarisation from Equation 2.22 becomes [1]:

$$P = \frac{I_{\text{max}} - I_{\text{min}}}{I_{\text{max}} + I_{\text{min}}} . \tag{2.24}$$

2.2 Modulation and Stokes Parameters

Based on the detection principle for X-ray polarisation (see Section 4.1), a measured $\cos^2$ distribution is expected. This can be fitted with [1]:

$$N(\phi) = A^P + B^P \cos^2(\phi - \phi_0) . \tag{2.25}$$

Here A^P and B^P represent constants that are specific for a certain degree of polarisation P. This can be rewritten as [1, 2]:

$$\begin{aligned} N(\phi) &= A^P + \frac{B^P}{2}\left(1 + \cos 2\phi \cos 2\phi_0 + \sin 2\phi \sin 2\phi_0\right) && (2.26) \\ &= A^P + \frac{B^P}{2} + \frac{B^P}{2} \cos 2\phi \cos 2\phi_0 + \frac{B^P}{2} \sin 2\phi \sin 2\phi_0 && (2.27) \\ &= I + U \cos 2\phi + Q \sin 2\phi . && (2.28) \end{aligned}$$

With the Stokes parameters:

$$I = A^P + \frac{B^P}{2} \tag{2.29}$$

$$U = \frac{1}{\mu}\frac{B^P}{2}\cos 2\phi_0 \tag{2.30}$$

$$Q = \frac{1}{\mu}\frac{B^P}{2}\sin 2\phi_0\,. \tag{2.31}$$

The modulation factor μ represents the response of a polarimeter to a 100 % polarised beam. It is defined as [1]:

$$\mu = \frac{N_{\text{max}}^{100\,\%} - N_{\text{min}}^{100\,\%}}{N_{\text{max}}^{100\,\%} + N_{\text{min}}^{100\,\%}} \tag{2.32}$$

$$= \frac{B^{100\,\%}}{2A^{100\,\%} + B^{100\,\%}}\,. \tag{2.33}$$

To calculate the polarisation degree of an unknown beam the modulation factor can be used [1]:

$$P = \frac{1}{\mu}\frac{N_{\text{max}}^{\text{meas}} - N_{\text{min}}^{\text{meas}}}{N_{\text{max}}^{\text{meas}} + N_{\text{min}}^{\text{meas}}} \tag{2.34}$$

$$= \frac{1}{\mu}\frac{B^P}{2A^P + B^P}\,. \tag{2.35}$$

Based on the relation $I_{\text{pol}}^2 = U^2 + Q^2 + V^2$ and $P = \frac{I_{\text{pol}}}{I_{\text{tot}}}$ it follows for a beam without circular polarisation (V=0) [1]:

$$P = \frac{I_{\text{pol}}}{I_{\text{tot}}} = \frac{\sqrt{Q^2 + U^2}}{I_{\text{tot}}} = \frac{1}{\mu}\frac{B^P}{2A^P + B^P}\,. \tag{2.36}$$

Additionally, to get the total intensity I_{tot} the fit function of the modulation curve in Equation 2.25 can be integrated [1]:

$$I_{\text{tot}} = \frac{1}{2\pi}\int_0^{2\pi} N(\phi)\,\mathrm{d}\phi \tag{2.37}$$

$$= A^P + \frac{B^P}{2}\,. \tag{2.38}$$

Thus, it follows that:

$$2\mu\sqrt{Q^2 + U^2} = B^P\,. \tag{2.39}$$

2.3 Minimal Detectable Polarisation

To quantify the response of a polarimeter the “Minimal Detectable Polarisation” (MDP) can be used [1]. For this, first the probability P to detect a modulation with N events, the amplitude a and the angle ϕ for the incident polarisation with amplitude a_0 and angle ϕ_0 are needed. For independent and normally distributed Stokes parameters this probability distribution is given as [2, 3]:

$$P\left(N, a, a_0, \phi, \phi_0\right) = \frac{Na}{4\pi} \exp\left(-\frac{N}{4}\left(a^2 + a_0^2 - 2aa_0 \cos 2\left(\phi - \phi_0\right)\right)\right) . \tag{2.40}$$

To get the minimal detectable polarisation first the probability to detect a linear polarisation without an incident polarisation ($a_0 = 0$) needs to be calculated [2, 4]:

$$P\left(N, a, \phi\right) = \frac{Na}{4\pi} \exp\left(-\frac{N}{4}a^2\right) . \tag{2.41}$$

In the next step, this probability density needs to be integrated to get the probability for all measured amplitudes bigger than a minimal detectable amplitude (MDA) and for all measured angles:

$$\begin{aligned} P\left(N\right) &= \int_{\mathrm{MDA}}^{\infty} \int_0^{2\pi} P\left(N, a, \phi, \right) \mathrm{d}\phi \mathrm{d}a \qquad (2.42) \\ &= \int_{\mathrm{MDA}}^{\infty} \int_0^{2\pi} \frac{Na}{4\pi} \exp\left(-\frac{N}{4}a^2\right) \mathrm{d}\phi \mathrm{d}a \qquad (2.43) \\ &= \exp\left(-\frac{N}{4}\mathrm{MDA}^2\right) . \qquad (2.44) \end{aligned}$$

Based on this, the confidence level C that a polarisation was detected can be calculated:

$$\begin{aligned} C &= 1 - P\left(N\right) \qquad (2.45) \\ &= 1 - \exp\left(-\frac{N}{4}\mathrm{MDA}^2\right) \qquad (2.46) \end{aligned}$$

This is now solved for the minimal detectable amplitude MDA:

$$\mathrm{MDA} = \frac{2}{\sqrt{N}} \sqrt{-\ln\left(1 - C\right)} . \tag{2.47}$$

For a confidence level of 99 % this results in [2]:

$$\mathrm{MDA}_{99\,\%} = \frac{4.29}{\sqrt{N}} . \tag{2.48}$$

To get the minimal detectable polarisation the minimal detectable amplitude needs to be divided by the modulation factor μ of the detector [2]:

$$\mathrm{MDP}_{99\,\%} = \frac{\mathrm{MDA}_{99\,\%}}{\mu} = \frac{4.29}{\mu\sqrt{N}} . \tag{2.49}$$

These are the minimal detectable amplitude and the minimal detectable polarisation for the idealized case with no background events. For a realistic case that includes background events with a signal event rate R_S and a background event rate R_B the minimal detectable amplitude is a fraction of the detected signal [4]:

$$\mathrm{MDA}_\mathrm{S} = \mathrm{MDA}_{99\,\%} \frac{R_\mathrm{S} + R_\mathrm{B}}{R_\mathrm{S}} . \tag{2.50}$$

With T as the measurement time $N = \left(R_\mathrm{S} + R_\mathrm{B}\right) T$ the minimal detectable polarisation is [4]:

$$\mathrm{MDP}_\mathrm{S} = \frac{4.29}{\mu R_\mathrm{S}} \sqrt{\frac{R_\mathrm{S} + R_\mathrm{B}}{T}} . \tag{2.51}$$

For the case of $R_\mathrm{S} \gg R_\mathrm{B}$ this is reassembling the case of no background that was considered for Equation 2.49.

The expression for MDP (Equation 2.49) allows to calculate the necessary modulation factor that a detector must achieve to reach a given minimal detectable polarisation with a confidence level of 99 %. An example of this is presented in Figure 2.2. One can see that a lower minimal detectable polarisation leads to a higher needed modulation factor of the detector. The same happens if the number of detected photons is reduced. Based on Equation 2.49, one can also estimate that an improvement of the modulation factor by one percent ($\mu_2 = 1.01\mu_1$) decreases the needed amount of photons and thus, for a constant rate also the measurement time for the same minimal detectable polarisation by approximately 2 %.

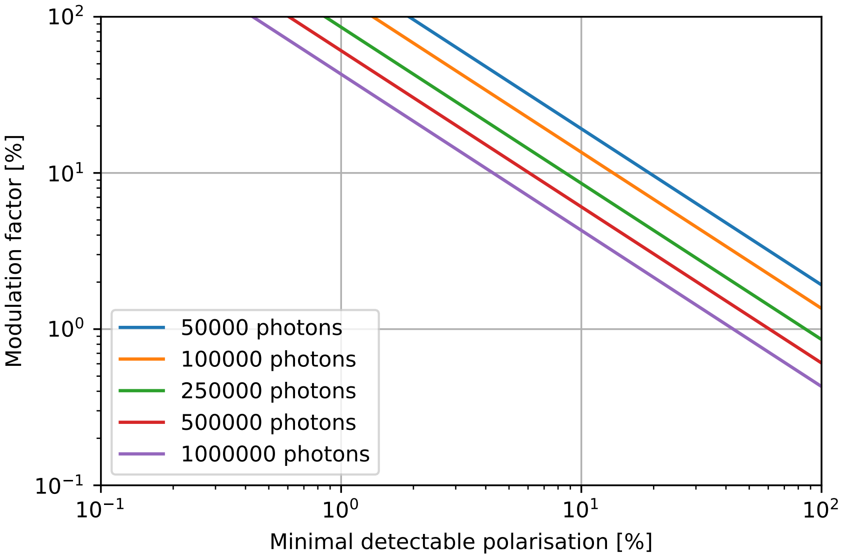

Figure 2.2: Visualisation of the required modulation factors of a detector to achieve a given minimal detectable polarisation with 99 % confidence level for different amounts of detected photons. Based on Equation 2.49.

2.4 Creation of Polarised X-rays

To evaluate X-ray polarimeters, a setup that creates polarised X-rays of various energies is necessary. In this section the basics of such a setup consisting of an X-ray tube to first generate unpolarised X-rays (Section 2.4.1) and Bragg diffraction (Section 2.4.2) to polarise the X-rays will be discussed. Additional sources of polarised X-rays can be found in Chapter 3 where they will be explained in the context of applications of X-ray polarimeters.

2.4.1 X-ray Tube

X-ray tubes itself produce no polarised X-rays, but they can be used to create an X-ray beam that is then polarised via Bragg diffraction (see Section 2.4.2). A scheme of an X-ray tube is shown in Figure 2.3. It works as follows: at the start a cathode is heated based on an applied voltage U_H. Due to the heating the cathode emits electrons. The rate of electron emissions can be regulated by the applied voltage. These electrons are then accelerated away from the cathode to an anode due to the potential difference U between cathode and anode. Because the full setup of cathode and anode is in a vacuum tube, there is no scattering or absorption of the electrons during the acceleration, and they gain the energy $E = eU$. The electrons hit the anode and produce X-rays via the following mechanisms [5]:

- The electrons are deflected in the Coulomb field of the atoms in the anode and loose energy via the emission of “Bremsstrahlung”. This creates a continuous energy spectrum, and its shape depends on the energy of the electrons and the composition of the anode.

- The electrons interact with shell electrons of the atoms in the anode and excite them to higher shells, if they have sufficient energy. The de-excitation of these states via the emission of photons creates characteristic X-ray lines whose energy depends on the shells of the atoms in the anode.

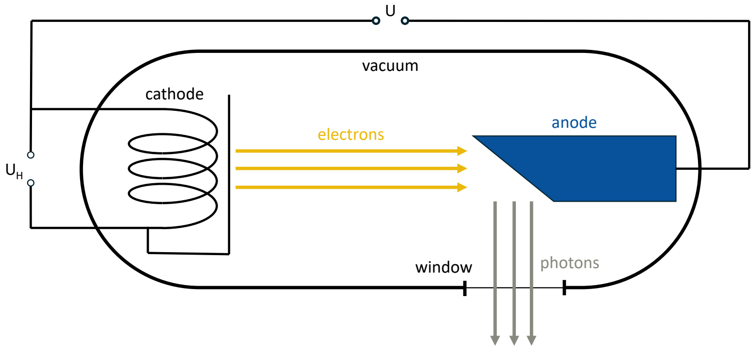

Figure 2.3: Sketch of an X-ray tube. Besides a high potential based on the voltage U, the cathode is heated with a current based on the voltage U_H. Due to this heating the cathode emits electrons. These electrons are then accelerated towards the anode in the electric field between cathode and anode. The electrons interact with the anode and produce X-ray photons. These can exit the setup via an X-ray window. The whole setup is within a vacuum tube to ensure that the electrons do not interact with any gas molecules on their way from the cathode to the anode. Based on [5].

2.4.2 Bragg Diffraction

If a monochromatic X-ray beam with an energy E is diffracted on a crystal with the lattice step d and the grazing angle θ (see Figure 2.4) then there is a constructive interference of the diffracted beam if the Bragg condition is fulfilled [1, 5]:

$$2d \sin\theta = n\lambda = n\frac{hc}{E}\,. \tag{2.52}$$

Here n marks the diffraction order, h the Planck constant, c the speed of light in vacuum and λ the wavelength. Thus, the rotation of the crystal with respect to the incoming X-ray beam via the angle θ can adapt the setup for a constructive interference of different beam energies. Additionally, only the beam component that has a polarisation perpendicular to the diffraction plane is diffracted while the parallel component is absorbed by the crystal. Thus, with an angle of $\theta = 45^\circ$ the parallel component can be filtered while the perpendicular component is diffracted. This allows to polarise a non-polarised monochromatic beam that fulfils the Bragg condition (Equation 2.52) at $\theta = 45^\circ$. The X-ray beam for this case can be created with an X-ray tube (see Section 2.4.1). In this case the Bragg diffraction with the crystal can be also used as a monochromator, if additionally a collimator for the diffracted beam is used to get rid of energies that fulfil the Bragg condition with different angles.

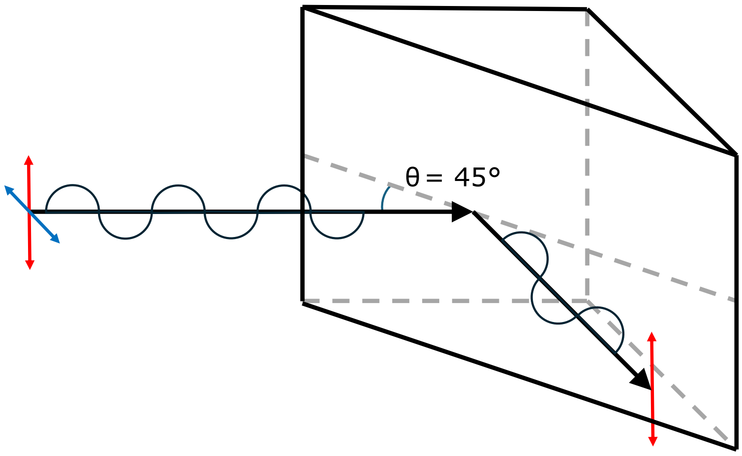

Figure 2.4: Sketch of the diffraction of an X-ray beam on a crystal. The incoming beam is unpolarised and thus is a superposition of polarisation parallel (blue) to the diffraction plane and polarisation perpendicular (red) to the diffraction plane. The beam is monochromatic and fulfils the Bragg condition for a diffraction angle of $\theta = 45^\circ$. In this case the polarisation component parallel to the diffraction plane is filtered while the perpendicular component (red) is diffracted. Thus, the diffracted beam is linearly polarised. Based on [1].

CHAPTER 3

Applications

X-ray polarimetry is a useful tool in several applications. This chapter will provide a brief overview of these applications with a focus on X-ray astronomy (Section 3.1) and applications at accelerators with polarised X-rays (Section 3.2).

3.1 X-ray Astronomy

Besides the use of a Bragg crystal to create a polarised beam, as it was shown in Section 2.4.2, it can be also used as a device to analyse the polarisation of the incoming beam. This is a so called "Bragg polarimeter". For this, it is used that the diffracted beam has a maximum intensity if the polarisation of the incoming beam is parallel to the diffraction plane and a minimum intensity if the polarisation is perpendicular to the diffraction beam — both under the assumption that the Bragg condition is fulfilled. Thus, it works only for a narrow energy band of some tens of eV. The only possibility to change the energy is the measurement via higher orders of diffraction (n in the Bragg condition) or by using a different crystal with a different lattice step d. Rotating the device around the beam axis and measuring the intensity in dependence of the rotation angle generates a modulation curve which can be used to study the angle of polarisation and the polarisation degree (see Section 2.1). Such devices were the first to confirm the polarisation of an astronomical X-ray source: the Crab Nebula. For this, Bragg polarimeters were mounted to sounding rockets that were spinning and pointing with their spin axis towards the Nebula during their brief flight of a few minutes flight time. The spin of the rocket created the necessary rotation of the Bragg polarimeter. The intensity profile was measured with a proportional counter. Because of the Bragg condition the polarimeter was limited to a small energy band and thus had a low sensitivity. Due to this, no single measurement of a launch could detect polarisation, but the combination of the results led to the first significant measurement of polarised X-rays emitted by the Crab Nebula: a polarisation of $P = (15.4 \pm 5.2)\,\%$ [6].

The OSO-8 satellite also used two Bragg polarimeters for redundancy. With their graphite crystals they could perform polarisation measurements at 2.6 keV and 5.2 keV [7]. While it could only measure a significant polarisation again for the Crab Nebula, some limits on the polarisation of other sources were obtained [8]. Despite this, the polarisation measurements for the Crab Nebula were improved to $P = (19.2 \pm 1.0)\,\%$ at 2.6 keV and $P = (19.5 \pm 2.8)\,\%$ at 5.2 keV [9].

There is a range of astronomical X-ray sources that emit X-rays and for which studying their polarisation can be a used to further investigate the phenomenology of the sources. The Crab Nebula is part of a group of diffuse X-ray sources that is called Pulsar Wind Nebulae (PWNe) and serves as a prototype for this class. A first model [10, 11] of these objects described a central pulsar that emits a large part of its rotational energy as a spherically symmetric magnetised wind. This wind is decelerated by a strong shock and the particles of the wind emit synchrotron radiation in the magnetic field of the nebula. This picture was challenged by the measurements of the Chandra X-ray observatory [12] and pointed into the direction of an an-isotropic wind [13, 14]. Furthermore, the formation of the jet that is emitted by the object could be explained by a predominant toroidal magnetic field. It could collimate the particles due to magnetic hoop stress, but this mechanism is extremely ineffective. Another explanation would be a collimation by a strongly asymmetric shock by the an-isotropic wind [15, 16]. In this case, the collimation by the magnetic hoop stress is much more effective as the wind is not relativistic. To test these models, X-ray polarimetry can be an important measurement tool [17, 18]. It can be used to probe the velocity of the wind and the magnetic field in the nebula as the X-rays are expected to show a high degree of polarisation due to the emission as synchrotron radiation.

Besides PWNe there are a lot of other classes of astronomical objects that emit X-rays, and it is expected that most of these sources emit at least partially polarised X-rays. Some examples are pulsars, magnetars and neutron starts. In [1] a comprehensive overview of various sources is given and explained how measuring the polarisation of their X-rays can help to further understand them.

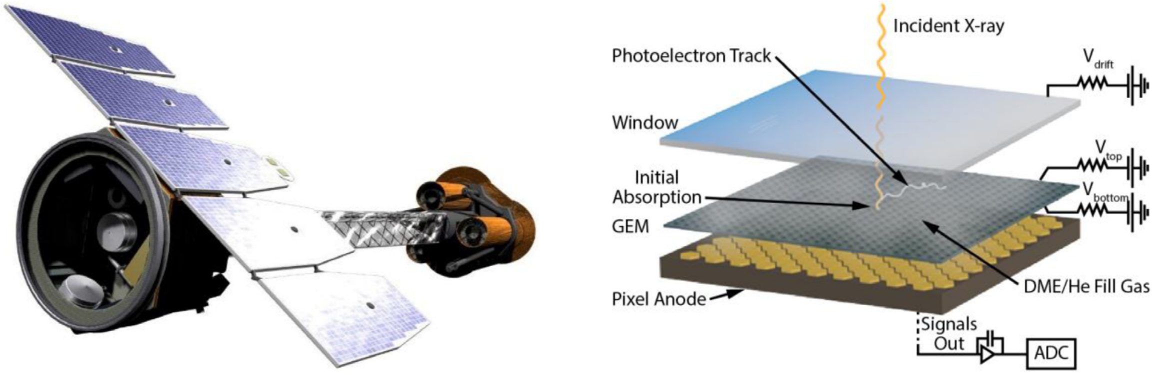

(a) Illustration of the IXPE satellite

(b) Schematic of the GPD

Figure 3.1: Illustration of the imaging X-ray polarimetry explorer (IXPE) and schematic of its gas pixel detectors (GPD). The GPDs are mounted in the focus of the three X-ray telescopes that are visibly in the right side of the illustration. Within the GPDs the X-rays interact with the gas via the photo electric effect. The resulting photoelectrons create an ionisation track that is amplified via a gas electron multiplier (GEM) and detected by a pixelized ASIC [19].

The newest instrument to measure the polarisation of such X-ray sources is the imaging X-ray polarimetry explorer (IXPE) [19]. It is a satellite that launched to low earth orbit in December of 2022 and features three so called gas pixel detectors (GPDs) [20] that operate in the focal points of three X-ray telescopes (see Figure 3.1(a)). These detectors use a similar working principle as the detectors that will be presented in Chapter 7, as they track the photoelectron of the photo electric effect in a gaseous detector (the theoretical background will be discussed in Chapter 4). It features a readout ASIC with 300 by 352 hexagonal pixels 700 µm below a gas electron multiplier (GEM) (see

Figure 3.1(b)). Its operating with pure Dimethyl ether at 800 mbar as detector gas and is optimised for the energy band from 2 keV to 8 keV. The detectors were tested at a facility at the Institute of Space Astrophysics and Planetology of the Istituto Nazionale di Astrofisica based on the polarisation of an X-ray beam from an X-ray tube (Section 2.3) with a Bragg crystal (Section 2.4.2) [19]. The same facility and setup were used to generate polarised X-ray beam to test the detectors described in this thesis. The results of these measurements will be presented in Chapter 10.

3.2 Material Science

Another application of measuring the polarisation of X-rays is material science at synchrotron light sources. In general synchrotron light is linearly polarised in the plane of the synchrotron and circularly polarised in an angle to it. It occurs if an accelerated charge e with energy E is put on a circular path with radius r_0. In this case the emitted power is [21]:

$$P = \frac{e^2 c}{6\pi\epsilon_0 r_0^2}\left(\frac{E}{m_0 c^2}\right)^4 = \frac{e^2 c\gamma^4}{6\pi\epsilon_0 r_0^2} . \tag{3.1}$$

Based on the proportionality $P \propto m_0^{-4}$ it is clear why electrons are used as accelerated particles for synchrotron light machines and not for example nearly 2000-times heavier protons. The spectral power distribution of the synchrotron radiation is [21]:

$$\frac{\mathrm{d}P}{\mathrm{d}\omega} = \frac{e\gamma^4 I}{3\epsilon_0\omega_\mathrm{c}} S_\mathrm{S}\left(\omega/\omega_\mathrm{c}\right) , \tag{3.2}$$

with $\omega_\mathrm{c} = \frac{3c\gamma^4}{2r_0}$ as critical frequency that divides the spectrum into two halves with the same power. $S_\mathrm{S}\left(\omega/\omega_\mathrm{c}\right)$ can be expressed as [21]:

$$S_\mathrm{S}\left(\omega/\omega_\mathrm{c}\right) = \frac{9\sqrt{3}}{8\pi}\frac{\omega}{\omega_\mathrm{c}}\int_{\omega/\omega_\mathrm{c}}^{\infty} K_{5/3}\left(\omega/\omega_\mathrm{c}\right)\mathrm{d}\frac{\omega}{\omega_\mathrm{c}} . \tag{3.3}$$

Here $K_{5/3}$ indicates the modified Bessel function.

Depending on the energy of the electron beam the resulting energy spectrum can span over a few orders of magnitude. But for experiments with synchrotron radiation often a monochromatic beam is desired. For this, monochromators can be used that work based on the same principle as a Bragg polarimeter (see Section 2.4.2). In a simple picture, a monochromator is a combination of two Bragg crystals and their angle with respect to the beam line and with respect to each other are set for required beam energy at the output, based on the Bragg condition (Equation 2.52). While the beam with all its photon energies illuminates the first crystal it reflects the different energies with different angles. The second crystal is installed at the place where the desired photon energy is expected and installed at an angle that fulfils the Bragg condition for the energy as a second filter and directs these photons in the desired direction. By the introduction of moving parts to change the angles and positions of the crystals the monochromator can be adapted to different energies. A detailed overview of monochromator designs and their optimisation for different applications can be found in [22].

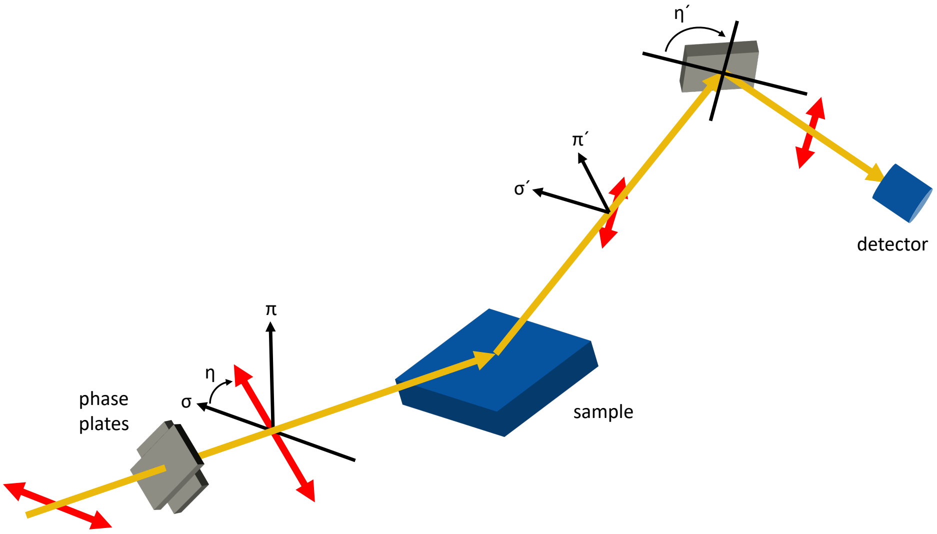

Figure 3.2: Schematic of an X-ray diffraction measurement at a synchrotron beam line. A polarised beam enters on the left side. Its polarisation can then be influence with phase plates. The beam then illuminates a sample that influences the polarisation of the diffracted beam. This polarisation can then be studied as displayed here with a Bragg polarimeter consisting of a Bragg crystal and a counting detector that both can be rotated around the beam axis of the diffracted beam to get the modulation. Based on [23].

After the monochromator, additional elements like phase plates can be used to influence the direction of the polarisation. Then the beam is scattered off a test sample. The outgoing beam can then be analysed, which is often done with a Bragg polarimeter. A sketch of such a setup is presented in Figure 3.2.

There are two possible applications of a polarisation sensitive detector in such a setup. One is to include the detector in the beam line to parasitically monitor the polarisation of the beam [23]. In this application gaseous detectors, as developed in this thesis, are beneficial as they can be set up with a low efficiency and thus a low influence on the beam. For this purpose, the detector needs windows for the beam to enter and exit and additionally, the readout should be outside of beam trajectory. For such an application a parallel design with the beam passing the detector in parallel to the readout would be beneficial. Such a concept will be presented and discussed in Section 7.5.

The other option for a polarisation sensitive detector would be to replace the rotatable Bragg crystal and counting detector that analyses the beam after the sample. The advantage would be that the polarisation of the beam can be directly analysed by the detector without the necessity of moving parts to rotate a crystal and a detector. With this, the intensity distribution of the beam after the sample with respect to the angle η' can be measured. This can be for example used to measure the magnetic properties of the sample [23]. Furthermore, the analysis of the polarisation after a sample can be used to see if there are impurities in the crystal structure of a sample as this would influence locally the lattice step in the Bragg condition (see Section 2.4.2) and thus influence the polarisation of the outgoing beam. Details on X-ray diffraction and applications can be found for example in [24].

CHAPTER 4

Gaseous Detectors

In this chapter the theoretical background for the detection process of polarised X-rays is covered. First, the interaction of soft X-rays with matter and how the polarisation influences this will be explained (Section 4.1). This is followed by a description of the interactions of photoelectrons with a gas in Section 4.2. Section 4.3 will discuss how the products of these interactions are transported to the readout of the detector and what happens during this process. Finally, Section 4.4 describes the amplification process in the detector to get a signal that is measurable by the readout and Section 4.5 will introduce the Penning effect that influences the gas gain. If not indicated differently, Sections 4.3 to 4.5 are based on [25].

4.1 Interaction of Soft X-rays with Matter

There are three main interactions of photons with matter: The photoelectric effect, the Compton effect and pair production. The cross-sections of these effects are energy dependent and leads to the fact that for soft X-rays the photo effect is dominant. In the photoelectric effect, the photon transfers its complete energy to a shell electron of an atom. If the energy of the photon E is higher than the binding energy of the electron E_B, it is emitted. In this case, its kinetic energy T is the difference of the energy of the photon and the binding energy [26]:

$$T = E - E_\mathrm{B} \,. \tag{4.1}$$

The process can be written as follows [26]:

$$\gamma + \mathrm{A} \longrightarrow \mathrm{A}^{+} + \mathrm{e}^{-} \,, \tag{4.2}$$

with A representing the atom. For photon energies higher than the ionisation energy of the K-shell of an atom but much lower than the mass of an electron $E \ll m_\mathrm{e}c^2$, the total cross section for the K-shell can be written in a non-relativistic approximation as [26]:

$$\sigma_\mathrm{K} = \sqrt{32}\alpha^4\epsilon^{-3.5}Z^5\sigma_\mathrm{Th}f\left(\xi\right) \,, \tag{4.3}$$

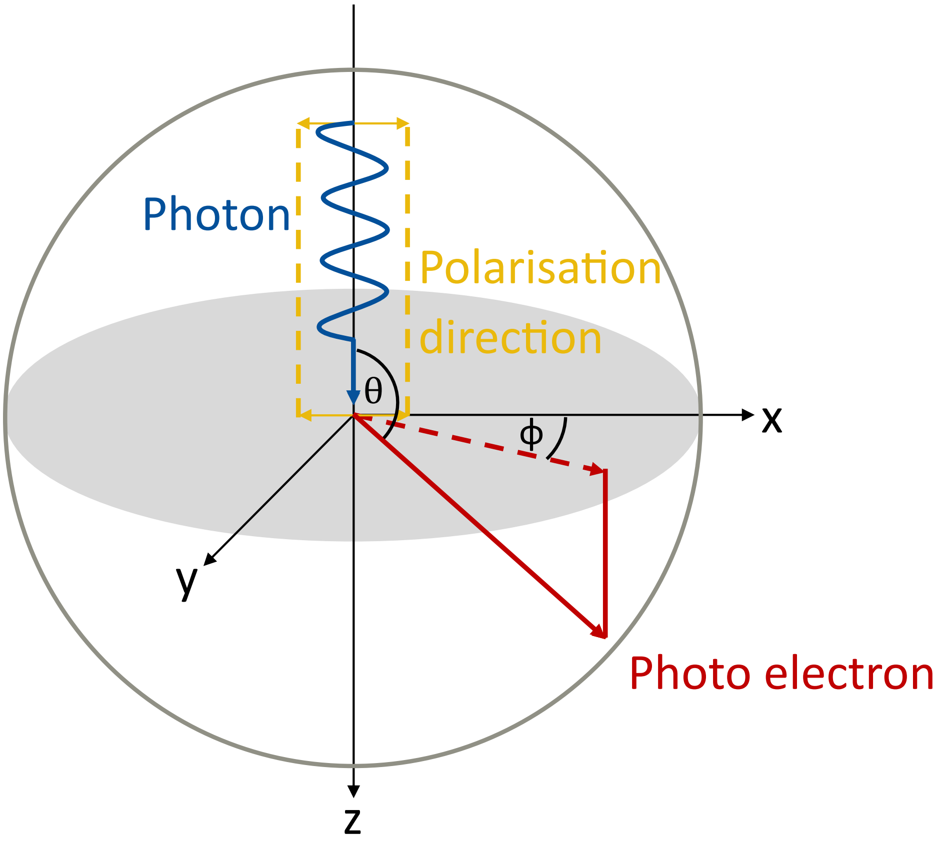

Figure 4.1: Illustration of the photo effect and the coordinate system. Based on [1]

with the energy $\epsilon = E/m_e c^2$, the fine structure constant $\alpha = 1/137$, and the Thompson cross-section $\sigma_{\mathrm{Th}} = \frac{8}{3}\pi r_e^2$ that describes the scattering of low-energetic photons on electrons. The factor $f(\xi)$ is the Born approximation that considers the angular momentum transfer from the photon to the electron. It can be written as [26]:

$$f(\xi) = 2\pi Z\alpha \sqrt{\frac{1}{2\epsilon}} \frac{\exp(-4\xi \mathrm{arccot}\xi)}{1 - \exp(-2\pi\xi)}\,, \tag{4.4}$$

with

$$\xi = \sqrt{\frac{\epsilon_K}{\epsilon - \epsilon_K}} \tag{4.5}$$

$$\epsilon_K = \frac{E_K}{m_e c^2} = \frac{1}{2} Z^2 \alpha^2\,. \tag{4.6}$$

Based on Equations 4.3 and 4.4 the proportionalities of the total cross section are [26]:

$$\sigma_K \propto Z^n \qquad \text{with } n = 4 - 5 \tag{4.7}$$

$$\sigma_K \propto E^{-m} \qquad \text{with } m \leq 3.5\,. \tag{4.8}$$

The mean free path λ of a photon can then be calculated with [26]:

$$\lambda = \frac{1}{n\sigma_{\mathrm{K}}} \tag{4.9}$$

$$n = \frac{\rho}{A} N_{\mathrm{A}} \,, \tag{4.10}$$

with the particle number density n, the material density ρ, the nucleon number A, the atomic number Z of the atom, and the Avogadro constant N_{A}.

For the emission of photoelectrons also their direction is important. For this the differential cross-section of the photo effect can be studied. For the non-relativistic case and for interactions with K-shell electrons it is [1]:

$$\frac{\mathrm{d}\sigma}{\mathrm{d}\Omega} = \left(\frac{e^2}{mc^2}\right)^2 \frac{Z^5}{137^4} \left(\frac{mc^2}{E}\right)^{\frac{7}{2}} 4\sqrt{2} \frac{\sin^2\theta}{(1+\beta\cos\theta)^4} \cos^2\phi \,. \tag{4.11}$$

In this equation ϕ represents the polarisation angle, e the elementary charge, m the mass of the electron, c the speed of light, θ the angle between the flight direction of the photon and the flight direction of the photoelectron and β the velocity $\beta = \frac{v}{c}$ of the photoelectron. For non-spherical orbitals, the differential cross section changes to [1]:

$$\frac{\mathrm{d}\sigma}{\mathrm{d}\Omega} = \frac{\sigma_{\mathrm{tot}}}{4\pi} \left[1 + \frac{b}{2}\left(\frac{3\sin^2\theta\cos^2\phi}{(1+\beta\cos\theta)^4} - 1\right)\right] \,. \tag{4.12}$$

Here, b represents an asymmetry factor for the orbital that in case of spherical symmetric orbitals like 1s and 2s equals 2 and for others is less than 2. Furthermore, σ_{tot} is the total photo ionisation cross section. While this theoretically changes the modulation response to a polarised beam, in the X-ray range the contribution of non-spherical symmetric orbitals is negligible compared to the contribution of the spherically symmetric orbitals and thus the proportionality of the differential cross section can be written as [1]:

$$\frac{\mathrm{d}\sigma}{\mathrm{d}\Omega} \propto \frac{\sin^2\theta\cos^2\phi}{(1+\beta\cos\theta)^4} \,. \tag{4.13}$$

Based on the factor $\cos^2\phi$ one can see that the differential cross section of the photo effect and thus the emission of photoelectrons peaks in the direction of the polarisation plane. So, in a projection perpendicular to the direction of the photons one should see a $\cos^2$-distribution of emission angles of photoelectrons. Thus, tracking the photoelectrons to measure their distribution enables measuring the plane of the polarisation. At low energies ($\beta \ll 1$) the photoelectrons are mainly emitted in a plane orthogonal to the photon beam ($\theta = \frac{\pi}{2}$) while with increasing energies this shifts in the forward direction. This can be seen in a plot of the normalised cross sections for different energies and angles θ in Figure 4.2. One can see that for the given energy range of 2 keV to 10 keV all distributions peak close to $\theta = \frac{\pi}{2}$.

Besides the emission of the photoelectron there is a possibility for the emission of an Auger electron [26]. This can happen if the photoelectron was emitted from an inner shell and this free spot is filled by an electron of a higher shell in the atom. The energy between the two shells can be either emitted

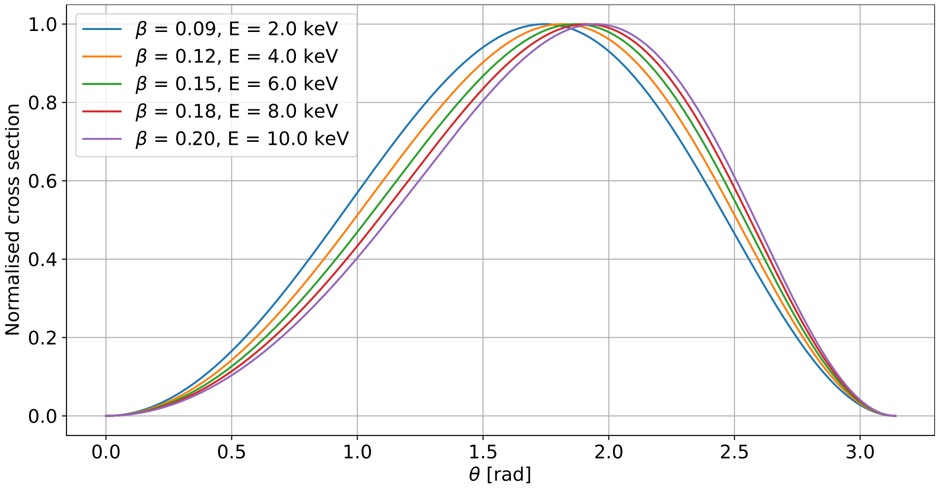

Figure 4.2: Dependence of the cross section of the photoelectric effect on the angle in forward direction θ and the velocity β of the photoelectron. The calculation for the energy of the photon were done using the first ionisation energy of argon (15.7 eV [27]) which is negligible with respect to the photon energy. With rising energy, the photoelectrons tend to be released slightly in the forward direction but in the given energy range from 2 keV to 10 keV all distributions peak close to $\frac{\pi}{2}$ which is orthogonal to the beam direction. Based on [1, 26].

by a photon or transferred to another electron of the atom that escapes it with this additional energy. This electron is called Auger electron and its direction is not correlated with the polarisation of the X-ray beam like the direction of the photoelectron. In the case of the emission of a photon, this can either interact again with the gas via the photo effect or leave the active area of the detector and thus reduce the detected energy in the event.

4.2 Electron Interactions with the Gas

In order to track photoelectrons and to subsequentially reconstruct the polarisation of an X-ray beam (see Sections 4.1 and 9.3) it is important to understand how photoelectrons interact with the gas after the emission from the atom. There are two important effects to consider: the electron can ionise gas atoms which creates electron-ion pairs and thus the electron loses energy, and the electron can scatter in the interactions with atoms and thus, change its direction. Based on [26], these two processes are explained in Sections 4.2.1 and 4.2.2.

4.2.1 Ionisation

The energy loss of the photoelectrons with energies in the low keV range is as follows [28]:

$$-\frac{\mathrm{d}E}{\mathrm{d}x} = \frac{e^4 nZ}{8\pi\epsilon_0^2 mc^2\beta^2}\left[\ln\frac{m\gamma^2c^2\beta^2E_{\max}}{2I^2} - \left(\frac{2}{\gamma-\frac{1}{\gamma^2}}\right)\ln 2 + \frac{1}{\gamma^2} + \frac{1}{8}\left(1-\frac{1}{\gamma}\right)^2\right]. \tag{4.14}$$

Here, n represents the number density of atoms, Z the atomic number, γ the Lorentz factor of the electron, $E_{\max}$ the maximum energy that can be transferred to a shell electron, and I the ionisation potential. It shows that the energy loss is inversely proportional to the energy of the photoelectron. Based on this, the energy loss of a photoelectron is not linear but peaks towards the end of the track. This creates a so-called Bragg Peak at the end of a photoelectron track where the most ionisations occur. The difference in the energy loss of a photoelectron at the start and the end of its ionisation path through a volume can be used to differentiate these parts of tracks, based on the detected ionisation.

The range of the photoelectron in dependence of its kinetic energy E can be estimated with the following empirical relation [25]:

$$R\left(E\right) = AE\left(1 - \frac{1}{1 + CE}\right) \tag{4.15}$$

with the parameters:

$$A = 5.37 \times 10^{-4}\,\frac{\mathrm{g}}{\mathrm{cm\,keV}} \tag{4.16}$$

$$B = 0.9815 \tag{4.17}$$

$$C = 3.12304 \times 10^{-3}\,\frac{1}{\mathrm{keV}}\,. \tag{4.18}$$

In this case $R\left(E\right)$ describes the practical and material independent range. The relation was tested with experimental data in the range from 300 eV to 20 MeV and it was shown that it holds for materials with low to intermediate atomic numbers Z [29]. Intermediate atomic numbers are here in the range of copper ($Z = 29$). To get from the practical range R to the range r the density ρ of the medium must be considered:

$$r\left(E\right) = \frac{R\left(E\right)}{\rho} \tag{4.19}$$

4.2.2 Scattering

The main scattering interaction is Rutherford scattering. Its cross section can be expressed as follows [26]:

$$\frac{\mathrm{d}\sigma}{\mathrm{d}\Omega} = \frac{e^2 Z^2 \alpha^2 \hbar^2}{4\beta^2 p^2 \sin^4\frac{\theta}{2}}\,. \tag{4.20}$$

Here β and p represent the velocity and the momentum of the electron, and θ the scattering angle. One can see that the cross section is proportional to Z which represents the atomic number. For a gas mixture the effective atomic number can be used. It is the average atomic number of the individual gases, weighted by their mixing ratio. Based on the proportionality, reducing the effective atomic number of the gas mixture leads to a lower cross section of Rutherford scattering and thus to less scattering in terms of occurrence and high scattering angles. As the scattering angle is a random distribution based on the cross section, each scattering of the photoelectron weakens the correlation of the direction of the electron with the polarisation of the X-ray beam. Thus, decreasing the cross section and using a reconstruction that concentrates on the initial part of the photoelectron path, helps reconstructing the polarisation. The cross section is for example in a Helium-based gas mixture ($Z = 2$) smaller than in an Argon-based gas mixture ($Z = 18$). Therefore, less scattering is expected.

4.3 Drift and Diffusion

The electron-ion pairs in the gas, that are generated by ionising radiation would recombine after some time. As these are necessary for the detection process, the recombination should be prevented. This is done via a sufficiently strong electric fields that separate electrons and ions. In this thesis, only the movement of the electrons is relevant as they are the charges that are amplified and detected by the GridPixes in the given detectors (see Chapter 7). Therefore, only the electron transport within the gas volume will be discussed. For the description of the diffusion these electrons will start as a point like could at $t = 0$ and $z = 0$ with z being the drift direction and t the time. In a general case with an electric field $\vec{E}$ and a magnetic field $\vec{B}$ the acceleration of the electrons is given by the Lorentz force [26]:

$$m\frac{\mathrm{d}\vec{v}}{\mathrm{d}t} = q\left(\vec{E} + \vec{v} \times \vec{B}\right) , \tag{4.21}$$

with the charge of the electron $q = e$. Due to the gas, an additional velocity-dependent frictional force $F_{\text{friction}} = -K\vec{v}\,(t)$ is acting on the electrons [25]:

$$m\frac{\mathrm{d}\vec{v}}{\mathrm{d}t} = q\left(\vec{E} + \vec{v} \times \vec{B}\right) - K\vec{v}\,(t) \ . \tag{4.22}$$

The friction K and the mass of the electron can be used to define a characteristic time [25]:

$$\tau = \frac{m}{K} . \tag{4.23}$$

In a microscopic picture this characteristic time can be interpreted as the mean time between collisions of the electrons and gas atoms or molecules. For the case of a much smaller characteristic time then the drift time ($\tau \ll t$) Equation 4.22 has a steady state solution with $\frac{\mathrm{d}\vec{v}}{\mathrm{d}t} = 0$ [25]:

$$\frac{1}{\tau}\vec{v} - \frac{e}{m}\left(\vec{v} \times \vec{B}\right) = \frac{e}{m}\vec{E} . \tag{4.24}$$

The solution for the velocity can be written as [25]:

$$\vec{v} = \frac{e}{m}\tau|\vec{E}|\frac{1}{1 + \omega^2\tau^2}\left(\hat{\vec{E}} + \omega\tau\left(\hat{\vec{E}} \times \hat{\vec{B}}\right) + \omega^2\tau^2\left(\hat{\vec{E}} \cdot \hat{\vec{B}}\right)\hat{\vec{B}}\right) , \tag{4.25}$$

with $\hat{\vec{E}}$ and $\hat{\vec{B}}$ as the unit vectors of the electric field and the magnetic field, and with $\omega = \frac{e}{m}B$ as the cyclotron frequency of the electron in the magnetic field. For the case of no magnetic field $B = 0$ it follows:

$$\omega\tau = 0 , \tag{4.26}$$

and thus [25]:

$$\vec{v} = \frac{e}{m}\tau\vec{E} = \mu\vec{E} . \tag{4.27}$$

The parameter $\mu = \frac{e}{m}\tau$ in Equation 4.27 is called the mobility of the electron. For a given drift of length L Equation 4.27 leads to the following drift time:

$$t = \frac{L}{|\vec{v}|} = \frac{L}{\mu|\vec{E}|} \,. \tag{4.28}$$

The point like cloud of electrons diffuses during the drift, due to the electron concentration gradient not being in an equilibrium state within the gas. After a given time, this cloud has a Gaussian-based density distribution [25]:

$$n = \left(\frac{1}{\sqrt{4\pi D t}}\right)^3 \exp\left(\frac{-r^2}{4Dt}\right) \,. \tag{4.29}$$

Here D is the diffusion constant and $r^2 = x^2 + y^2 + (z - vt)^2$ with the coordinate axes x, y, z and the drift velocity v. In a microscopic picture with electrons starting at $t = 0$ and the velocity v the probability for a free path is given by [25]:

$$g\left(l\right) \mathrm{d}l = \frac{1}{l_0} \exp\left(-\frac{l}{l_0}\right) \mathrm{d}l \,, \tag{4.30}$$

with the mean free path $l_0 = v\tau$. In an approximation of isotropic scattering with respect to the drift direction the mean square displacement in one direction at a time t and after a large number of encounters n is [25]:

$$\int \left(\sum_1^n l_i \cos\theta_i\right)^2 \prod_1^n g\left(l_k\right) \mathrm{d}l_k \frac{\mathrm{d}\cos\theta_k}{2} = n\frac{2}{3}l_0^2 = \frac{2}{3}\frac{l_0^2}{\tau}t \,, \tag{4.31}$$

$l_i \cos\theta_i$ is the displacement between the $(i-1)$-th and the i-th collision. This leads to the diffusion coefficient D [25]:

$$D = \frac{l_0^2}{3\tau} = \frac{v l_0}{3} = \frac{v^2\tau}{3} = \frac{2}{3}\frac{\epsilon}{m}\tau \,. \tag{4.32}$$

With the thermal energy $\epsilon = \frac{3}{2}kT$ and the electron mobility $\mu = \frac{e}{m}\tau$ this results in [25]:

$$\frac{D}{\mu} = \frac{kT}{e} \,. \tag{4.33}$$

With this, the diffusion width σ after a drift of length L can be expressed as [25]:

$$\sigma^2 = 2Dt = \frac{2DL}{\mu E} = \frac{4\epsilon L}{3eE} \,. \tag{4.34}$$

So far, the calculations assumed an isotropic drift, but it was observed in experiments (e.g. [30]) that the diffusion in direction of the electric field differs from the diffusion orthogonal to this. This is called “electric anisotropy”.

For the anisotropic case, a different density distribution to the one in Equation 4.29 follows [25]:

$$n = \frac{1}{\sqrt{4\pi D_{\mathrm{L}} t}} \left(\frac{1}{\sqrt{4\pi D_{\mathrm{T}} t}} \right)^2 \exp \left(-\frac{x^2 + y^2}{4D_{\mathrm{T}} t} - \frac{(z - vt)^2}{4D_{\mathrm{L}} t} \right) . \tag{4.35}$$

Here D_{T} and D_{L} are the transversal and the longitudinal diffusion coefficients replacing the isotropic diffusion coefficient D. For the detectors that will be presented in Chapter 7, the transversal diffusion influences the width of detected tracks. The longitudinal diffusion influences the time, when an electron is detected. As the time is proportional to the position in z-direction, the longitudinal diffusion thus influences the resolution in the z-direction.

4.4 Gas Amplification

A single electron that arrives at the readout cannot create a signal that is distinguishable from the electronic noise. This is apparent, as the equivalent noise charge (ENC) of the used ASICs (see Chapter 5) is in the order of several hundred electrons. This noise is suppressed by a discriminator with an adjustable threshold. Thus, to detect the electrons they need to be amplified, such that they generate a signal above the threshold. For this, a region with a high electric field, the amplification field E, can be used which is entered by the electrons after the drift field. In such conditions a single charge can start an avalanche of charges, leading to a charge multiplication.

The multiplication of charges in a high electric field due to gas amplification is described by the first Townsend coefficient α. It describes the change of the number of charges $\mathrm{d}N$ per unit length $\mathrm{d}s$ [25]:

$$\mathrm{d}N = N\alpha \mathrm{d}s . \tag{4.36}$$

This coefficient depends on the cross sections for ionisation and excitation of the used gases as this determines if the electrons have sufficient energy to further ionise the gas. Furthermore, it depends on the electric field E and the gas density ρ. There is no fundamental expression for the Townsend coefficient and thus it needs to be measured for each individual gas mixture. Based on Equation 4.36 the number of electrons after the path from s_0 to s_{a} with a start of N_0 electrons can be calculated with [26]:

$$N(s_{\mathrm{a}}) = N_0 \exp \left(\int_{s_0}^{s_{\mathrm{a}}} \alpha (E(s)) \, \mathrm{d}s \right) . \tag{4.37}$$

As the gas gain G is the ratio of the electrons at the start and the end it follows [26]:

$$G = \frac{N(s_{\mathrm{a}})}{N_0} = \exp \left(\int_{s_0}^{s_{\mathrm{a}}} \alpha (E(s)) \, \mathrm{d}s \right) . \tag{4.38}$$

For the case that the Townsend coefficient α does not depend on s, the gas gain can be expressed as [26]:

$$G = \exp \left(\alpha \left(s_{\mathrm{a}} - s_0 \right) \right) \tag{4.39}$$

As α is usually energy dependent and the energy distribution of the electrons depends on the electric field, this requires a constant electric field. The gain describes only the mean of the amplification. As the ionisation is a statistical process the size of an electron avalanche has a distribution. For strong homogeneous fields, the distribution was described by Legler [31] based on the parameter [25]:

$$\chi = \frac{\alpha\left(E\right)U_i}{E}\,, \tag{4.40}$$

with the Townsend coefficient α, the electric field E, and the ionisation potential U_i of the gas. These distributions are a solution of the following equation [31]:

$$\nu\alpha P' - \left(\alpha_0 - \alpha\right)P + \alpha_0 + \exp\left(\alpha x_0\right)\int_0^{\nu\exp\left(\alpha x_0\right)} P\left(\nu'\right)P(\nu\exp\left(\alpha x_0\right) - \nu')\mathrm{d}\nu' = 0\,, \tag{4.41}$$

with $\nu = n/\overline{n}$ and [31]:

$$\alpha_0 = \frac{\alpha}{2\exp\left(-\alpha x_0\right) - 1}\,. \tag{4.42}$$

While an explicit expression of the probability distribution does not exist the variance for high amplifications and thus for a high number of average electrons in an avalanche $\overline{n}$ was calculated by Alkhazov as [25, 32]:

$$\begin{aligned} \sigma^2 &= \overline{n}^2 f_0\left(\chi\right) && (4.43)\\ &= \overline{n}^2\frac{\left(2e^{-\chi}-1\right)^2}{4e^{-\chi}-2e^{-2\chi}-1} && (4.44)\\ &\approx \overline{n}^2\left(2e^{-\chi}-1\right)^2\,. && (4.45) \end{aligned}$$

In strong non-uniform fields often the Pólya distribution is used that is defined as follows [25]:

$$P\left(n\right) = \frac{1}{\overline{n}}\frac{\left(\theta+1\right)^{\theta+1}}{\Gamma\left(\theta+1\right)}\left(\frac{n}{\overline{n}}\right)^{\theta}\exp\left(-\left(\theta+1\right)\frac{n}{\overline{n}}\right)\,, \tag{4.46}$$

with

$$\sigma^2 = \frac{\overline{n}}{\theta+1}\,. \tag{4.47}$$

Figure 4.3 shows this distribution for a range of values of $f = 1/(\theta+1)$. Even though measurements have shown that the distribution in Equation 4.46 does not describe the data completely for the homogeneous field case [33], it is still frequently used to characterise the gas gain distribution for such cases.

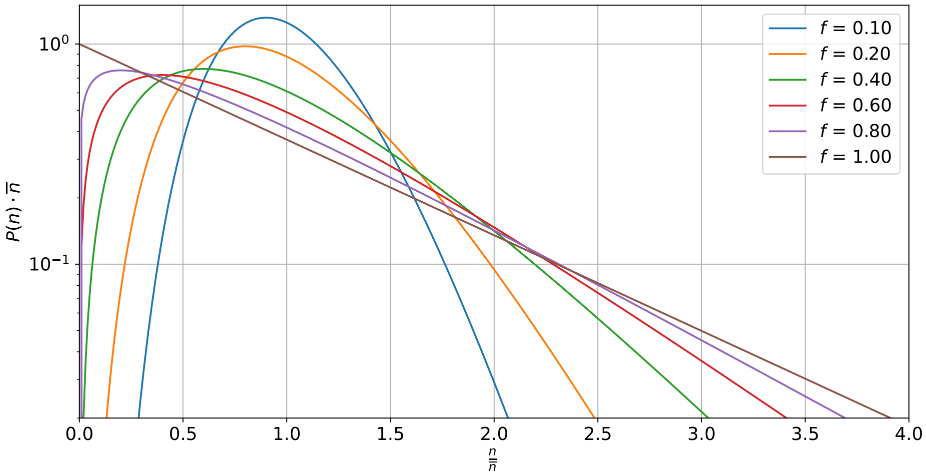

Figure 4.3: Pólya distribution for different values of $f = 1/(\theta + 1)$. Based on [25]

.

4.5 Penning Effect

In gas mixtures in which the excitation energy of one element of the mixture is higher than the ionisation potential of another gas element the ionisation process [25]

$$\mathrm{A^*B} \longrightarrow \mathrm{AB^+e^-} \tag{4.48}$$

can occur in which an exited atom or molecule ionises another atom or molecule and thus creates an electron-ion pair. This effect is called the “Penning effect”. As it depends on the excitation and ionisation energies, it directly depends on the gas choice. Furthermore, the efficiency of this process depends on the mixing ratio and the pressure of the gas. This effect changes for each gas mixture the effective mean energy per electron ion pair as the efficiency of this process must be considered in addition to just the mean energies per electron ion pair for the individual gases. Furthermore, this can increase the gas gain as it is an additional source of electrons for the amplification avalanche. Unfortunately, the exact contribution of the effect to the ionisation is not known [25] and therefore measurements or models based on measurements are required.

CHAPTER 5

Timepix and Timepix3

For the operation of the detectors that are described in this thesis (more details in Sections 7.2 and 7.3) two pixel ASICs were used: the Timepix and the Timepix3. They are the base for GridPixes (see Section 7.1) that combine these ASICs with a micro-patterned gas amplification stage. This chapter describes the features and capabilities of the Timepix (Section 5.1) and the Timepix3 (Section 5.2).

5.1 The Timepix ASIC

The Timepix is a pixel ASIC (application-specific integrated circuit) developed by the Medipix2 collaboration [34] based on the Medipix2 ASIC. It features a 256 x 256 pixel matrix with a pixel pitch of 55 µm which results in an active area of about $1.96\,\mathrm{cm}^2$. The ASIC features a common threshold that is composed of a fine and a coarse threshold digital to analogue converter (DAC) plus an additional pixel threshold that can be varied individually per pixel in 16 steps to tune the pixel matrix for a uniform response. The ASIC is taking data in a frame-based mode which means that as long as an externally provided shutter signal is low the pixels accumulate data. When the shutter is set to high, the accumulation stops, and the data can be read out. In comparison to a photo camera a high shutter signal can be interpreted as a closed shutter and a low signal, as an open shutter. But in contrast to a photo camera no mechanical shutter is present in the Timepix, and the shutter is purely digital. At the end of a shutter period, all 65536 pixels are read out without zero suppression. This means that all pixels sent their data, even if they did not detect any signals that above the threshold. In terms of what data is accumulated by the pixels the Timepix has four different modes that can be set individually per pixel (a scheme of the first two modes is presented in Figure 5.1):

- The **Time over Threshold** (ToT) mode measures the detected charge in a pixel by measuring the time to discharge a capacitor. The current for discharging the capacitor is set via a DAC. This current is called the Krummenacher current [35]. The time is measured in terms of clock cycles of the system clock of the ASIC, so that a calibration curve to convert counted clock cycles to charge is needed. The ToT counter starts as soon as the analogue signal rises above the threshold. It stops when either the analogue signal falls below the threshold or if the shutter signal is switched to its “closed” state. The latter happens independent of the analogue signal and effectively interrupts active ToT measurements. The ToT counter is presented in Figure 5.1 by the grey ToT signal: a discriminator signal is as long high as the analogue signal is above the threshold. During this time frame the ToT measures the signal length in units of clock cycles. This can be interpreted as a charge measurement, as the pixel is discharged by the adjustable Krummenacher current.

- The **Time of Arrival** (ToA) mode counts the clock cycles from a threshold crossing in a pixel until the end of the frame that is marked by "closing" the shutter signal of the ASIC. So, the higher the counted value in clock cycles is, the earlier in time the pixel detected a signal. This is presented in Figure 5.1 by the grey ToA signal: as soon as the analogue signal crosses the threshold, the number of clock cycles is counted until the shutter signal is set to high. Thus, the time of the detection is measured with respect to the shutter signal.
- The **Medipix** mode counts the amount of threshold crossings within a frame to count the signals in a pixel.
- The **Binary** mode shows if a pixel measured a signal within a frame (1) or not (0).

For the first three modes each pixel features a counter that can count up to 11810 and then keeps this value as an overflow indicator. The counter is reset to 0 only after a readout of the pixel or after a reset of the ASIC. For the system clock of 40 MHz this effectively limits the ToA mode to shutter times of 295.25 µs. For calibration purposes the ASIC features an analogue input for test pulses. These pulses are generated externally as voltage steps and are connected to an internal input capacitance of 8 fF per pixel. This input can be pixel-wise disconnected so that test pulse injection patterns into the pixel matrix can be generated and cross-talk influence on tests can be minimised. Furthermore, each pixel can be deactivated by masking it, to exclude noisy pixels from the readout but also to allow for scan patterns together with the test pulse injection to test and calibrate the ASIC.

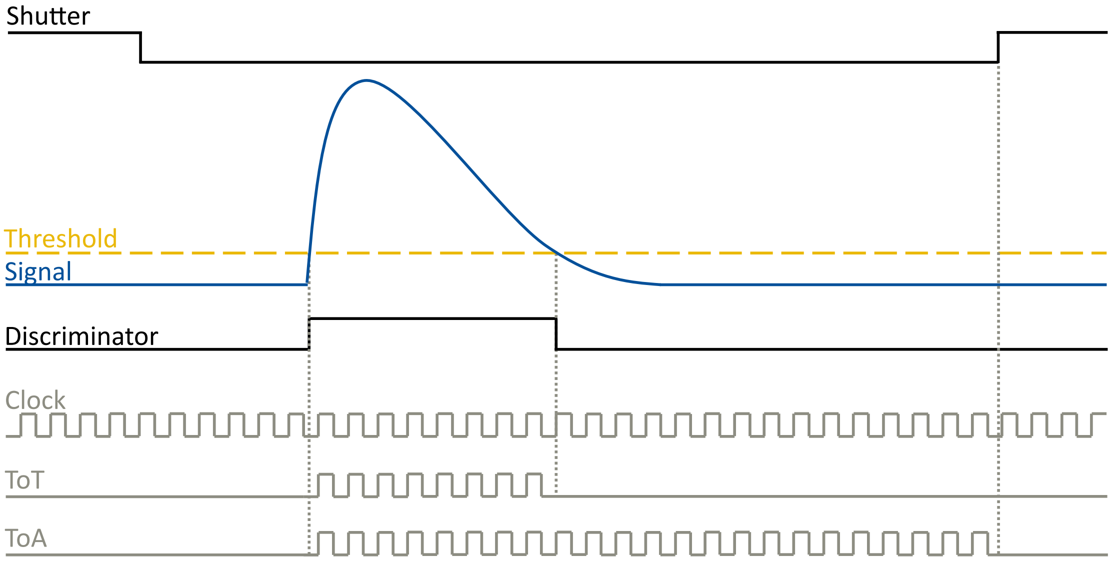

Figure 5.1: Sketch of the readout procedure of the Timepix ASIC. When the shutter signal is low, the pixels are active. If during this time the signal crosses the threshold a discriminator signal switches its state to high. Depending on the readout mode, either the time over threshold (ToT) is counted in terms of clock cycles or the time of arrival (ToA) in terms of clock cycles until the "closing" of the shutter. Based on [36].

5.2 The Timepix3 ASIC

The Timepix3 is a pixel ASIC developed by the Medipix3 collaboration [37]. It is the successor of the Timepix ASIC (see Section 5.1). It also features a 256 x 256 pixel matrix with a pixel pitch of 55 µm. Figure 5.2 shows a timing diagram of the Timepix3.

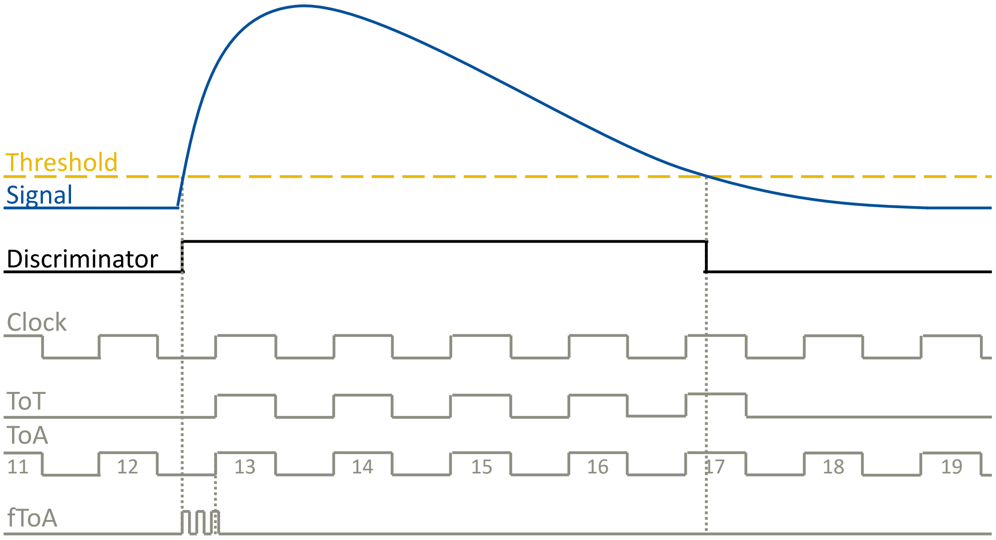

Figure 5.2: Sketch of the readout procedure of the Timepix3 ASIC. While the analogue signal is above threshold a discriminator signal is high. In the combined ToT and ToA mode of the Timepix3, the ToT counts the clock cycles of a high discriminator signal. This gives a measurement of the charge injection into a pixel. For the Timepix3 a global timer is running which is read out after a rising edge of the discriminator signal. This is a measurement of the time of detection. In case of this sketch the ToA 13 will be assigned to the hit. In case of an active fToA of the Timepix3 an additional counter with a higher frequency is used to count the clock cycles between the rise of the discriminator signal and the next rising edge of the ToA, to improve the time resolution. Based on this design, a higher ToA count corresponds to a later detection, while a higher fToA count corresponds to an earlier detection. For the Timepix3 the ToT and ToA clocks are 40 MHz clocks and the fToA clock is a 640 MHz clock. In this sketch these two clocks are not to scale. Based on [38].

The Timepix3 offers several improvements over Timepix:

- **Internal test pulses**: In addition to the possibility to provide external test pulses, the Timepix3 incorporates an internal test pulse circuitry. The amplitudes of these test pules are controlled via two voltage DACs: the “VTP_fine” and the “VTP_coarse”. The test pulses are then generated by multiplexing between these two voltage levels and connecting these voltage pulses to a 3 fF input capacitance of the pixels. Thus, a charge pulse is created.
- **Threshold range**: Similar to the Timepix the Timepix3 features two threshold DACs the “Vthreshold_fine” and the “Vthreshold_coarse”. For the overall threshold of the Timepix3 the voltages of these two DACs are added up. In comparison to the Timepix, the fine threshold DAC of the Timepix3 has a smaller dynamic range and just 512 instead of 1024 voltage steps. At the same time, the coarse threshold now features 256 voltage steps instead of 16. In the combination of both, most threshold voltages can be represented by three different combinations of the fine and the coarse threshold DACs.

- **Temperature sensor**: The Timepix3 features a possibility to measure the chip temperature via an internal band gap voltage. While this voltage changes with the temperature a second band gap voltage can be read out that is constant with respect to the temperature. The comparison of these two voltages can be used to calculate the temperature of the Timepix3. For reading them out both can be connected to an output of the ASIC via the DAC settings and then an external ADC can be used.

- **ToT/ToA readout**: Instead of selecting either a measurement of the charge in ToT mode or the time in ToA mode the Timepix3 offers a combined ToT/ToA mode. Here, the charge is measured as it was described or the Timepix. But the time measurement uses a global timer within the Timepix3 and does not rely on a shutter signal. A sketch of the readout of this mode is presented in Figure 5.2.

- **ToA measurement**: In comparison to the Timepix the ToA of the Timepix3 has no overflow but rolls over to 0 after it reaches its maximum value. Furthermore, it does not count until the "closing" of the shutter but is based on a global timer in the Timepix3 that is read out when a signal in a pixel crosses the threshold. Thus, an event with a higher ToA appears later in time than an event with a lower ToA. Based on the 14 bits of the ToA and the 40 MHz system clock of the Timepix3 there are unique ToAs for a cycle of 409.6 µs.

- **ToA resolution**: Additionally to the ToA which runs on the system clock of the Timepix3, also a fast ToA (fToA) is present. It runs on a 640 MHz clock that is generated internally and can be activated in all modes that use the ToA. With this, the time binning can be reduced to 1.5625 ns. The fToA runs in the opposite direction of the ToA as it counts the clock cycles from the threshold crossing till the next rising edge of the ToA clock. Thus, higher fToAs mean earlier in time while higher ToAs mean later. This is sketched in Figure 5.2, where the fToA counts three clock cycles until the rising edge of the ToA. Thus, the timestamp for this example can be calculated as:

$$T = 13 \times 25.0000\,\mathrm{ns} - 3 \times 1.5625\,\mathrm{ns} = 320.3125\,\mathrm{ns}\,. \tag{5.1}$$

- **Event counter mode**: The Medipix mode of the Timepix was updated perform an integrated charge measurement (iToT) in addition to the signal counting on each individual pixel. This mode is called "Event count & iToT" mode.

- **Data-driven readout**: Additionally to a frame-based mode, which is called "sequential" readout for the Timepix3, a data-driven readout mode is implemented that pushes the data out of the ASIC as soon as it was processed by the pixel.

- **Zero suppression**: All modes of the Timepix3 offer an intrinsic zero suppressed readout, so only pixels that detected signals above the threshold are read out. This reduces the needed data rate especially in low occupancy operations and also reduces the dead-time.

- **Data output**: The Timepix3 features 8 data output links that can be set to a range of output bandwidths with a maximum of 640 Mbps per link in case of an output clock of 320 MHz sending the data in double data rate (DDR). The output clock can be either generated and provided externally or it can be generated internally with a phased lock loop block (PLL) running on the 40 MHz system clock of the Timepix. Furthermore, all links can be individually activated and deactivated.

- **Protocol-based communication**: The Timepix3 offers a protocol-based communication to write data to the ASIC and to receive data from it. The structure of the protocol for sending data is presented in Figure 5.3. If the data is sent to the periphery of the Timepix3 the input commands are always 64 bits long. The term "periphery" represents the general registers of the ASIC like DACs or the configuration registers. Commands for the pixel matrix can be up to 393264 bits long as they contain 6 bits of individual information for each of the 65536 pixels. These 6 bits contain the 4-bit pixel threshold, 1 bit to mask the pixel and 1 bit to activate test pulses for the pixel. Besides the data payload there is a 4- to 8-bit operation header that indicates the operation that should be triggered by the command and a 40-bit synchronisation header that indicates if the operation should be performed by all Timepix3s that receive the command or just by one. Therefore, this header can contain the chip ID that is individual for each Timepix3 and consists of the wafer ID the Timepix3 was produced on and the position that the Timepix3 had on the wafer. The composition of the synchronisation headers is presented in Figure 5.4. The response and readout words of the Timepix3 are all 48 bits long. The composition of the readout words is presented in Figure 5.5. Besides an indication of 4 bits if the data was read out sequentially or data-driven and a 16-bit address of the pixel from which the data originated, each word contains 28 bits of data. The specific data depends on the readout mode of the Timepix3.

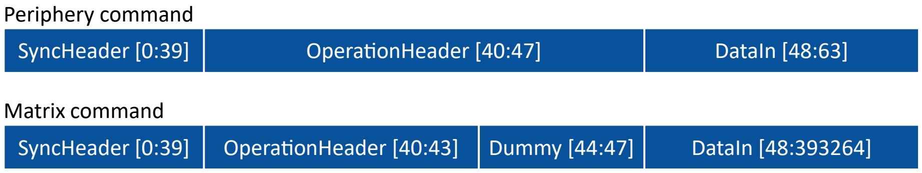

Figure 5.3: Composition of input words for the Timepix3. Each command starts with a 40-bit header that contains the information which Timepix3 ASICs should perform the command. This is followed by an operation header that contains the information which command should be performed. This is either 8 bits long if it is a command for the periphery (DACs and configuration registers) of the ASIC or 4 bits long if it is a command for the pixel matrix. In the latter case the remaining 4 bits are filled with zeros. For periphery commands the input word is concluded with 16 bits of data. Its composition is specific for each operation header. For matrix commands the data consists of up to 393216 bits which breaks down to 6 bits per pixel in the pixel matrix. Based on [38].

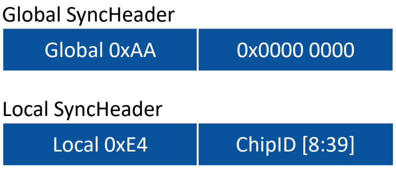

Global SyncHeader

Global 0xAA	0x0000 0000

Local SyncHeader

Local 0xE4	ChipID [8:39]

Figure 5.4: Composition of synchronisation headers of the Timepix3. For these headers there are two options: the global header is used to address all connected Timepix3s, and the local header only addresses a specific Timepix3. The former is indicated with the first 8 bits containing AA in hexadecimal while the latter is indicated with E4. The global synchronisation header is followed by 32 binary zeros while the local synchronisation header is followed by the 32-bit chip ID of the Timepix3 that should perform the command. The chip ID is unique to each Timepix3 and consists of the wafer number and the position of the chip on the wafer. Based on [38].

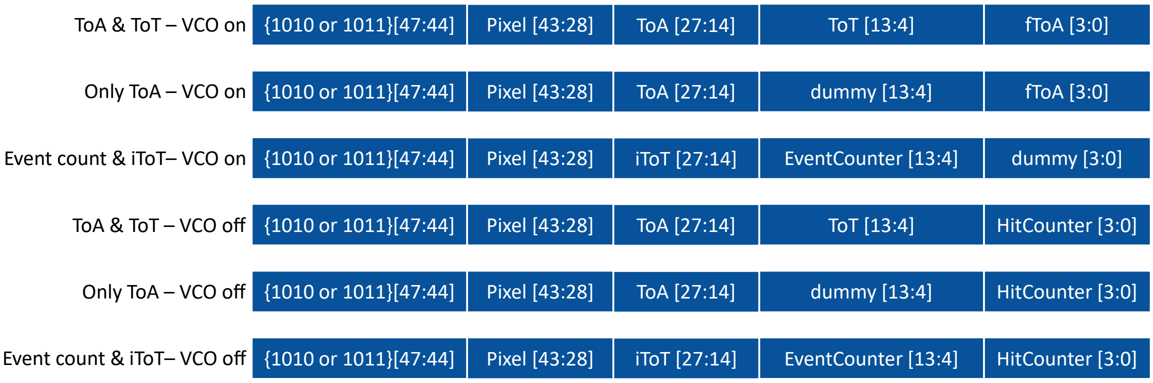

ToA & ToT – VCO on	{1010 or 1011}[47:44]	Pixel [43:28]	ToA [27:14]	ToT [13:4]	fToA [3:0]
Only ToA – VCO on	{1010 or 1011}[47:44]	Pixel [43:28]	ToA [27:14]	dummy [13:4]	fToA [3:0]
Event count & iToT– VCO on	{1010 or 1011}[47:44]	Pixel [43:28]	iToT [27:14]	EventCounter [13:4]	dummy [3:0]
ToA & ToT – VCO off	{1010 or 1011}[47:44]	Pixel [43:28]	ToA [27:14]	ToT [13:4]	HitCounter [3:0]
Only ToA – VCO off	{1010 or 1011}[47:44]	Pixel [43:28]	ToA [27:14]	dummy [13:4]	HitCounter [3:0]
Event count & iToT– VCO off	{1010 or 1011}[47:44]	Pixel [43:28]	iToT [27:14]	EventCounter [13:4]	HitCounter [3:0]

Figure 5.5: Composition of output words during a readout of a Timepix3. Such an output word is transmitted for each hit during a readout. The overall scheme of the words is the same but the content of the last three blocks depends on the readout mode of the Timepix3. The first 4 bits indicate if the readout is performed in sequential (1010) or in data-driven (1011) readout. The next 16 bits contain the coordinates of the pixel that recorded the hit. The following 14 bits store the recorded ToA in the ToA & ToT and in the only ToA mode. In the event count & iToT mode the iToT is stored in these 14 bits. The next 10 bits contain the ToT in the ToA & ToT mode and a counter of detected hits in the event count & iToT mode. In case of the only ToA mode these bits contain no information and are just filled with binary zeros. The final 4 bits also contain a counter of hits if the 640 MHz clock (VCO) is switched off. They contain the fToA if it is switched on. In case of the event count & iToT mode these 4 bits contain no data and are filled with binary zeros if the 640 MHz clock is switched on or just a repetition of the final 4 bits of the 14-bit counter if it is switched off. Based on [38].

CHAPTER 6

Timepix3 Control and Readout System

To control and readout Timepix3 ASICs a data acquisition (DAQ) system was developed [1]. This chapter will first give an overview of the design of the DAQ system (Section 6.1), followed by an introduction into hardware (Section 6.2), firmware (Section 6.3) and software (Section 6.4). Sections 6.5 and 6.6 will give an in-depth description of the scans and calibrations of the readout system and the user interfaces. Finally, the monitoring system for the chip will be discussed (Section 6.7). Within the scope of this thesis, also some improvements were added to the readout system of the Timepix: the Timepix operating software (TOS) that works with the Timepix operating firmware (TOF). Details on this system can be found in [39] and [40].

6.1 Conceptual Design

The goal of the development of the Timepix3 control and readout System (tpx3-daq) was to build an open-source system that is modular and scalable. A schematic overview of the full system is shown in Figure 6.1. There are three main levels within the architecture: the *Hardware & firmware level*, the *Software & storage level* and the *User interface level* or short *UI level*. Each major part of the readout system will be described in detail in the following sections.

On the *Hardware & firmware level* modularity is achieved via different supported FPGA (field-programmable gate array) boards (Sections 6.2 and 6.3) and different supported intermediate boards. Additionally, the microcontroller that is used for monitoring (details in Section 6.7) can be connected to different sensors depending on the application and is itself completely optional. The scalability is achieved by supporting up to 8 Timepix3s that are connected to one intermediate board. For the future it is planned to support multiple intermediate boards that are connected to the same FPGA but also operating multiple FPGAs in parallel will be supported.

At the *Software and storage level* a common software controls all connected Timepix3 ASICs independently if they are organised in the readout as several ASICs connected to one intermediate board or via multiple FPGA boards connected to multiple intermediate boards. The chip specific settings are stored in common configuration files that differentiate between Timepix3s using their unique name — the Chip ID. In this level also the storage of data is handled by separated systems for

---

[1] https://github.com/GasDet-Bonn/tpx3-daq

the Timepix3 data and the monitoring data. Thus, the monitoring stays optional and depending on the needs of the setup also readout and monitoring can be operated on different readout computers.

In the third level, the *UI level*, control interfaces and information of the scripts in the software and storage level are forwarded to user interfaces. These interfaces offer users access to all functionality, settings and status information that are needed to operate the front-end electronics. Depending on the setup either a command line interface or a graphical user interface can be used, in addition to a plotting and alerting tool for the monitoring system. Furthermore, it is possible to develop a new interface based on the connections to the software to include the system in other readout infrastructures.

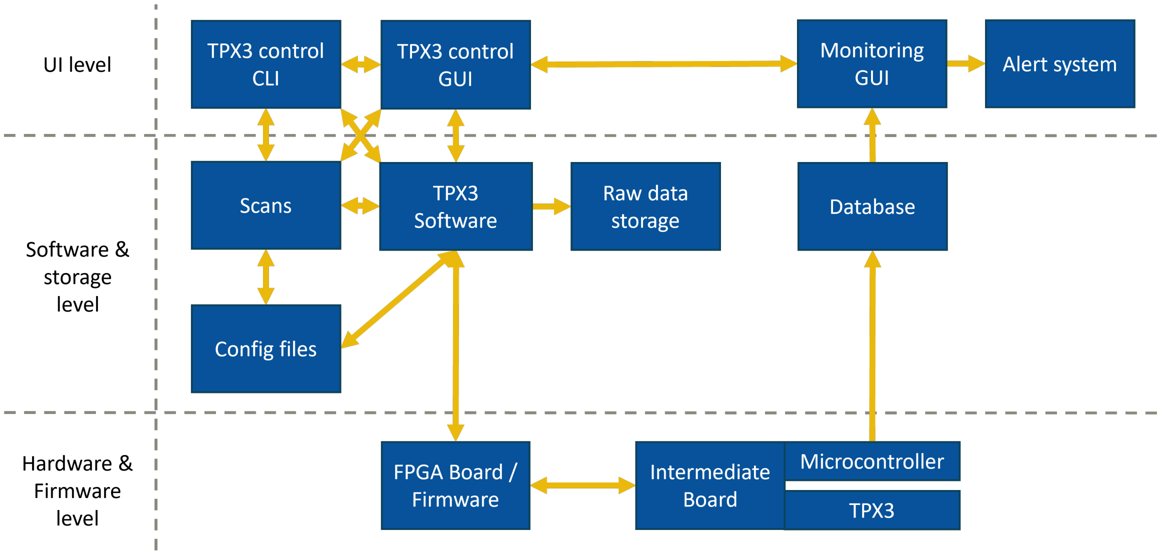

Figure 6.1: Schematic of the tpx3-daq.

6.2 Hardware

The hardware design of the Timepix3 readout system adopts the hardware design of the Timepix readout system [39, 40] which is similar for DAQ systems that use the Front-end Concentrator Card (FEC) of the RD51 Scalable Readout System (SRS) [41] as an FPGA board.

The Timepix3 is glued and wire bonded to a PCB that is called “Carrier Board”. A rendering of this board is presented in Figure 6.2. One can see the Timepix3 in the top centre and the pads for the wire bonds to connect it to the low voltage power supply and the readout below. To the left side an additional pad is visible that is used for a wire bond to connect a high voltage either for a GridPix (see Section 7.1) or for biasing a semiconductor sensor. On the backside several capacitors are visible that buffer power consumption changes of the Timepix3 to keep a constant voltage level. Furthermore, two plugs are visible that are used to connect the high voltage via the connector on the top right (J2) and to connect the low voltage and the readout via the connector on the bottom centre (J1).

These two plugs are used to connect the carrier board to a custom PCB, named “Intermediate Board”. A rendering of the intermediate board is presented in Figure 6.3. It offers connectivity to a low voltage power supply (J3) for powering the Timepix3 and additional devices like signal drivers on the board (labelled as 0 to 7 and CLK). Additionally, there are DisplayPort connectors for the input

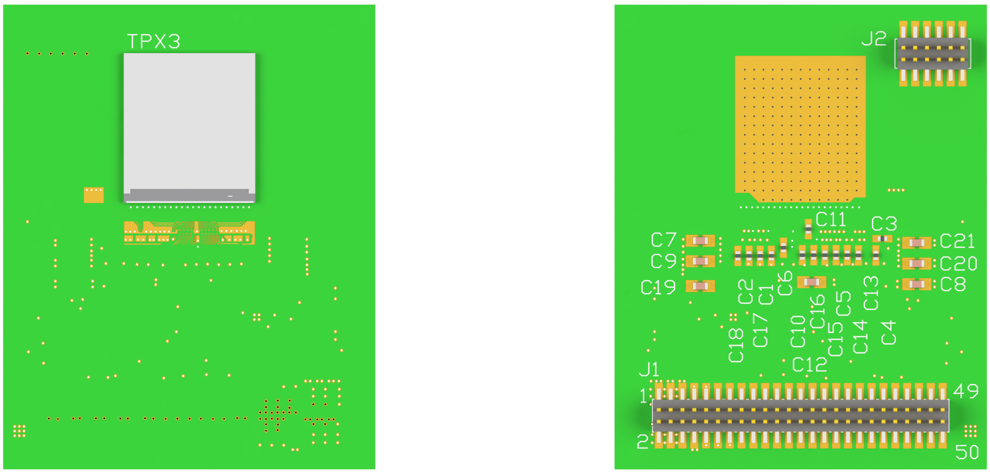

(a) Top view (b) Bottom view

Figure 6.2: Rendering of the carrier board for the Timepix3 readout system. A carrier board for a single Timepix3 is presented. [42]

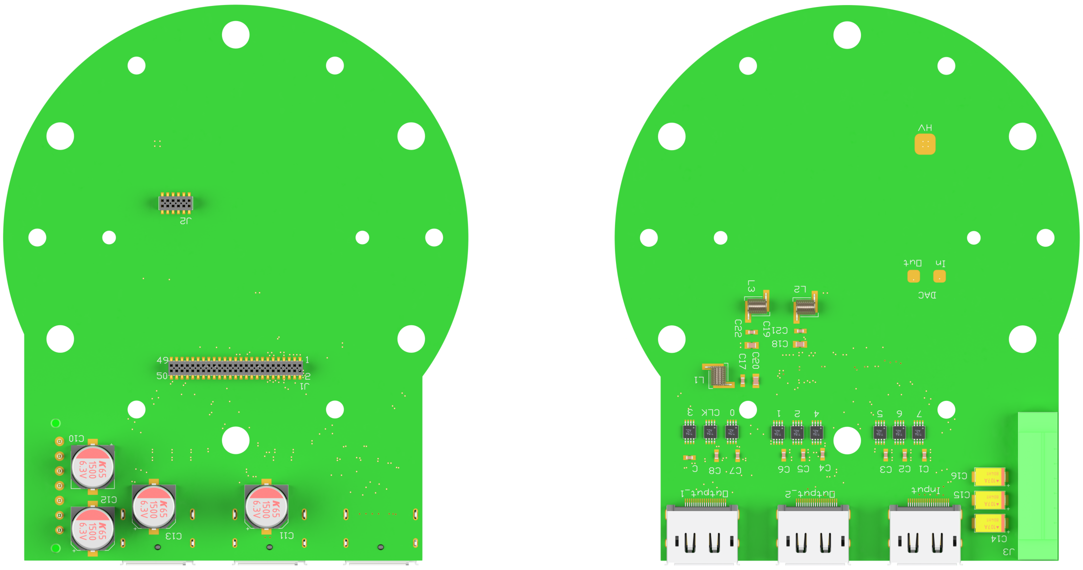

(a) Top view (b) Bottom view

Figure 6.3: Rendering of the intermediate board for the Timepix3 readout system. Carrier boards with up to 8 Timepix3 ASICs can be plugged into the intermediate board. [42]

and output signals of the Timepix3. Optional USB and Ethernet connectors are used for monitoring purposes (see Section 6.7) and SHV or LemoHV connectors for high voltage power supplies for a potential grid on the Timepix3 and other detector electrodes like an anode or a field cage (more details in Section 7.3). The "Intermediate Board" supports 8 output links for Timepix3 data. As the Timepix3 can be configured to use between 1 and 8 of its output links, "Carrier Boards" with up to 8 Timepix3 ASICs are compatible with the intermediate board. But the usage of multiple Timepix3s reduces the maximum data output rate, as less links per ASIC are available.

The "Intermediate Board" is connected via three DisplayPort cables to the "Adapter Card". This is a custom PCB that adapts the DisplayPort connection to the connection interface of the FPGA board. The specific interface of the FPGA depends on its type and therefore needs its own adapter card. For example, the ML605 board has an FMC plug, while the SRSv6 offers a PCI interface. The "Adapter Card" can host additional devices like signal drivers depending on the specific needs of the setup.

The FGPA board runs the firmware for the readout system (see Section 6.3) and connects via Ethernet to the readout PC that runs the DAQ software (see Section 6.4). Table 6.1 shows a list of supported FPGA boards with their capabilities, relative cost and plug type for the adapter card. As the adapter card always connects the FPGA-specific plug to DisplayPort, the intermediate board and the carrier board can be operated independent on the selection of the FPGA board if the necessary capabilities of for the operation of a detector do not exceed the capabilities of the FPGA board.

Table 6.1: List of FPGA boards that are supported by the Timepix3 readout system

Board	FPGA	Manufacturer	Supported rate	Cost	Connector
MIMAS A7	AMD Artix 7	Numato Lab	Low	Low	80-pin GPIO
ML605	AMD Virtex 6	AMD (deprecated)	Medium	Medium	FMC
SRS FECv6	AMD Virtex 6	SRS Technology	Medium	Medium	PCI
VCK 190	Versal AI Core	AMD	High	High	FMC+

6.3 Firmware

The firmware of the tpx3-daq readout system runs on the FPGA boards that were presented in Section 6.2 and Table 6.1. The main purpose of the FPGA and its firmware is to connect the readout PC that communicates asynchronously via Ethernet and the Timepix3 that needs a precise timing of provided input signals and also a precise timing to sample the output signals. The FPGA provides the connections and signals based on the firmware for this.

Data Output

Figure 6.4 describes the processing of Timepix3 data within the FPGA from the output of the adapter card up to the common part of the communication modules of the FPGA. In total eight such processing pipelines are implemented — one for each output link in the hardware. In the first step the two differential LVDS (low-voltage differential signaling) signals per output link of the Timepix3 are combined into a single signal that can be used in the FPGA. In the next step this signal is sampled with a clock that is generated within the FPGA. The data is transmitted in double data rate (DDR) by the Timepix3. This means that there is a data bit at each rising and falling edge of the output clock.

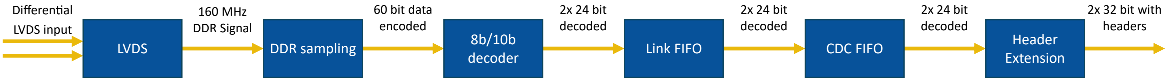

Figure 6.4: Schematic of the firmware part of the tpx3-daq readout system that is responsible for processing the data generated by the Timepix3. The data starts at the left side as a differential LVDS output of the Timepix3 and ends on the right side. This chain of processing steps is done for each of the 8 links that are implemented in the firmware.

Thus, the sampling clock needs twice the frequency to sample all bits just with the rising edge of this clock. For the sampling, the phase of the clock can be shifted to match the phase of the data. In the default state of the tpx3-daq readout the Timepix3 output is 160 MHz DDR which leads to a sampling clock of 320 MHz in the FPGA. In the next step, the data is decoded by an 8b10b decoder that runs on the sampling clock of 320 MHz. This converts back the 8b10b encoded 60-bit word of the output of the ASIC into the originally recorded 48-bit word. At this stage, every 48-bit word of the Timepix3 is split up into two 24-bit words, which are stored in a FIFO-buffer[2]. This is necessary to handle time periods in which more data arrives at the input of the data processing chain than can exit it at the same time. An additional small FIFO buffer is added afterwards at a so-called clock domain crossing (CDC). This enables the possibility to run all previous blocks not on clocks generated by the FPGA but on an internal clock of the Timepix3. This clock is generated by the PLL of the Timepix3 and is synchronised to the output data. Via the configuration registers, this internal clock can be connected to an output pad and then transmitted to the readout system. This can be used as replacement for the FPGA internal sampling clock. Thus, these first blocks would run on the same clock as the data, if there are no length differences in the transmission cables. But with this, the first block would run on a different clock generation than the later blocks and thus small delays between these two clock domains are possible. This CDC FIFO connects these domains and ensures via the buffer that no data is lost due to small delays.

After the FIFOs, the 24-bit words are extended to 32-bit words via the addition of an 8-bit header. Table 6.2 shows in the last two rows the possible headers for data the originates from the Timepix3. The least significant bit indicates if the 24 data-bits are the first or the second part of a 48-bit word. The next four bits indicate on which data link the data was received. This helps to sort the data and is important for the interpretation of the data which recovers the original 48-bit words (see Section 6.8). Additionally, this enables in possible setups with multiple Timepix3 ASICs to assign data to a specific ASIC.

After adding the header to the words an arbiter combines the data of all active data links into one data stream. This concludes the chain of blocks that is repeated for every link in the firmware. Starting with the arbiter, each logic block is only once in the firmware, independent on the number of links. An overview scheme of the full output part of the firmware is presented in Figure 6.5. One can see that besides the output of the link-specific chains there are additional inputs to the arbiter. One is the output of a timer block that adds timestamps to the data stream. It is based on a 40 MHz timer that runs on the FPGA based on the 40 MHz clock that is provided as system and reference clock to the Timepix3. Using only the 14-bits ToA timestamps with a 40 MHz clock leads to unique timestamps for a time span of 409.6 µs. To provide a longer time span with unique timestamps the additional timer on the FPGA runs synchronously on the FPGA and sends a 48-bit timestamp every 102.4 µs to the arbiter.

---

[2] First In, First Out - the first element that is written to the buffer is also the first element that is read from the buffer

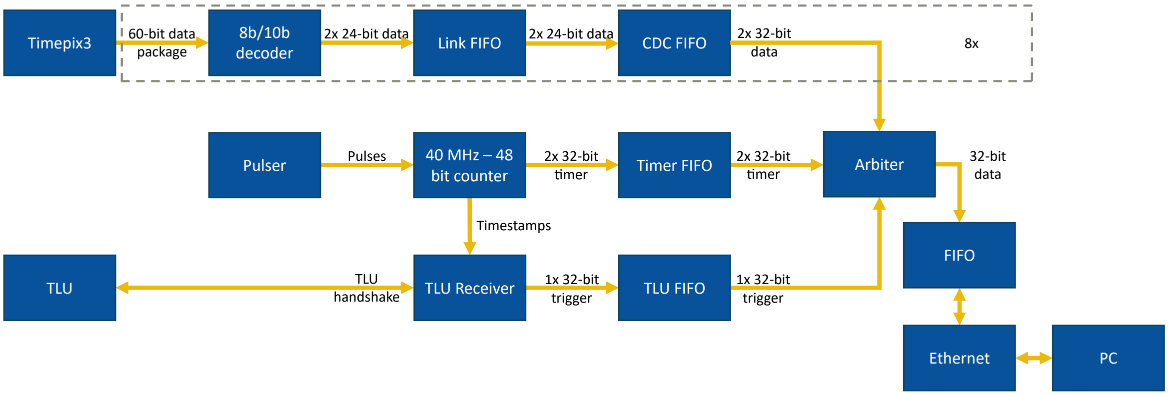

Figure 6.5: Schematic of the firmware part of the tpx3-daq readout system that is responsible for handling all data outputs to the readout PC.

These additional timestamps are called “ToA extensions” and have their own header as presented in Table 6.2. With these settings there are four ToA extensions per ToA cycle of the Timepix3 which means that based on the two most significant bits of the ToA there should be always a fitting ToA extension close by in the data stream. This extension results in unique timestamps for a cycle of 81.4 days. Specifically for the time walk calibration of the Timepix3 (see Section 6.5.9), a second timestamp is available. It is called the “Shutter timer”. This timer runs on a 320 MHz clock and always generates a timestamp on the first rising edge of the 40 MHz system clock that is transmitted to the Timepix3 after setting the shutter to its “open” state. In the time walk calibration it is needed to get a reference for the start of test pulse injections to the Timepix3. As test pulses are triggered by opening the shutter and start with the first rising edge of the system clock, this was also used as the signal for the creation of the timestamp. As visible in Table 6.2 the shutter timestamps have their own header so that they can be identified in the data stream.

A third optional block that can output data to the arbiter is a block for the EUDET/AIDA trigger logic unit (TLU) (see [43]). This device can create trigger signals with unique trigger IDs for multiple independent devices and delivers these signals to them via a handshake-based protocol. The tpx3-daq readout system combines them with a timestamp based on the 40 MHz timer and forwards them via a buffer to the arbiter. As displayed in Table 6.2 all TLU data has 1 as the MSB while the remaining 31 bits contain the trigger ID and the timestamp. Via the MSB the data can be differentiated from all other data sources, and it can then in an offline analysis be used to correlate data from the Timepix3 readout with data from other devices.

The combined data after the arbiter is forwarded in a common buffer in which the data is stored until a data request from the PC is received via Ethernet. Then the data is sent to the PC.

Data Input

A scheme of the input part of the firmware is presented in Figure 6.6. This part of the circuitry generates the signals that are sent to the Timepix3 and thus controls its operation. Furthermore, the settings of several firmware modules can be controlled. All signals have in common that they are generated on PC by the readout software (see Section 6.4) and then transmitted via Ethernet to various bus systems in the firmware.

Table 6.2: List of different headers for data transmissions from the FPGA to the PC

Header (binary)	Header (hexadecimal)	Use
1XXX XXXX		TLU words
0101 0001	51	ToA extension word 1
0101 0010	52	ToA extension word 2
0111 0001	71	Shutter timer word 1
0111 0010	72	Shutter timer word 2
000A AAA0		Hit word 1 on data link A
000A AAA1		Hit word 2 on data link A

For the data input of the Timepix3 a serial parallel interface (SPI) bus synchronises the data that is sent to the ASIC with the 40 MHz system clock. This is important because the Timepix3 uses this clock to sample the input data. Furthermore, the SPI bus sets the “Enable In” signal that indicates to the Timepix3 that there is a data input. For this, “Enable In” must be set to active before the first bit of the input data but after the rising edge of the previous system clock cycle so that the bits are correctly interpreted. In addition to these “synchronous” signals there are three “asynchronous” signals that are independent of the system clock. These signals are generated by a general-purpose input/output (GPIO) bus in the firmware. They can be directly toggled via commands in the software and are connected to the input of the Timepix3. Additionally, the “T0_Sync” signal that resets the internal timers of the Timepix3 is connected to the timer resets of the pulser for the ToA extension and the TLU receiver. Not shown is the connection of the 40 MHz system clock and the connection of the shutter to the pulser for the shutter timer.

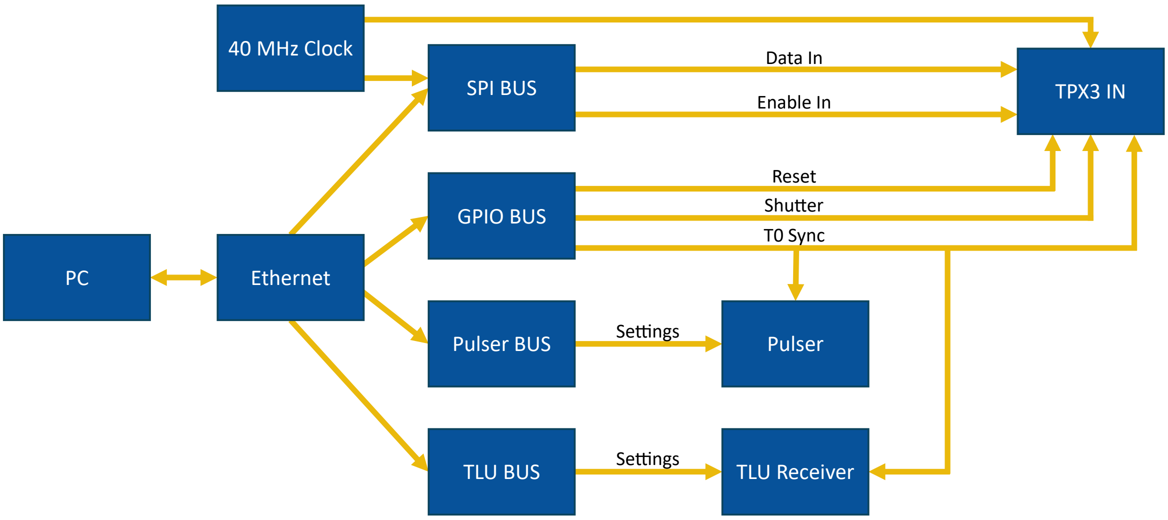

Figure 6.6: Schematic of the firmware part of the tpx3-daq readout system that is responsible for generating the input signals for the Timepix3 and the internal modules of the firmware based on commands provided by the readout PC.

6.4 Software Overview

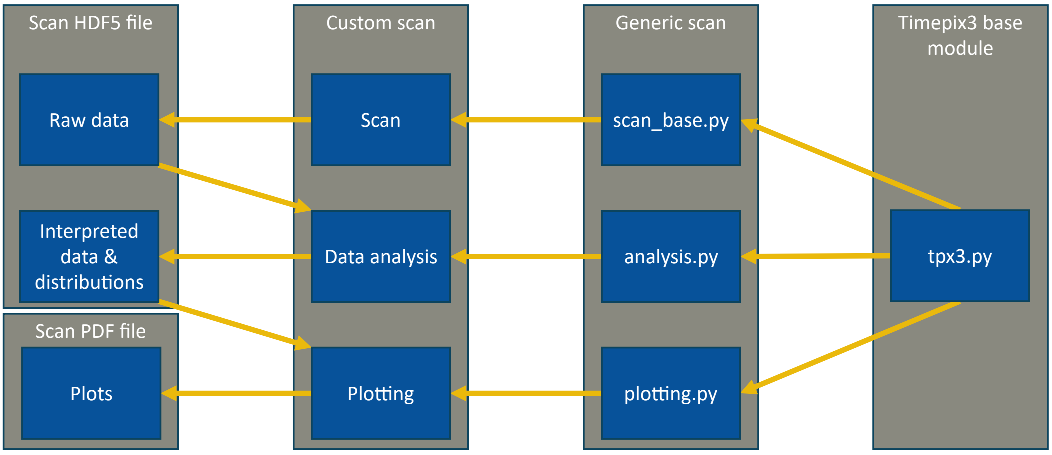

Figure 6.7: Architecture of the tpx3-daq software. The communication protocol of the Timepix3, all registers of it and the necessary functions to read from and write to the Timepix3 are defined in one base module that is called “tpx3.py”. A generic scan is defined based on this and offers all common functionality for custom scans. With this generic scan the custom scans are created by using the necessary parts of the generic scan with scan-specific settings. These scans store then first their raw data into an HDF5 file and during the analysis also add interpreted data and calculated distributions into it. At the end, plots are generated and stored as PDFs.

The software of the tpx3-daq readout system is written in Python and is based on the basil[3] framework. A schematic overview of the software is shown in Figure 6.7. Starting on the right side of the scheme, a base Python module for the operation of the Timepix3 is defined: “tpx3.py”. It contains definitions of all available registers of the Timepix3 (like general configuration or DACs), the definition of all available read and write functions and the implementation of the communication protocol of the Timepix3. The base module generates bit words that are sent via Ethernet to the FPGA and from there to the Timepix3 to control it. The configuration of the Timepix3 is stored locally and can be modified and sent to the chip. Thus, a configuration can be applied again after a reset. Based on this module, a generic scan consisting of the “scan_base.py”, the “analysis.py” and the “plotting.py” is defined. These three modules implement all common functions for performing and analysing scans and for plotting their results. Details about this generic scan can be found in Section 6.5.2. This generic scan is used as a template for all custom scans. They are a combination of a scan function to collect the data, an analysis function to interpret and analyse the data and a plot function. The plot function compiles all relevant plots of a scan into a PDF file. The individual scans use for this the common functionality defined by the generic scan plus additional functionality that its specific for only one individual scan.

For all scans, the raw and interpreted data is stored in HDF5 files — a file format designed for storing and organising large amounts of data. Thus, it is possible to repeat the data analysis without repeating the scan or to repeat the plotting without repeating the analysis. This creates the possibility for re-analysing and re-plotting of results for example with different start parameters or boundaries for fit parameters, or different axis scalings for plots. Details about all scans are described in Section 6.5.

---

[3] https://github.com/SiLab-Bonn/basil

6.5 Scans

To setup and operate Timepix3 ASICs and to get useful results, several scans and calibrations are needed. The following sections will give an overview of these scans and show why they are needed, how they work, what results are expected, and how these results can be used.

6.5.1 Hardware Initialisation

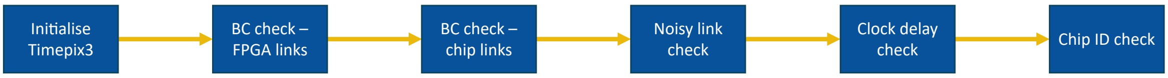

Figure 6.8: Steps of the tpx3-daq hardware initialisation. “BC” represents here the hexadecimal comma symbol that is transmitted by active links of the Timepix3, if 10b8b encoding is active.

As part of the modular design approach of the readout system (see Section 6.1) a lot of different hardware configurations are possible. To start with a setup the “Hardware initialisation” scan must be performed to set up the software and the firmware for the communication. The following steps are executed (a schematic overview of these steps is presented in Figure 6.8):

1. The communication with the FPGA and the Timepix3 is initialised and the startup sequence of the Timepix3 is performed.
2. All registers of the Timepix3 are set according to the settings in the software and the detected FPGA and firmware in the previous step. If a FPGA link never detects a comma symbol (BC in hexadecimal - every active link of a Timepix3 transmits it if 8b10b encoding is active) it gets assigned the status code 0 for not connected (see Table 6.3). All other links are temporarily marked with the status code 1 for operational links.
3. All FPGA links are activated and then the chip links are activated individually. For each step it is saved if on one of the FPGA links the comma symbol is detected. This generates a binary 8×8 matrix with the FPGA links representing one dimension and the chip links representing the other dimension. Combinations that resulted in a detection of the comma symbol are set to 1, all other combinations are set to 0.
4. All chip links are deactivated and the FPGA links are activated individually. For each activation step it is checked if even without an active chip link data is detected. If this is the case, the status code 6 for a noisy link is assigned to the corresponding FPGA link (see Table 6.3).
5. For each remaining working combination (based on step 3), the chip link and the corresponding FPGA link are activated. For each combination, the sampling clock delay (see Section 6.3) is set in steps to each possible value and the number of 8b10b decoder errors is recorded. Errors can occur if the phase of the FPGA-generated sampling clock and the data output of the Timepix3 do not match and thus the data is misinterpreted. Based on the distribution of sampling errors per sampling clock delay, the delay that is furthest away from errors is selected as this ensures that even with slight variations over time no errors should occur. If for an FPGA link no delay is found that yields no sampling errors this link gets assigned the status code 4 which represents links with sampling issues (see Table 6.3).

6. In the last step the remaining combinations are individually activated with the ideal sampling clock delay. With each combination the chip ID is requested by the software. The command is transmitted in the broadcast mode (see Section 5.2) as the ID is not known to the software at this point and this step should additionally work with setups with multiple ASICs such that there are different chip IDs depending on the link. The response to the request is received by the software and interpreted to extract the chip ID. Based on this, a table is generated that stores the detected chip IDs for the individual FPGA links. This is especially important for setups with several Timepix3 as the data packages do not contain information about the chip ID and the only possibility to know from which Timepix3 a data package originates is to assign the information via the FPGA links that were used for the transmission of the package. If for an FPGA link no chip ID or no valid chip ID was received the link is marked with the status code 8 for chip ID issues (see Table 6.3).

Table 6.3: Link status results of the hardware initialisation

Link status	Implemented in Firmware	Connected	Errors	Active
0	Yes	No	-	No
1	Yes	Yes	No	Yes
2	Yes	Yes	No	No
3	Yes	Yes	Sampling	Yes
4	Yes	Yes	Sampling	No
5	Yes	Yes	Noisy	Yes
6	Yes	Yes	Noisy	No
7	Yes	Yes	ChipID	Yes
8	Yes	Yes	ChipID	No
9	No	-	-	-

Additionally to the discussed status codes, there are the codes 3, 5 and 7 (see Table 6.3). These codes cannot be assigned by the hardware initialisation but only manually by the user. These codes are for links that showed errors in the initialisation but are activated manually mainly for debugging purposes. Finally, there is the status code 9 which is neither assigned by the initialisation nor can it be manually set by the user. It is predefined by the FPGA board and its firmware as not all boards support all links. Links with this status code cannot be activated and thus do not show up in the user interfaces at all.

6.5.2 Generic Scan

Figure 6.9: Steps of a generic tpx3-daq scan.

To define functions for common approaches of different scans and calibrations a generic scan was implemented. This generic scan offers the functionality to operate the Timepix3 but also the analysis and plotting tools to get the scan results. All scans except for the hardware initialisation are based on the following template (a schematic overview of this is presented in Figure 6.9):

- The **initialisation** of the scan (“__init__”) sets up the communication with the readout FPGA and the Timepix3. Furthermore, it creates the directories for the scan results and initialises the HDF5 file to store the results. The filename is always a combination of the “scan_id” which represents the name of the scan and the timestamp of the start of the scan.

- The **start** of the scan resets the Timepix3 to get always the same starting point and then writes the required configuration to the registers of the ASIC. This includes the general configuration of the Timepix3, the configuration of the internal PLL and the DACs. Additionally, the configuration of the Timepix3 is stored in the HDF5 file for the scan results. Finally, it is checked if the results of the last “Hardware Initialisation” are still valid so that they can be used for the scan.

- The **create_scan_masks** function can be used to split the pixel matrix readout into multiple steps where only a certain part of pixels is scanned. This is important as with too many active pixels at the same time, especially with internal test pulses, the Timepix3 would draw too much current which would lead to voltage drops that can spoil the ASICs performance. Furthermore, it could also create cross-talk between pixels so that pixels do not just detect test pulses that were injected into them but also pulses that were injected into neighbouring pixels. This behaviour of the Timepix3 does not characterise normal detector operation and the masks allow to avoid it during the scans. The setup of the different matrices for the scan steps mainly depends on the number of matrix steps. Within the GUI and the CLI of the DAQ software 4, 16, 64 and 256 steps can be selected. The square root of the number of steps defines the distance in x and y of the active pixels. As an example, for 64 steps every eighth pixel in x- and in y-direction will be active at the same time. Depending on how the matrices for the individual steps are created and written to the Timepix3, the number of steps significantly influences the duration of the scan. For example, in the naive approach that was used in the first version of the mask creation, with every step the full matrix was written to the ASIC. In a test with using the mask steps 100 times a scan with 16 steps took 4.93 minutes while a scan with 256 steps took 65.27 minutes. So, a scaling of 16 in the number of steps resulted in a scaling of 13.2 in the duration which means that the duration scaled almost proportionally with the number of steps. In a second version of the mask creation only columns of the ASIC are written in which the matrix changed. This means that for 256 steps in most steps only every fourth column gets a new configuration. In a test with the same scan approach a scan with 16 steps now lasted 2.85 minutes while a scan with 256 steps lasted 9.87 minutes. So, the scaling in time with the new implementation is 3.5 which is in the order of the square root of the step scaling.

- The **create_threshold_list** function creates a list of coarse threshold and fine threshold (see Section 5.2) combinations to optimally scan a given threshold range. This is important as the addition of the voltages of the coarse and the fine threshold only theoretically led to uniform voltage steps with each DAC step (one LSB step of the fine threshold is by design 500 µV while it is 80 mV for a coarse step). Especially at the start or the end of the fine threshold range where for the next threshold step, a change of fine and coarse threshold is needed the real voltage step size can differ from the theoretical expectation. This is the case because both DACs will in reality slightly differ from their design values. So if as an example, the coarse threshold would have as LSB step the expected 80 mV while the fine threshold would have a LSB step of 499 µV instead of the expected 500 µV then changing to the next threshold at the end of the fine threshold range (coarse threshold is increased by 1 DAC step and the fine threshold is decreased by 159 DAC steps) would result in a voltage step of 659 µV instead of the expected 500 µV. This shows that even with a deviation of just 0.2 % on one of the DACs a significant unexpected voltage step can be introduced. Severity of this problem depends on the selected threshold range. It occurs in all threshold ranges with more than 512 threshold steps, as this always requires at least one step of the coarse threshold DAC. Therefore, the “create_threshold_list” function uses that 2267 out of 2912 possible theoretical thresholds can be represented by at least three different combinations of the fine and the coarse threshold. Using this information, the function optimizes the used combinations of fine and coarse thresholds to omit coarse threshold steps in the centre region of the threshold range as this should normally be the important part of the range for the scan. Furthermore, the resulting list of threshold DAC settings minimises the number of coarse threshold steps. This is achieved by the following approach:

    1. If the highest possible coarse threshold of the start threshold is a possible coarse threshold of the end threshold, then the user-provided range can be covered without changing the coarse threshold. Thus, the coarse threshold and the corresponding fine thresholds are provided for the scan.

    2. If coarse threshold steps are necessary, a list of all possible threshold combinations for the threshold in the middle of the given range is created. For this list it is then checked for which coarse threshold the corresponding fine threshold is closest to the middle of the fine threshold range. This ensures that the fine threshold range for this step is symmetric around the central threshold in the given threshold range and thus, that there are no coarse threshold steps close to it. A coarse step will be done at the start and the end of this fine threshold range.

    3. At the newly determined points for coarse threshold steps the next step is done. This is similar for the start and the end of the range but mirrored in the direction. Thus, only the direction of increasing thresholds will be explained. For the remaining range, the highest possible coarse threshold that can represent the end of the previous range is searched. Based on this a list of all possible fine thresholds that do not generate a total threshold within the previous range is generated. The highest fine threshold together with the found coarse threshold represents the end of the new range.

    4. The process is recursively repeated until the user-defined threshold range is covered by the newly calculated range.

    5. The map of coarse and fine threshold steps is stored and provided for the scan.

- The **get_shutter_sleep_time** function ensures that when test pulses are used the shutter is opened long enough to detect all pulses in the pixels. This is important as not only pulses could be missing from a scan without it, but also some time is needed such that the capacitance in the pixels can be discharged for the ToT measurement. If this time is too short, it results in a saturation effect of the ToT as there is a limited time to count a given number of clock cycles.

6.5.3 Threshold Scan

The threshold scan is a basic scan that injects test pulses of a fixed amplitude for different thresholds and records the pixel activity for each of the thresholds. The scan is performed in the “Counter + iToT” mode of the Timepix3. For each threshold 100 test pulses are injected which is set via the “TP_number” register of the internal test pulse configuration of the Timepix3. Based on the counter mode, one can see how many of these 100 pulses are detected per pixel and per threshold. After all thresholds are scanned the data is interpreted (see Section 6.8) and a list of recorded hits per pixel per threshold is created. An example plot of this scan is presented in Figure 6.10. One can see that towards lower thresholds the pixels do not just record the injected 100 pulses but additionally noise hits. With increasing thresholds these noise hits get less frequent, and most pixels record only the injected pulses as hits. A few pixels still show some noise hits. With further increasing threshold some pulses do not result in a sufficient charge injection into the pixels that a signal above the threshold is recorded. Thus, the number of hits decreases. With a sufficiently high threshold, no hits are recorded.

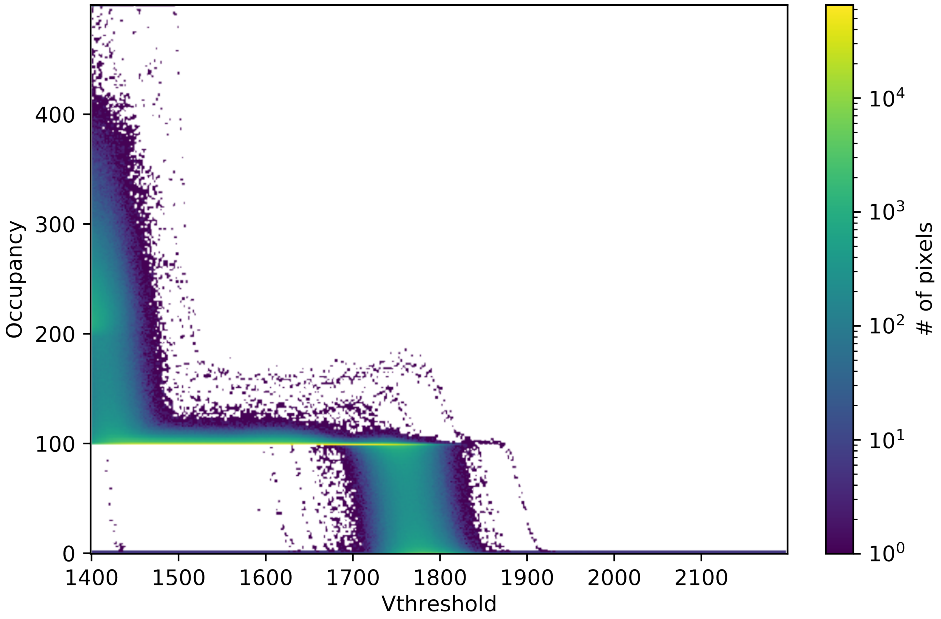

Figure 6.10: Number of recorded hits per pixel and per threshold for a threshold scan of a Timepix3. For each threshold and pixel 100 test pulses were injected. For low thresholds, the pixels are noisy which results in more detected hits than the injected number of pulses. With higher threshold most pixels record exactly the injected number of pulses while there are a few pixels that show noise hits. At some threshold it is sufficient to cut away test pulse injections into pixels which results in a drop of the recorded number of hits. If the threshold is high enough no hits are recorded any more.

To fit the measured hits in dependence of the threshold for all pixels individually a Z-curve is used:

$$f(x) = -0.5a \times \operatorname{erf}\left(\frac{x-\mu}{\sqrt{2} \times \sigma}\right) + 0.5a\,. \tag{6.1}$$

which is based on the error function. This fit function is used if the ASIC is set to negative polarity and thus the threshold increases with higher threshold DAC values. If the ASIC is used with positive polarity, the relevant hits are at thresholds lower than the position of the noise peak. In this case the threshold increases with lower threshold DAC values and thus a S-curve is needed for the fit:

$$f(x) = 0.5a \times \operatorname{erf}\left(\frac{x-\mu}{\sqrt{2} \times \sigma}\right) + 0.5a\,. \tag{6.2}$$

The fit parameter μ marks the threshold at which the function dropped to 50 % of its amplitude. It is interpreted as the threshold that corresponds to the injected test pulse amplitude. The fit parameter σ indicates the width of the curve. It is interpreted as a measurement of the noise in the pixel because the lower the noise in the pixels the pixel is, the sharper the drop from 100 measured pulses to 0 measured pulses should be. Combining the fitted μ of all pixels in a histogram and fitting it with a Gaussian gives the overall threshold of the ASIC that corresponds to the amplitude of the injected test pulses. An example plot for this, based on the same data as in Figure 6.10 is presented in Figure 6.11. The results of the fit can be used by further scans for example for a threshold calibration.

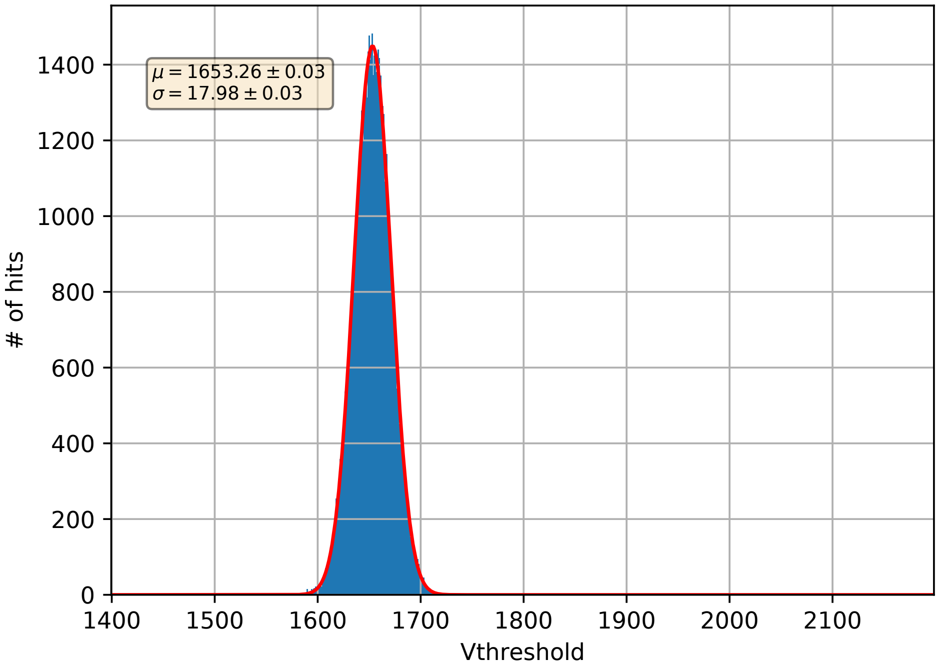

Figure 6.11: Resulting thresholds based on the parameter μ of the Z-curve or S-curve fit for all pixels. The resulting distribution is fitted with a Gaussian.

6.5.4 Test Pulse Scan

A test pulse scan works like a threshold scan but switches the roles of the threshold and the test pulse amplitude: the threshold is fixed, and the test pulse amplitude is changed with each step. This also changes the expected curves: for an ASIC with negative polarity increasing test pulse DAC values increase the test pulse amplitude and thus a S-curve is expected (see Equation 6.2). And for a positive polarity of the ASIC decreasing test pulse DAC values increase the test pulse amplitude and thus a Z-curve is expected (see Equation 6.1). This scan can be used to check the response of the Timepix3 to various pulse amplitudes for a given threshold.

6.5.5 Equalisation

Due to imperfections in the production process of the ASIC all pixels have a slightly different response to signals. Based on this, the ASIC features a 4-bit register per pixel to adjust the threshold per pixel (see Section 5.2). The goal of the equalisation is to find a value for the 4-bit register for all pixels to get a response of the ASIC that is as uniform as possible.

For the equalisation two threshold scans (see Section 6.5.3) are performed: one with all pixels set to their minimum pixel threshold and one with all pixels set to their maximum pixel threshold. This is done to determine the range of the pixel threshold for each pixel individually and to scan how individual pixels behave compared to other pixels. Both threshold scans are analysed in a first step like a standard threshold scan. This results in a threshold distribution for each of these two scans. These distributions are $\mathrm{th}_0^{x,y}$ and $\mathrm{th}_{15}^{x,y}$ with the coordinates x and y of the pixels. These parameters are used to calculate the step size of the 4-bit pixel threshold:

$$\text{Step size} = \frac{\frac{1}{n}\left(\sum_{x,y}^{n} \mathrm{th}_{15}^{x,y} - \sum_{x,y}^{n} \mathrm{th}_{0}^{x,y}\right)}{16} . \tag{6.3}$$

The variable n represents the number of active pixels which is in the ideal case 65536 for the Timepix3. But it is possible that some pixels are not working or masked by the user and thus do not show up in the threshold distributions. The division by 16 is done to map the difference of the means of the threshold distributions to the possible 16 pixel thresholds. The pixel threshold $\mathrm{pth}^{\mathrm{x,y}}$ is then calculated with:

$$\mathrm{pth}^{x,y} = 8 - \frac{\mathrm{th}_0^{x,y} - \frac{1}{n}\sum_{x,y}^{n} \mathrm{th}_0^{x,y}}{\text{Step size}} . \tag{6.4}$$

Here the difference of the threshold of a pixel and the mean threshold of all active pixels calculated. So, pixels that are close to the mean get a low variation of the pixel threshold while pixels that are further away from the mean get a higher variation. The result is normalized to the step size to project from the difference in the chip threshold to the difference in terms of the pixel threshold. The result is then further subtracted from 8 to move the resulting distribution in the range from 0 to 15 as required by the DAC value for the pixel threshold. To deal with pixels that are not in the range from 0 to 15, all pixels with a result < 0 get assigned the pixel threshold 0 and all pixels with a result > 15 get assigned the pixel threshold 15. In the last step of the calculation the pixel thresholds are rounded to integers. As an example, a map of the resulting value is presented in Figure 6.12(a). This can be used to check if there are any systematic effects visible in the matrix, like faulty columns. The resulting values of all pixels can be additionally put into a histogram like in Figure 6.12(b). The resulting distribution is fit with a Gaussian. With this it can be assessed if the distribution has the expected mean (which should be 7.5) and if the data does not deviate from the expected distribution. Also, it can be checked if no bin is overrepresented or under-represented, which should especially be checked for the bins 0 and 15 as they also represent the over- and underflow. In a future iteration of this scan, it is planned to suggest broken pixels based on the results to the user for masking.

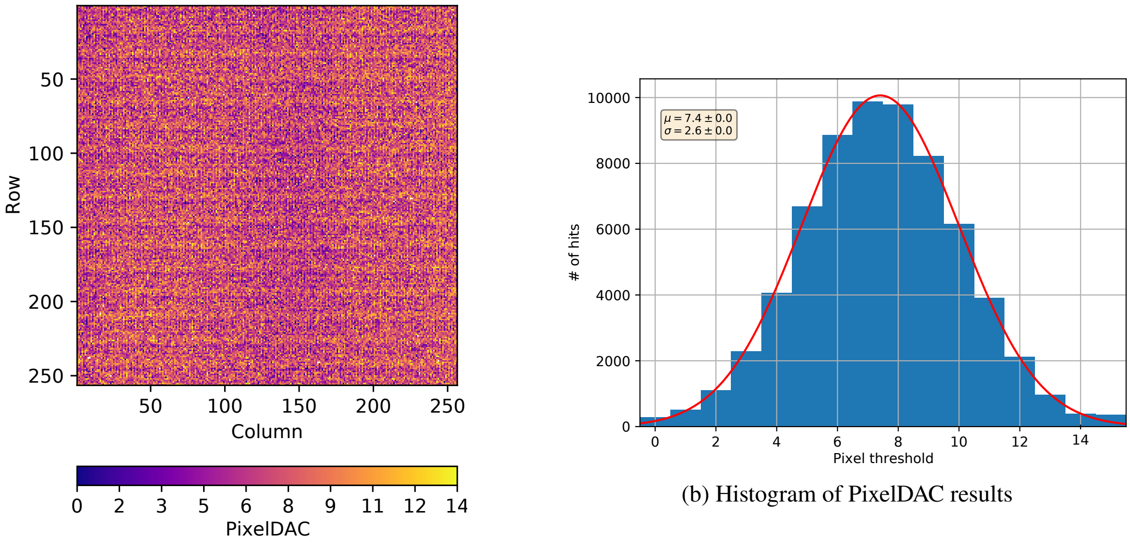

(a) PixelDAC result per pixel

(b) Histogram of PixelDAC results

Figure 6.12: Result of an equalisation of a Timepix3 performed with the tpx3-daq. (a) presents the resulting PixelDAC for each pixel in a 2-dimensional map, (b) presents a histogram of the resulting PixelDACs that was fitted with a Gaussian.

6.5.6 PixelDAC Optimisation

An important condition for a successful equalisation is that the range of the pixel thresholds is optimally used: if the range of the pixel threshold is too big compared to the width of the threshold distribution of the pixels, then only a few of the 16 pixel thresholds will be used and thus not the full potential of the pixel threshold is used. For an extreme case with a very broad pixel threshold range only the central pixel threshold will be used and thus all pixels will get the same pixel threshold which is equivalent to no equalisation at all. In the opposite case, if the pixel threshold range is too small compared to the threshold distribution of the pixels, a lot of pixels are not any more in the range of the pixel threshold and thus will get assigned a pixel threshold of 0 or 15 for the underflow and overflow. This also spoils the equalisation result. Based on these considerations the range of the pixel threshold needs to be optimised. To do this the Timepix3 DAC “Ibias_PixelDAC” can be changed.

To find the optimal value for this DAC, a similar scan as the equalisation (see Section 6.5.5) is performed. It involves a threshold scan with all pixels at the minimum and another with all pixels at the maximum pixel threshold. Unique to this scan is, that it is only performed with every sixteenth pixel. This speeds up the scan as only one matrix step per threshold is needed and it does not spoil the scan results as not the individual pixel behaviour is important but the overall ASIC behaviour with respect to the “Ibias_PixelDAC”. The speed-up is necessary as the equalisation scan is repeated several times but with different values for the “Ibias_PixelDAC”. In the first step the scan is by default performed with the value 127 which is the middle of the 8-bit DAC and based on the ASIC design its default configuration. The second step is then performed at 63. Based on the results of these two steps a linear regression towards the optimal value is started. The value of “Ibias_PixelDAC” for step i is calculated with (i starts at 1):

$$\text{Ibias\_PixelDAC}_i = \begin{cases} 127 & \text{for } i = 1 \\ 63 & \text{for } i = 2 \\ \text{Ibias\_PixelDAC}_{i-1} + \frac{\text{Ibias\_PixelDAC}_{i-2} - \text{Ibias\_PixelDAC}_{i-1}}{\Delta_{i-2} - \Delta_{i-1}} \times \left(\Delta_i^\sigma - \Delta_{i-1}\right) & \text{for } i > 2\,. \end{cases} \tag{6.5}$$

Here Δ_i represents the difference of the means of the threshold distributions with the pixel thresholds at $p = 0$ and at $p = 15$ for step i:

$$\overline{\text{th}}_{p,i} = \frac{1}{n} \sum_{x,y}^{n} \text{th}_{p,i}^{x,y} \tag{6.6}$$

$$\Delta_i = \left(\overline{\text{th}}_{15,i} - \overline{\text{th}}_{0,i}\right)\,. \tag{6.7}$$

The Δ_i^σ represents the expected value of Δ_i to use the pixel threshold range optimally. With the threshold distributions for the pixel threshold $p = 0$ and at $p = 15$ it is calculated with:

$$\sigma_{p,i} = \sqrt{\frac{1}{n-1} \times \sum_{x,y}^{n} \left(\text{th}_{p,i}^{x,y} - \overline{\text{th}}_{p,i}\right)^2} \tag{6.8}$$

$$\Delta_i^\sigma = 3.3 \times \left(\sigma_{15,i} + \sigma_{0,i}\right)\,. \tag{6.9}$$

The regression runs until

$$\Delta_i = \Delta_i^\sigma \pm 2\,. \tag{6.10}$$

This condition is usually met after three to five iterations. If substantially more iterations are needed it could indicate an issue with the low voltage power supply of the Timepix3, because changes in the supply voltages change the resulting distributions. The final value for “Ibias_PixelDAC” is stored in the local configuration of the software and automatically used for the Timepix3 operation until the DAC is manually changed or a new “PixelDAC Optimisation” is performed.

6.5.7 Threshold Calibration

As every Timepix3 is slightly different also the same threshold DAC settings can result in slightly different thresholds. Furthermore, it is important to know during the analysis, which threshold in terms of electrons the threshold DAC settings represent. For this purpose, the threshold calibration scan is used. It automatically performs a select-able number of threshold scans - each with a different test pulse amplitude. The position of the S-curves or Z-curves in the threshold scan changes based on the amplitude of the test pulses. Thus, the calibration curve is obtained by plotting the resulting shift of the S-curves or Z-curves for the different test pulse amplitudes. For this, the voltages of the test pulse amplitudes are converted to charge with the input capacitance of the Timepix3 of $C = 3\,\mathrm{fF}$ [37]:

$$Q = 3\,\mathrm{fF} \times U_{\mathrm{testpulse}}\,. \tag{6.11}$$

The resulting calibration curve is fitted with a linear function. The resulting fit parameters can be used to convert any threshold in DAC values to a threshold in electrons. An example of such a calibration result is presented in Figure 6.13.

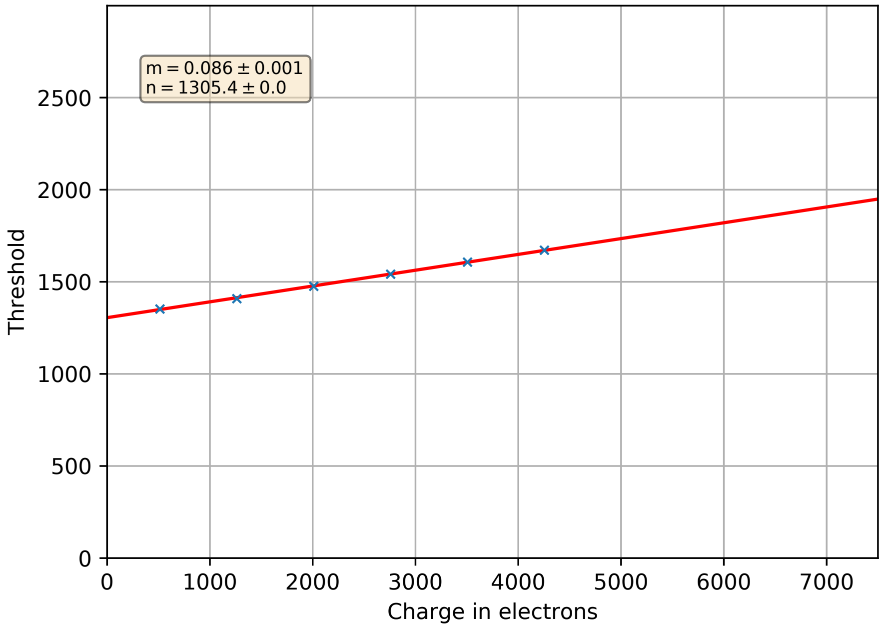

Figure 6.13: Result of a threshold calibration of a Timepix3 performed with the tpx3-daq. Each data point is the resulting μ of one threshold scan for different test pulse amplitudes. The points are fitted with a linear function. In this example, a threshold setting of 1350 would result in a threshold of 519 electrons.

6.5.8 Time over Threshold Calibration

As the Timepix3 records charges in the pixels in terms of Time over Threshold (ToT) clock cycles (cc) a calibration is necessary for the conversion from clock cycles to charges in electrons. The goal of this calibration scan is to measure the conversion parameters for a specific chip. To do this, a scan like the “Test pulse scan” is performed (see Section 6.5.4). The difference is, that for this calibration the combined ToT/ToA mode of the chip is used instead of the HitCounter/iToT mode. This is necessary to measure the ToT response to each injection of test pulses for different amplitudes. During the scan for each test pulse amplitude 10 pulses are injected. This is done such that for each pixel the average of these injections can be calculated to reduce the influence of noise. Based on this, only pixels that show at least 10 recorded hits are used for analysis. An example plot of the recorded hits per test pulse amplitude and per pixel is presented in Figure 6.14(a). One can see that for low amplitudes most pixels do not record any hits while some pixels record noise hits. With increasing amplitudes most pixels record exactly the expected 10 hits. At even higher amplitudes most pixels tend to record 20 hits. The reason for this is that with high amplitudes a negative overshoot of the pulse after the positive signal can reach a sufficient amplitude to cross the threshold and create a second hit. Thus, most injections lead to two recorded hits. If one would continue until even higher amplitudes the same could happen with a positive overshoot of the signal after the negative overshoot, resulting in 3 hits per injection and thus in a plateau of 30 hits. After averaging the recorded ToT per pixel, per injection and per amplitude a calibration curve per pixel can be plotted. An example of this is presented in Figure 6.14(b). One can see that most pixels follow the same curve and only very few pixels show a divergent behaviour.

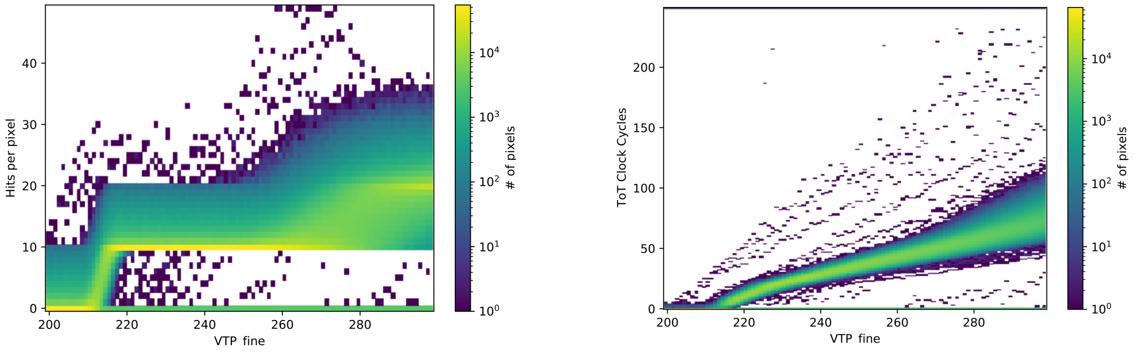

(a) Recorded hits per pixel

(b) Average recorded ToT per pixel

Figure 6.14: Result of a ToT calibration of a Timepix3 performed with the tpx3-daq. (a) presents the recorded hits per pixel and per pulse amplitude, (b) presents the hit-averaged ToT per pixel and per pulse amplitude.

To get an overall calibration function for the ASIC the average of all pixels for each test pulse amplitude is calculated. Besides the threshold of 10 hits per pixel there is an additional threshold of 60 % active pixels on the chip to further prevent noise at low amplitudes. The resulting calibration curve is fitted with the following function:

$$\mathrm{ToT}\,(\mathrm{voltage}) = a \times \mathrm{voltage} + b - \frac{c}{\mathrm{voltage} - t}\,. \tag{6.12}$$

Here, a, b, c and t represent fit parameters. An example of this is presented in Figure 6.15. The fit parameters can be used to transform the measured charge in clock cycles into a charge in electrons. For this also the input capacitance of the Timepix3 of $C = 3$ fF [37] must be considered.

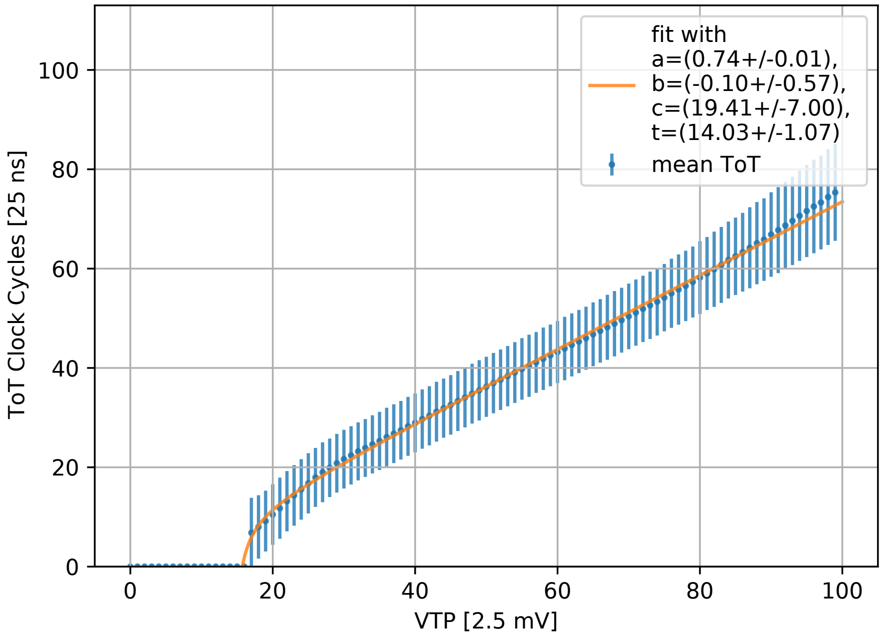

Figure 6.15: Result of a ToT calibration of a Timepix3 performed with the tpx3-daq. Each data point is the average recorded ToT of all pixels. A fit with Function 6.12 was performed. The error bars are calculated by the standard deviation of the recorded pixel ToTs.

6.5.9 Time Walk Calibration

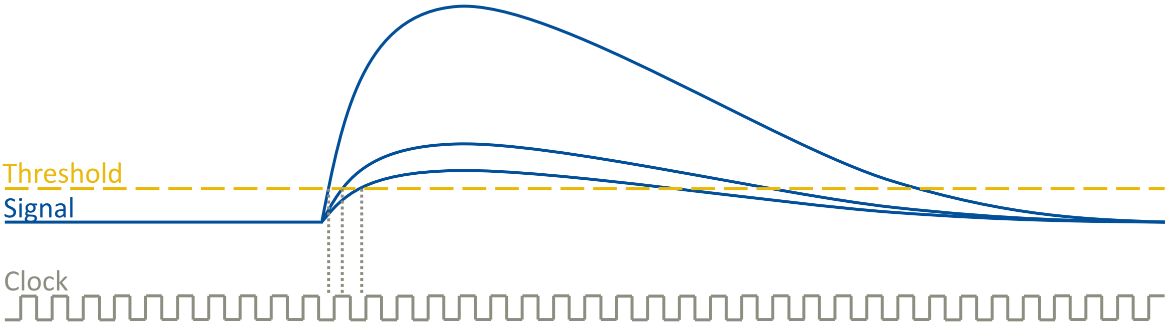

Figure 6.16: Sketch of the time walk effect for pulses with different amplitudes. Pulses with higher amplitudes cross the threshold at earlier clock cycles and thus get assigned an earlier timestamp despite starting at the same time as pulses with lower amplitudes.

Due to the digitisation of analogue pulses in the pixels of the Timepix3, pulses that arrive in pixels at the same time can differ in their recorded start time based on the amplitude of the pulses. This behaviour is sketched in Figure 6.16. One can see that a pulse with a higher amplitude is recorded with an earlier timestamp than a pulse with a lower amplitude. Thus, the timing depends on the amplitude and threshold. Without corrections this behaviour introduces a systematic error on the timing and thus reduces the time resolution.

An additional effect is visible on the Timepix3: the fast time of arrival (fToA) register for hits runs on 640 MHz. But every double column of the ASIC is supplied with a slightly phase shifted 640 MHz clock to reduce power consumption and noise on the ASIC. Due to this setup, simultaneous hits with the same pulse amplitudes would have a different time stamp if they were detected in different double columns. This introduces an additional systematic error and thus decreases the time resolution.

To account for this effect a time walk calibration is required. Like other scans this is done in several steps per amplitude with different active pixels to limit the power consumption of the chip and to prevent cross talk between pixels. The scan is performed in the combined ToT/ToA mode with active VCO so that the bits 3 to 0 of each hit are used for the fToA (see Table 6.4). To get a time reference for the ToA an additional timer in the firmware was introduced: the shutter timer (see Table 6.2). It runs on 320 MHz, and it sends out its current timestamp at the first Timepix3 system clock rising edge (the system clock runs at 40 MHz) after the opening of the shutter. This is important as the shutter from the firmware gets synchronised to the system clock in the Timepix3 and this triggers the generation of the test pulses. The period and the phase of the test pulses and thus the distance in time to the opening of the synchronised shutter is fixed via the settings of the test pulse register of the Timepix3.

Figure 6.17 shows the recorded fToA for all pixels for different test pulse amplitudes. One can see that the overall pattern moves with increasing test pulse voltages. This is the expected effect of the time walk, as higher pulses cross the threshold earlier. Additionally, the effect of the different clock phases for different double columns of the Timepix3 is visible: a repeating pattern of shifts of the measured fToA along the x-axis.

For the same scan Figure 6.18 shows the measured ToA for all pixels for different test pulse voltages. As for the fToA also a shift of the ToA is visible with increasing pulse amplitudes, however it is less pronounced. This is expected as the ToA features a time binning of 25 ns while the fToA features a time binning of 1.5625 ns (see Section 5.2), thus the time walk can be better resolved with the fToA. Combining the measurement of the fToA and the ToA and correcting for the fToA clock phases via

$$T^{x,y}_{\text{total}}\,(A) = T^{x,y}_{\text{ToA}}\,(A) \times 40\,\text{ns} - T^{x,y}_{\text{fToA}}\,(A) \times 1.5625\,\text{ns} - x \times 1.5625\,\text{ns}\,, \tag{6.13}$$

with $T^{x,y}_{\text{total}}\,(A)$ as the measured total time for the pixel x, y and the pulse amplitude A, leads to the plots displayed in Figure 6.19.

One can see that the pattern due to the clock phases is completely gone and only the effect of the time walk remains. To calibrate this effect for measured data first the average time walk for all pixels per test pulse voltage is calculated and then plotted in Figure 6.20(a). This shows the expected behaviour: low pulse amplitudes (high VTP_fine) have a high time walk and the higher the amplitude gets, the smaller the effects gets until it saturates at a minimum.

To get the final calibration curve it is necessary to convert the test pulse amplitudes to ToT clock cycles. In principle an existing ToT calibration can be used for this purpose. This requires that both scans, the time walk calibration and the ToT calibration, were performed with exactly the same settings to assign representative calibrations. Therefore, it was decided to do the ToT calibration for the time walk calibration intrinsically, especially as the scan is performed in the combined ToA/ToT mode so that for each amplitude not only a time but also a charge measurement is present. Furthermore, the ToT calibration via this method can be much cleaner because based on the timing, multiple hits in a pixel for a single pulse can be differentiated and for example overshoots can be excluded from the analysis. As this improves the stand-alone ToT calibration with no additional cost of time, it is planned for the future to use only the time walk calibration to get both calibrations.

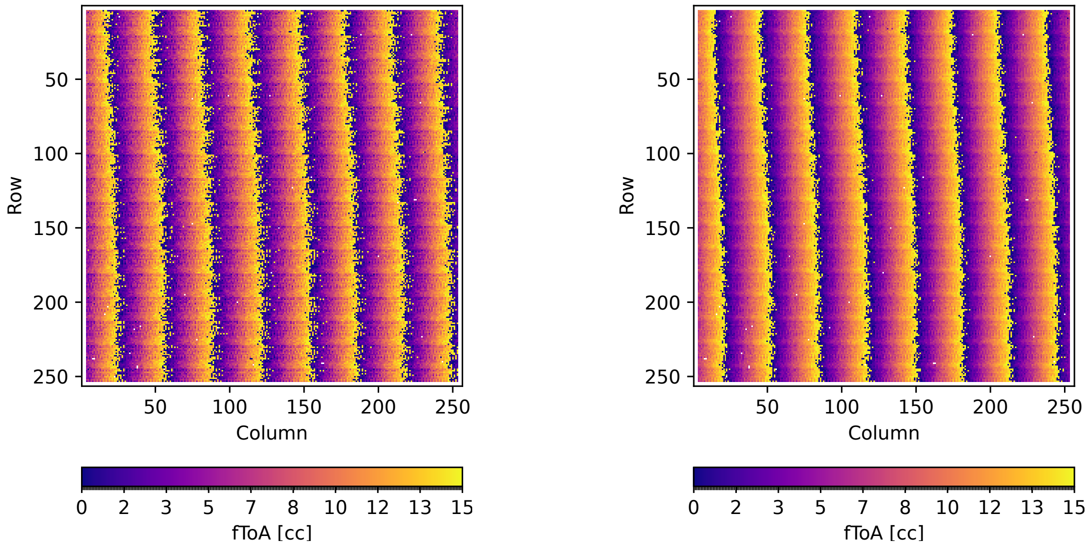

(a) 62.5 mV

(b) 100.0 mV

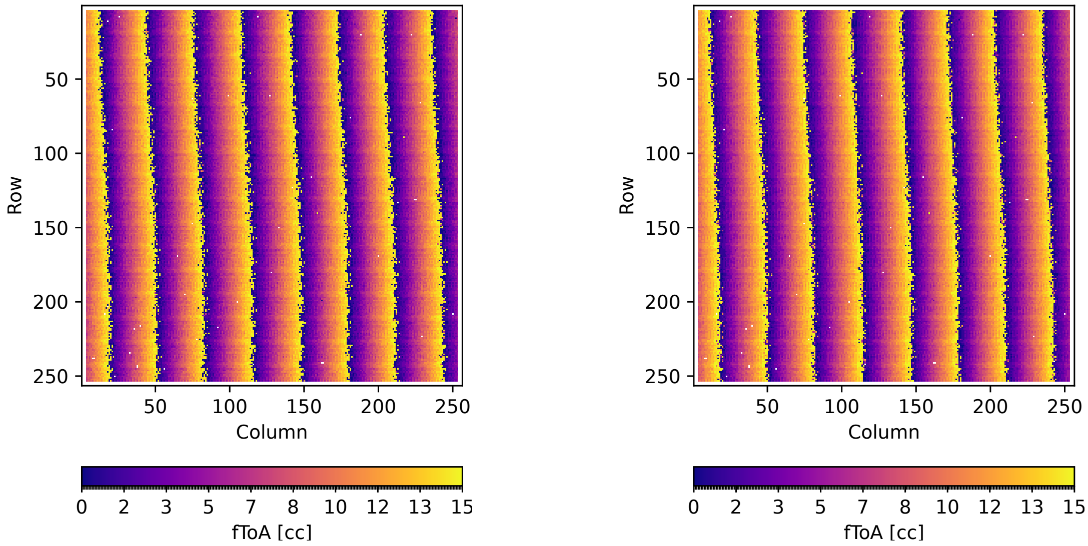

(c) 147.5 mV

(d) 185.0 mV

Figure 6.17: Resulting fToA per pixel for four different test pulse amplitudes in the Timepix3 time walk calibration.

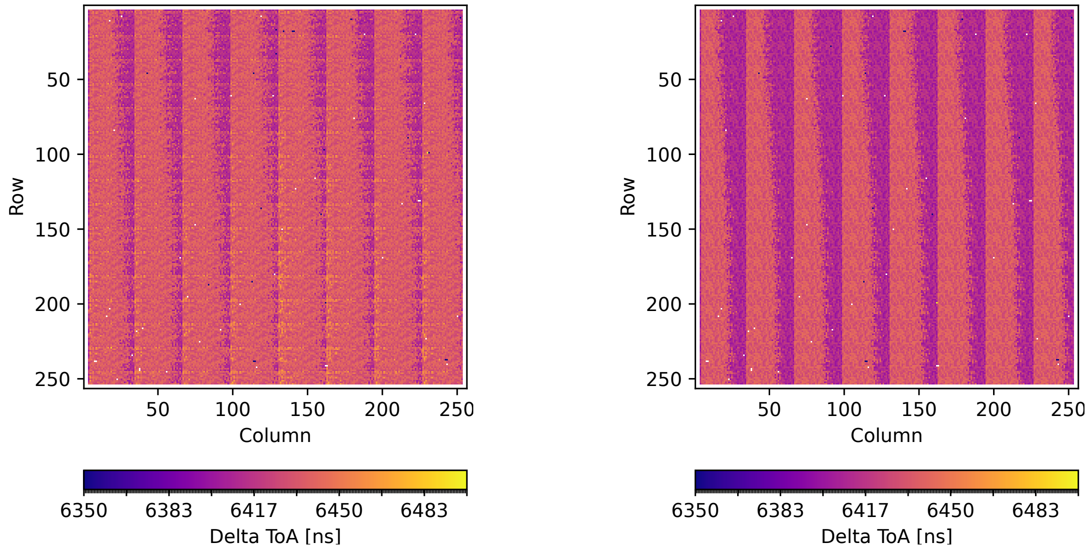

(a) 62.5 mV (b) 100.0 mV

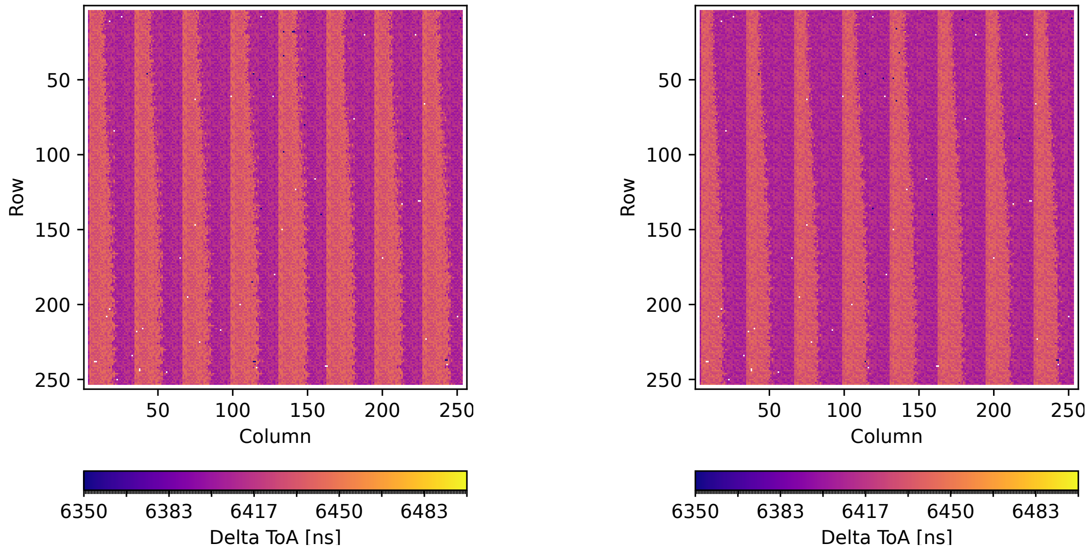

(c) 147.5 mV (d) 185.0 mV

Figure 6.18: Resulting ToA per pixel for four different test pulse amplitudes in the Timepix3 time walk calibration.

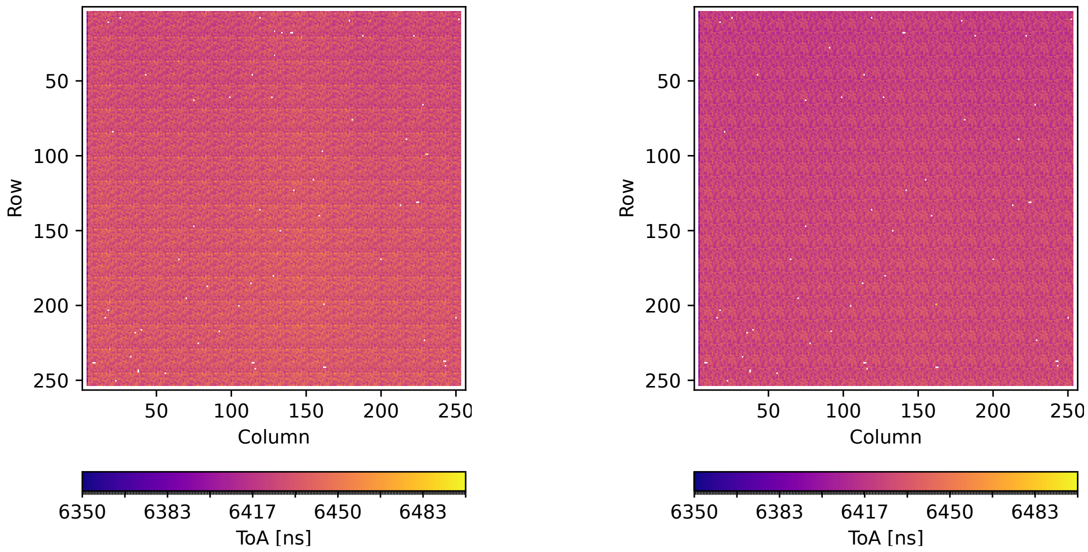

(a) 62.5 mV

(b) 100.0 mV

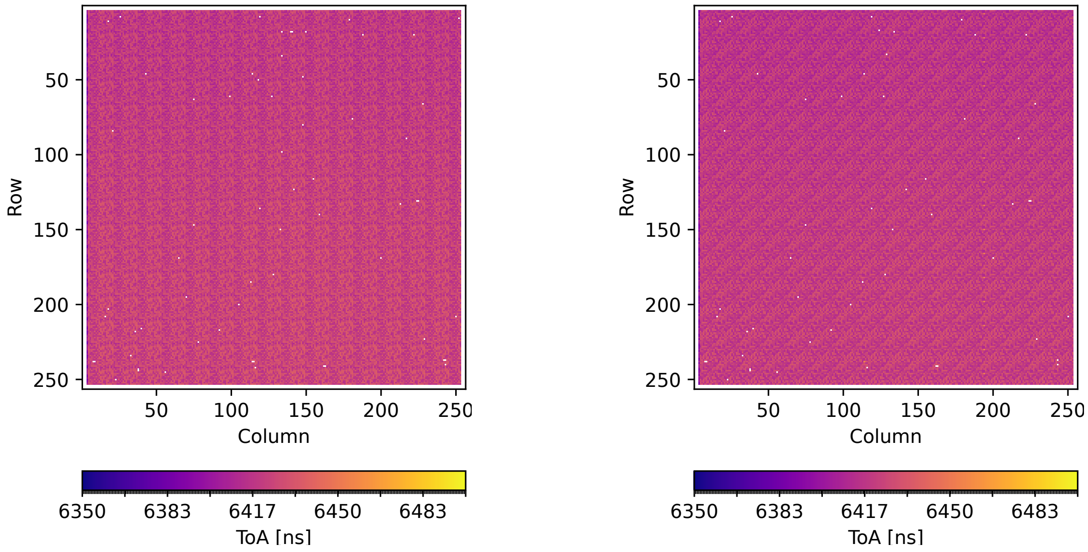

(c) 147.5 mV

(d) 185.0 mV

Figure 6.19: Resulting combined and corrected fToA and ToA per pixel for four different test pulse amplitudes in the Timepix3 time walk calibration.

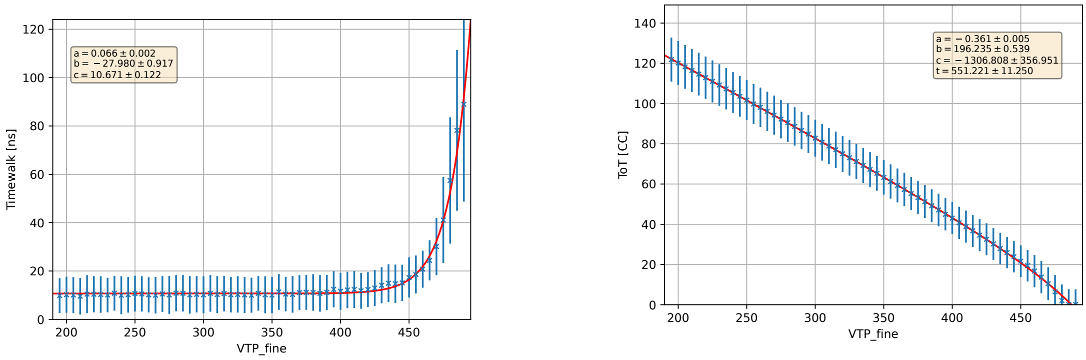

(a) Time walk calibration in units of the test pulse DAC.

(b) ToT calibration based on the results of the time walk calibration

Figure 6.20: Time walk calibration results for a Timepix3. (a) shows the time walk in units of the fine test pulse DAC, (b) shows the ToT calibration based on the data of the time walk calibration. The combination of both can be used to get a time walk calibration in units of the recorded ToT in clock cycles. The errors are based on the standard deviations for the time walk distributions and the ToT distributions of the pixels.

An example for a ToT calibration based on the data of the time walk calibration is presented in Figure 6.20(b). Using this to transform the x-axis of Figure 6.20(a) from test pulse voltages to ToT leads to the final calibration plot in figure 6.21. One can see the expected behaviour based on the scheme presented in Figure 6.16: for low ToTs and thus for signals with a low amplitude a substantial time walk is observed while the effect gets smaller with higher pulses and converges towards an offset. This offset is mainly generated by the time difference between the FPGA internal shutter timer and the Timepix3 internal timer due to the transmission of the signals via the DisplayPort cables. As long as the setup is not changed, this offset keeps constant. But also, after a change of the setup the same time walk calibration can still be used as it is introducing a constant offset into all timestamps and thus, the relative timing of hits is not influenced. However, in a setup with multiple detectors running synchronously this offset must be considered. To get the parameters for the time walk calibration a fit with an exponential function is performed:

$$\text{Time walk}\,(\text{ToT}) = \exp\left(a \times \text{ToT} + b\right) + c\,. \tag{6.14}$$

The resulting fit parameters can then be provided to the data interpretation (see Section 6.8) to correct the time walk and the clock phases in the raw data.

6.5.10 Noise Scan

To investigate how the noise of the Timepix3 behaves with respect to the threshold a “Noise Scan” can be performed. For this scan, all pixels are active at the same time and thus no matrix steps are done per threshold step. Furthermore, the scan is performed in the “Counter + iToT” mode of the Timepix3, to not just scan if a pixel was active during a readout interval but also if there were multiple hits in a pixel in such an interval. After recording the data for the different threshold steps, it is interpreted and two plots are created: a histogram of the number of active pixels per threshold step and a histogram of the number of recorded hits per threshold step. Examples for these two plots are presented in Figure 6.22. One can see that at low thresholds the number of active pixels is in the order of hundreds and the

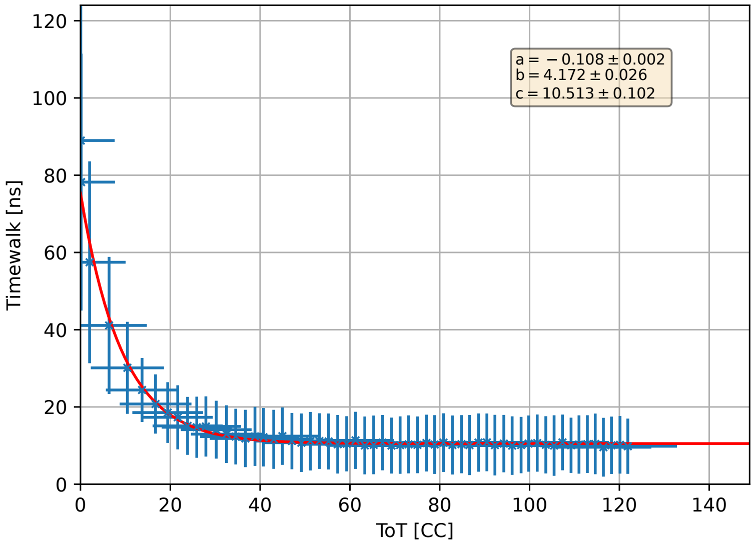

Figure 6.21: Result of the time walk calibration of GridPix W15-G6. The data was fitted with Equation 6.14. The resulting fit parameters can be used an in input for the interpretation of raw Timepix3 data (see Section 6.8). The errors are based on the standard deviations for the time walk distributions and the ToT distributions of the pixels.

number of hits in the order of thousands. This is expected for thresholds close to the noise level of the ASIC. With increasing thresholds, the number of active pixels quickly drops to about 10 active pixels showing about 1000 hits. So only very few pixels are active, but they record still a substantial number of hits. Towards the end of the threshold range one can see that the number of hits drastically changes in a Z-curve shape while the number of active pixels only changes by 1. This hints into the direction that this one pixel has a high noise level and thus recorded most of the remaining hits. With increasing threshold an increasing number of hits were below the threshold until this pixel was completely silent. At the highest thresholds, the number of active pixels equals the number of recorded hits, thus each remaining pixel records one hit. This hints towards broken pixels as they do not seem to be influenced by the threshold but also just produce one hit which could happen if the signal within the pixel just crosses the threshold once during the readout but never goes below the threshold until the pixel is read out. Such pixels should be masked.

6.5.11 Run

The “Run” is the simplest “Scan” as it does not perform any mask or DAC steps and also does not supply the ASIC with test pulses. Its purpose is to record data based on charge injections into the pixel pads for example via avalanches in a gaseous detector (see Section 7.1). This is done in one of the modes of the Timepix3 (ToT/ToA, only ToA, HitCounter/iToT) that is selected by the user. For the version of the DAQ software that was used during this thesis all modes were operated in data-driven readout, and the sequential readout was not implemented at the time. The scan starts, as all scans, by writing the configuration to the ASIC. Additionally, the ToA extension clock in the FPGA is stared via the DAQ software and a timer reset is applied to the extension clock and the internal Timepix3 clocks. As both are reset via the same signal the only time difference between both clocks comes from the

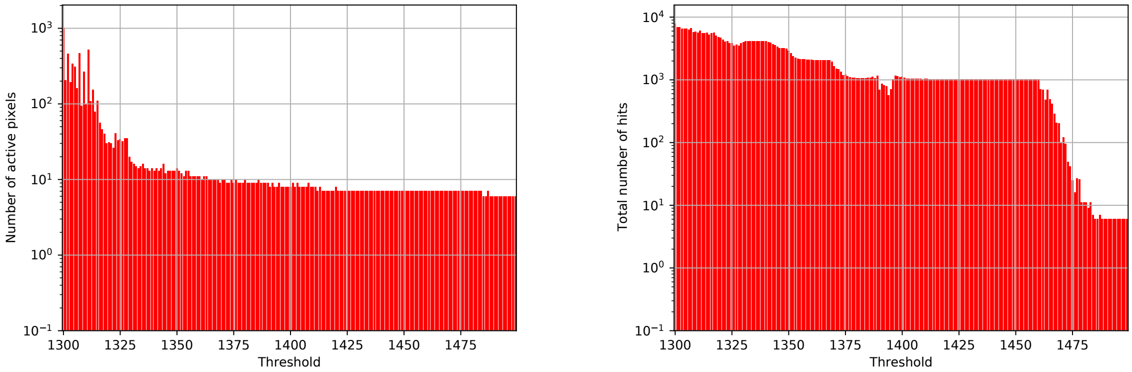

(a) Number of active pixels per threshold step

(b) Number of recorded hits per threshold step

Figure 6.22: Results of a noise scan of a Timepix3. For each threshold step all pixels were active but no test pulses were injected such that all hits are noise hits. The scan is performed in the HitCounter/iToT mode such that not only the number of active pixels can be recorded but also the number of hits.

transmission time of this signal from the FPGA to the ASIC via the DisplayPort cables. This constant offset is corrected in the raw data interpretation (see Section 6.8). After this reset the shutter of the Timepix3 is opened and the data receiver in the DAQ software is started. The scan runs until the user stops it, or a user defined runtime is reached. Then the shutter is closed and the data is saved.

In contrast to the other scans, the run does not offer an analysis or a plotting function. This is done such that runs can be performed in quick succession without interruptions of the analysis and the plotting. Furthermore, especially the plotting requirements can be vastly different depending on the application, therefore the intention is that the tpx3-daq just records the data and the analysis of the data and plotting tools can be developed independent on the readout system.

6.6 User Interfaces

In this section the different user interfaces will be presented. For directly controlling the readout system there are a command line interface (CLI) and a graphical user interface (GUI). These were developed in the scope of [42]. Additionally, an application programming interface (API) is offered to either script functionality or to include the readout system into existing readout frameworks. In the last section three different event displays that were developed for the readout system are presented.

6.6.1 Command Line Interface

For a console-based operation the tpx3-daq software offers a command line interface (CLI). It offers all scans and all settings to fully operate Timepix3s via defined commands. It is always possible to use commands and to then set the individual parameters within the command while it is also possible to append the parameters directly to the command to speed up operations for experienced users. For example, the command “Set_DAC” shows a list of available DACs to select and then asks for the selected DAC for the new value while showing the possible range. But one could also use “Set_DAC 7 1300” to set DAC 7 (which corresponds to the threshold DAC) to value 1300 with just one command input. Additionally, several commands can be concatenated so that they are processed one after the other. This can be used to automate a set of scans with different parameters. For example, the concatenated command “init + Set_DAC 7 1300 + Run 600 + Set_DAC 7 1310 + Run 600” first initialises the communication with the Timepix3 via the “Hardware Initialisation” scan and then performs two runs with a runtime of 600 s for two different thresholds (DAC value 1300 and 1310).

6.6.2 Graphical User Interface

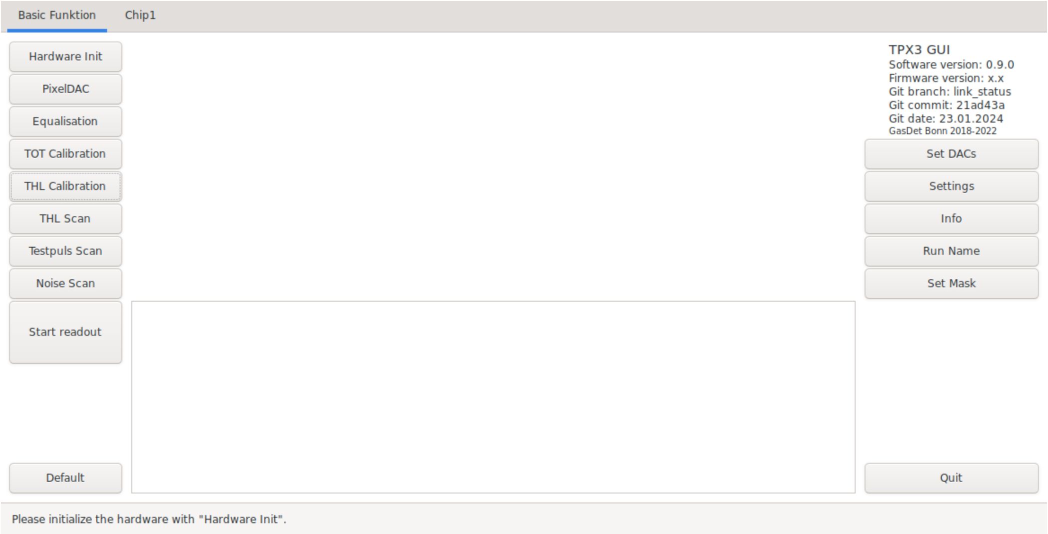

TPX3 GUI
Software version: 0.9.0
Firmware version: x.x
Git branch: link_status
Git commit: 21ad43a
Git date: 23.01.2024
GasDet Bonn 2018-2022

Please initialize the hardware with "Hardware Init".

Figure 6.23: Screenshot of the graphical user interface of the Timepix3 readout system. The main window of the GUI is shown. It gives access to all scans and settings of the Timepix3.

All functionality that is offered by the CLI (Section 6.6.1) is also available in a GTK-based graphical user interface (GUI). A screenshot of the GUI is presented in Figure 6.23. One can see that all scans are available on the left side of the interface while settings are available on the right side. The scans are ordered by how they would be normally done with a new Timepix3. By clicking on a scan or a setting, a new window opens that contains all possible parameters that can be changed by the user. After a scan is started the centre of the main window shows the current state of the scan via a progress bar, the step that is currently performed and an estimate for the remaining time. In the bottom of the main window a status bar presents the chip ID of the connected Timepix3 and how many readout links are active. As this is based on the result of a “Hardware Initialisation” first this scan must be performed. More details on the CLI and the GUI can be found in [42].

6.6.3 Application Programming Interface

To be used by other programs all scans can be included as Python function calls with all necessary parameters. These parameters are for example the threshold range for the threshold scan or the number of injections for all test pulse-based scans. Additionally, one can provide an equalisation file and a mask file so that only unmasked pixels are used for the scan and the equalisation is applied for the pixel thresholds. Via this interface the scans are also included in the command line interface (see Section 6.6.1) and the graphical user interface (see Section 6.6.2). This also enables to call scans as standalone scripts without any top-level control interface. Finally, the main module “tpx3.py” can be included into Python scripts to directly access functions of the Timepix3. This can be useful to define unit tests of the readout system for example via writing to individual registers of the Timepix3, reading them back and comparing the received data to send data.

6.6.4 Event Displays

To show the hits on the Timepix3 during operation an event display based on a generic online monitor is used[4]. For this, first an online interpretation of the raw data is done. This is a simplified version of the raw data interpretation that will be discussed in Section 6.8. In particular, it does not contain error corrections or any handling of the additional timing data of the FPGA. This is done to speed up the interpretation process so that it can run online without high requirements in terms of computing resources. Based on the interpreted data, a 2D plot of active pixels, a histogram of active pixels per event and a histogram of ToT per pixel and per event is generated and displayed in a Java application. As in a data-driven readout of the Timepix3 an “event” would require a time-based reconstruction of data, instead a readout cycle is used to define what is considered as an “event”. This only influences the event display as it serves the purpose to visualise the data. The length of such a cycle can be defined by the user. For all these plots the online monitor offers the possibility to integrate over a selectable number of events. The selection of the integration of 0 events leads to an indefinite integration. As an example, this can be useful to get an online occupancy of the Timepix3 with the 2D plot of active pixels. A screenshot of the online monitor in operation is presented in Figure 6.24(a).

As alternatives for the online monitor its online interpretation process can be used for two additional event displays. One is directly included into the GUI and displays the matplotlib generated 2D plots of active pixels directly in the GTK3 window. The advantage of this event display is, that it can be directly accessed from within the GUI without the need of an installation of other programs or the need to start a separate script. A screenshot of this is presented in Figure 6.24(b).

The second option is a data handler that hosts the data from the interpretation on an event basis on a JSON server. Thus, every plotting tool that supports JSON inputs can be used to visualise the data. This was used to include an event display directly into the Grafana[5]-based monitoring tool (see Section 6.7). There it can be used directly together with other monitoring parameters, like the ASIC temperature to monitor the full detector operation in one place. A screenshot of the event display is shown in Figure 6.25. It is visible that for this event display also the ToA information of the data is used to create a 3D plot of events in addition to the 2D plot.

---

[4] `https://github.com/SiLab-Bonn/online_monitor`

[5] `https://grafana.com`

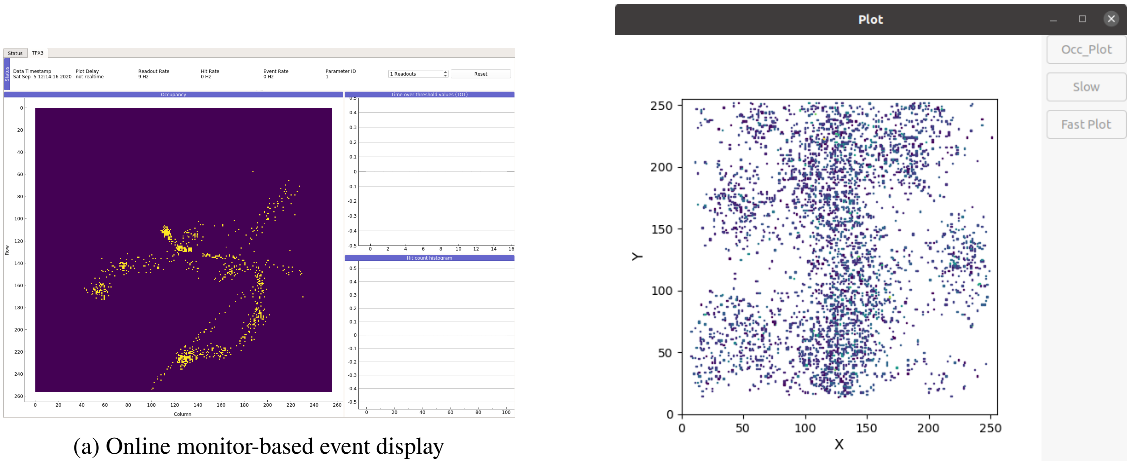

Data Timestamp: Sat Sep 5 12:14:16 2020
Plot Delay: not realtime
Readout Rate: 9 Hz
Hit Rate: 0 Hz
Event Rate: 0 Hz
Parameter ID: 1

(a) Online monitor-based event display

(b) Event display of the tpx3-daq GUI

Figure 6.24: Screenshots of two Timepix3 event displays that are part of the tpx3-daq.

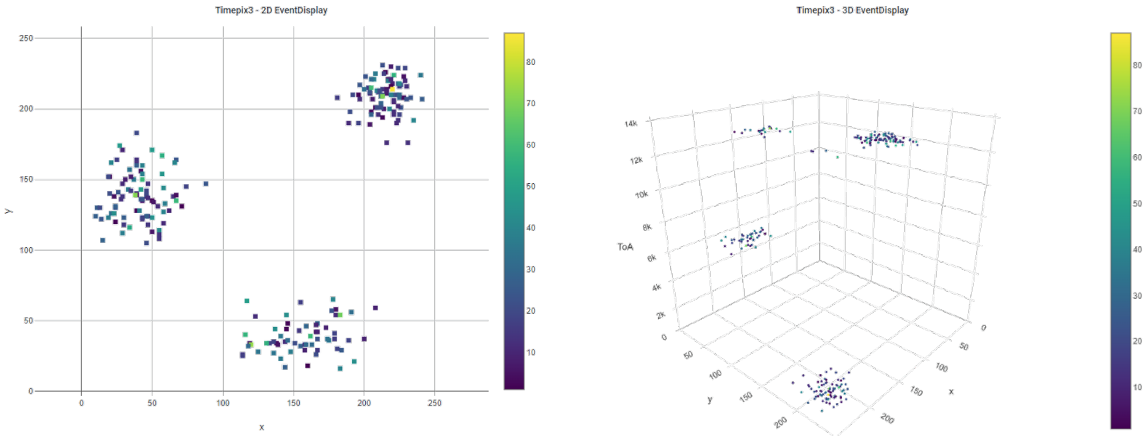

Figure 6.25: Screenshot of the Grafana-based event display for tpx3-daq. The left plot is a 2D projection of the current event, the right plot shows the event in 3D based on the additional ToA data. The z-scale of the 3D plot automatically adjusts to the range of ToAs within the data of the time frame. For photons, as visible in the event display, the expected ToA span is in the order of 5 clock cycles which is much smaller than the displayed range. Therefore, the photons look flat in z-direction. But in the comparison of the 2D and the 3D plot one can see that the ToA helps to distinguish events that look like the same cluster in the 2D projection.

6.7 Monitoring

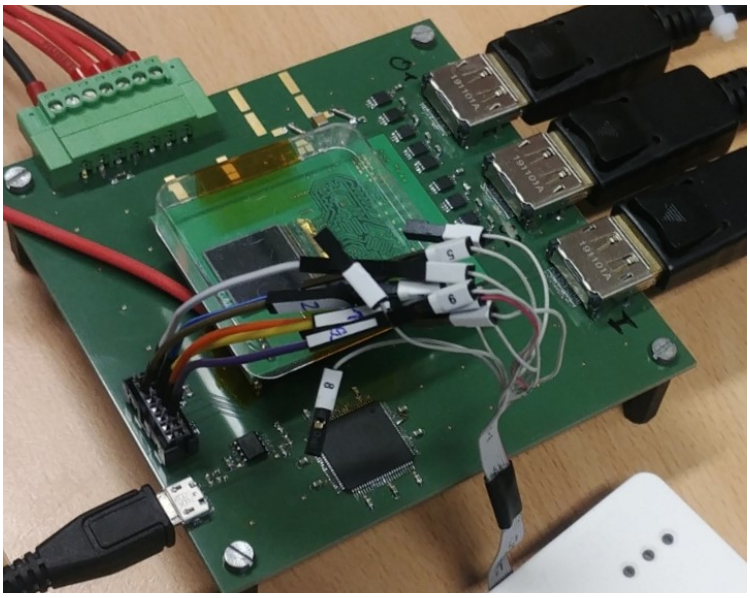

Figure 6.26: Picture of a Timepix3 setup with an intermediate board that features a microcontroller for monitoring. The microcontroller is the bigger quadratic square on the PCB in the bottom centre of the picture. It is connected to the USB micro-B plug and cable to the left that connects it to the monitoring readout software. Directly above the USB plug a JTAG plug is visible. It is used to flash a new firmware to the microcontroller and to run a debugger on it. For this purpose, the white box at the bottom right of the picture is used.

For monitoring purposes, the Timepix3 features an analogue output pad. By default, it is floating but via a command ("ExtDACsel") it can be connected to each of the internal DACs and additionally to some internal voltages. Two of these internal voltages can be used to read the temperature of the ASIC: the "BandGap_output" serves as a reference voltage and the "BandGap_Temp" changes with the temperature of the ASIC. Using these two voltages and based on a calibration curve and a conversion function the temperature can be estimated. The conversion function is [37]:

$$T = 88.75\,^{\circ}\mathrm{C} - 607.3\,\frac{^{\circ}\mathrm{C}}{\mathrm{V}} \times (\mathrm{BandGap\_output}\,[\mathrm{V}] - \mathrm{BandGap\_temp}\,[\mathrm{V}])\ . \tag{6.15}$$

For reading out the analogue output of the Timepix3 a "ATXmega 128A1U" micro controller is used. It features two ADCs with 12-bit resolution and in total 8 analogue inputs for these ADCs. This is important so that the monitoring can be easily adapted to up to eight Timepix3s on one PCB such that each of the ASICs would have their own monitoring channel. During the development of the monitoring system an evaluation board of this micro controller was used (the "XMEGA A1U XPLAINED PRO EVALUATION KIT") and connected via wires to the detector PCB. In later versions the detector PCBs directly feature the micro controller. A picture of a setup with a Timepix3 intermediate board that features a microcontroller is presented in Figure 6.26. The ExtDACsel pin of the Timepix3 is directly connected to one of the ADC inputs of the microcontroller. The microcontroller itself is connected via a USB micro-B plug and cable to a readout PC that runs the monitoring readout software. The power supply is done via the already available 3.3 V on the intermediate board that also provides power to the LVDS drivers. Additionally, the PCB features a JTAG connector that is used to flash the microcontroller and debug the microcontroller firmware in a development and testing context. In a future version of the intermediate board and also the adapter card it is planned to add an Ethernet port to both PCBs to connect the microcontroller directly to the FPGA. The reason for this is, that in the current implementation the microcontroller is not aware of the context of the Timepix3 readout, especially it does not know which signal is connected to the ExtDACsel via the settings of the Timepix3. Via the Ethernet port this information will be given to the microcontroller and additionally also how many Timepix3s are featured on the carrier board such that the ADCs of the microcontroller can be set accordingly. Another possibility of this is, to communicate to the FPGA an ID of the intermediate board. This enables the possibility to communicate intermediate board specific features to the readout system and to adapt its settings to it. So far, the microcontrollers on the intermediate boards already feature a unique ID that is used by the monitoring software, but it can be only read out via the USB connection.

6.8 Decoding of Raw Timepix3 Data

The data of the Timepix3 and the additional data generated in the FPGA are sent to the PC in 32-bit words (see Section 6.3). Therefore, hit data of the ASIC (48 bit) and timestamp data (48 bit) are split-up into two 32-bit words, each containing 24 bit of the original data word and an 8-bit header. To use the data, these two words need to be put correctly together to get the full 48 bit of the original word. Within the tpx3-daq this process is called “raw data interpretation”. It is a Python script[6] that was developed independent from the readout software.

As a first step, the words are sorted by their headers (see Table 6.2). With this, a list of data words per header is created and sorted based on the order in which the data words were received. Additionally, a list of indices is created for each list of data words. These are the indices of the words in the list of all data words. This is necessary to combine all individual lists to a full list again after interpretation.

The second step is, to combine the two 32-bit words to the expected 48-bit words (word 1 and 2 as seen in Table 6.2, the 8-bit headers per 32-bit word are removed). Here the first word of a word 1 list gets combined with the first word of the word 2 list and so on. The combination is done by shifting words 1 by 24 bits in MSB direction and applying then a logical AND of the shifted word 1 and word 2. As overall index of the new 48-bit word the index of word 1 is used.

In the third step, the combined ToA extension words are assigned to the combined hit words. For this, the hits are assigned to the last ToA extension that was recorded before the hit based on the overall word indices. For the most cases this is sufficient as one ToA extension timestamp fits for all arriving hits in the next 102.4 µs based on the ToA extension settings. But due to transmission delays from the Timepix3 ASIC to the FPGA it can happen that early hits in such a 102.4 µs cycle do not belong to the newest ToA extension but the previous one. To check for this, the interpretation logic used the fact that the ToA extension is read out for times per ToA cycle (409.6 µs). This results in a 2-bit overlap of both timers, which is used to check for consistency of both timers. If these 2 bits of a data word do not fit to the currently assigned ToA extension, the data word is shifted to the previous extension. For parallelisation purposes the steps described above are done for each link individually. Afterwards the data is concatenated and sorted based on the overall indices.

---

[6] `https://github.com/GasDet-Bonn/tpx3_interpretation`

In the next step, the data words are split up into the individual hit information based on the settings of the Timepix3. The different layouts of the data words for the different Timepix3 modes are displayed in Table 6.4. Based on the readout mode, the data is interpreted, and the results are put into a table that contains a column for each of the hit information. This also includes the original index of the hit, the ToA extension and a combined timestamp that consists of the ToA and the ToA extension.

If a scan result of a time walk calibration is available, the timestamps of the data are corrected. This is done based on the fit parameters a, b and c of the time walk calibration:

$$\text{timewalk} = \mathrm{e}^{a \times \mathrm{ToT} + b} + c\,. \tag{6.16}$$

The result of this calculation is subtracted from each timestamp to get the original time of the hit. Additionally, the clock offset based on the different clock phases per double column is corrected (x indicated the column number of a pixel):

$$\text{clock-offset} = \quad \bmod x/2\,. \tag{6.17}$$

Depending on the selection of the user this table is stored either in the same HDF5 file as the raw data or new one with a copy of the chip configuration.

Table 6.4: Content of Timepix3 hit words [37]. The 4-bit headers in bits 47 to 44 are determined by the readout approach: 1010 represents the sequential readout while 1011 represents the data-driven readout.

	Bits				
Mode	47 to 44	43 to 28	27 to 14	13 to 4	3 to 0
ToT + ToA + VCO	0101 or 1011	Pixel	ToA	ToT	fToA
ToT + ToA	0101 or 1011	Pixel	ToA	ToT	Hit counter
Only ToA + VCO	0101 or 1011	Pixel	ToA	Dummy	fToA
Only ToA	0101 or 1011	Pixel	ToA	Dummy	Hit counter
Counter + iToT + VCO	0101 or 1011	Pixel	iToT	Hit counter	Dummy
Counter + iToT	0101 or 1011	Pixel	iToT	Hit counter	Hit counter

The described interpretation works for runs that do not contain too much data[7] and also did not have any issues (discarded data or decode errors on the FPGA) during the run. To perform the interpretation of such runs some improvements and error corrections are needed:

- To be able to interpret runs with a lot of data, multi-threading of the interpretation of individual data chunks was introduced. This reduces the amount of RAM that is necessary and also efficiently uses multiple cores of the CPU. Additionally, runs with a lot of data chunks are sliced in a way that at no time more than 400 million data packages are analysed at the same time and thus must be stored in the RAM of the PC. These slices are then concatenated.

- Data chunks in which data was discarded, or in which decode errors occurred on the side of the FPGA, are flagged and its data is removed from the interpretation. This is necessary as in such chunks data could be missing and thus the assignment of word 1 and word 2 is no longer

---

[7] The exact amount of data that is too much depends on the PC that is used for the data interpretation. Especially the RAM but also the processor single core speed have an influence.

possible. In most cases this is obvious as the number of words 1 and words 2 in such a chunk is different but even if the number is the same it is safer to remove the chunk as a misalignment here could change the alignment of word in all following chunks.

- Removing corrupted data (as in the previous item) may lead to a trailing 32-bit word of a hit, while the other 32-bit word was removed with the previous chunk. Therefore, the first words of a chunk after a deleted chunk are checked for such words and if they are found they are deleted from the chunk to again prevent misalignment of data words.
- It may occur that chunks without an error flag are missing data which can be detected based on different numbers of word 1 and word 2. If this misalignment is found after the previous two corrections the chunk is also removed and the following chunk is checked for trailing words.

These error corrections are performed at the start of the decoding procedure (in full of for a slice of the data set). After that, all chunks that are not flagged with errors are analysed as described above. In normal operations of the readout system, no chunks are flagged and thus 100 % of the data is decoded. In some cases that can be for example linked to discharges in the detector, the recorded data is corrupted and thus, flagged chunks appear. Despite this, in none of the tested runs so far more than 0.1 % of the data had to be discarded because of flagged chunks.

6.9 Test of the Timepix3 Readout System

To test the readout system and to prepare for measurements, the system was checked within a broad range of parameters to check their influence. Additionally, scans were repeated multiple times with stable run parameters to investigate stability of the scans. For this a sequence of the PixelDAC optimisation, the equalisation, the threshold scan, the noise scan, the ToT calibration, and the threshold calibration was performed and repeated 10 times. Table 6.5 shows the results of the scans. One can see that in the comparison of the same scan the results are most of the time equal over all iterations or close together and compatible within the errors. Specifically of interest are the results of the ToT calibration and the threshold of the chip. For the former the resulting charge in electrons for 50 and 100 clock cycles was calculated for better comparison. For both, most iterations show very close results with only a few electrons of difference. For iterations 2 and 9 a bigger difference is observed in the order of 50 electrons for 50 clock cycles and 100 electrons for 100 clock cycles. Despite the bigger difference it is still in the order of a 1 % effect on the charge measurement. For the resulting threshold that is displayed in the last row of the table, the biggest observed difference is 19 electrons which is in the order of a 2 % deviation.

In addition to a few parameters per scan, for the equalisation also a pixel-wise comparison was performed. Figure 6.27 shows the pixel-wise difference of the first five equalisations. One can see that in the majority of cases the pixels got the exact same pixel threshold and basically always the results are compatible with an error of ±1 pixel thresholds. Just about 10 pixels show a bigger difference. Combining the results presented in Table 6.5 and Figure 6.27 it can be inferred that the readout system is stable and that the scans give reproducible results. Thus, the readout system can be used for detector operations.

Table 6.5: Results of a sequence of Timepix3 scans that was repeated 10 times.

Iteration	1	2	3	4	5	6	7	8	9	10
PixelDACOpt Result	82	82	83	83	83	82	83	84	84	83
Equalisation Mean	7.7	7.7	7.7	7.7	7.7	7.7	7.7	7.7	7.7	7.7
Equalisation Width	2.4	2.4	2.4	2.4	2.4	2.4	2.4	2.4	2.4	2.4
Threshold Mean	2016.31	2016.43	2016.27	2016.67	2016.76	2016.50	2016.88	2016.67	2016.64	2016.65
Threshold Sigma	2.57	2.55	2.62	2.57	2.57	2.60	2.60	2.52	2.54	2.62
Noise Mean	4.2	4.1	4.3	4.2	4.3	4.3	4.2	4.2	4.3	4.3
Noise Sigma	0.9	0.9	0.9	0.9	0.9	0.9	0.9	0.9	0.9	0.9
Threshold [DAC]	1793	1798	1796	1799	1796	1794	1802	1794	1798	1798
ToT Calib a	0.66	0.67	0.66	0.66	0.66	0.66	0.66	0.66	0.67	0.66
ToT Calib Δ a	0.00	0.00	0.00	0.00	0.00	0.00	0.00	0.00	0.00	0.00
ToT Calib b	−7.55	−7.72	−7.63	−7.65	−7.68	−7.58	−7.61	−7.66	−7.65	−7.68
ToT Calib Δ b	0.17	0.17	0.17	0.16	0.17	0.17	0.17	0.17	0.16	0.17
ToT Calib c	6.13	5.60	5.96	5.37	5.48	6.05	5.87	5.95	5.84	5.33
ToT Calib Δ c	1.73	1.66	1.78	1.63	1.69	1.78	1.73	1.73	1.69	1.67
ToT Calib t	23.24	23.32	23.21	23.34	23.29	23.16	23.27	23.24	23.25	23.33
ToT Calib Δ t	0.52	0.52	0.56	0.53	0.55	0.57	0.53	0.53	0.53	0.55
ToT [e-] (50 CC)	4083	4034	4089	4089	4091	4085	4087	4091	4029	4091
ToT [e-] (100 CC)	7621	7519	7627	7628	7630	7623	7625	7629	7514	7630
ThresholdCalib m	0.074	0.074	0.074	0.074	0.074	0.074	0.074	0.074	0.074	0.074
ThresholdCalib n	1738.9	1739.4	1739.8	1740.3	1739.1	1739.7	1739.5	1739.5	1739.6	1739.8
Threshold [e-]	785	778	773	766	782	774	777	777	776	773

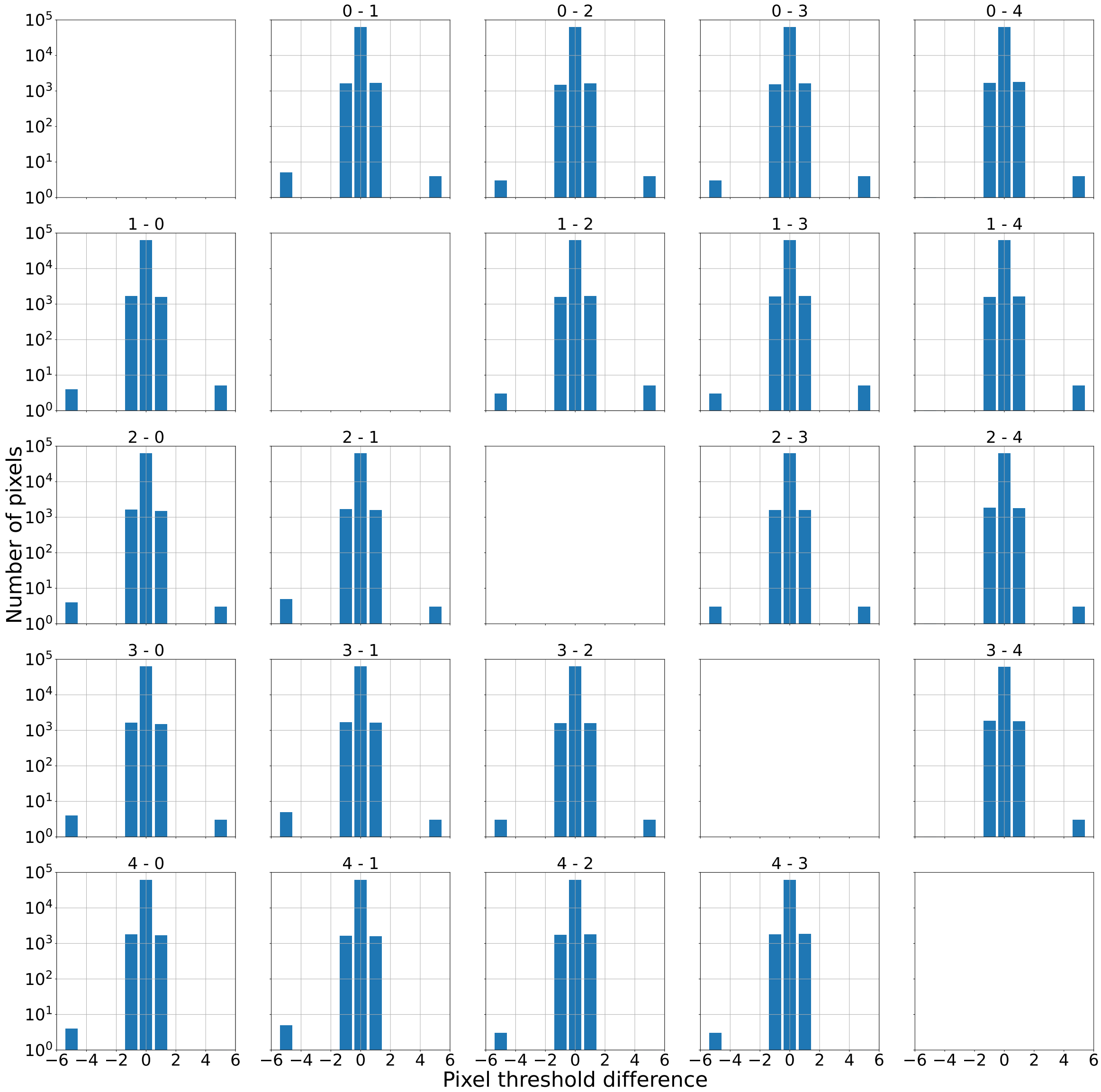

Figure 6.27: Pixel-wise comparison of five equalisations of the same Timepix3. For each pixel, the resulting pixel threshold of one equalisation subtracted from the pixel threshold for the same pixel of another equalisation. The title of each plot displays the indices of the used equalisations. For example, in “1-0” the result of equalisation 0 was subtracted from the result of equalisation 1. The diagonal is not plotted because the subtraction of a result from itself is always 0 and thus contains no useful information. Besides a maximum of 10 pixels all equalisations are compatible with an error of ±1.

CHAPTER 7

GridPix X-ray Detectors

In this chapter the GridPix detectors and their working principle will be explained. Section 7.1 introduces the GridPix, explains how it is built and how it works. In Sections 7.2 and 7.3 two detectors will be explained; one based on a GridPix with Timepix, and one based on a GridPix with Timepix3. At the end of the chapter, Section 7.5 will introduce a concept for an alternative GridPix-based detector for X-ray polarimetry.

7.1 GridPix

The GridPix is a combination of a photo-lithographically post-processed integrated grid (InGrid) that serves as a gas amplification stage, and a pixelised readout ASIC like the Timepix or the Timepix3. Figure 7.1 shows a microscope picture of a GridPix with a Timepix3. The grid is a $1\,\mu\text{m}$ thick aluminium layer that is placed on insulating SU-8 pillars at a height of $50\,\mu\text{m}$ above the readout ASIC. The holes in the grid are aligned with the pixels of the ASIC. With this setup a high voltage in the order of 300 V or more can be applied to the grid and due to the grounding of the ASIC an electric field in the order of $60\,\frac{\text{kV}}{\text{cm}}$ is present between the grid and the ASIC. Thus, charges that enter this region though the grid holes are accelerated towards the ASIC and gain enough energy such that an electron avalanche is started (see Section 4.4). Each pixel serves as a charge collecting anode and each signal above the threshold can correspond to a charge collection of a single avalanche. By tuning the threshold and the gas gain, the collection efficiency can be optimised to the point of single electron detection with a high probability. This design also enables the possibility for a high position resolution, which is then mainly influenced by the diffusion of the charges during their drift towards the grid. Furthermore, the alignment of the grid and the pixels ensures that no Moiré pattern emerges.

A sketch of the production of a GridPix is shown in Figure 7.2, its following description is based on [45–47]. This production can be done either with single ASICs or on wafer scale. It starts with cleaning of the wafer and then a silicon-enriched silicon nitride layer is deposited on the wafer (step (a) in Figure 7.2). This is done via chemical vapour deposition (CVD). This layer serves in the GridPix as a discharge protection of the ASIC and the pixels. Such discharges can appear in gaseous detectors in regions with high electrical fields. Without the protection layer a single discharge can destroy an ASIC but with this layer it was proven that GridPixes can survive conditions with frequent discharges [48]. As this layer would also cover the wire bonding pads of the ASICs and thus prevent the electrical

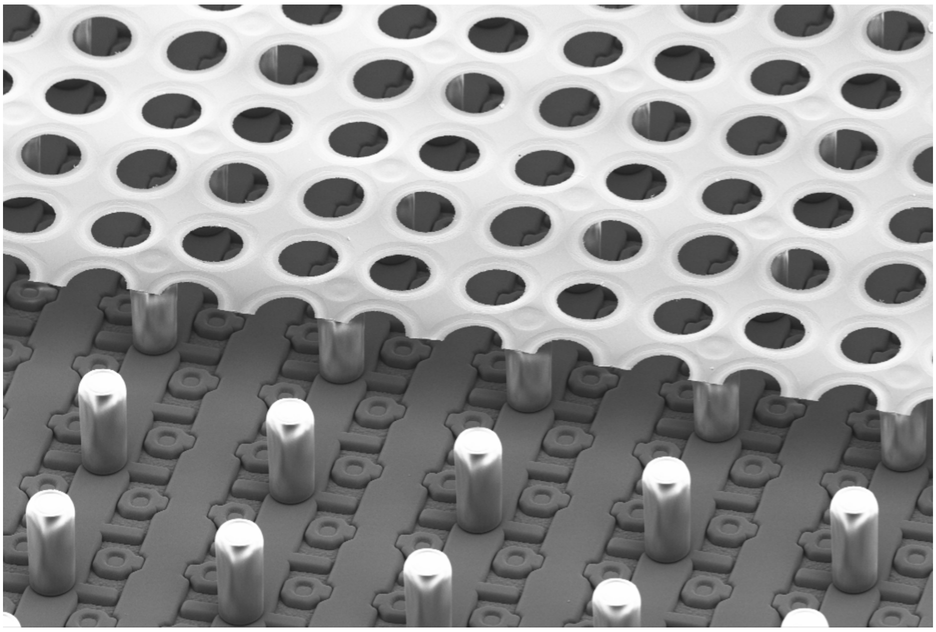

Figure 7.1: Microscope picture of a GridPix. The grid on the lower part is removed to get better visibility of the pillars and the pixel plane. Between every second pixel in x and y direction an insulating pillar is placed to hold the grid at a height of 50 µm. The holes in the grid align perfectly with the pixels and thus feature the same 55 µm pitch. [44]

connection of the ASICs to low voltage and the readout system, they are covered with a polyimide layer that is removed in a later processing step. In the next step a 50 µm layer of the negative photoresist SU-8 is spin coated on the wafer (step (b) in Figure 7.2). It serves as spacer layer for the deposition of the grid but also the pillars that will hold the grid are formed from it. In addition to the pillars, there is a continuous rectangular “block” of SU-8 that surrounds the ASIC and covers the outer few pixel columns and rows. This is called “dyke” and its propose is to add mechanical stability to the InGrid that is for example needed for dicing the wafer into individual GridPixes. The pillars and dykes are then formed by exposing the SU-8 on their positions with ultraviolet (UV) light via a mask. This cross-links the SU-8 and prevents it from being removed with chemical solvents in later steps. In the next step (step (c) in Figure 7.2) the 1 µm thick aluminium layer is sputtered on the SU-8. Additionally, a layer of a positive photoresist is placed and exposed with UV and a mask that creates a layer to protect the aluminium at positions where no grid holes should be formed. The unprotected aluminium is removed by chemical etching. Before the remaining unexposed SU-8 is removed the wafers are diced into individual GridPixes. With the dissolving of the SU-8 (step (d) in Figure 7.2) the GridPixes are finished and can be used for detectors.

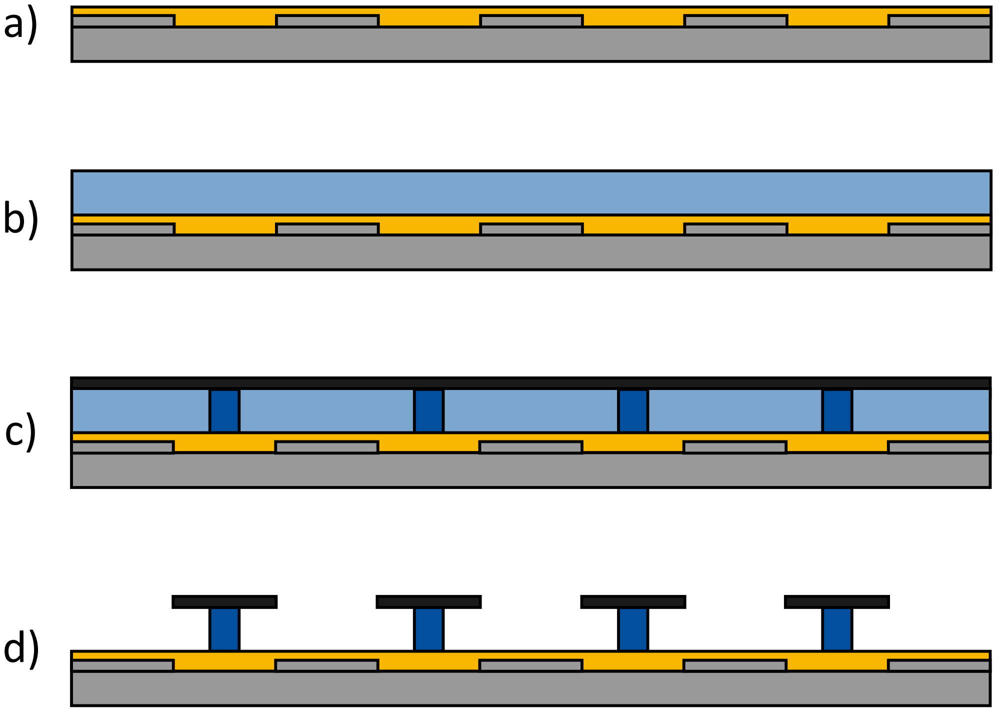

Figure 7.2: Schematic production steps of GridPixes. In a) a silicon enriched silicon nitride layer as a spark protection is deposited on the ASIC. In b) the negative photoresist SU-8 is deposited on the wafer with a thickness of 50 µm. It serves as material to form the pillars and the dykes at the edges of the ASIC but also as a spacer for the aluminium layer of the grid. In c) the pillars (and dykes) were already developed by UV exposition and a 1 µm thick aluminium layer was sputtered on top the SU-8 layer. Between c) and d) the wafer is diced into individual chips before unexposed SU-8 and other residues are dissolved. The finished GridPixes remain.

7.2 Timepix-based Detector

The Timepix-based detector is an X-ray detector based on the design for the detector used at the CAST-experiment for Axion search (see [49, 50]). An explosion view of the detector is presented in Figure 7.3. At the top, the detector features a copper plate that serves as a cathode. In the middle of the plate a segmented rectangular cutout is visible. This serves as an entrance window for X-rays as the copper blocks soft X-rays. To close the gas volume, a 2 µm thick Mylar foil is glued to the cathode which is much more transparent for the X-rays. The foil is additionally aluminised such that the electric potential of the cathode is also present at the X-ray window and no field inhomogeneities are introduced. The segmentation of the cathode serves as a strong back for the Mylar foil such that a high pressure difference between the outside and the inside can be used. Furthermore, it minimises the bulge that is formed by the foil due to the gas pressure and thus, the influence on the homogeneity of the electric field. The cathode plate is mounted to a PMMA cylinder with a rubber O-ring seal in between. This cylinder is called the “drift ring” and encloses the main detection volume in which the X-rays interact with the gas. For various applications, these drift cylinders can be produced in variable lengths resulting in drift lengths of for example 1 cm, 2 cm, and 3 cm. These drift cylinders also feature two brass gas connectors that are pushed into the cylinder and sealed with O-rings to supply a constant gas flow to the detector. Within the drift cylinders, there is the possibility to mount field cages to reduce field inhomogeneities due to edge effects. On the bottom of the field cage the intermediate board of the Timepix readout system is mounted, again sealed by an O-ring between the PCB and the drift ring. Thus, the intermediate board not only serves the purpose to supply the Timepix with needed voltages and the connections to the readout system, but additionally as endcap of the gas volume. The carrier board of the Timepix readout system is mounted onto the intermediate board. On this board the Timepix-based GridPix is glued and electrically connected via wire bonds. Between the carrier board and the intermediate board, a PMMA structure serves as a stabilisation of the carrier board and additionally as a holder for an anode. The anode is made of FR4 that is covered with copper and has a rectangular cutout in the middle for the GridPix. The PMMA structure defines the relative height of the anode with respect to the GridPix and together with a thinning of the FR4 close to the bonds of the GridPix ensures that it can be mounted without touching the wire bonds. The anode is important as an electric field just between the cathode and the GridPix would easily be inhomogeneous because of the different sizes of the electrodes. Thus, extending the GridPix with a surrounding anode ensures a homogeneous electric field above the GridPix. The voltage of the anode must be chosen based on the voltage of the grid and the distance of anode and grid to ensure a homogeneous electric field.

This detector works as follows: X-ray photons enter the detector trough the X-ray window within the cathode and then interact with the gas via the photoelectric effect (see Section 4.1). As a result, a photoelectron is released. It has sufficient energy to further ionise the gas along its path while losing energy and scattering off gas atoms and molecules (see Sections 4.2.1 and 4.2.2). The created electron-ion pairs drift apart due to the electric field that is present due to the potential difference between cathode, anode, and grid. The voltages are set such that the electrons drift towards the GridPix. The electrons drift along the field lines with a gas-dependent drift velocity and diffuse during the drift due to scattering (see Section 4.3). When the electrons reach the GridPix they go through the grid holes into a region with a higher electric field than the drift field. In this region the electrons gain enough energy to start avalanches that are detectable by the pixels of the Timepix.

7.3 Timepix3-based Detector

The Timepix3-based detector follows the design of the Timepix-based detector. It was developed in the scope of [42] and is built in a way such that parts of the Timepix3-based detector like for example the cathodes with the X-ray windows can be reused. At the anode side of the detector the Timepix specific PCBs are replaced with the Timepix3 specific PCBs that again serve as an end cap of the detector and seal the gas volume with an O-ring between the intermediate board and the PMMA drift cylinder. An explosion view of the detector is presented in Figure 7.4. As the carrier boards for Timepix3 are wider than the Timepix carrier boards, the drift cylinders of the Timepix-based detectors are not compatible because an additional cutout on the inside of the ring is needed to provide sufficient space. Therefore, new drift rings with drift lengths of 1 cm, 2 cm and 3 cm were manufactured such that different drift setups could be tested. The scheme of the detector in Figure 7.4 shows the setup with the 3 cm drift ring. In principle the drift ring can support the addition of a field cage on the inside to improve the field homogeneity. Studies of the electric field in [42] showed that with a 3 cm drift ring and a 500 $\frac{\mathrm{V}}{\mathrm{cm}}$ drift field, the field inhomogeneity in the volume above the active area is smaller than 1 %. This would get even smaller with lower drift lengths or higher drift fields. Therefore, no field cage was used with this detector. Instead, one of the feed-thoughts for connecting the field cage to high voltage was used as a feed-through to connect the anode to high voltage and the other was sealed with epoxy resin.

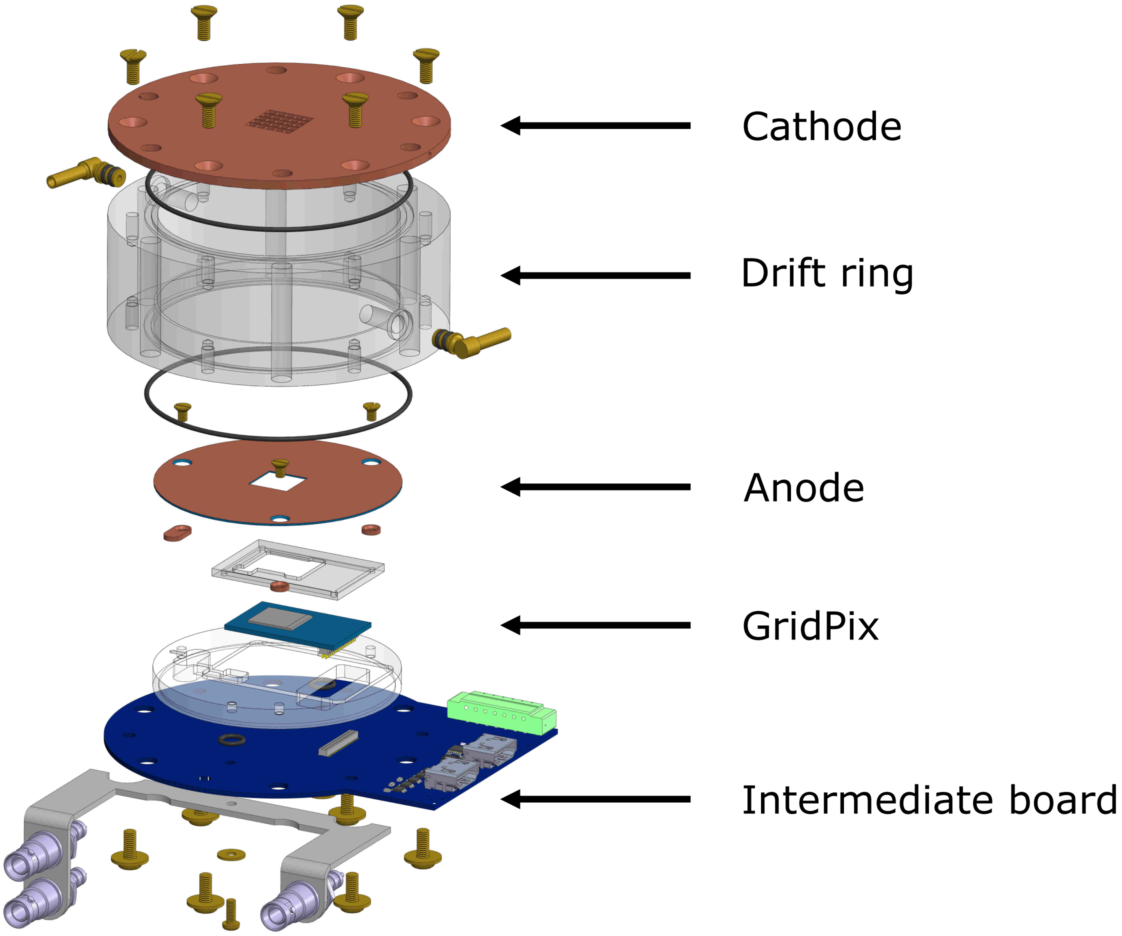

Figure 7.3: Exploded view of a CAST-like GridPix X-ray detector. The X-ray photons enter the detector from the top through an X-ray window within the cathode. In the drift volume they interact with the gas which leads to electron-ion pair creation. These pairs are separated due to the electric field that is applied between the cathode and the anode. It is usually in the order of hundreds of Volts per centimetre. Within the anode, there is a rectangular cutout for the GridPix. The electrons drift towards the GridPix and get through its grid holes. Then they create gas amplification avalanches due to an electric field in the order of tens of thousands of Volts per centimetre between the grid and the Timepix. The avalanches are detected as charge injections in the pixels of the Timepix. The GridPix is glued on a PCB that is called carrier board, and it is electrically connected to it via wire bonds. The carrier board is plugged into the intermediate board. It offers all connections for the detector operation like low voltage, high voltage, and data connections, but also serves as an end cap for the gas volume. Based on [49].

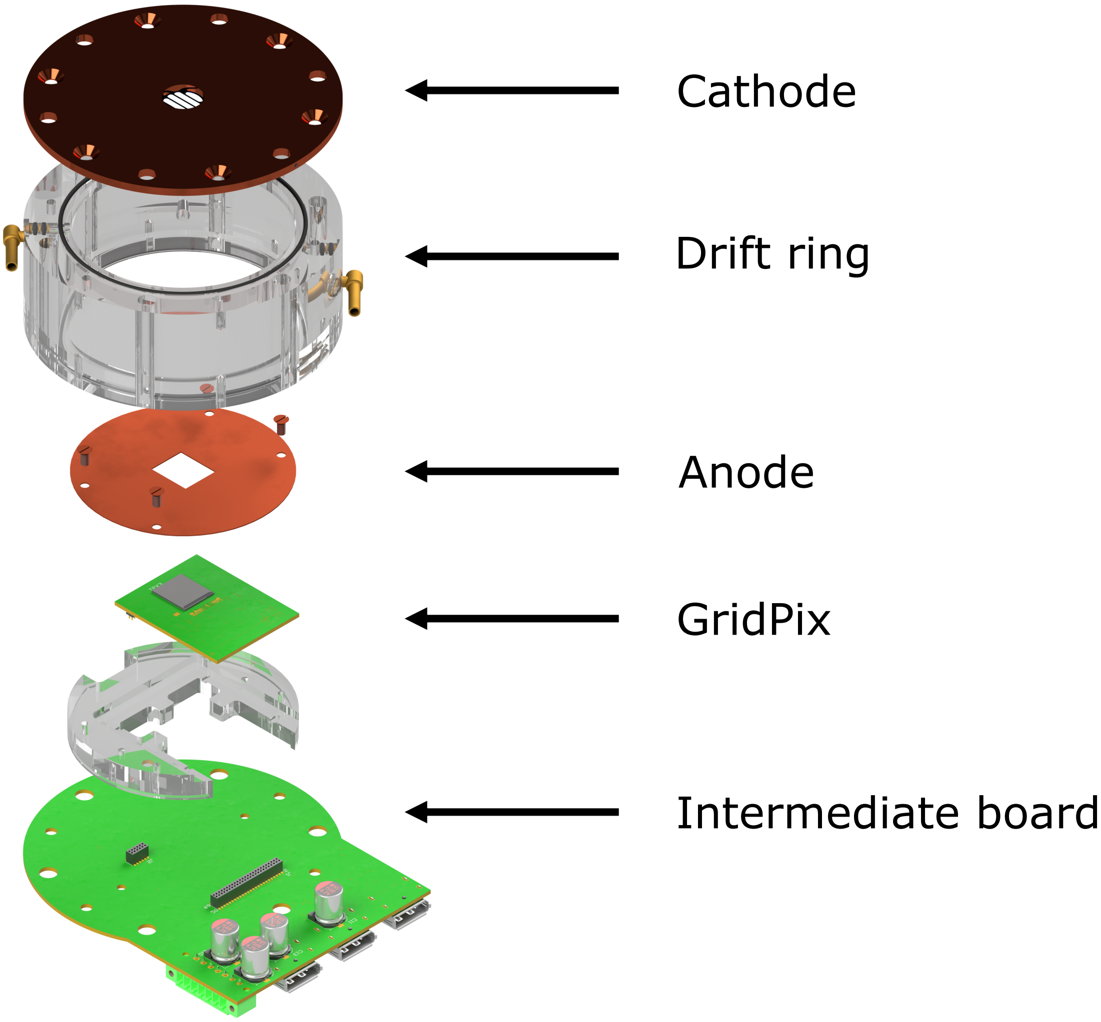

Figure 7.4: Exploded view of a CAST-like GridPix3 X-ray detector. The detector uses the same principle and setup as the Timepix-based detector presented is Section 7.2 and Figure 7.3. It is built such that some parts like the cathode of the Timepix-based detector could be reused. The main differences are the new carrier board that features a GridPix-based on Timepix3 and a new intermediate board that is required to operate and read out the Timepix3. Based on [42].

7.4 The Parallel Detector

While the detectors presented in Sections 7.2 and 7.3 follow an orthogonal approach with the X-ray beam entering the detector orthogonal to the readout ASICs, there is also the possibility to build a detector in which the beam enters parallel to the ASICs. A sketch of such a detector setup is presented in Figure 7.5. Compared to the orthogonal approach there are several advantages:

- As the cross section of the photo effect is inversely proportional to the energy (see Section 4.1). In an orthogonal detector the efficiency for detecting photons in the gas volume drops with increasing energies. In the parallel approach this effect could be reduced by using multiple GridPixes in beam direction. While the distribution of photon interaction points is exponential for all soft X-ray photon energies, with the highest probability behind the entrance window, the decay length of the exponential gets longer with rising energies. Thus, the likelihood to detect low energy photons on later GridPixes is lower than for high energy photons. This could be additionally used as a rough, probability-based energy measurement.

- In this approach the drift length is decided by the height of the beam entrance into the detector with respect to the ASICs. Thus, the photoelectrons start always on the same height with respect to the ASICs. This would remove the energy dependence of the drift and furthermore remove the probability distribution of absorption heights with respect to the GridPix that also influences the diffusion.

The main disadvantage of this approach is, that the projection of the $\cos^2$-distribution of photoelectron angles is no longer “symmetrical” in the used axes. This is the case because in such a detector this projection is in the y-z plane with y being a space axis, while z being a time-based axis. So, different resolutions of these two axes can introduce spurious modulation. Another disadvantage is, that in this approach it is likely that photoelectrons, especially from photons with higher energies, hit the grid and thus the Bragg peak is not detected. This is the case because of the now used y-z plane that leads to a lot of photoelectrons going into the direction of the grid. This could spoil the reconstruction as it gets harder to differentiate start and end of the track and thus lead to spurious modulation and also introduce a bias on the energy measurement as this would lead to missing energy.

Examining the advantages and disadvantages, such a detector should be tested especially with Timepix3-based GridPixes that enable simultaneous and trigger-less time and charge measurements. For such a detector the reconstruction needs to be adapted and especially the spurious modulation needs to be studied. If the spurious modulation can be minimised, the advantages of increasing the efficiency and losing some of the energy dependence could increase the energy band in which such a detector can be operated. Furthermore, it can decrease the number of photons that have to enter the detector to get to a measurement of the polarisation with a given confidence level.

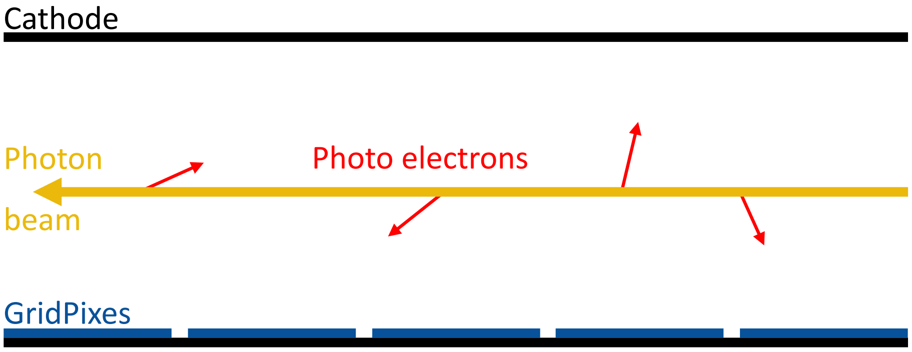

Figure 7.5: Sketch of a parallel GridPix X-ray polarimeter. The photon beam traverses the detector in parallel to the GridPixes and the cathode. Thus, all photoelectrons start at the same height with respect to the to the GridPixes. Furthermore, the efficiency dependence on the photon energy can be eliminated by using multiple GridPixes in the beam direction.

CHAPTER 8

GridPix X-ray Detector Simulation

The GridPix detectors presented in Chapter 7 offer several variables like drift length, electric field strength and gas parameters that all influence the detection of X-rays photons and the measurement of their polarisation in various ways. Thus, an end-to-end simulation was implemented within the scope of this thesis that helps to test these parameters and study their influence on X-ray polarisation measurements without the need to produce all the detectors and to operate them with all the different parameters. End-to-end means in this case that the simulation starts with beam and detector parameters, then simulates a requested number of events and in the end stores the data in the same format as the readout systems for Timepix and Timepix3 would do it. Therefore, the same analysis and reconstruction tools that will be described in Chapter 9 can be used for the simulation data which also helps to validate these tools. Besides the usage of the simulation to study GridPix-based polarimeters, it can be used for all GridPix X-ray detectors and with some modifications also for other GridPix-based detectors. For example, in [42] the simulation was used for studies of a new detector for the international X-ray observatory (IAXO). In this chapter, first the implementation of the simulation will be discussed in Section 8.1 followed by a description of all simulation parameters in Section 8.2. In the end, Section 8.3 will discuss the limits and idealisations of the simulation and present ideas for future improvements of it. Results based on the simulation will be discussed in Chapter 10.

8.1 Implementation

To simulate the behaviour of a GridPix detector a software based on Degrad [51] and Garfield++ [52] was implemented[1]. The simulation starts by either reading or generating a so called “gasfile”. This file contains parameters of the gas for simulating the drift and diffusion, like drift velocity and longitudinal and transversal diffusion coefficients. This file is based on a Magboltz [53] simulation. The simulation is implemented such that if no gasfile is provided a new one is generated automatically for the current set of detector parameters via the Magboltz interface of Garfield++. In the next step Garfield++ is used to simulate the absorption of photons in the gas volume. Therefore, a photon is put at the upper end of the detector, which corresponds to the point closest to the cathode within the gas volume. The photon gets the energy based on the input of the user and its direction is the negative z-axis, which is perpendicular to the GridPix and points towards it. The z-coordinate of the absorption

---

[1] https://github.com/GasDet-Bonn/GridPix_xray_simulation

point of the photon is stored if it is located within the gas volume. This is repeated until 100 000 photons are absorbed within the gas volume. By counting the photons that were simulated but not absorbed within the gas volume the absorption efficiency can be estimated by

$$E_{\text{Detector}}^{\text{Simulation}} = 1 - \frac{\text{Total photons} - 100000}{\text{Total photons}} \,. \tag{8.1}$$

The simulation does not contain a simulation of the X-ray window. Therefore, for the full efficiency of the detector the result from Equation 8.1 needs to be multiplied by the transmission probability for the window. In addition to the efficiency estimation the z-coordinates of the absorption points are put into a histogram and fit by an exponential function. An example for such a plot is presented in Figure 8.1.

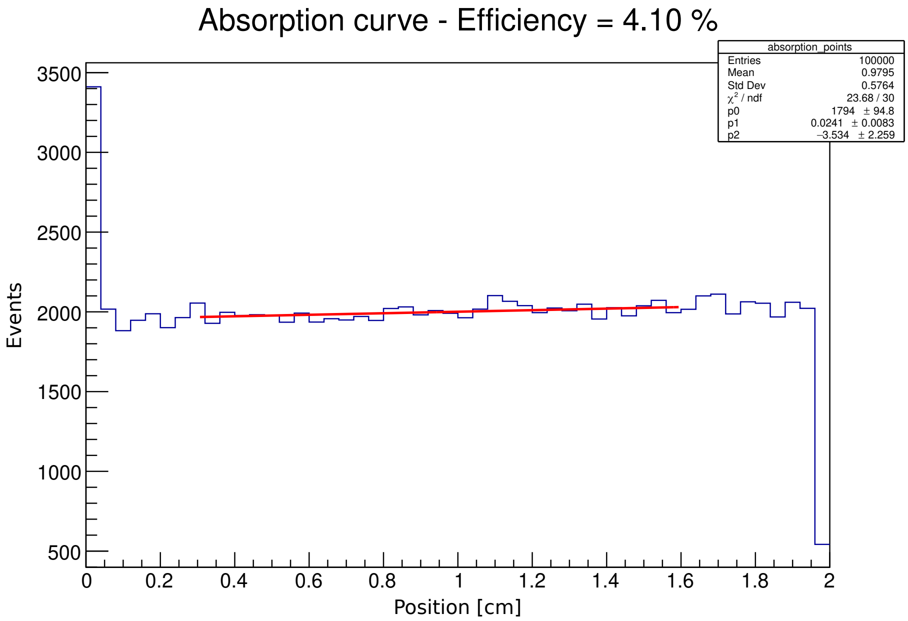

Figure 8.1: Simulation results for photon absorption points in He/DME with a mixing ratio of 80 %/ 20 % for normal pressure and a photon energy of 4 keV. The simulation was performed as part of the GridPix X-ray simulation with Garfield++. In total 100 000 photons were simulated. Deviations in the first and in the last bin are binning effects. To avoid the binning effects a fit of an exponential function was only performed with the central part of the histogram. The fit result is used in a later part of the simulation as a probability distribution to draw the start points of photoelectrons. The efficiency is also estimated based on the number of photons that were simulated versus the number of photons that actually interacted within the gas volume.

In a later part of the simulation, this exponential function is used to sample the starting points of the photoelectrons. As an alternative, the user can select to simulate one photon at the start of an event. So, for each event a Garfield++ simulation of a photon is started and repeated until it interacts within the gas volume. Then its interaction point is used as the start point for the photoelectron. This approach is mainly beneficial for simulations with a small number of photons and a high efficiency because otherwise the number of photons that are simulated in the combination of all events would quickly exceed the 100 000 photons that are simulated to create the probability distribution.

After the simulation of the photon absorption, Degrad is used to simulate the photoelectron track. In the default implementation, Degrad emits the photoelectron in a random direction perpendicular to the direction of the photon. For the simulation, this was changed such that the photon is always emitted in the direction of the positive x-axis which would be parallel to the wire bond pads of the Timepix/Timepix3. Degrad then simulates the interaction of the photoelectron with the gas such that a list of positions and times is created. This list contains the starting points of electron-ion pairs along the track. The electron ion pairs come from the ionisation of the gas by the photoelectron (see Section 4.2.1). For the interactions of the photoelectron with the gas, Degrad also considers Coulomb scattering (see Section 4.2.2). A two-dimensional plot of the start positions of electron-ion pairs for an example event is presented in Figure 8.2. The track starts at 0 µm/0 µm and goes into the direction of the positive x-axis, as it was implemented in Degrad. Each point represents an electron-ion pair due to ionisation of the gas and one can see an accumulation of them towards the end of the track — the Bragg peak. The scattering of the photoelectron is also visible.

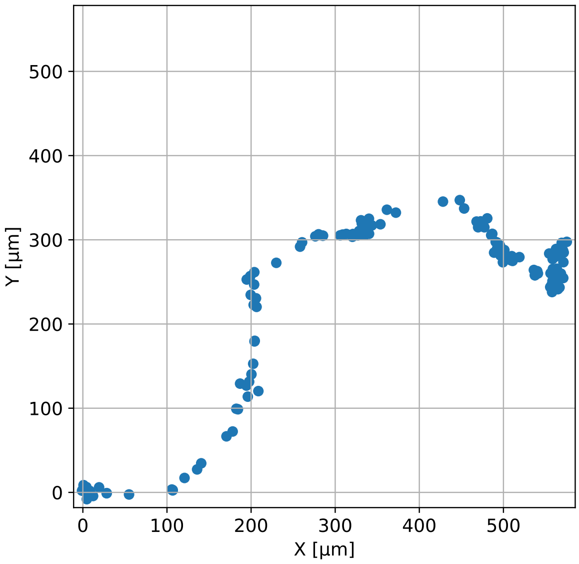

Figure 8.2: Example photoelectron track simulated with Degrad. The simulation was performed with He/DME with a mixing ratio of 80 %/20 % for normal pressure and a photon energy of 4 keV. Each point represents a creation point of a new electron-ion pair by via ionisation caused by the photoelectron. The photoelectron starts at 0 µm/0 µm into the direction of the positive x-axis. Towards the end of the track an accumulation of electron ion pairs is visible which is called Bragg peak.

As the direction of the photoelectron is not always the same but follows a $\cos^2$-distribution (see Section 4.1), the directions of the photoelectrons must be adapted to this. This can then be achieved by rotating the events according to the expected distribution. Therefore, the output coordinates are used and based on the settings of the polarisation degree P and direction ϕ_0, rotated by drawing angles from a $\cos^2$-distribution that represents these parameters. It is defined by:

$$A(\phi) = P \cdot \cos^2(\phi + \phi_0) + (1 - P) \ . \tag{8.2}$$

The example event that was shown in Figure 8.2 is again shown in Figure 8.3(a) with a rotation angle of 5.84 rad that was drawn from the $\cos^2$-distribution.

The rotated coordinates, the z-coordinate, and the time that are both not influenced by the rotation, are in the next step used as an input for the drift of the electrons in the electric drift field. For the simulation of the drift, there are three approaches implemented: two approaches based on Garfield++ functions with “AvalancheElectron” of “AvalancheMC” and with “DriftElectron” of “AvalancheMicroscopic” [2]. The third approach uses the drift and diffusion parameters of the gasfile to calculate the distributions for longitudinal and transversal diffusion and then draws from them in a Monte-Carlo approach. The standard deviation of the expected transversal spread of the electrons is based on the transversal diffusion D_t and the drift length L:

$$\sigma_t = D_t \cdot \sqrt{L}\,. \tag{8.3}$$

The standard deviation of the expected drift time due to the longitudinal diffusion D_l with the drift velocity v_D is:

$$\sigma_l = D_l \cdot \sqrt{\frac{L}{v_D^2}}\,. \tag{8.4}$$

Based on these two standard deviations, the time and position of each electron after the drift are drawn from Gaussian distributions.

The two Garfield++ based approaches both perform a simulation of the diffusion in multiple steps along the drift path with an adjustable simulation resolution. This has the advantage that not just the start and the end point of the drift are known, as for the third approach, but there are intermediate points. This enables the possibility to probe field inhomogeneities because for each step of the drift the local electric field can be considered. In contrast to this, the third approach assumes a homogeneous electric field and thus, constant diffusion parameters. But this advantage comes at the cost of calculation time as the third approach gets its result for all electrons in an event in the order of a second while the two Garfield++ approaches would need minutes. The main difference of “AvalancheElectron” and “AvalancheMC” is that the first one can also simulate electron avalanches if the field strength is sufficient. Therefore, it would be mainly interesting to use this approach with a full field map of a GridPix detector that not only contains the drift field but also the amplification field. In this case the same function could simulate the drift of the electrons towards the grid and then their amplification below the grid. This comes at the cost of additional computation time due to an additional check for ionisation processes. Thus, “AvalancheMC” should be used for simulations of the drift if a map of the field is available. For a homogeneous field and a high number of events the Monte-Carlo approach should be used.

Based on the final x and y coordinates of the electrons, they are assigned to pixels of the Timepix and Timepix3 based on a 55 µm binning of the coordinates according to the pixel pitch and a shift of the Degrad coordinate origin at 0 µm/0 µm to the centre of the ASIC. At this point, there is the option that this already produces the final data of the event without consideration of the gas amplification. In this case, the pixel coordinates and the number of detected electrons by each pixel are saved. The number of electrons is saved as ToT where one ToT clock cycle represents one electron. This must be considered when applying the ToT calibration (see Section 6.5.8) to the data. For Timepix3, in addition to the ToT the times of the first electron detection per pixel are saved as ToA. For this, the

---

[2] The documentation of Garfield++ functions can be found at `https://garfieldpp.web.cern.ch/garfieldpp/documentation`

start time of the event is considered as ToA = 0 and then the resulting times in nano seconds are converted into the ToA and the fToA with the ToA running in 25 ns steps into the forwards direction and the fToA running in 1.5625 ns in the backwards direction (see Section 5.2). Additionally, the ToA extension (see Section 6.3) is generated by the event number multiplied by 1000. This gives unique timestamps to all events and the possibility to check if the time-based reconstruction (Section 9.1) works as expected. For the Timepix3 data it is also important that it is stored as if the decoding of the data (Section 6.8) was already performed. Thus, the Timepix3 output of the simulation can be used as a direct input for the reconstruction (Chapter 9). The event that was shown in Figures 8.2 and 8.3(a) is again presented in Figure 8.3(b) but after diffusion and pixel binning. A colour scale to indicate how many electrons were detected per pixel was added. The track shows the same shape, but one can see that some details get smeared due to the diffusion and the binning. The Bragg peak is still clearly visible due to the high number of electrons that are detected by the same pixel.

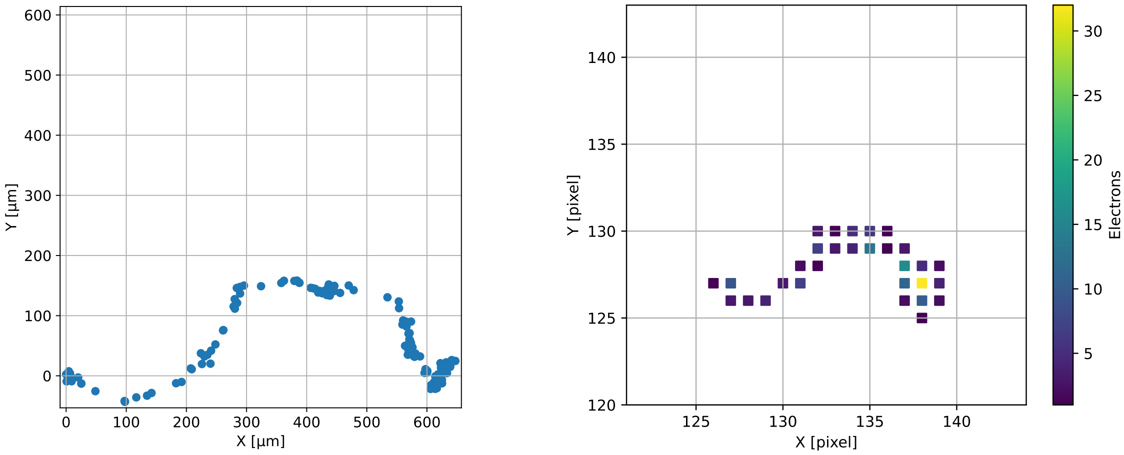

(a) Rotated Degrad photoelectron track

(b) Diffused and pixelized photoelectron track

Figure 8.3: Simulated photoelectron track after rotation and diffusion. To get from a raw photo electron track as presented in Figure 8.2 to a simulated event first the track is rotated around the centre at 0 µm/0 µm by a degree that is drawn from a $\cos^2$-distribution. The result can be seen in (a). In this case the event was rotated by 5.84 rad. After that, all electrons are diffused based on their distance to the grid and on the diffusion parameters of the gas. At the end, their resulting positions are binned by 55 µm to match the pixel pitch of the Timepix and the Timepix3 and furthermore the centre of the Degrad simulation is shifted towards the centre of the ASIC. The result for the same track can be seen in (b). The track starts at the left on pixel 126/127 and goes to the right. At the end of the track the Bragg peak is visible. Due to the number of electrons, the diffusion, and the size of the pixels it is possible that multiple electrons are detected by the same pixel. Therefore, the number of electrons per pixel is indicated by the colour scale.

For the simulation of the gas gain there are several problems whose influence is not yet quantified:

- Charge-up effects of the protective layer (see Section 7.1) of GridPix due to charge deposition. This effectively lowers the electric field between the grid and the ASIC and thus, reduces the gas gain because it depends exponentially on the electric field (Section 4.4). This effect varies with the rate as this leads to a different equilibrium state of charge deposition and charge drainage. Charge-up was observed in several measurements with the GridPix (e.g. [54]) but not yet quantified.

- The collection efficiency of the avalanches in the pixels is not known. For this it must be considered that despite the pixel pitch of 55 µm the active area is smaller and in a hexagonal shape. Furthermore, the active area of the pixels of the Timepix3 is smaller than for the Timepix. Using the transversal diffusion within the amplification gap indicates that not all charges of the avalanche are detected by the pixel [54]. As a first step, some measurements to quantify the difference of Timepix and Timepix3 were performed in [42].
- The transfer rate of the Penning effect (see Section 4.5) has not been quantified for a lot of gas mixtures. But, for some gas mixtures it was shown that this effect can increase the gas gain by up to a factor of 10 [54] and thus, a simulation of the amplification process without the effect is majorly spoiled.

To implement a possibility for a gas gain simulation despite these problems a data-driven approach was chosen: The gas gain distribution is measured and fitted. The resulting fit parameters are then used as an input for the simulation to create a probability distribution. For each avalanche from this probability distribution a gas gain is drawn. One must be aware, that in this approach the fit parameters are specific to the detector setup. This means, that for one specific gas mixture with specific mixing ratios and amplification field, there is a unique set of parameters for the gas gain distribution. Furthermore, these parameters will be influenced by the event rate that was used to take the data, and environment conditions like temperature and pressure. Also, it cannot be excluded that the parameters are specific to a single GridPix because of slight differences in the protective layer among production batches. Therefore, for a simulation with these settings these additional systematic effects should be considered. In case of such a simulation the size of the avalanche replaces the ToT per pixel in the data. For pixels with several detected electrons, each of them will get an avalanche size based on the given distribution and the results will be added up per pixel. This is another idealisation as in reality several avalanches above the same pixel would influence each other.

8.2 Simulation Parameters

Currently, the simulation supports the following input parameters, which are except for the first parameter mandatory:

- The path to a generated gasfile for the detector settings. This can be provided to speed up the simulation as without it, the simulation will generate it as a first step. This is especially helpful if a range of parameters is simulated that does not influence the gasfile such that always the same gas file can be used. An example would be the simulation of different photon energies for the same detector configuration.
- A job number to identify the simulation. This can be used to give each simulation a unique number that is then part of the folder and file names generated by the simulation.
- A selection of the X-ray absorption approach. Either 100000 photons are simulated at the start of the simulation and their absorption points are plotted and fitted to then draw for each event from the fitted distribution or for each event individually a photon is simulated. The former approach is especially faster if the detector efficiency is low or if a high number of events is simulated.

- A selection of the drift simulation approach. One can select to either use “AvalancheElectron” of “AvalancheMC”, “DriftElectron” of “AvalancheMicroscopic” or a Monte Carlo approach using the longitudinal and transversal diffusion coefficients and the drift velocity from the Magboltz generated gas file. The last approach is the fastest but assumes a homogeneous electric field. The other two approaches can work with a field map.
- The length of the drift cylinder in cm.
- The energy of the photons in eV.
- The first gas of the gas mixture. All gases that are supported by Garfield++ are supported by this simulation.
- The second gas of the gas mixture.
- The percentage of the first gas in the gas mixture.
- The percentage of the second gas in the gas mixture. If one gas is used, then some gas should be given as second gas but with 0 %. More gases in the mixture than two are currently not supported.
- The temperature of the gas in degrees Celsius.
- The pressure of the gas in Torr.
- The strength of the electric drift field in $\frac{\mathrm{V}}{\mathrm{cm}}$.
- The degree of polarisation between 0.0 and 1.0.
- The offset of the polarisation angle in rad. By default, the polarisation points in the direction of the positive x-axis.
- Three parameters that are the fit parameters of the Pólya distribution for a data-driven Monte Carlo simulation of the gas gain. If all parameters are set to 0, then the primary electrons per pixel are counted as ToT.
- The number of events that are simulated. Due to the absorption efficiency of the detector, the number of simulated photons can be substantially higher, because photons that do not interact within the gas volume are repeated until they do so.
- A selection if the truth-data should only contain a short list of information per event that include the interaction point of the photon, the emission angle of the photoelectron, and the number of ionised electrons by the photoelectron. The other option stores this list but additionally per event also the Degrad output that includes position, energy, and time information of all ionisation electrons from the photoelectron. The latter option increases the storage space requirements for the simulation substantially.
- A selection if files of the simulation are packed into a tar.gz archive after the simulation finished.

- A selection for which ASIC the output is generated. Currently Timepix and Timepix3 are supported. One can select one of them or both at the same time. The Timepix output option mimics a zero-suppressed readout in the ToT mode of the Timepix. The Timepix3 output option mimics a data-driven readout of the Timepix3 in the ToT/ToA mode for which already the interpretation of the raw data was performed (see Section 6.8).

8.3 Limits of the Simulation

As discussed in Section 8.1 there are several limitations and idealisations that need to be considered when the data from the simulation is used. Most importantly there are unquantified effects that influence the gas amplification. As they have a strong influence on the amplification no complete simulation of it is part of the simulation but instead a data-driven approach based on measured gas gain distributions. As they are also influenced by these effects and thus, bring several systematic effects with their data, an additional approach is possible that does not consider the amplification at all but stores the number of electrons that enter a hole of the grid per event.

For better comparability of different simulations that will be discussed in Chapter 10, a simulation without gas amplification was chosen as there were no data for all combinations of parameters. Thus, the simulations could be performed without the need of existing data. So, for the interpretation of the simulated data and especially for the comparison with real data it must be considered that there is an additional smearing on the charge measurement due to the gas gain distribution.

An additional effect that is not part of the simulation and connected to the gas gain is the influence of the threshold of the ASIC. The threshold of the ASIC effectively cuts into the gas gain distribution and thus, avalanches on the lower end of the distribution do not create signals that cross the threshold and consequently do not create hits. In the data, this especially influences electrons at the start of the photoelectron track as here mostly individual electrons enter a grid hole while at the Bragg peak multiple electrons enter. And for multiple electrons its more likely that the combination of their avalanches is sufficient to create a signal that crosses the threshold. The influence of this effect on the measurement depends on the gas gain and the threshold of the ASIC. The effect of this threshold-related hit efficiency will be discussed in Section 11.5.

As final simplification, the simulation assumes a perfectly homogeneous electric drift field. This ignores some effects that could lead to spurious modulation like field inhomogeneities due to the X-ray window or between anode and grid of the detector. But at the same time, this is ideal to study if there is spurious modulation based on the geometry of the ASIC or the pixels and also based on the reconstruction because there should be no other intrinsic effects of the simulation that could create spurious modulation.

CHAPTER 9

Reconstruction of X-ray Polarisation

For the reconstruction of the polarisation and further event parameters, several steps are necessary. This chapter will explain these steps. It starts in Section 9.1 with the reconstruction of the events based on hit timestamps, which is necessary to convert the continuous Timepix3 data stream into individual events. Then the space-based cluster reconstruction for Timepix and Timepix3 data will be explained in Section 9.2. With the clustered events, the polarisation angle per event is reconstructed with two different approaches (Sections 9.3 and 9.4). Furthermore, the position of the photon absorption point (Section 9.5) and the energy per event (Section 9.6) will be reconstructed. As the last step, the determination of the gas gain of the detector will be explained and discussed in Section 9.7.

9.1 Reconstruction of Events based on Time

The data-driven readout of the Timepix3 provides a continuous data stream of individual hits, compared to the frame-based readout of the Timepix, which transfers the hits of all pixels as one frame (see Sections 5.1 and 5.2). Therefore, before the clustering of events in space is possible, there needs to be an event reconstruction based on the timestamps for the Timepix3 data. For this step, the fToA data is ignored as a binning of 25 ns of the ToA is sufficient to differentiate events. Consequently, the reconstruction based on time uses the “ToA_Combined” information per hit (see Section 6.8). As the data of the Timepix is already stored in time-based frames and due to the lack of individual timestamps for the pixels in the ToT mode, this step is skipped for this type of data.

The time-based reconstruction of events for the Timepix3 is implemented in the “raw data manipulation” of TimepixAnalysis[1] [50]. Here the variable “clusterTimeCutoff” defines the ToA clock cycle gap between consecutive hits in the data stream that is needed to split these hits into two events. The “raw data manipulation” iterates over all hits in the data and decides if the hits are combined into one event. This is based on the ToA_Combined of the current and the last hit, and on the “clusterTimeCutoff”. To combine hits to one event, one of the following rules must be fulfilled:

1. The ToA_Combined of the current hit equals the ToA_Combined of the previous hit.
2. The ToA_Combined is smaller than the ToA_Combined of the previous hit plus the clusterTimeCutoff.

---

[1] `https://github.com/Vindaar/TimepixAnalysis`

3. The ToA_Combined is bigger than the ToA_Combined of the previous hit minus the clusterTimeCutoff.
4. In the original implementation of the "raw data manipulation" it was additionally checked if the ToA plus 16384 is smaller or equals the last ToA plus the clusterTimeCutoff. This was done as the ToA and not the ToA_Combined was used which has 14 bits and thus overflows and starts again at 0. Thus, events that have a ToA close to the overflow could have a big gap in the ToAs that needs to be considered for the event reconstruction. For this thesis, the ToA_Combined was used for this reconstruction which only overflows after 81 days (see Section 6.3) so that practically for none of the data taken in this thesis an overflow had to be considered.

To test the influence of the clusterTimeCutoff sample runs with an X-ray tube and various heating currents to produce different photon rates were taken, interpreted with the approach presented in Section 6.8 and then reconstructed with different values for clusterTimeCutoff. The runs were taken with a 1 cm drift cylinder, a gas mixture of 50 % Argon and 50 % CO_2 with a pressure of 1 023 mbar and with a polarised X-ray source with the energy of 6.4 keV. The highest rate was given by the maximum available heating current of the given setup. Additionally, a simulation run with the same detector parameters and beam energy is used for comparison. It is expected that for a very large cut-off "double hits" appear because multiple photoelectron tracks are then considered as one. For a tight cut-off it could happen that a track is split up into multiple events. As a first test, one measurement run was reconstructed first with a cut-off of 1 and then with a cut-off of 100 (cut-offs are in units of ToA clock cycles). The number of hits per event was plotted and the result is presented in Figure 9.1. While the difference in the main peak is small, one can see that for the lower cut-off there are much more events with a very low number of hits than for the higher cut-off. This is expected because some of the hits get separated from their original event due to the low cut-off and are considered as additional events. This does not just add some artificial additional events but also removes some hits from real events and thus could lead to a change of results.

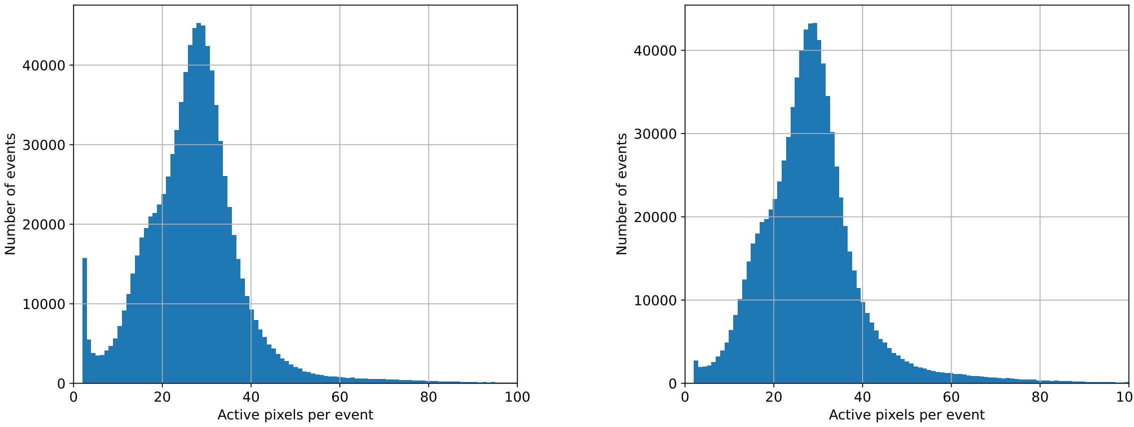

(a) clusterTimeCutoff = 1

(b) clusterTimeCutoff = 100

Figure 9.1: Number of active pixels per event for different clusterTimeCutoffs. For a low cut-off, some hits are separated from their events and thus appear as additional clusters at the lower end of the spectrum.

A more in-depth test was performed with the data for the four different event rates and the simulation data for a bigger range of the cut-off. The result of this test is presented in Figure 9.2 in terms of the normalised number of events reconstructed with a given cut-off. The normalisation is based on the minimum number of reconstructed events per run and was done for better comparability of the different runs. One can see that for low cut-offs the number of reconstructed events strongly increases which is expected as more and more hits are separated from their respective events and thus appear as additional events. The expected strong drop of the number of events towards higher cut-offs is not visible which can be explained by the different timescales of the event rate and the cut-off: With the highest rate of 7 kHz there would be on average an event every about 143 µs while with the cut-off of 150 a time span of 3.75 µs is covered. Therefore, an about 40 times higher ToA cut-off would be needed to see this effect. This means that between the two effects of combining events and of splitting up events, there is a reasonable range in which the cut-off can be chosen for all tested event rates.

One additional effect that can be observed for the data points in Figure 9.2 is, that with increasing rates there is a stronger linear decrease of the number of reconstructed events. One possible explanation for this is that during the measurements an “afterglow” effect was observed in the pixel matrix. This means that even after switching off the beam there were still pixels detecting hits especially at the region of the beam spot. It decayed over the time if no source was active. This effect got stronger with the event rate and also led to an increase of the decay time. The current assumption is that the effect is caused by noise created by trapped charges on the protective layer of the GridPix. As this effect should not just occur after a run but also leads to additional hits during the run that are not correlated with events, this could explain the observed decrease with the cut-off as with a higher cut-offs less of these hits will be considered as individual events. Furthermore, this fits the behaviour that the linear decrease is more prominent at higher event rates and is not at all present in the simulation data, as the afterglow also got stronger with the event rate and is not present in the simulation. Considering the obtained results, a cut-off of 100 ToA clock cycles was chosen as its far from the cut-offs that lead to event combinations or event splitting.

9.2 Clustering of Events based on Space

After an event was identified by time-based combination of hits for Timepix3 data (Section 9.1) or based on the frames of Timepix data, a reconstruction based on space is necessary to combine pixel hits into clusters. With this reconstruction, it is possible to separate events that are caused by multiple photons but occur in Timepix data in the same frame or were close enough in the ToA of the Timepix3 data to be considered as one event by the time-based reconstruction. For this purpose, a clustering approach is used. It is implemented in “TimepixAnalysis” [50] in the script “reconstruction” that follows after the execution of the “raw data manipulation”. For this thesis, the default clustering algorithm was used. Based on the definition of a “searchRadius” in units of pixels the algorithm works as follows: Around each active pixel within an event a square is defined with the side length of the “searchRadius”. It is then recursively scanned for each pixel within the square of a starting pixel if their respective squares contain further active pixels. This continues, until no new pixels are found within the squares. All pixels within this condition are considered as part of the same event. If in an event based on frames for Timepix or based on the reconstruction with time for Timepix3 contains multiple clusters that independently fulfil this condition, they are stored as individual clusters. Thus, single events from the previous step are split into multiple clusters in this step.

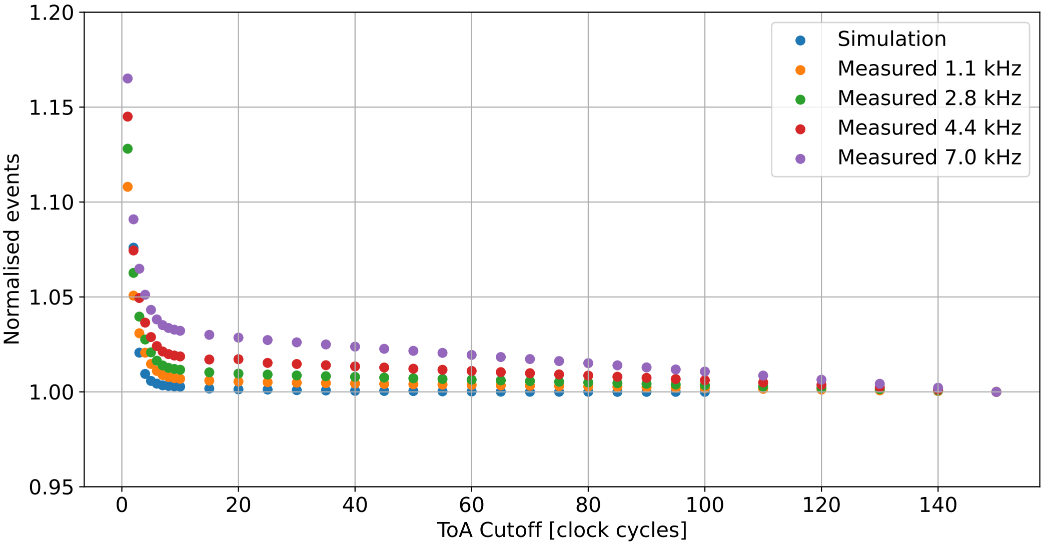

Figure 9.2: Number of reconstructed events by the raw data manipulation of TimepixAnalysis for different cut-offs of the ToA_Combined. Four different measurements with a range of event rates were tested and in addition a simulated run. For each data set the number of reconstructed events was normalised to the minimal number of reconstructed events. For very low cut-offs single photon events are split up into multiple events.

Like the time-based reconstruction, the influence of different search radii was tested with the same data set but with the already performed raw data manipulation with a ToA cut-off of 100 clock cycles. The plot in Figure 9.3 shows the relative number of reconstructed clusters for this. One can see that for low search radii the number of reconstructed clusters increases. This is expected because the smaller the search radius is the likelier is it that a single event is split into multiple clusters. Above a radius of 40 pixels the number of reconstructed clusters gets constant for the simulation and for all event rates. Based on this a search radius of 50 pixels was chosen.

9.3 Cut-based Reconstruction of the Polarisation Angle

For the reconstruction of the polarisation angle, it is important to only track the start of the detected photoelectron cluster. Only this part contains reliable information about the polarisation. This information is lost after multiple scattering of the photoelectron. Therefore, a reconstruction approach is needed that can differentiate between the start and the end of the photoelectron track and handles the scattering. For the differentiation of the start and the end of the track it is helpful that the Bragg-Peak (see Section 4.2.1) occurs at the end of the track which means that more ionisation electrons appear at the end of the track. Thus, a higher charge deposition in the measured track is expected towards the end. For the reconstruction, a two-step approach similar to the reconstruction for the GasPixelDetector [1, 20] is used. It was tested in [55, 56] for a Timepix-based GridPix detector to reconstruct two-dimensional data. The idea is to use the first step to determine which part of the track represents the start and which part represents the end of the track. In the second step, only active pixels in the start part of the track are used to reconstruct the angle of the photoelectron. Thus, the influence of scattering on the reconstruction of the angle is reduced. The reconstruction works as follows:

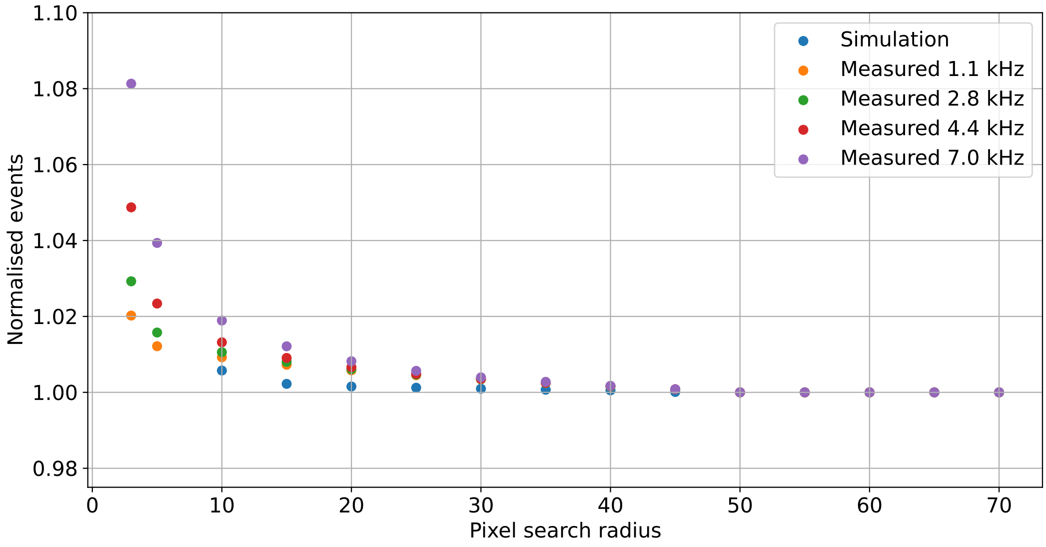

Figure 9.3: Number of reconstructed clusters by the reconstruction of TimepixAnalysis for different pixel search radii for the clustering. Four different measurements with a range of event rates were tested and in addition a simulated run. For each data set the number of reconstructed clusters was normalised to the minimal number of reconstructed clusters. For very small search radii single photon events are split up into multiple clusters.

1. The centre of charge is calculated for all coordinates (x, y for Timepix and x, y, z for Timepix3):

$$\bar{x} = \frac{\sum_i x_i q_i}{\sum_i q_i} \qquad \bar{y} = \frac{\sum_i y_i q_i}{\sum_i q_i} \, . \tag{9.1}$$

   Here, i represents the i-th active pixel and q_i the charge that this pixel measured.

2. The coordinates of the active pixels are shifted by the calculated centre of charge to set the centre of charge to the origin of the coordinate system:

$$x'_i = x_i - \bar{x} \qquad y'_i = y_i - \bar{y} \, . \tag{9.2}$$

3. Based on the shifted coordinate system the covariance matrix C that represents the second moment of the charge distribution is calculated:

$$C = \frac{1}{N} \sum_i \begin{pmatrix} x'^2_i & x'_i y'_i \\ y'_i x'_i & y'^2_i \end{pmatrix} \, . \tag{9.3}$$

4. The axis that maximises the second moment of the charge distribution is searched. This is done by calculating the eigenvectors and eigenvalues of the covariance matrix C. The eigenvector with the biggest eigenvalue represents the searched axis $\vec{p}$. This axis can be interpreted as a first estimate of the initial direction of the photoelectron. Based on this, a first estimate of the

emission angle of the photoelectron in the xy plane with respect to the x axis can be calculated:

$$\phi_1 = \arctan \frac{p_y}{p_x} \,. \tag{9.4}$$

5. For the new axis p the one-dimensional projections of all pixels on this axis are calculated:

$$d_i = \left(\begin{pmatrix} x'_i \\ y'_i \end{pmatrix} \cdot \begin{pmatrix} p_x \\ p_y \end{pmatrix} \right) \,. \tag{9.5}$$

   Based on this calculation the track is also split into a "left" part for $d_i < 0$ and a "right" part with $d_i \geq 0$.

6. To decide if the "left" part or the "right" part corresponds to the start of the track the results for d_i are used to calculate the skewness s of the charge distribution:

$$s = \frac{\sum_i q_i d_i^3}{\sum_i q_i} \,. \tag{9.6}$$

   If $s \leq 0$ then the "left" part of the track is considered as the start of the track and the "right" part is considered as containing the Bragg Peak and thus being the end of the track. For $s > 0$ the assignments of start and stop to the parts of the track are swapped. This concludes the first part of the reconstruction that considers all active pixels. In the following steps, only the pixels are used that are considered as part of the start of the track based on the skewness.

7. The remaining pixels are used to repeat steps one to four of the first part of the reconstruction. This results in a second axis that maximises the second moment of the charge distribution and its angle in the xy plane with respect to the x-axis. This new angle is interpreted as the reconstructed photoelectron angle for the event.

Timepix3 data includes a third coordinate per pixel via the timestamp of the pixel that can be converted via the drift time into a spatial information. For this data, the reconstruction approach needs to be adapted to use the additional information. As the interesting angle for the polarisation measurement is still in the xy plane the third coordinate is mainly interesting for an improvement of finding the start of the photoelectron track. For the 3D reconstruction the centre of charge in step 1 is also calculated for the z-axis and the covariance matrix is extended to a 3D matrix:

$$C = \frac{1}{N} \sum_i \begin{pmatrix} x'^2_i & x'_i y'_i & x'_i z'_i \\ y'_i x'_i & y'^2_i & y'_i z'_i \\ z'_i x'_i & z'_i y'_i & z'^2_i \end{pmatrix} \,. \tag{9.7}$$

For this covariance matrix again the eigenvectors and eigenvalues are calculated and the eigenvector with the biggest eigenvalue corresponds to the axis that maximises the second moment of the charge distribution. One approach would be to follow steps 5 and 6 with step 5 being changed from 2D vectors to 3D vectors. The points are projected onto the new axis and it is divided on the centre of charge into two parts and based on the skewness it is decided which part is considered as the start part and the end part of the track. With this again steps 1 and 2 are repeated with the remaining pixels.

The angle is then calculated as the angle of the projection of the new axis into the xy plane as this is the interesting angle for measuring the polarisation of the beam.

With Timepix3 data it is possible to do both steps in 3D or just the first step in 3D and then the second step in 2D. The latter can be beneficial, because with 3D information it is easier to differentiate start and end of the track due to the additional information of the z-axis. But in the second step, only the angle in the xy-plane is of interest and there the additional axis can spoil the reconstruction angle, especially with the lower number of pixels in the second step than in the first step.

A reconstructed example event is presented in Figure 9.4. In this, the first centre of charge based on all pixels is indicated in red together with a red arrow that indicates the axis that maximises the second moment of the charge distribution and points to the Bragg peak. A red dashed line indicates the orthogonal to this axis that is used to divide the track in a start and an end part with the assignment based on the third moment of the charge distribution. For the remaining pixels in the start part (indicated in orange) the process is repeated, resulting in a new centre of charge (green dot) and a new axis that maximises the second moment (green arrow).

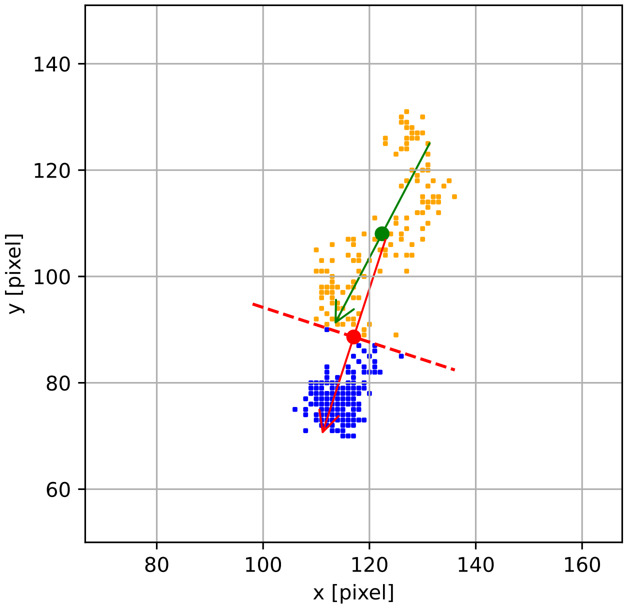

Figure 9.4: Example of a reconstructed event with the cut-based reconstruction. The red dot marks the centre of charge with all pixels, the red arrow indicates the axis that maximises the second moment of the charge distribution and the red dashed line indicates the orthogonal cut to this distribution and is used to split start and end of the track. The orange pixels indicate hits that are considered for the second step of the reconstruction as they are assigned to the start of the track. The blue pixels are cut and thus do not influence the second step. The green dot marks the centre of charge of the orange pixels and the green arrow the axis that maximises the second moment of the charge distribution of these pixels. Its angle with respect to the x-axis in positive direction is considered the polarisation angle of this event.

9.4 Weight-based Reconstruction of the Polarisation Angle

In addition to the cut-based reconstruction presented in Section 9.3, a weight-based reconstruction was implemented. This reconstruction reassembles the reconstruction for the Gas pixel detector [1, 20], adapts it for Timepix, and Timepix3 data and extends it for Timepix3 data to 3D. The first part of the reconstruction works exactly as the cut-based reconstruction: first the centre of charge is calculated, then an axis is searched that maximises the second moment of the charge distribution and the orthogonal to this divides the track. Then the third moment of the charge distribution is used to decide which part is considered the start and which part is considered to be the end of the track. Only pixels that are part of the start of the track are then used to calculate a new centre of charge. But at this point this reconstruction approach defines an additional requirement for these pixels. First, the distance D of each pixel to the centre of charge is calculated:

$$D_{\mathrm{2D}} = \sqrt{(x-\bar{x})^2 + (y-\bar{y})^2} \tag{9.8}$$

$$D_{\mathrm{3D}} = \sqrt{(x-\bar{x})^2 + (y-\bar{y})^2 + (z-\bar{z})^2}\,. \tag{9.9}$$

For each pixel, this distance is then compared to an inner and an outer radius:

$$r_{\mathrm{inner}} = r_{\mathrm{inner}}^{\mathrm{sim}} \times M_2^{\mathrm{max}} \tag{9.10}$$

$$r_{\mathrm{outer}} = r_{\mathrm{outer}}^{\mathrm{sim}} \times M_2^{\mathrm{max}}\,. \tag{9.11}$$

where $r_{\mathrm{inner}}^{\mathrm{sim}}$ and $r_{\mathrm{outer}}^{\mathrm{sim}}$ are values that must be obtained from simulation and M_2^{max} is the maximum of the second moment of the charge distribution to reduce the energy dependence of the radii. With this, the new centre of charge is calculated with pixels that fulfill the condition of being part of the start of the track and that show additionally a distance to the first centre of charge between r_{inner} and r_{outer}. The goal of this setup is that the new centre of charge can be used as reconstructed absorption point of the initial photon to achieve a good position resolution. Therefore, the inner radius ensures that the absorption point is pushed away from the Bragg peak and from scattering towards the start of the track. The idea of the outer radius is that in an event with an Auger electron (see Section 4.1) that carries no information about the polarisation, the track of this electron is at least partially removed and thus its influence on the polarisation reconstruction is smaller. How a simulation can be used to gain the two parameters for the radius will be presented in Section 10.1.

With the absorption point as new centre of charge, a second step follows to update the reconstructed angle of the first step. In contrast to the cut-based reconstruction, all pixels are used in this reconstruction for the second step but a weight to the charge is applied based on the distance D of the pixel to the absorption point:

$$Q_{\mathrm{new}} = Q \cdot \exp\left(-\frac{D}{w}\right)\,. \tag{9.12}$$

Here w represents a weight which just as the radii, is based on simulations. These simulations can be performed with the software that was presented in Chapter 8 and results of this are presented in Section 10.1. With this approach, pixels that are closest to the estimated absorption point have the highest influence on the reconstruction on the angle. Similar as for the cut-based reconstruction, the weight-based reconstruction can be performed fully in 2D or if time data for the z-axis is available, it can be fully or partially (only the first step) performed in 3D.

Figure 9.5 presents the weight-based reconstruction for the same example event as in Figure 9.4 where the cut-based reconstruction was used. One can see that for the weight-based reconstruction the second centre of charge that is used as an estimate of the absorption point is much closer to the centre of the chip (127.27/127.27) that was set as beam spot, compared to the cut-based reconstruction. Additionally, the arrow resulting from the second reconstruction step fits better to the hits at the start of the track for the weight-based reconstruction than for the cut-based reconstruction. If this leads to a systematic improvement, the reconstruction with the weight-based approach should lead to a higher modulation factor for the same data set in comparison to the cut-based approach. A simulation-based test of this will be presented in Section 10.1.

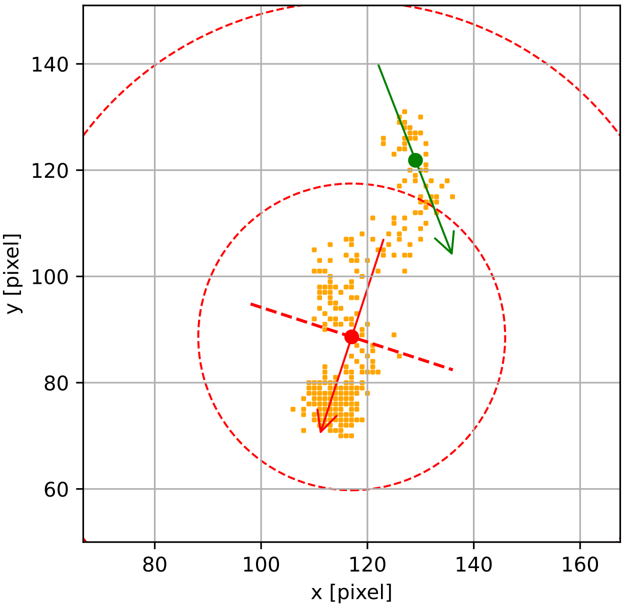

Figure 9.5: Example of a reconstructed event with the weight-based reconstruction. The red dot marks the centre of charge of all pixels and the red arrow marks the axis that maximises the second moment of the charge distribution and points in the direction of the Bragg peak. Around the centre of charge, two circles are indicated by dashed lines and drawn with radii dependent on simulation parameter and the value of the second moment for the axis that is indicated by the arrow. In the second step a new centre of charge is calculated. It is indicated by the green dot. For this, only pixels that are between the two circles are considered and that are additionally on the opposite of the Bragg peak with respect to an orthogonal to the red arrow through the first centre of charge. The second centre of charge is also interpreted as the absorption point of the initial photon and thus as start of the photoelectron track. To reconstruct the angle of the photoelectron with respect to the x-axis in positive direction all pixels are considered but their charge is weighted with Equation 9.12 based on the distance to the absorption point. With this again the axis is searched that maximises the second moment of the charge distribution.

9.5 Position Reconstruction

For the possibility to use the X-ray polarimeter for imaging and even position resolved polarisation reconstruction it is important to define to which position an event is assigned and which position resolution is achievable with it. Ideally the assigned point per event should be the two-dimensional absorption point of the photon with respect to the chip as this represents the position at which the photon entered the detector. Therefore, the start of the photoelectron track can be used for this. As presented in Sections 9.3 and 9.4 there are two points in each reconstruction that are calculated for each event: the centre of charge of all hits and the centre of charge of a subset of hits with the criteria for the subset being different for both reconstruction approaches. Using the centre of charge of all hits (red dots in Figures 9.4 and 9.5) would be a very rough estimate of the absorption point as its position with respect to the absorption point on an event basis is heavily influenced by scattering and thus by the gas parameters and the photon energy. The statistical distributions of these effects would fold into the distribution for the position resolution and make it worse. The centre of charge, based on the subset of pixels (green dots in Figures 9.4 and 9.5), should be a better approach. This is the case, as the goal in the reconstruction is already to bring the centre close to the start of the photoelectron track so that the direction of the track can be reconstructed. Furthermore, this centre of charge for the weight-based reconstruction should lead to a better position resolution of the absorption point as the selection of the hits for the subset is further refined in comparison to the cut-based reconstruction. This will be tested in Section 10.5.

9.6 Reconstruction of the Energy

The mean number of generated electron-ion pairs depends on the energy of the incoming photons and the mean required energy to create an electron-ion pair in the given gas mixture. Thus, measuring the number of electrons per event gives an estimate of the energy of the events photon. For the detectors that are discussed in this thesis (see Sections 7.2 and 7.3) there are two possibilities to do this measurement:

- One can measure the total collected charge per event. This is an equivalent to the energy because every primary electron is amplified via the gas amplification. So, the number of primary electrons and thus the energy is approximately given by the total collected charge per event divided by the gas gain. This contains uncertainties based on the statistical distribution of the number of primary electrons, the statistically distributed gas gain per electron and the systematic effect that some charges are not detected when their avalanche is below the threshold.

- Another method is to measure the number of active pixels per event. In an idealised case, the number of pixels should be equal to the number of primary electrons under the condition that each electron enters one grid hole, and thus active pixels see only one avalanche. This also contains uncertainties based on the statistical distribution of the number of primary electrons. Furthermore, in gases with low diffusion, several electrons can enter the same grid hole. Finally, a systematic effect comes from the fact that some pixels might be missing as the avalanche did not exceed the threshold.

Figure 9.6 shows a comparison of these two spectra with the same measurement run as in Figure 9.1. This shows that due to the discussed additional influences on the pixel-based spectrum the resolution in the charge-based spectrum is better. This is evident by comparing the lower energetic part of the main peak in both spectra because in the charge-based spectra an individual peak can be identified while in the pixel-based spectrum it only appears as shoulder of the main peak. The main peak can be identified as the photo peak that is related to the 6.4 keV photons of the source, the smaller peak to the left can be identified as argon escape peak at about 3.2 keV.

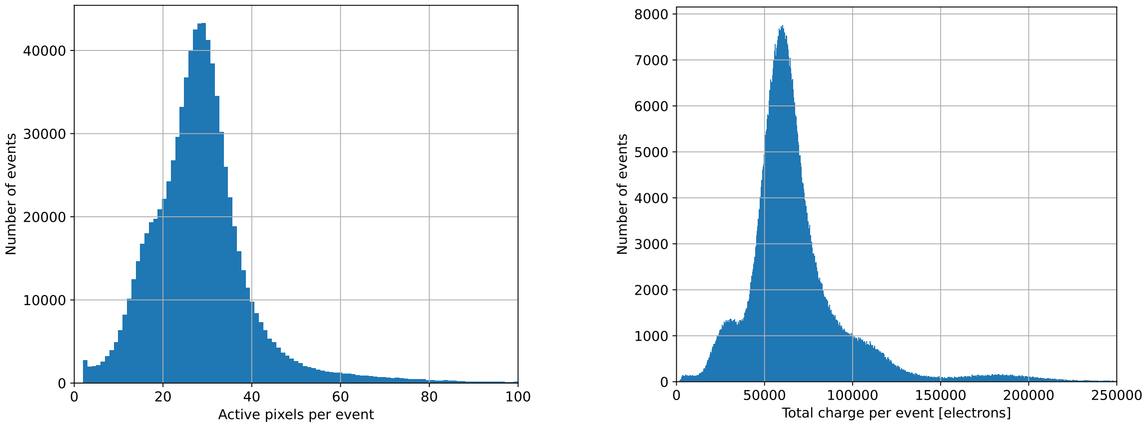

(a) Pixel spectrum

(b) Charge spectrum

Figure 9.6: Comparison of the pixel-based and the charge-based energy spectra for the same measurement run. One can see that the resolution in the charge-based spectrum is better as especially the shoulder on the left of the peak in the pixel-based spectrum can be identified as individual peak in the charge-based spectrum.

9.7 Reconstruction of the Gas Gain

The gas gain is defined as the mean amplification of individual charges (see Section 4.4). There are several possibilities to reconstruct the gain based on measured data. Historically for GridPix-based X-ray detectors (see e.g. [49]) the charge per pixel and per event was plotted and fitted with the Pólya distribution [25] in the following parametrisation:

$$P(Q) = \frac{K}{G}\frac{(\Theta+1)^{\Theta+1}}{\Gamma(\Theta+1)}\left(\frac{Q}{G}\right)^{\Theta}\exp\left(-(\Theta+1)\frac{Q}{G}\right). \tag{9.13}$$

Here G represents the gas gain as mean of the distribution while Q represents the charge per pixel per event. K is a scaling factor and Θ is together with G related to the width σ of the distribution:

$$\sigma^2 = \frac{G^2}{\Theta+1}. \tag{9.14}$$

The idea of this approach is, to use the Pólya distribution to extrapolate to avalanches with low amplification that are not detected due to the threshold of the ASIC. Simply calculating the mean of the measured distribution and using it as the gas gain would not account for low-amplification avalanches. Thus, such a gain would be biased towards higher amplifications and show a dependency on the threshold of the ASIC.

But a fit with the Pólya distribution is problematic: First, as discussed in Section 4.4, the Pólya distribution deviates from measurements as it is mainly an experimental description of the gas gain distribution for non-uniform electric fields. But there is no probability distribution for Legler's equation [31] for the distribution in strong uniform fields Thus, quite often the Pólya distribution is also used for these setups. Another problem is that there is not a single threshold for the whole ASIC, but the thresholds of the pixels form a Gaussian distribution (see Section 6.5). The width of this distribution is reduced by the threshold equalisation, but it cannot converge the thresholds to one value. Thus, some distribution remains. This Gaussian distribution of thresholds gets folded into the start of the measured charge per pixel distribution and thus this part is not a good measurement of the amplification distribution. In principle this could be resolved by measuring the threshold distribution and then unfolding the charge per pixel per event distribution. This could be done by injecting test pulses into all pixels and comparing their response. But doing this, not measurable systematic effects like a variation of test pulse input capacitances for different pixels and a slight variation of the test pulse voltages arriving at the pixels make it questionable. This is the case, because it is not clear if the threshold distribution is measured or just systematic effects that are different for events that enter the pixels via the pixel pad instead of the test pulse capacity. This would also influence the equalisation of the ASIC (see Section 6.5.5), but this is an equalisation of the threshold of the pixels and not of the ToT response, therefore the equalisation does not necessarily mitigate this effect.

Furthermore, a data-driven approach by plotting the charge per pixel per event distribution for individual pixels was not successful. Despite being only a valid approach for large data sets to get a reasonable distribution for individual pixels, it did not show an expected cut-off of the distribution for a single, constant threshold. This indicates that there might be also a slight variation over time of the thresholds of individual pixels which further impedes correcting for the threshold effect in the measured distribution. Therefore, the problem arises that the charge per pixel per event distribution cannot just be simply fit with the Pólya distribution but several bins at the start must be excluded from the fit, as they are influenced by the threshold distribution. But the number of bins to exclude cannot be directly determined because of the discussed problems to measure the threshold distribution. Also, no clear transition point is visible in the charge per pixel per event distribution which could enable a data driven approach. Furthermore, by variation of this cut-off point one can show that the resulting fit changes and thus the gas gain changes.

An example of the same dataset but with two different start ranges for the fit is presented in Figure 9.7. One can see that with a range that also covers lower charges, a peak is fitted but there are some deviations at higher charges in the exponential decay. This also results in a bad reduced χ^2. For ranges that start with higher charges the exponential decay is quite well described by the fit, also resulting in a χ^2 below 1, but the peak is no longer a part of the fit.

Figure 9.8 shows the resulting gas gains via the fit of the Pólya distribution for various ranges of the fit. One can see that there is a strong dependence on the selected fit range and that there is no point that can be confidently chosen to determine the gas gain. Summarising all discussed effects, the gas gain determination via the Pólya distribution fit would depend on the real gas gain, the threshold distribution of the ASIC and the chosen cut-off point for the fit and thus it is not a feasible approach to determine the real gas gain.

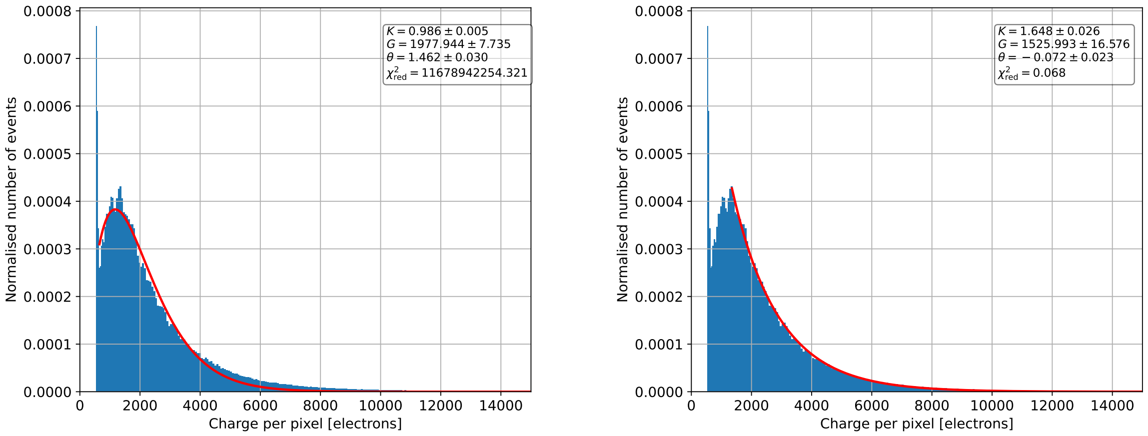

(a) Fit start: 650 electrons

(b) Fit start: 1 350 electrons

Figure 9.7: Comparison of the fit of the Pólya distribution for the same charge per pixel histogram with two different ranges for the fit. For a range that starts at lower charges the peak is fitted but the exponential decay at higher charges is badly described. For ranges that start at higher charges the peak is no longer part of the fit and the exponential decay is described much better.

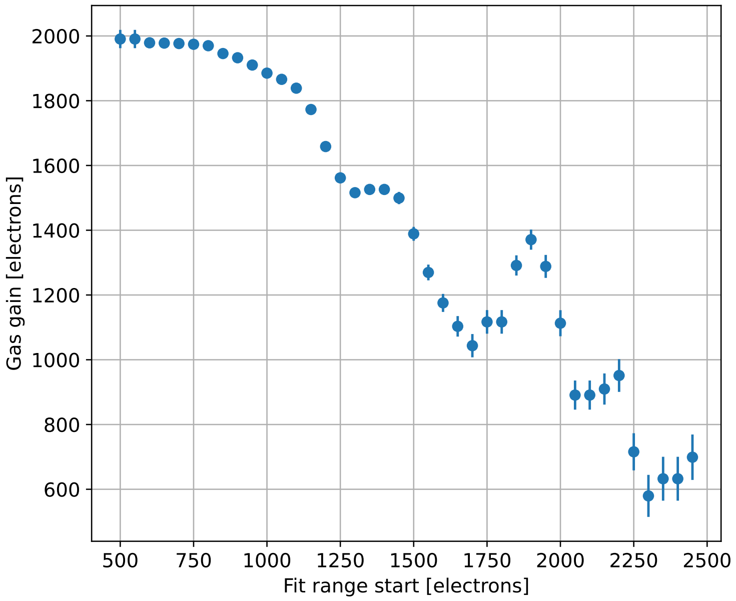

Figure 9.8: Resulting gas gains via the fit of the Pólya distribution for the same charge per pixel histogram with different ranges for the fit. This shows that there is a string dependence just on the fit settings if the Pólya distribution is used to determine the gas gain.

Another approach would be to use the two energy spectra discussed in Section 9.6, fit them both and then divide the mean of the photo peak in the charge spectrum by the mean of the photo peak in the pixel spectrum. With the assumption of single electron detection this would be a valid approach for the gas gain as then the factor between these two means should be the amplification of these single electrons. Based on the discussion of the two spectra in Section 9.6, this is problematic for the application of X-ray polarimetry as the low diffusion would especially bias the pixel spectrum with multiple electrons that enter the same grid hole.

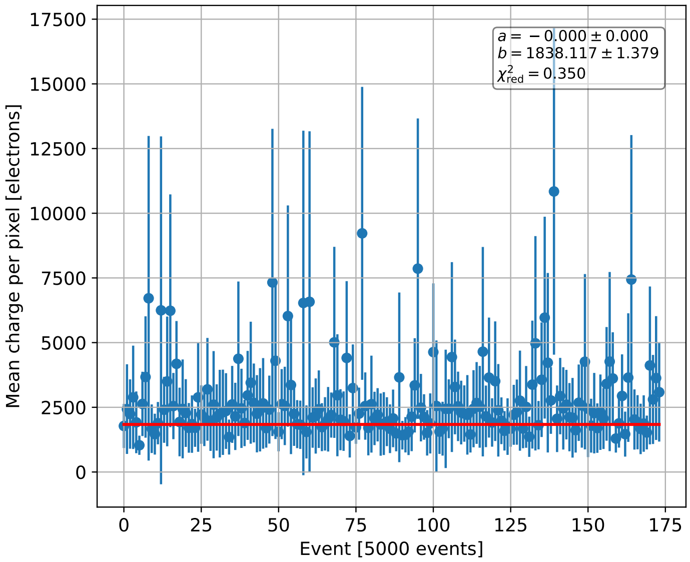

Figure 9.9: For each event, the average charge per pixel was calculated and it is plotted together with the standard deviation per event. For better visibility only every 5000-th event was plotted. To the result of all events a fit of a linear function $ax + b$ was performed. No gradient is visible, and the fitted offset can be considered as a measurement of the gas gain.

Based on the method of dividing the two energy spectra, one could also perform this division of total charge by the number of active pixels on an event basis. For the same dataset as in Figure 9.7 this is presented in Figure 9.9. Despite that there are big changes in the mean from event to event and that the displayed standard deviation is significantly higher compared to the values, the resulting fit of a linear function worked with a reasonable reduced χ^2 and showed no gradient of the gain over time. This method has the same influence by multiple electrons entering the same grid hole and also by the threshold distribution. But there are two advantages: on one hand, this method can be used to monitor the stability of the gain over time as each event serves as an estimate of the gain. On the other hand, which is especially important for low diffusion applications as X-ray polarimetry, one can select pixels for this method to exclude parts with high probabilities for multiple electrons in the same grid hole. For X-ray polarimetry the highest probability for this should be at the end of the track due to the Bragg peak (see Section 4.2.1). As part of the reconstruction approach for the polarisation plane (see Section 9.3) the event is already cut in two parts to exclude the end of the track and thus also the Bragg peak. Therefore, it was tested how this approach behaves if all pixels are used, just the pixels at the start of the track are used and also for comparison if just the pixels at the end of the track are used. Based on the assumption of reduction of the number of active pixels, due to multiple electrons in one grid hole compared to a smaller effect on the total detected charge, the expectation is that the reconstructed gas gain for the start of the track is lower than for the end of the track. Based on this, the gas gain determined with all pixels should be between these two. The corresponding plots for same measurement run as in Figure 9.9 are displayed in Figure 9.10. In the comparison of the gain based on the linear fit one can see that for the start of the track it is 1550 ± 1, which is significantly lower than for the end of the track (1907 ± 3). The comparison with the result based on all pixels in Figure 9.9 (1838 ± 1) shows that this is in-between the results of the start and the end of the track, but much closer to the result of its end part. The observed behaviour fits the expectation because a lower probability of multi-hits should also result in a lower observed gas gain.

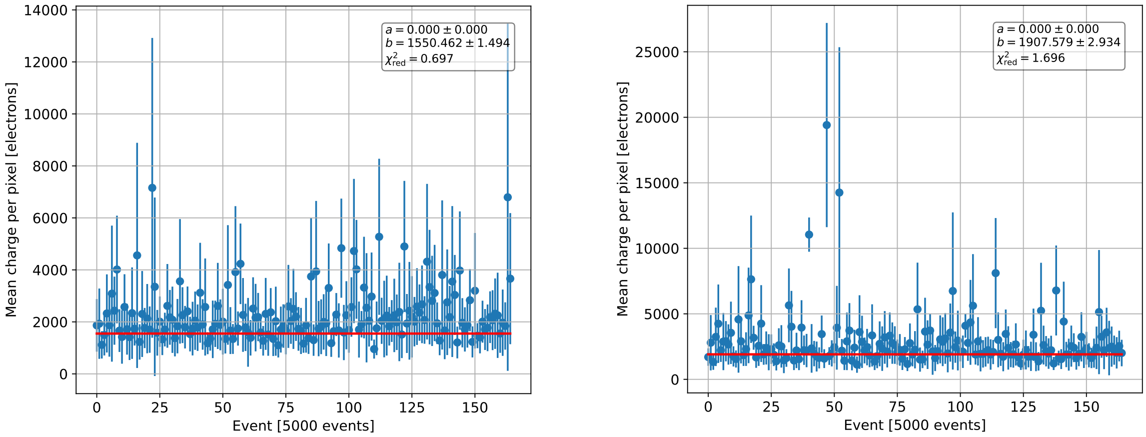

(a) Start of the tracks

(b) End of the tracks

Figure 9.10: Comparison of the mean charge per pixel with only pixels from the start part of the track in (a) and only pixels from the end part of the track in (b). Both were fitted with a linear function and the offset b of it can be considered as the gas gain. For the start of the track the gas gain is significantly lower than for the end part of the track. This is the case, because in the start part the probability for multiple primary electrons that are detected by the same pixel is lower due to the Bragg peak within the end part of the track. This biases the gas gain of the end part towards higher values.

The behaviour that was observed based on the measurement run, can also be cross checked with a simulation of the same detector parameters and beam energy. As the simulation (see Chapter 8) can store the number of primary electrons that were detected by the same pixel instead of the gas gain, the same method should ideally lead to a gain of one, because then only single hits are considered for the gas gain. Figure 9.11 shows the results for the method with start and end for the simulated data. One can see that again the offset of the linear fit is lower when the hits of the start of the track are considered then when the hits of the end of the track are considered. This confirms that the probability for multiple primary electrons in the same pixel is lower in the start than in the end. Using this approach results in a reconstructed gas gain that is closer to the real gas gain. But the result of an offset of (2.76 ± 0.01) pixels shows that there is still a considerable number of multiple hits that bias the gas gain. Thus, the result should be interpreted as an approximation but not as a definitive measurement of the gas gain.

Based on the discussion of methods to determine the gas gain and the shown examples, the method with an event-based division of total charge by the number of active pixels, with a limitation to the starting part of the track was chosen.

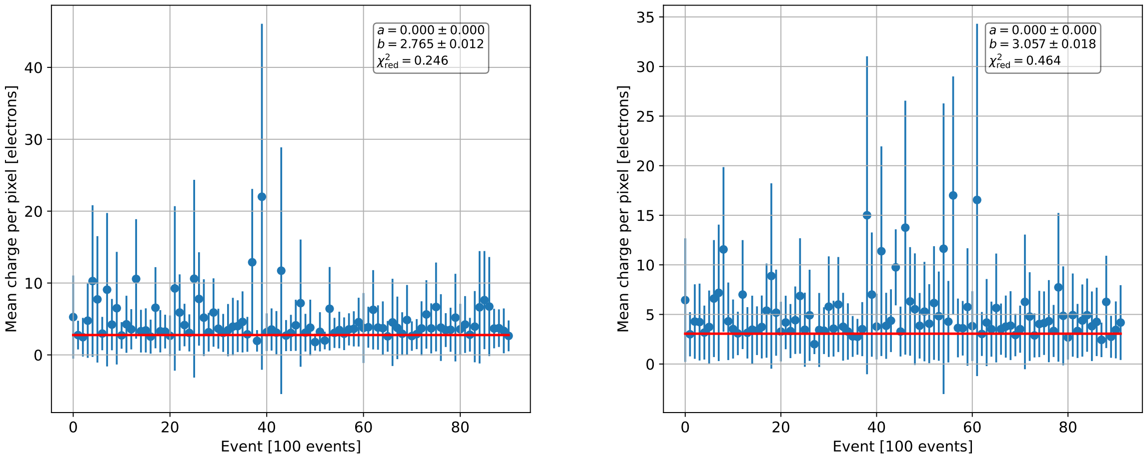

(a) Start of the tracks

(b) End of the tracks

Figure 9.11: Comparison of the mean charge per pixel with only pixels from the start part of the track in (a) and only pixels from the end part of the track in (b) for simulated data. In the simulation there was no gas amplification and for each pixel it is just stored how many primary electrons are detected. Thus, an offset of $b = 1$ would mean that no hits with multiple primary electrons in the same pixel were part of the analysis. The lower offset for the start of the track shows that this selection reduces the number of multi-hits and thus a reconstruction of the gas gain with this approach is closer to the real gas gain.

CHAPTER 10

Simulation Results

In this chapter the results of the simulations for the Timepix-based detector and the Timepix3-based detector will be presented and discussed. First, in Section 10.1 the performance of the different reconstruction approaches is tested. Based on these results, Section 10.2 presents simulation results of the influence of detector parameters on the detection efficiency and the polarisation reconstruction. In Section 10.3 the influence of the drift velocity on the 3D reconstruction of Timepix3 data is evaluated. Sections 10.4 and 10.5 investigate the influence of the position of the beam spot on the chip on the polarisation reconstruction and the resolution of the photon absorption point reconstruction. In Section 10.6 the possibility of an eccentricity cut to improve the polarisation reconstruction is studied.

10.1 Test of Reconstruction Approaches

To test the different polarisation reconstruction approaches that were presented in Section 9.3, a series of simulations with the detector simulation (see Chapter 8) were performed and reconstructed. The following detector parameters were selected as they were also used for some of the measurements with the detectors:

- Gas mixture: Helium / Dimethyl ether (DME) with a mixture of 80 % / 20 %
- A drift length of 2 cm
- Photon energies between 2 keV and 10 keV in 1 keV steps
- A drift field of 700 V/cm
- A pressure of 1 023 mbar and a temperature of 20 °C
- A polarisation of 100 % in x-direction and unpolarised data
- Generation of Timepix and Timepix3 data

The resulting data mirrors the output of the Timepix and Timepix3 readout systems. It was first analysed with the “raw_data_manipulation” and the “reconstruction” of TimepixAnalysis that were presented in Sections 9.1 and 9.2, based on the parameters for the ToA cut-off and the pixel search radius that were discussed and tested in these sections. As described in Section 8, the Timepix3 output of the simulation does not require a preprocessing by the interpretation that was presented in Section 6.8, as the output is generated as interpreted data. Firstly, simulation data for Timepix and Timepix3 were checked and compared at the level of simulation and TimepixAnalysis outputs. This way, the compatibility and consistency of simulation and reconstruction was checked. Coordinates and charges were checked for active pixels in several events. Also, the relevant distributions were compared, such as the number of hits per event. An example is shown in Figure 10.1. For most of the comparisons no differences were found and if differences occurred, they were minimal and induced by individual hits in $\mathcal{O}(10000)$ events. The difference of these hits could be explained by a different event assignment in Timepix3 data, based on the ToA.

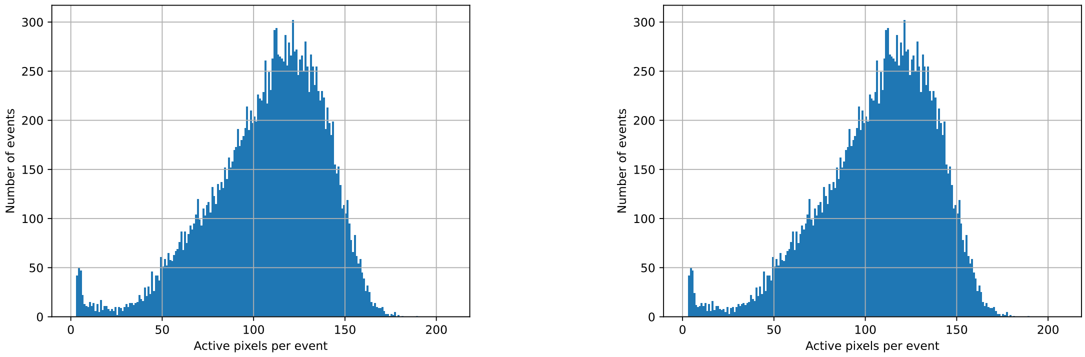

(a) Timepix

(b) Timepix3

Figure 10.1: Comparison of the pixel spectra of the same simulation run with Timepix (a) and Timepix3 (b) data. Besides a few individual events the results for the two ASICs are the same.

Based on these results, the simulation and TimepixAnalysis work as expected and are compatible for Timepix and Timepix3 data. Thus, for the reconstruction tests only the Timepix3 data was used. For cross checking the reconstruction of Timepix and Timepix3 data, the ToA of the Timepix3 data was ignored to mimic Timepix data.

In the next steps, the parameters “inner radius”, “outer radius” and “weight” for the weight-based polarisation reconstruction (see Section 9.3) had to be studied and fixed. For this, first a range of outer radii from 0.2 to 6.0 with an inner radius of 0.0 were tested. As the two radii are used to apply cuts on the pixels that are used to reconstruct the absorption point, it was investigated how they influence the distance of the reconstructed absorption point to the expected absorption point in the centre of the chip:

$$\text{Distance} = \sqrt{x_{\text{diff}}^2 + y_{\text{diff}}^2} \tag{10.1}$$

Figure 10.2 shows the dependence of this distance on the outer radius for a setup with 2 cm drift and for two energies. For each energy, there is one data set for 2D and one for the 3D reconstruction approach. The former represents the performance that can be achieved with Timepix and Timepix3 data if no ToA information are used, and the latter shows the performance for Timepix3 data if ToA information are used. In case on the 3D reconstruction, the time was converted to a space coordinate via the drift velocity, which can be obtained from the Magboltz part of the simulation. Details and a discussion about its influence can be found in Section 10.3. As the distance of the measured and the expected absorption point is purely a result of the first step of the reconstruction, the dimensionality of the second step has no effect. One can see, that overall the position gets reconstructed with a higher precision for the lower energy than for the higher. This is the case because the tracks for the lower energy are shorter and thus there is less probability for a higher offset. Furthermore, one can see that the behaviour of the distance with respect to the value of the radius roughly inverts from 2 keV to 7 keV. So lower radii are preferential for lower energies and higher radii are preferential for higher energies. This is the case because the different track lengths and the diffusion that influences the track width have a bigger effect on the lower energies. Photons with a lower energy have a higher probability to interact early in the gas. Thus, its electrons have a longer remaining drift distance. As the diffusion also affects the charge distribution along the track, it changes the influence of the radii. This is the case because the radii are calculated based on the charge distribution. It is also visible that for the lower energy the 2D approach performs better while for the higher energy the 3D approach works better. A plausible explanation is that at 2 keV an event resembles more a slightly eccentric cluster than a track and thus, additional information could spoil the reconstruction of the absorption point. But the difference of the two approaches is only in the order of 0.25 pixels. Based on the simulation results, the radius was set to 3.5 because its works very good for most energies and even for 2 keV the decrease of the precision is only in the order of 1 pixel with respect to the optimum, such that the influence on the second reconstruction step should be minor. In the case that such a polarimeter is not operated for a broader energy band but with a well described monochromatic beam, the radius can be optimised to perfectly fit this energy.

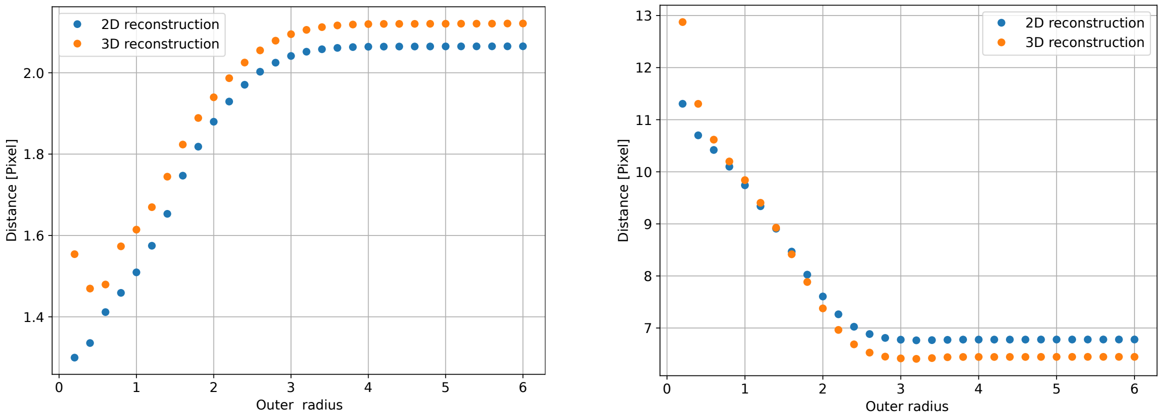

(a) 2 keV

(b) 7 keV

Figure 10.2: Distance of the reconstructed absorption point from its expected position for different outer reconstruction radii. As an example, results for 2 keV in (a) and 7 keV in (b). For each energy, the performance of the 2D and the 3D reconstruction is presented. As the distance of the absorption point is purely a result of the first step of the reconstruction, the dimensionality of the second step has no effect.

After fixing the outer radius to 3.5, the procedure was repeated with the inner radius in a range from 0.2 to 3.4 and again the distances of the reconstructed absorption points to the expected absorption point were calculated. The plots in Figure 10.3 show the results of this test for two of the energies. One can see, that with the addition of the inner radius the precision of the reconstruction of the absorption point for the higher energy is improved to nearly the same level as for the lower energy. Furthermore, now the 3D reconstruction works better than the 2D reconstruction for both energies. The goal of this inner radius is to exclude hits from the calculation of the absorption point that are close to the Bragg peak but not already discarded due to the orthogonal axis trough the centre of charge of all hits (see Section 9.4). This has a bigger effect on higher energies, as their tracks are longer. Thus, there are more pixel hits left after the orthogonal cut, which could negatively influence the absorption point reconstruction. It is expected that the 3D reconstruction performs better in this case, because scattering occurs in all dimensions and thus the 3D approach is also sensitive to scattering in the z-direction. Based on the results, an inner radius of 1.6 was chosen as it leads to good results over the whole energy range.

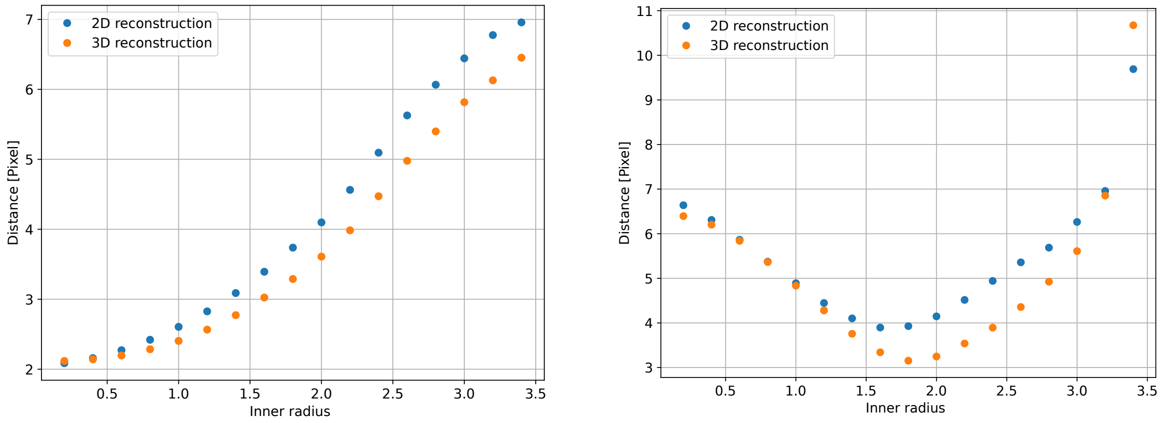

(a) 2 keV

(b) 7 keV

Figure 10.3: Distance of the reconstructed absorption point from its expected position for different inner reconstruction radii for 2 keV in (a) and 7 keV in (b). For each energy, the performance of the 2D and the 3D reconstruction is presented. As the distance of the absorption point is purely a result of the first step of the reconstruction, the dimensionality of the second step has no effect.

With the extracted radii of 1.6 for the inner radius and 3.5 for the outer radius the reconstruction was performed for weights for the second step in a range from 0.1 to 3.0 with a step size of 0.1. This was done with a complete reconstruction in 2D, the complete reconstruction in 3D and with the first step in 3D and the second step in 2D (further called “3D-2D”). For all combination of weights (see Equation 9.12), energies, and reconstructions the reconstructed polarisation angle was plotted in a histogram and fitted with a $\cos^2$-distribution:

$$N(\phi) = A \cdot \cos^2(\phi - C) + B\,. \tag{10.2}$$

From this fit, the modulation factor μ can be extracted:

$$\mu = \frac{A}{A + 2B}\,. \tag{10.3}$$

Figure 10.4 shows the result of this test for two energies. While for 2 keV the modulation factor increases with the weight and then reaches a plateau, for higher energies a maximum of the modulation factor is visible. Based on the definition of the weight, a higher weight leads to a slower decrease of the effective pixel charge with the distance to the absorption point. If the weight is too small, even pixels close to the absorption point quickly have no effect on the angular reconstruction and it gets ambiguous. If the weight is too big, far away pixels and thus scattering and the Bragg peak gain influence on the reconstruction, reducing its performance. For 2 keV there is no visible "track" and it is more an eccentric cluster. This is due to scattering of the photoelectron and diffusion of the ionisation electrons. Thus, the effect of higher weights on the angular reconstruction and the modulation factor seems to be minimised. In the comparison of the three reconstruction approaches, one can also see that the full 3D reconstruction has the worst performance while the full 2D and the 3D-2D reconstruction are close in their performance with slight advantages for the second one. The results of the tests of different reconstruction radii already showed that the 3D reconstruction leads to a slightly better reconstruction of the absorption point, thus this approach is better suited for the first step. The goal of the second step is to reconstruct the angle of the track within the x-y-plane. The results indicates, that while using only 3D data, the additional information in the third dimension spoils this reconstruction leading to a lower modulation factor. Thus, a 2D reconstruction in the second step is preferred. Based on the results, a weight of 1.2 was chosen.

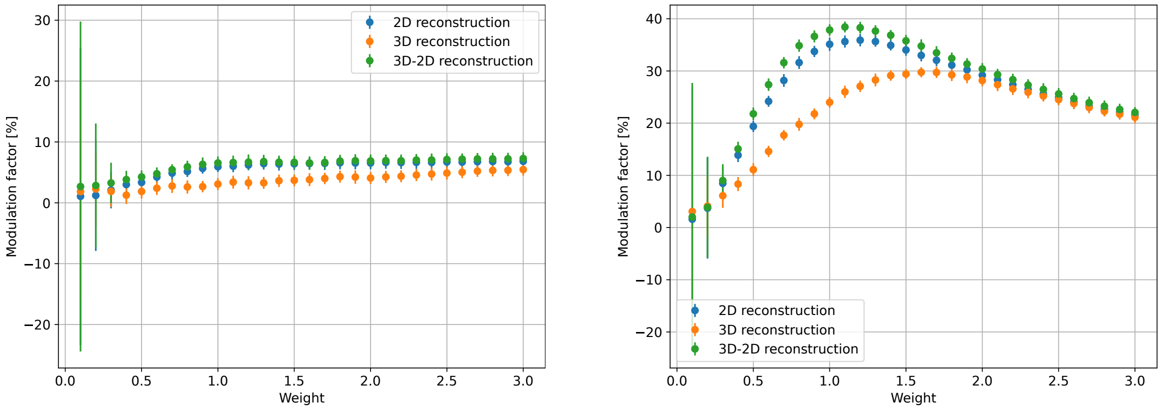

(a) 2 keV

(b) 7 keV

Figure 10.4: Distance of the reconstructed absorption point from the expected for different reconstruction weights. As an example, results for 2 keV in (a) and 7 keV in (b). For each energy, the performance of three approaches is presented: one with both reconstruction steps in 2D, one with both steps in 3D and one with the first step in 3D and the second step in 2D.

With all reconstruction parameters fixed, it is possible to compare all reconstruction approaches in terms of the modulation factor μ. The results are presented in Figure 10.5 which also includes the results of the cut-based reconstruction. While the cut-based reconstruction could not reconstruct the polarisation for 2 keV and 3 keV, it was successful with the weight-based reconstruction. Overall, the weight-based reconstruction resulted in higher modulation factors than the cut-based reconstruction. For both, it is visible that the 3D-2D reconstruction gives mostly better results than the full 2D and the full 3D reconstruction. In conclusion the weight-based reconstruction shows the best performance and if 3D data is available the first step should be reconstructed in 3D and the second step in 2D.

Using the results of the weight-based approach for the 2D reconstruction and the 3D-2D reconstruction, the expected performance increase due to simultaneous readout of time and charge of the Timepix3 can be estimated. Therefore, the minimal detectable polarisation (see Section 2.3)

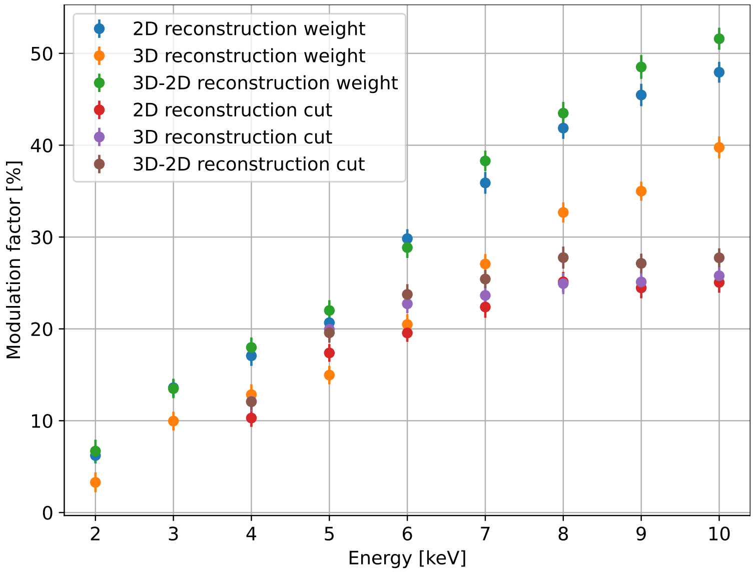

Figure 10.5: Simulated modulation factors for a mixture of Helium and DME with a ratio of 80 %/20 % in a detector with a 2 cm drift cylinder. The modulation factors for different reconstruction approaches are presented. For the cut-based reconstruction as for the weight-based reconstruction the data was once reconstructed completely in 2D, once with the 3D-2D approach.

can be used to calculate the number of necessary photons to reach a confidence level of 99 % for a polarisation measurement. This was done for both approaches, and the resulting numbers are compared in Figure 10.6. For each energy, a value of 100 % represents the number of photons that are needed by the 2D approach to reach the confidence level. So, a value of less than 100 % means that the 3D-2D approach needs less photons to reach the same confidence level. One can see that the two approaches are close but for most energies using the 3D data leads to a reduction of the necessary photons by about 10 %. For two energies the 3D-2D reconstruction performed a bit worse than the 2D reconstruction, resulting in more required photons for the same confidence level. For the Timepix3 data all approaches can be performed to find the optimal reconstruction for the specific parameters of the data set.

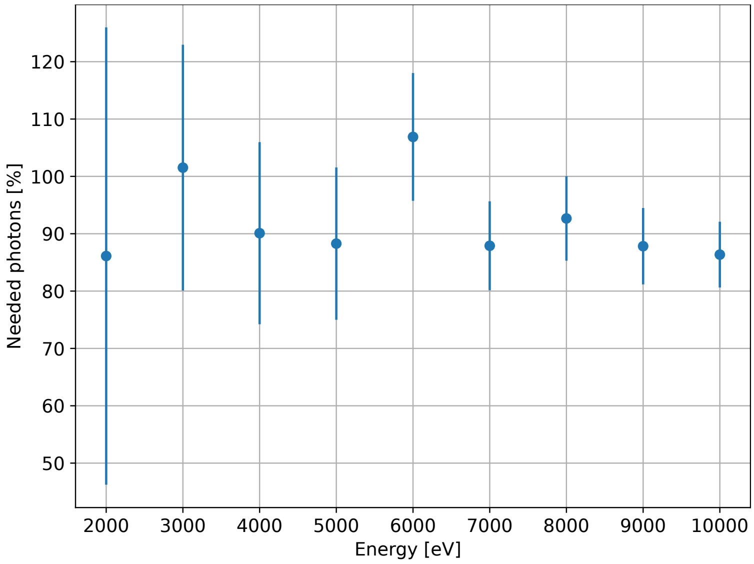

Figure 10.6: Comparison of how many photons are needed for a 99 % confidence level of measuring a polarisation for a 100 % polarised source with 3D data, based on the 3D-2D weight-based reconstruction with respect to 2D data. Based on a simulation of He/DME in a mixture of 80 % / 20 %.

10.2 Detection Efficiency

Several parameters of GridPix detectors in combination with the gas mixture have an influence on how many photons lead to a measurable event within the detector. Several effects are influenced by the cross-section for the photoelectric effect (see Section 4.1). These are the effects that influence the detection efficiency:

- The energy of the X-ray photons.
- The transmission probability of the X-ray window. Depending on the thickness and the composition of the window, the cross-section for the photoelectric effect in the window rises and thus, more photons interact within the window and thus do not enter the gas volume.
- The composition of the gas mixture as it defines the effective atomic number Z and thus the cross-section of the photoelectric effect.
- The pressure of the gas as it influences the density and thus the cross-section of the photo effect.
- The length of the drift cylinder. The cross-section of the photo effect leads to an exponential probability density function for X-ray interactions with respect to the length of the photon path within the gas volume and the length cuts into this distribution. Thus, a longer drift cylinder leads to a higher efficiency.
- The dead time of the detector readout. This neither influences the cross-section nor the number of photoelectric effects in the detector volume but it influences if all of them are visible for the ASIC or if it misses some during the readout. This is also influenced by the photon rate.

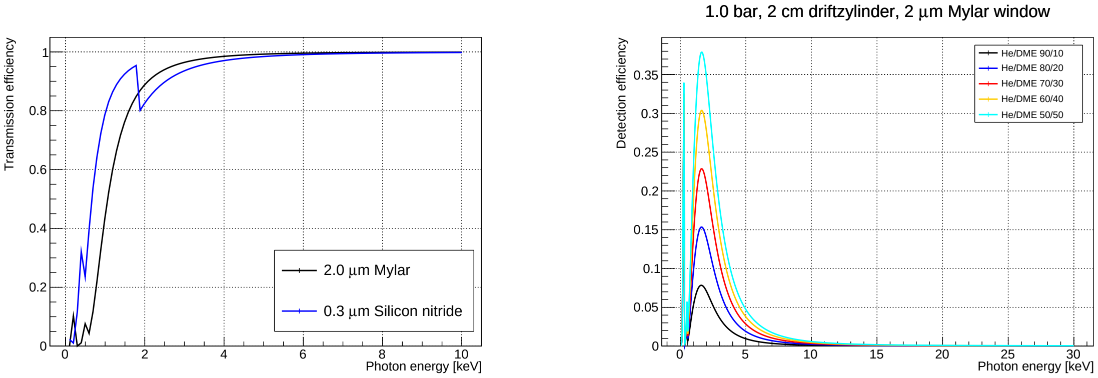

(a) Window transmission

(b) Detection efficiency

Figure 10.7: X-ray window transmission probabilities (a) for two different X-ray windows and detection efficiencies (b) for a 2 cm drift cylinder, a Mylar window and various mixtures of Helium and Dimethyl ether at 1 bar. Based on data from [57].

To estimate the detection efficiency, the transmission probability of the X-ray window and the absorption probability of the gas mixture can be estimated using data from [57]. The plot in Figure 10.7(a) shows how the transmission probability for a Mylar window and a silicon nitride window change with the photon energy. The plot in Figure 10.7(b) shows how the absorption probability in the gas volume changes based on the energy of the photons and the mixing ratio of the two gases. The combined efficiency E with the transmission probability P_{trans} and the absorption probability P_{abs} can be calculated with:

$$E = P_{\text{trans}} \cdot P_{\text{abs}} \, . \tag{10.4}$$

With the necessary number of detected photons (N_{MDP}), based on the minimal detectable polarisation (see Section 2.3), the number of photons that must enter the detector is:

$$N_{\text{total}} = N_{\text{MDP}} \cdot \frac{1}{E} \, . \tag{10.5}$$

For the following tests of the drift length, the detector pressure, and the mixing ratio of the gas a transmission efficiency for the window of $P_{\text{trans}} = 1$ was taken as it can be considered independently from the detector parameters as long as mechanical stability of the window is given. To take different windows into account the results can be simply multiplied by $1/P_{\text{trans}}$ to get the number of photons that must hit the X-ray window to get to a measurement of the polarisation with a given confidence level. Similar to this, additional efficiencies of a setup like absorption of photons between the source and the detector can be considered.

10.2.1 Drift Length

To test how the length of the drift cylinder influences the reconstruction, its parameters, and the efficiency of the detector, simulations with 1 cm, 2 cm and 3 cm drift were performed with a mixture of Helium and Dimethyl ether (DME) with a mixing ratio of 80 % / 20 % at normal pressure. The same energies as in Section 10.1 were selected: 2 keV to 10 keV in 1 keV steps. Based on the results in Section 10.1, the weight-based 3D-2D reconstruction was used. First, it was tested how the drift length influences the inner and outer radii of the reconstruction which influence the precision of the reconstruction of the absorption point (see Section 9.4). Therefore, the distance between the reconstructed absorption point and the expected absorption point are analysed for all drift cylinders and energies within a range of outer and inner radii. An example for 6 keV is presented in Figure 10.8. The results show that the drift length does not significantly influence the precision for the absorption point reconstruction for the outer radius. Additionally, the drift length has only a minor influence on the inner radius. This is expected because the drift length just changes the average drift distance, while the length of the tracks and the scattering stays the same. Thus, the cuts to find the absorption point have a small dependence on the drift length. Based on these results, the same radii as in Section 10.1 were chosen: 1.6 for the inner radius and 3.5 for the outer radius.

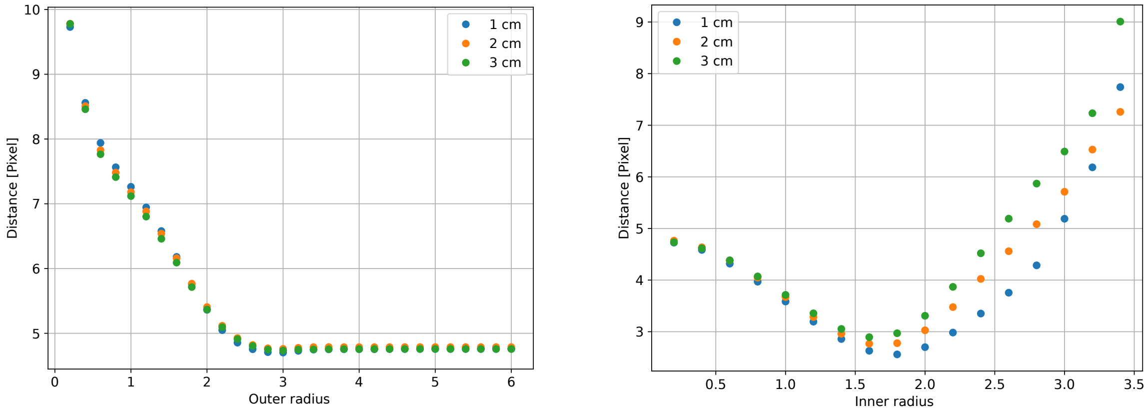

(a) Outer radius

(b) Inner radius

Figure 10.8: Dependence of the reconstructed absorption point on the inner (b) and outer (a) reconstruction radii for different drift lengths. Data for 6 keV.

With these radii, the influence of the weight of the angular reconstruction was investigated by the resulting modulation factors of $\cos^2$-fits. Figure 10.9 shows the result of this influence as an example for 6 keV. Similar to the results in Section 10.1, there is a weight that results in a maximum modulation factor. This changes with shorter drift lengths to lower weights. This can be explained by the lower diffusion due to the lower drift length: if the diffusion is smaller the width of the track is smaller. Thus, using pixels only very close to the absorption point can still result in a track with a clear direction compared to the case with high diffusion and thus broader tracks. For each drift length the weight that resulted in the maximum modulation factor at 6 keV was chosen as it is in the middle of the energy range.

Based on the optimal weights, Figure 10.10(a) shows the modulation factors for the three drift lengths and the full energy range. One can see that a longer drift results in a lower modulation factor

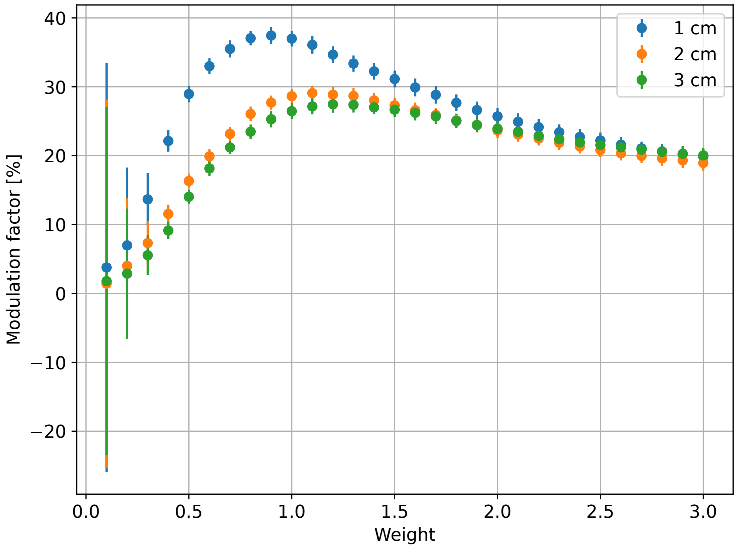

Figure 10.9: Modulation factor after a $\cos^2$-fit to the angular data for different weights in the second step of the angular reconstruction with different drift lengths. Data for 6 keV.

as the diffusion broadens the tracks with increasing distance and thus makes the angular reconstruction less precise. Using these modulation factors and the minimal detectable polarisation (see Section 2.3) the number of necessary reconstructed photons to confirm the polarisation of a 100 % polarised beam with a confidence level of 99 % can be calculated. This is presented in Figure 10.10(b). Based on the definition, a higher modulation factor and thus, the shorter drift leads to a lower number of necessary photons.

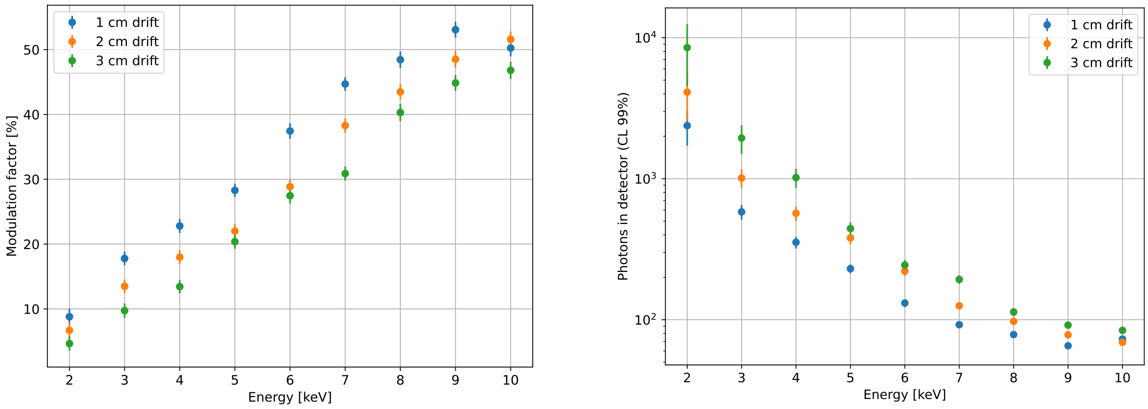

(a) Modulation factor

(b) Detected photons

Figure 10.10: Simulation results for different drift lengths. (a) shows the modulation factors of a $\cos^2$-fit of the angular data and (b) shows the number of photons that need to be detected to confirm the polarisation of a 100 % polarised source with a confidence level of 99 %.

As the drift length of the detector also influences the efficiency of the photon detection, the efficiencies from the simulation can be used to translate the necessary detected and reconstructed photons from Figure 10.10(b) into a number of photons that must enter the detector to achieve the given confidence level. The result of this calculation is presented in Figure 10.11. One can see that due to the efficiency increase of a 3 cm drift cylinder it leads to reasonable results over the whole energy range, only performing worse than the other cylinders at energies below 4 keV. Depending on the expected energies also the 2 cm cylinder can be chosen resulting at a better performance for lower energies. Based on these results, a 1 cm drift cylinder seems to be poorly suited for the given energy range and the used gas mixture.

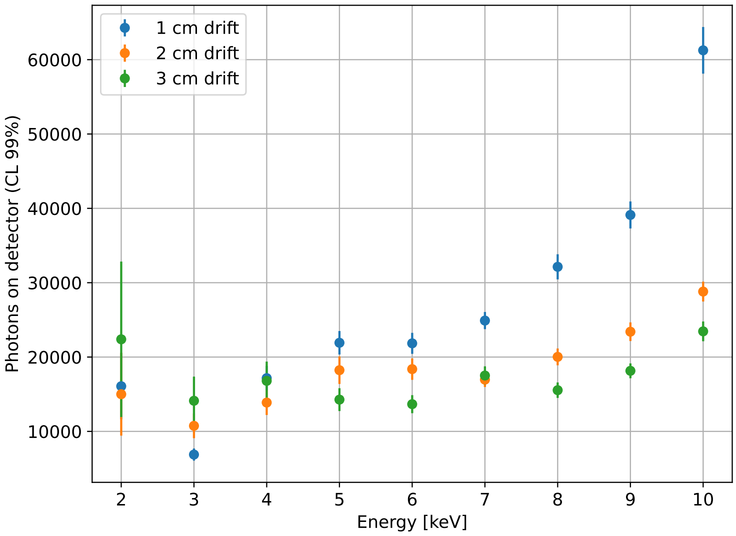

Figure 10.11: Number of photons that must enter the detector for different detector drift lengths to confirm the polarisation of a 100 % polarised source with a confidence level of 99 %.

10.2.2 Pressure

To investigate how the polarisation detection and its efficiency changes with the gas pressure, dedicated simulations were performed with a range of pressures from 0.5 bar to 1.5 bar in 0.1 bar steps and with a polarised beam in x-direction. For each pressure, the energies 2 keV, 6 keV and 10 keV were simulated. As in Section 10.1, a mixture of Helium and Dimethyl ether with a mixing ratio of 80 % / 20 % was used together with a 2 cm drift cylinder. Based on the results in Section 10.1, the 3D-2D reconstruction was used. Its parameters, the inner and outer radii and the weighting were tested again to investigate how the pressure influences them. Figure 10.12 shows as an example for 6 keV how the selection of the inner and outer radii influences the distance of the reconstructed absorption point to the expected absorption point. One can see that for both parameters the pressure mainly creates an offset but the overall behaviour and especially the minima of the curves are very similar. So, it can be concluded that the outer and inner radii can be selected independent of the pressure of the gas. This is also the case for 2 keV and for 10 keV. Therefore, the same radii as in Section 10.1, 1.6 for the inner radius and 3.5 for the outer radius were selected.

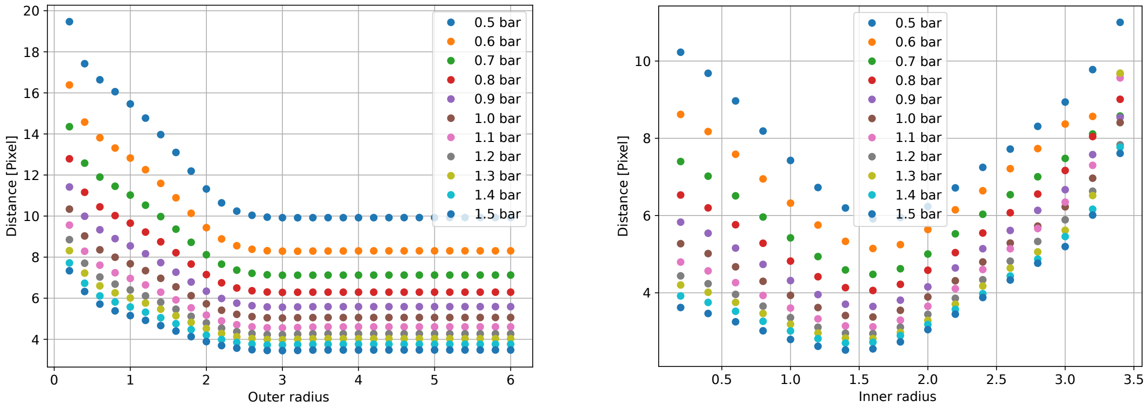

(a) Outer radius

(b) Inner radius

Figure 10.12: Dependence of the reconstructed absorption point on the inner (b) and outer (a) reconstruction radii for different pressures. Data for 6 keV.

Using the selected radii, different weights for the second step of the reconstruction were tested. As an example, Figure 10.13 shows the resulting modulation factors after a $\cos^2$-fit to the angular data for 6 keV. One can observe that in contrast to the radii there is a dependence on the detector pressure, so that different weights are optimal for different detector pressures. The same dependence is also observable for 2 keV and for 10 keV. To select the weights for the next step for each pressure the weight was chosen such that it led to the maximum modulation factor for 6 keV as it is in the middle of the energy range.

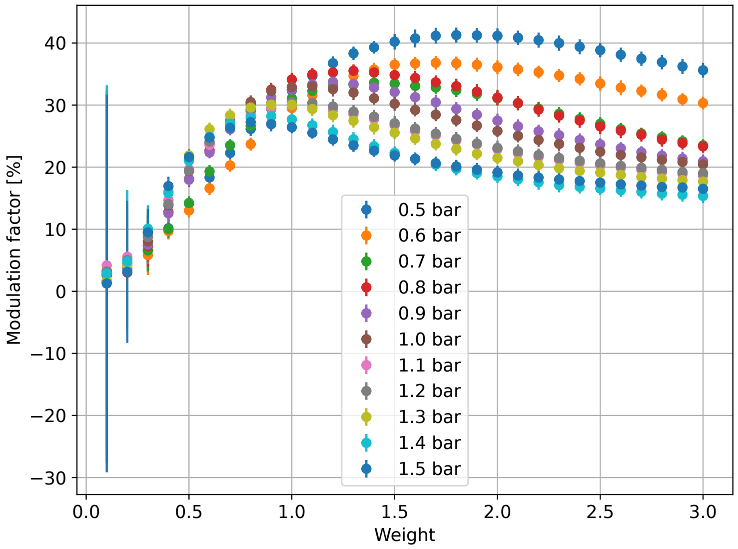

Figure 10.13: Modulation factor after a $\cos^2$-fit to the angular data for different weights in the second step of the angular reconstruction with different detector pressures. Data for 6 keV.

Using these weights, the modulation factors for all combinations of energies and pressures can be plotted. This plot is presented in Figure 10.14(a). Similar to the results presented in section 10.1 the modulation factor increases with the energy. Furthermore, one can observe that for all energies the modulation factor decreases with the pressure of the detector. This effect is the strongest for 6 keV. An increase in gas pressure increases the density of the gas which leads to shorter tracks and more scattering. This makes the reconstruction of the angle less precise and causes the lower modulation factor. If one uses the modulation factors and the minimal detectable polarisation (see Section 2.3) one can calculate how many photons need to be detected and reconstructed to confirm the polarisation of a 100 % polarised source with a confidence level of 99 %. This is done in Figure 10.14(b). One can see, that based on the definition of the MDP, the number of photons decreases with the modulation factor. Thus, the number of photons decreases with the photon energy and increases with the detector pressure.

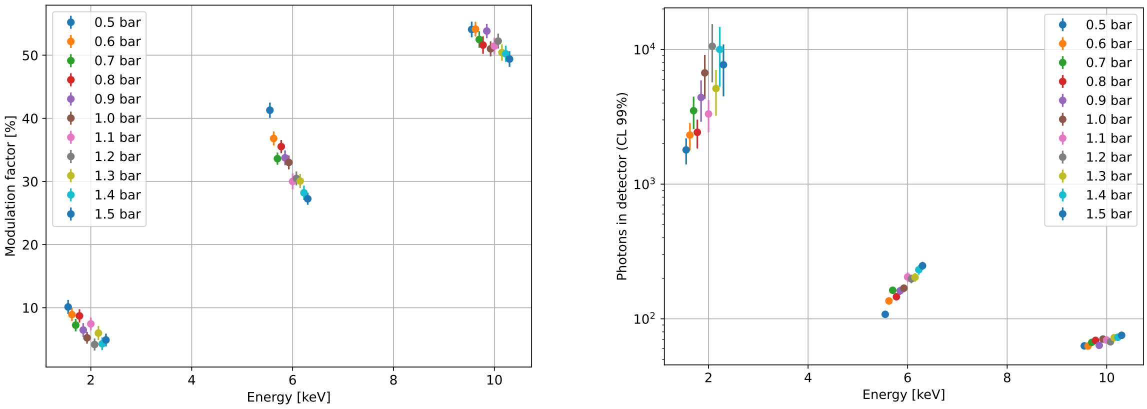

(a) Modulation factor

(b) Detected photons

Figure 10.14: Simulation results for different detector pressures. (a) shows the modulation factors of a $\cos^2$-fit of the angular data and (b) shows the number of photons that need to be detected to confirm the polarisation of a 100 % polarised source with a confidence level of 99 %. For both plots there are only the energies 2 keV, 6 keV and 10 keV but the individual data points were slightly shifted along the x-axis for better visibility.

To get a complete picture it is useful to consider the total number of photons that enter the detector. This factors in the detection efficiency that changes with the energy and the pressure of the gas. Figure 10.15 shows the result of this. For 10 keV the number of photons that must enter the detector strongly drops with the pressure despite that Figure 10.14(b) shows that the number of photons, that need to be detected and reconstructed, slightly increases with the pressures. This shows that the efficiency gain due to the higher pressure outweighs the loss due to the decreased reconstruction performance at higher pressures and thus a net gain is observed due to the pressure increase. The same can be said for 6 keV but the observed gain is by far not as strong as for 10 keV. For 2 keV it turns, and lower pressures perform better than higher pressures. This is the case because the detection efficiency for 2 keV is already quite high so the improvement due to higher pressures is not as relevant. On the other hand, the photoelectron tracks are at 2 keV already quite short and with a higher pressure they get shorter, and more scattering occurs. For this energy, these effects seem to outweigh the efficiency improvement resulting in a net loss.

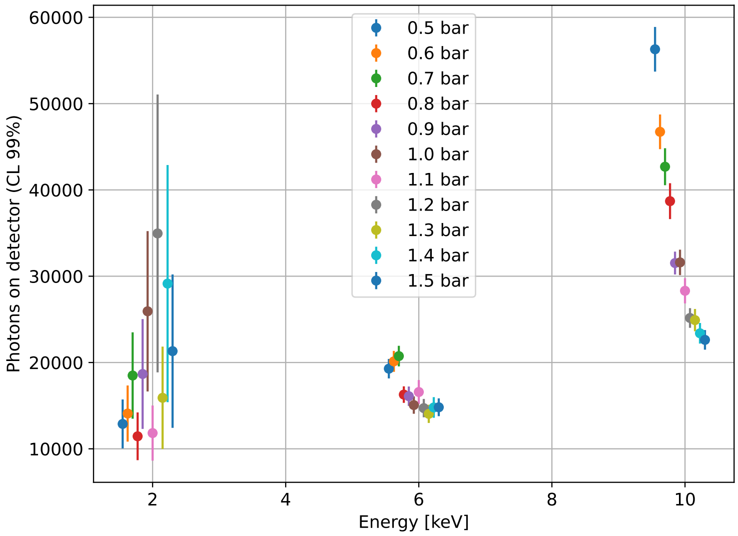

Figure 10.15: Number of photons that must enter the detector for different detector pressures to confirm the polarisation of a 100 % polarised source with a confidence level of 99 %. There are only the energies 2 keV, 6 keV and 10 keV but the individual data points were slightly shifted along the x-axis for better visibility.

10.2.3 Gas Mixture

Similar to the test of the influence of the gas pressure a test of the influence of the mixing ratio of the gas was performed with the same set of energy, detector, and beam parameters. As gas mixture Helium and DME was taken with DME percentages from 10 % to 100 % at normal pressure. As for the previous simulations, the weight-based 3D-2D reconstruction approach was used, and the influence of the gas mixture on the parameters of the reconstruction was checked. Figure 10.16 shows the influence of the outer and inner radii of the reconstruction on the precision of the reconstructed absorption point as an example for 6 keV. Similar to the behaviour that was already present for different detector pressures, the percentage of DME mainly creates an offset of the distance between reconstructed and expected absorption point but the overall behaviour is similar. Therefore, the radii can be selected independent of the mixing ratio of the two gases. The resulting radii are again 1.6 for the inner radius and 3.5 for the outer radius.

After fixing the inner and outer radii, the next step is to investigate the influence of the weight that is applied in the second step to give hits closer to the absorption point a higher influence. The result of the achieved modulation factors with different weights is presented in Figure 10.17 for 6 keV. In contrast to the radii, this shows different optimal parameter values for different mixing ratios. Therefore, for each mixing ratio its own weight was chosen based on the maximum modulation factor for 6 keV as it is in the middle of the energy range.

The optimal modulation factors for all energies and mixing ratios based on the weight selection are displayed in Figure 10.18(a). One can see that the modulation factor rises with the energy as already presented in Section 10.1 but falls with the percentage of DME. This is the case because a higher percentage of DME leads to a higher effective atomic number Z and a higher density of the gas, thus shortening the tracks and inducing more scattering. Thus, it gets harder to reconstruct the angle of events, resulting in a lower modulation factor. Using these modulation factors to calculate the number

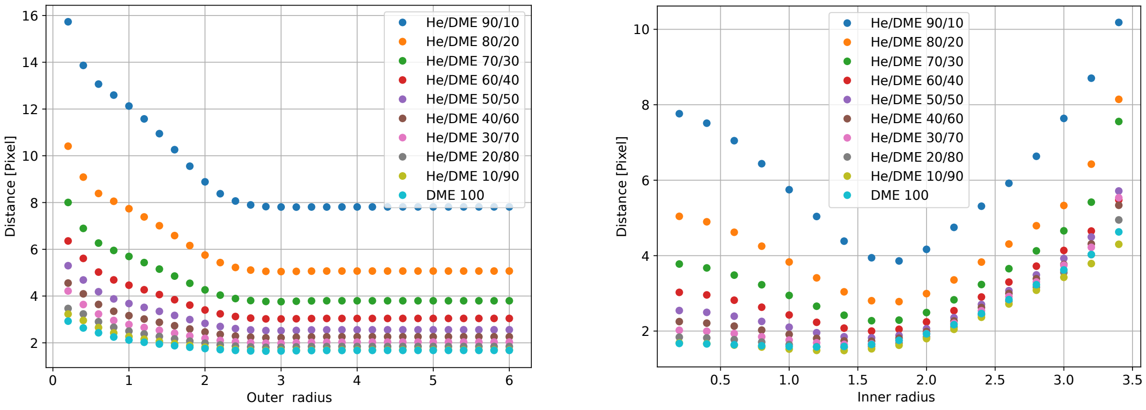

(a) Outer radius

(b) Inner radius

Figure 10.16: Dependence of the reconstructed absorption point on the inner (b) and outer (a) reconstruction radii for different mixing ratios of Helium and Dimethyl ether. Data for 6 keV.

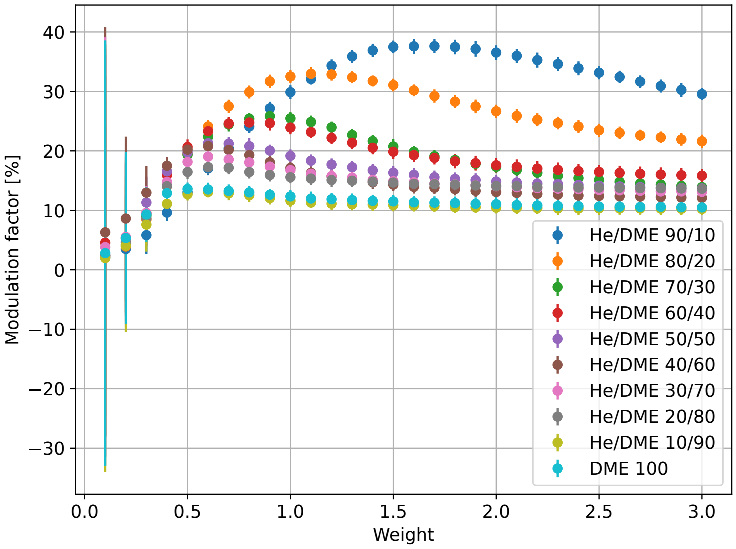

Figure 10.17: Modulation factor after a $\cos^2$-fit to the angular data for different weights in the second step of the angular reconstruction with different mixing ratios of Helium and Dimethyl ether. Data for 6 keV.

of photons that need to be detected and reconstructed to confirm the polarisation of a 100 % polarised source with a confidence level of 99 % (see the definition of the minimal detectable polarisation in Section 2.3), leads to the results presented in Figure 10.18(b). Based on the definition of the minimal detectable polarisation, the number of necessary photons drops with an increase of the modulation factor and thus drops with the energy and rises with the percentage of DME.

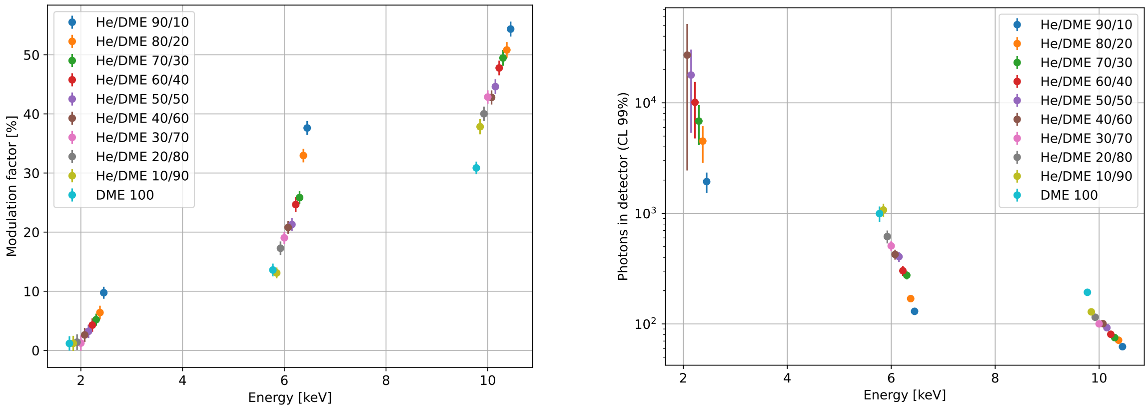

(a) Modulation factor

(b) Detected photons

Figure 10.18: Simulation results for different mixing ratios of Helium and Dimethyl ether. (a) shows the modulation factors of a $\cos^2$-fit of the angular data and (b) shows the number of photons that need to be detected to confirm the polarisation of a 100 % polarised source with a confidence level of 99 %. For both plots there are only the energies 2 keV, 6 keV and 10 keV but the individual data points were slightly shifted along the x-axis for better visibility. Points for higher DME percentages than 60 % for 2 keV are excluded from plot (b) as for these the polarisation reconstruction failed, which can be seen in plot (a) as there the points are close to a modulation of 0 %.

As the different mixing ratios of Helium and DME also result in different detection efficiencies for the photons in the gas, this efficiency has to be considered to get the whole picture of how many photons must enter the detector to reach the confirmation of the polarisation with the given confidence level. The resulting number of photons is presented in Figure 10.19. One can see that the influence of the mixing ratio on the number of photons that must enter the detector is quite different for the different energies. While for 10 keV a higher percentage of DME seems preferential, for 6 keV about 50 % are optimal and for 2 keV lower percentages are optimal with higher percentages not even giving reasonable results. This behaviour is caused mainly by two effects: for higher percentages, the detection probability increases which is the main reason why for 10 keV higher percentages are preferential. This is especially visible in the comparison between Figures 10.18(b) and 10.19 that shows that just with the number of necessary detected photons lower DME percentages perform better. But considering the detection efficiency the behaviour inverts. With the same comparison for 2 keV one can see that the behaviour in both metrics is the same: lower DME percentages perform better. Thus, the influence of the detection efficiency is not strong enough to counterweight the already present dependency. Thus, the observed behaviour of the required photons is mainly influenced by the reconstruction performance. Higher DME percentages increase the density of the gas, due to the higher density of DME than Helium, and thus the scattering is increased, and the track length is shorted. As the tracks for 2 keV are already quite short, this has a major impact on the reconstruction. For

6 keV an intermediate behaviour is observable. While for the number of necessary detected photons a lower DME percentage is preferential, this is partially reversed by the efficiency gain. This leads to the observable effect that for very high DME percentages the total number of necessary photons is high due to the worse reconstruction performance and for very low percentages it is high due to the low detection efficiency. This creates an optimum at about 50 % DME. For a polarimeter that should operate over the whole simulated energy range a medium DME percentage with a slight tendency towards lower percentages seems optimal, as this gives good results for all three simulated energies.

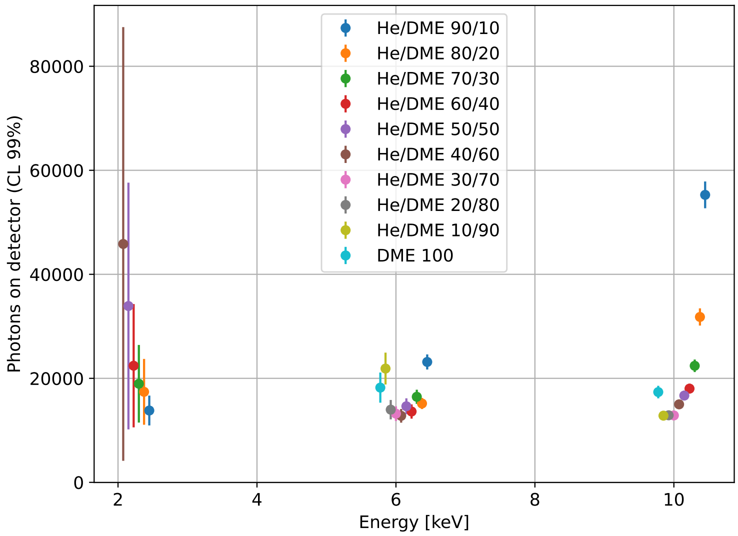

Figure 10.19: Number of photons that must enter the detector for different mixing ratios of Helium and Dimethyl ether to confirm the polarisation of a 100 % polarised source with a confidence level of 99 %. There are only the energies 2 keV, 6 keV and 10 keV but the individual data points were slightly shifted along the x-axis for better visibility. Points for higher DME percentages than 60 % for 2 keV are excluded from the plot as for these the polarisation reconstruction failed.

10.3 Influence of the Drift Velocity

For the third dimension of the Timepix3 data, it is important to consider that it is measured as a time while the other two coordinates are already space coordinates. Therefore, the time axis must be converted to a space axis. This can be done via the drift velocity that can be read from the files that are generated by the simulation (Chapter 8). The velocity is part of the Magboltz generated gas file. Converting the time-walk-corrected timestamps of the Timepix3 via the drift velocity to a space coordinate can be done by (cc is here used as a unit of clock cycles):

$$z[\mu\mathrm{m}] = \left(\mathrm{ToA}[\mathrm{cc}] \cdot 25\,\frac{\mathrm{ns}}{\mathrm{cc}} - \mathrm{fToA}[\mathrm{cc}] \cdot 1.5625\,\frac{\mathrm{ns}}{\mathrm{cc}}\right) \cdot v_{\mathrm{drift}}\left[\frac{\mu\mathrm{m}}{\mathrm{ns}}\right]. \tag{10.6}$$

For the three-dimensional reconstruction it is now an interesting question if the scaling of the z-axis leads to the optimal results or if a different scaling that effectively increases or decreases the importance of the z-axis with respect to the x- and y-axis can lead to a better performance of the reconstruction.

For this, the reconstruction was performed with a range of different z-scalings, based on different drift velocities. The test was performed with simulation runs at 2 keV, 6 keV and 10 keV for a 2 cm drift cylinder, filled with Helium and DME in ratios of 80 % and 20 % at normal pressure. In these conditions the drift velocity given by Magboltz is 3.59 µm/ns and for the test it was varied from 0.25 µm/ns to 10.00 µm/ns in 0.25 µm/ns steps. Based on Section 10.1, the weight-based 3D-2D reconstruction was used. For each scaling, a $\cos^2$-fit for the resulting angular distribution was performed and then the modulation factor was calculated based on the fit parameters. The result of this is presented in Figure 10.20, which shows that using the drift velocity from Magboltz (red dashed line) results in the optimal or close to the optimal modulation factors. Therefore, it is preferential for the reconstruction to have the same scaling for the z-axis as for the other two and a smaller or bigger influence of this axis based on a variation of the drift velocity does not lead to improvements.

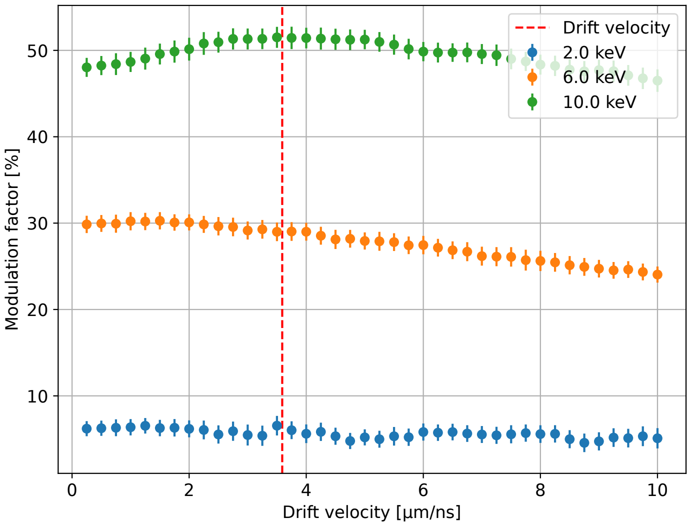

Figure 10.20: Modulation factors for different drift velocities. The data is based on simulations for 2 keV, 6 keV and 10 keV for a 2 cm drift cylinder, filled with Helium and DME in ratios of 80 % and 20 % at normal pressure. The data was reconstructed with the weight-based reconstruction in the 3D-2D approach. If the drift velocity changes, this also changes the resulting modulation factor. The red dashed line indicates the drift velocity for the detector setting based on Magboltz. It is 3.59 $\frac{\mu m}{ns}$.

10.4 Position Dependence

After the reconstruction approaches were tested in Section 10.1 and the influence of different detector parameters on the performance of the detector were tested in Section 10.2, in a next step the influence of the beam spot on the reconstruction was investigated. Due to the extended photoelectron tracks, some parts of the tracks could be outside the active area of the detector and thus negatively influence the performance. For this test, simulation data for a mixture of Helium and DME 80 %/20 % at normal pressure were taken. The drift cylinder in the simulations had a length of 2 cm and energies from 2 keV to 10 keV in 1 keV steps were used. The beam spot was first set to the centre of the chip and then moved in steps of 50 pixels along the x- and y-axis, resulting in 25 beam spots on the 256 by 256 pixel matrix. For the simulation, the beam was polarised in x-direction.

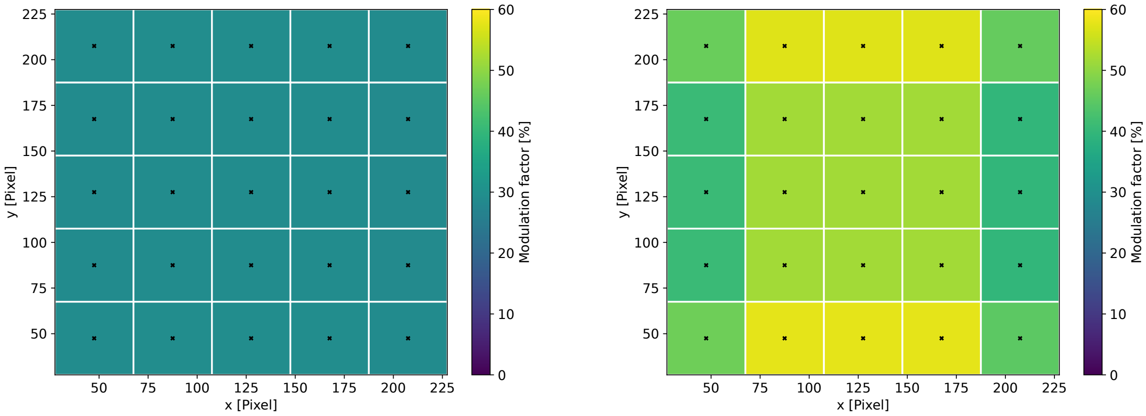

(a) 6 keV

(b) 10 keV

Figure 10.21: Modulation factors based on a $\cos^2$-fit of the angular reconstruction with the weight-based reconstruction for different beam spots. The results for a beam energy of 6 keV (a) and 10 keV (b) are displayed. The beam was polarised in x-direction. The beam spots are marked by black crosses and the surrounding square shows via the colour code the modulation factor.

Figure 10.21 shows the resulting modulation factors as an example for 6 keV and 10 keV. While for 6 keV no dependence of the resulting modulation factor on the beam spot is observable, for 10 keV the centre 9 bins show the same behaviour but the bins on the edges deviate in the calculated modulation factor. For energies below 6 keV also no dependence is observable while for the energies between 6 keV and 10 keV the pattern emerges, that is visible for 10 keV. This pattern can be explained as follows: for the central 9 beams spots the tracks are short enough such that the track rarely leaves the active area of the chip. Thus, the reconstruction is not influenced there. In the bins at the very left and the very right, the tracks are sufficiently long that they can leave the active area. Thus, for a lot of tracks the Bragg peak is missing which spoils the reconstruction of the start and the end of the track and also the absorption point (see Sections 9.3 and 9.4). Due to the truncation of a significant number of tracks, the angle is reconstructed in a wrong part of the track. This causes a randomly distributed offset in the angular distribution, lowering the modulation factor. This happens especially at the left and the right edge of the chip as the beam is polarised in the x-direction. Thus, the photoelectron is preferentially emitted to the left and to the right. Consequently, for the beam spots on the right side, mainly tracks that go to the right are falsely reconstructed Thus, in the angular spectrum the expected peak that corresponds to the right gets lowered and which effectively recedes the distance between maximum and minimum. This, by definition, results in a lower modulation factor.

A similar effect leads to the increase of the modulation factor at the upper and lower edges of chip. Here, mainly tracks that go upwards (for the upper edge) or downwards (for the lower edge) get falsely reconstructed, effectively lowering the minimum of the angular distribution in that direction. This systematically increases the modulation factor. The corresponding angular distributions for the central bin on the upper edge and the central bin at the right edge are displayed in Figure 10.22. Here, one can see the explained behaviour, resulting in an artificial reduction of one minimum for the upper edge and the artificial reduction of one maximum for the right edge.

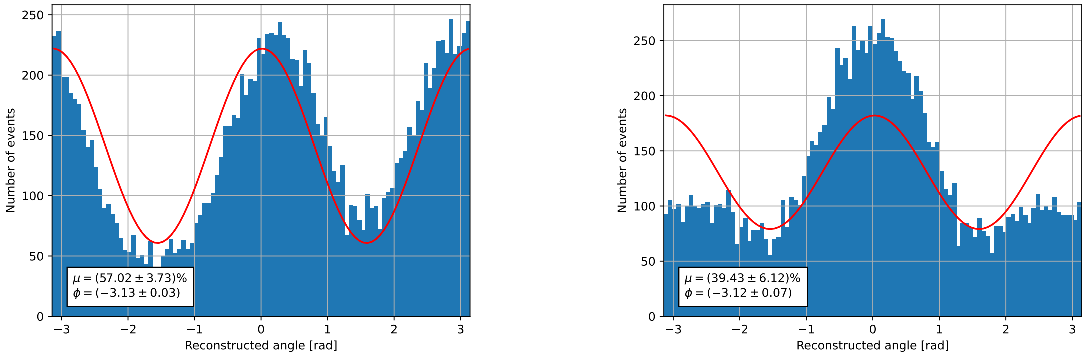

(a) Upper edge, centre

(b) Right edge, centre

Figure 10.22: Modulation curves for different beam spots. (a) shows the curve for a beam spot at the centre of the upper edge, (b) shows the curve for a beam spot at the centre of the right edge. Data for 10 keV with He/DME 80 %/20 % and normal pressure with polarisation in x-direction. While for the upper edge one minimum is reduced resulting in an artificially higher modulation, for the right edge one maximum is reduced resulting in an artificially lower modulation.

The effects can be further studied by analysing the reconstructed polarisation angle via the $\cos^2$-fit of the angular distribution and the reduced χ^2 as indication of the fit quality. Both are presented in Figure 10.23. One can see that despite the discussed effects at the edges of the chip, still for all bins except for the corners the expected angle was reconstructed. The reason for this is, that still a reasonable percentage of tracks can be reconstructed as intended and only one direction is spoiled which can be handled by the fit due to the symmetry of the distribution. In the corners, the reconstruction of two directions is spoiled creating a bias to the fit. These effects are also visible in the reduced χ^2 of the $\cos^2$-fit which should ideally be 1. Towards the edges, the bias is much higher than in the centre as one maximum or minimum deviates from the fit. In the edges, two of them deviate, leading to an even higher χ^2_{red}. As discussed, this effect gets stronger with the energy and is not visible for energies below 6 keV. This is the case because the photoelectron tracks get longer with an increase of the energy (see Section 4.2) and thus the distance of the outer beam spots to the edges of the chip are in this setup sufficient to detect the full track for most events. The overall behaviour changes with the parameters of the simulation, as they can for example lead to shorter or longer tracks. For a different polarisation axis, the behaviour is expected to rotate with it. For example, for a rotation of 45 ° all edges should show the same behaviour and the bins the corners should still show the worst reconstruction results as still two directions are suppressed, resulting in a bias. All these effects must be factored in for applications that are supposed to reconstruct the polarisation with a high position resolution. The easiest approach would be to only consider events in the central part of the chip, with the central part being defined for each energy, as then it can be ensured that the corresponding photoelectron tracks are always completely detected. In an advanced approach the area can be extended if the symmetries on the edges are used to get rid of biases.

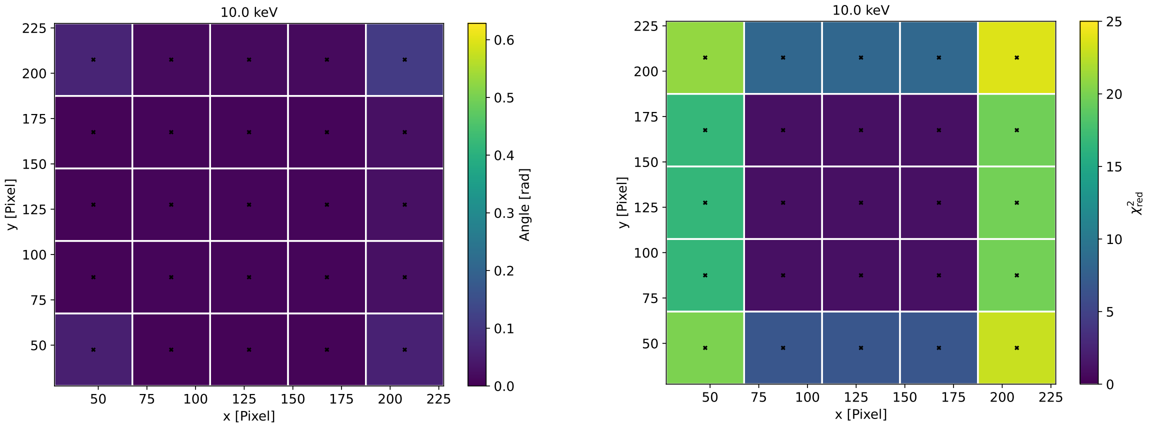

(a) Reconstructed angle

(b) Reduced χ^2

Figure 10.23: Reconstructed polarisation angle (a) and χ^2_{red} (b) for different beam spots based on a $\cos^2$-fit of the angular distribution for 10 keV. The beam was polarised in x-direction. The beam spots are marked by black crosses and the surrounding square shows via the colour code the modulation factor.

The cut-based reconstruction (see Section 9.3) and the weight-based reconstruction (see Section 9.4) were compared, as a final test of the position dependence on the reconstruction. The resulting modulation factors are displayed in Figure 10.24. One can see again, as already discussed in Section 10.1, that the weight-based reconstruction performs better as the cut-based reconstruction, resulting in a higher modulation factor. Furthermore, the performance of the cut-based reconstruction seems to be much more dependent on the beam spot. In this case the cut-based reconstruction performs on the left and right edges so bad that no modulation at all is reconstructed. The weighting of the pixels in the weight-based reconstruction helps to consider only the right pixels for the reconstruction, so if the absorption point is reconstructed this reconstruction should work. In contrast, the cut-based reconstruction strongly relies on identifying the start and the end of the track and in the second step all pixels still have the same weight, which could create additional error sources. In summary, this shows again that the weight-based reconstruction is preferential.

10.5 Position Resolution

Based on the simulation, the best achievable position resolution for different gas mixtures, detector parameters, and for the different reconstructions can be tested. For this, simulations with a predefined beam spot were performed so that the reconstructed absorption point could easily be compared to the expectation. Additionally, unpolarised simulations were used to avoid a bias into the direction of the polarisation which was already visible in Section 10.1 where the optimisation of the reconstruction radii showed a systematic offset. Using the detector for applications, this offset must be considered based on the measured degree of polarisation.

With the settings for the simulation the position resolution can be studied via histograms of the reconstructed absorption point minus the expected absorption point. The result of the position resolution for a mixture of Helium and DME at normal pressure is presented in Figure 10.25. It is based on the weight-based reconstruction with the first step in 3D, as it showed the best performance

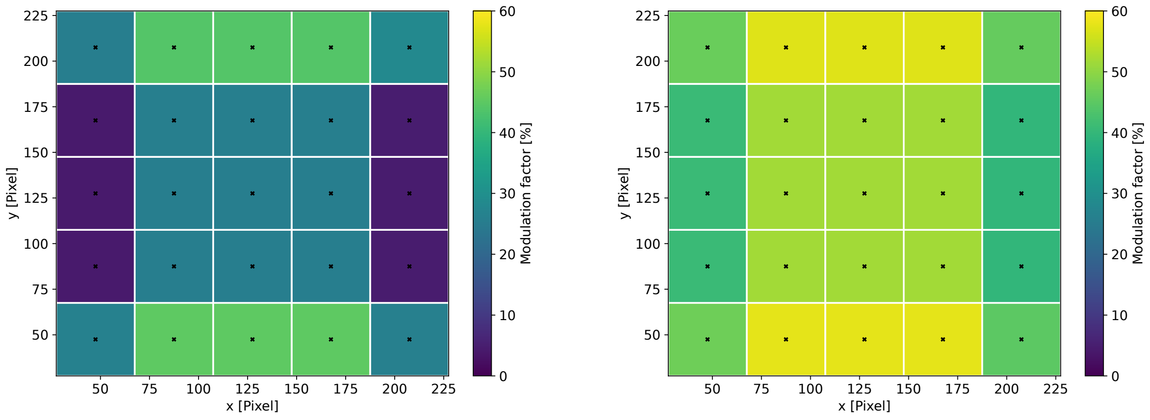

(a) Cut-based reconstruction

(b) Weight-based reconstruction

Figure 10.24: Modulation factors based on a $\cos^2$-fit of the angular reconstruction with the weight-based reconstruction for different beam spots. The results for 10 keV with the cut-based reconstruction (a) and the weight-based reconstruction (b) are presented. The beam was polarised in x-direction. The beam spots are marked by black crosses and the surrounding square shows via the colour code the modulation factor.

in Section 10.1. As the reconstruction of the absorption point is based on the first step, the resolution does not depend on the dimensionality of the second step. The position resolution is based on a fit of a Gaussian distribution to a histogram of the reconstructed positions minus the expected positions. For this, the resolution is considered as 1σ of the Gaussian distribution. One can see that the position resolution tends to be best around 4 keV to 6 keV. Because the same reconstruction parameters are used for all energies, they are only optimal only for a few energies. It is also visible that the resolution tends to be worse with longer drift cylinder which is a result of a higher diffusion and thus broader tracks. Overall, the presented results show that it is possible to achieve a resolution of up to 40 µm in the reconstruction of absorption points. Thus, it is possible to perform position-resolved polarisation measurements with GridPix-based X-ray polarimeters.

10.6 Eccentricity Cut

To improve the reconstruction, one can test if a cut on the eccentricity of events enhances the measured modulation and decreases the minimum required number of photons based on the minimal detectable polarisation. In this case the eccentricity is defined as:

$$\epsilon = \frac{M_2^{\max}}{M_2^{\min}}, \tag{10.7}$$

with $M_2^{\max}$ and $M_2^{\min}$ being the maximum and the minimum of the second moment of the charge distribution of the first step of the polarisation reconstruction (see Section 9.3). Such a cut could be useful as very round events are hard to reconstruct. This is the case because there is a lot of scattering is such events. Additionally, there is a height probability that start, and end of the track are close to each other or even overlapping, such that differentiating them is harder or impossible. To study the

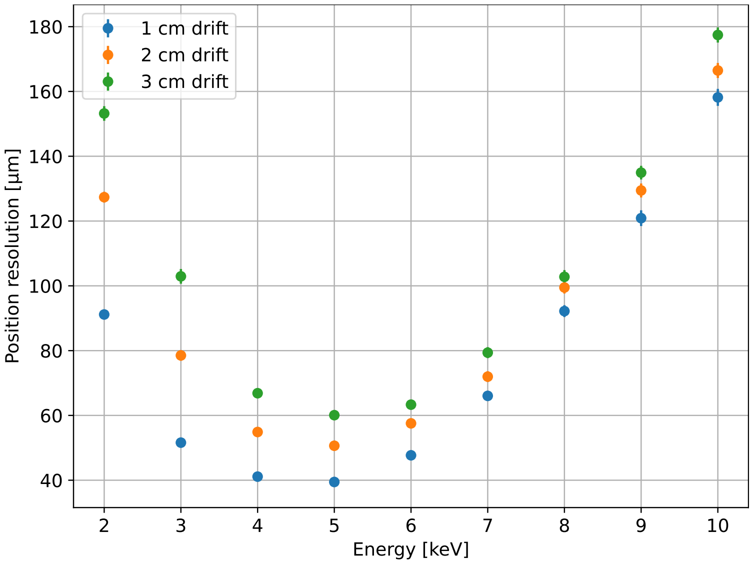

Figure 10.25: Simulated position resolution of the absorption points in a mixture of Helium and DME with a ratio of 80 %/20 % in a detector with a 2 cm drift cylinder. The weight-based reconstruction for Timepix3 data was used with doing the first step in 3D. As the calculation of the absorption point is not influenced by the second step of the reconstruction it does not matter if it is performed in 3D or in 2D.

influence of this cut, the simulated data of Section 10.1 were taken after the optimal radii (1.6 for the inner radius and 3.5 for the outer radius) and the weight 1.2 were used for the reconstruction. After this, different eccentricity cuts with a step size of 0.1 were applied. A cut means here that only events with an eccentricity higher than the cut value are considered for the modulation curve. As in Section 10.1, this was done with the reconstructions that were performed completely in 2D, completely in 3D and with the 3D-2D approach. For each combination of reconstruction approach, eccentricity cut, photon energy, and drift length a modulation curve was plotted and fitted with a $\cos^2$-distribution to get the resulting modulation factors. Some examples are presented in Figure 10.26. While the effect of the cut on the fully or partially 3D reconstructed data is small, it can show a substantial improvement of the modulation for the 2D reconstructed data. A possible explanation for this is, that the third axis of the 3D reconstructed events lowers the possibility that start, and end of a track are close to each other because the photoelectron needs to scatter accordingly in three instead of in two dimensions. Thus, the events in which start and end are misidentified should be lower with the (partially) 3D reconstruction than with the 2D reconstruction and thus, the effect of the cut should be smaller.

Whether a cut on the eccentricity can improve the detector performance cannot be decided just based on an improved modulation factor. The cut efficiency E_{cut} must be considered as well. This is important because an increased modulation factor leads to a lower number of needed photons for a given confidence level and a degree of polarisation based on the minimal detectable polarisation (see Section 2.3). At the same time, the cut removes events from the measurement and thus increases the number of photons that need to be detected to get to the same number of photons that are analysed. To study this, the cut gain

$$G_{\text{cut}} = E_{\text{cut}} \times G_{\text{mod}} \tag{10.8}$$

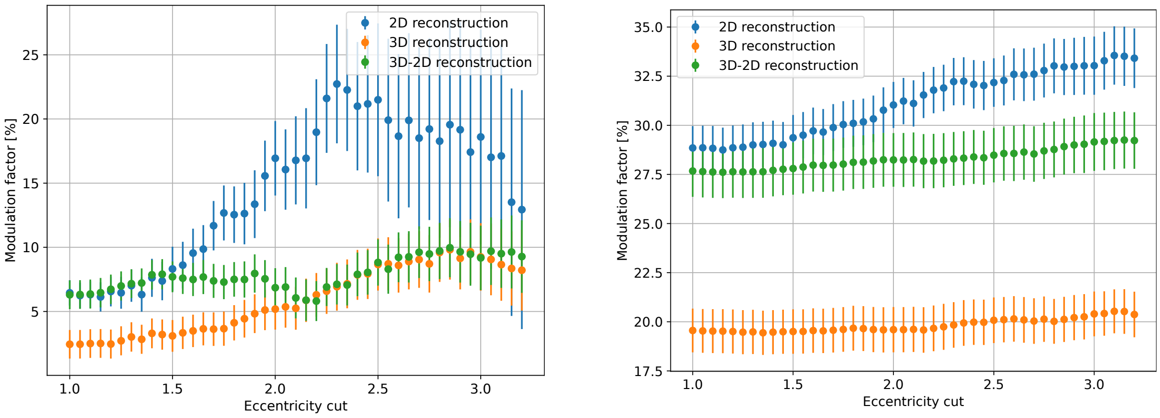

(a) 2 keV

(b) 6 keV

Figure 10.26: Influence of an eccentricity cut on the modulation factor. For 2 keV in (a) and 10 keV in (b) the modulation factor after a $\cos^2$-fit for a range of different eccentricity cuts is displayed for the results of the weight-based reconstructions with different dimensionalities.

was defined based on the cut efficiency E_{cut} and the gain due to the decreased number of needed photons, both with respect to no eccentricity cut. With this definition, a cut gain of 1 means that the cut did not change anything in a comparison with no cut while $G_{\text{cut}} > 1$ means that the cut results in a net-gain so that in total less photons are needed to get to the same confidence level. In contrast $G_{\text{cut}} < 1$ means that the cut results in a net-loss so that more photons as in a comparison with no eccentricity cut are needed. Figure 10.27 shows the cut gain for different energies and for the different reconstructions. One can see that while improvements are possible, especially for the 3D reconstruction at 2 keV, that there is no value for an eccentricity cut which gives a net gain for both presented energies and also for the full energy range from 2 keV to 10 keV. The gain for the 3D reconstruction at 2 keV is not relevant as the full 3D reconstruction has an overall worse performance and Figure 10.26(a) already showed that the cuts can bring the full 3D construction only to the same level as the full 2D reconstruction but still falls behind the combined one. Considering these results a cut on the eccentricity seems not to benefit the overall reconstruction efficiency.

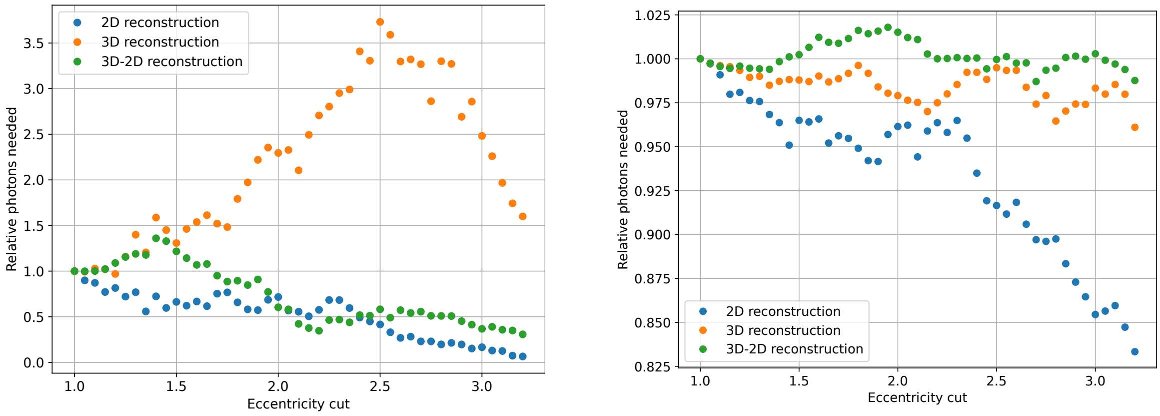

(a) 2 keV

(b) 6 keV

Figure 10.27: Efficiency gain due to an eccentricity cut. For 2 keV in (a) and 10 keV in (b) the efficiency gain for a range of different eccentricity cuts is displayed for the results of the weight-based reconstructions with different dimensionalities. This considers the gain due to improvements in the modulation factor and the loss due to the cut efficiency. Values below 1 mean a net loss in efficiency, values above 1 mean a net gain.

CHAPTER 11

Measurement Results

In this chapter the results of measurements with the Timepix-based detector and the Timepix3-based detector will be presented and discussed. These measurements were performed at two different facilities. Sections 11.1 and 11.2 will introduce the measurement setups and the simulation-based reconstruction parameters for the data. For the Timepix-based detector, Section 11.3 discusses an effect of incomplete charge measurements in some events that appears due to the shutter-based readout. The following Sections 11.4 to 11.8 present various measurement results, starting with the energy resolution, followed by investigations of the influence of the gas gain and the photon rate. Furthermore, the position resolution of the photon absorption point and the modulation factors of the polarisation measurements are presented. Section 11.9 discusses the spurious modulation of the detectors based on simulation and measurement data. The chapter is concluded with a performance comparison of the Timepix-based and the Timepix3-based detector in Section 11.10.

11.1 Detector Operation

To test the two detectors, the Timepix-based detector (Section 7.3) and the Timepix3-based detector (section 7.4), two different facilities were used: the Timepix-based detector was tested at the P09 beamline at PETRA III [23] and the Timepix3-based detector was tested at the Institute of Space Astrophysics and Planetology (IAPS) of the Istituto Nazionale di Astrofisica (INAF) with a testing setup that was used for the gas pixel detectors (GPDs) of the imaging X-ray polarimetry explorer (IXPE) [19]. Pictures of both setups with the respective detectors are presented in Figure 11.1. The setup at P09 reassembles the setup presented in Section 3.2 and Figure 3.2 but differs in one major aspect — the detector was placed directly in the beam axis without a sample between the beam line and the detector. Thus, the detector was studied with the linearly polarised primary beam. The setup for the Timepix3-based detector at IAPS used the principle presented in Section 2.4: an X-ray tube generates an X-ray beam that illuminates a Bragg crystal at an angle. The angle is set, such that the Bragg condition is fulfilled and thus, a polarised X-ray beam is reflected. Additional collimators after the Bragg crystal could be used to get a smaller beam spot. The detector itself was mounted on a movable platform such that it could be rotated around the z-axis and the position of the beam spot could be changed. At both facilities, tests with different gases and different beam energies were performed. Due to the rate limitations of the Timepix-based detector it was only operated in one polarisation orientation, which was chosen to be parallel to the x-axis. Additionally, runs with an ^{55}Fe source were taken as unpolarised reference measurements. For the measurements with the Timepix3-based detector three polarisation orientations were used: parallel to the x-axis, parallel to the y-axis and diagonal. Here, also runs with ^{55}Fe were taken as an unpolarised reference.

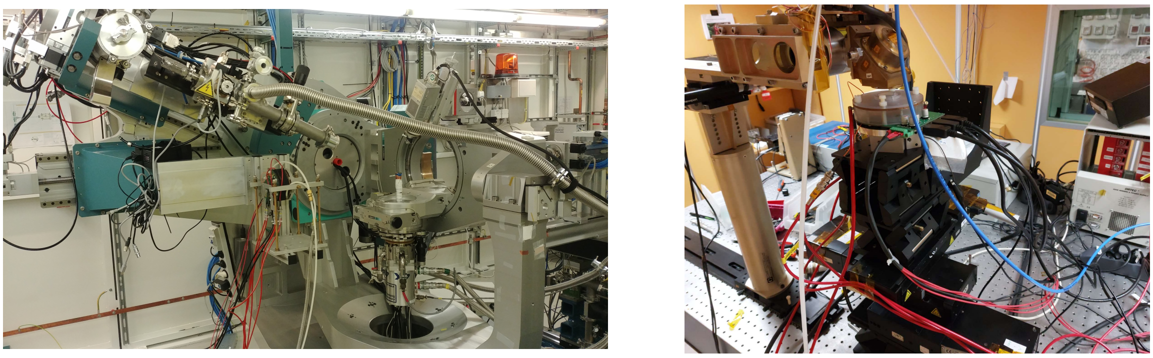

(a) P09 beamline at PETRA III

(b) GPD test setup at IAPS

Figure 11.1: Pictures of the setups to test the Timepix- and Timepix3-based detectors. The Timepix-based detector was setup at the P09 beamline at PETRA III (a) and the Timepix3-based detector was tested at a test facility of the gas pixel detectors for the imaging X-ray polarimetry explorer at the Institute of Space Astrophysics and Planetology of the Istituto Nazionale di Astrofisica.

11.2 Preparing the Reconstruction with Detector Data

The same procedure as presented in Section 10.1 was repeated for all gas mixtures, detector parameters and energies with which data was taken with the Timepix and the Timepix3 detectors. Therefore, simulations with these parameters were performed and then different radii and weights were tested to optimise the weight-based reconstruction. With this, it can be tested how these reconstruction parameters are influenced by the gas mixture and detector parameters. The results presented in Section 10.1 have already shown that for a gas mixture of Helium and DME with a mixture ratio of 80 %/20 % the length of the drift cylinder mainly influenced how well the absorption point could be reconstructed and the amplitude of the resulting modulation factor. The overall reconstruction behaviour with respect to the radii did not change significantly compared to the simulation. The only difference was that the length mainly created an offset in the distance of reconstructed and expected absorption points, but the result for the optimal radii was the same. However, the optimal weight of pixels depends on the detector configuration. Therefore, the simulations were used to determine the weight that works best for the detector configuration and the energy range for which it was used. Table 11.1 shows the final reconstruction parameters and also drift velocities and diffusions for the detector parameters.

Table 11.1: Simulation and reconstruction parameters for measured data

Gas	P [mbar]	Drift [cm]	v_D [$\frac{\mu m}{ns}$]	D_T [$\frac{\mu m}{\sqrt{cm}}$]	D_L [$\frac{\mu m}{\sqrt{cm}}$]	inner radius	outer radius	weight
He/CO_2 80/20	1050	2	14.28	139.6	138.8	1.6	3.5	2.0
He/CO_2 80/20	1500	2	11.80	120.2	117.3	1.6	3.5	1.5
He/DME 80/20	1050	2	3.59	99.7	102.5	1.6	3.5	1.3
He/DME 80/20	1500	2	2.51	92.4	92.4	1.6	3.5	1.1
Ar/CO_2 50/50	1023	2	15.17	101.0	114.7	1.6	3.5	1.8
Ar/CO_2 50/50	1023	1	15.17	101.0	114.7	1.6	3.5	1.6
Ne/CO_2 50/50	1023	2	14.99	101.1	115.2	1.6	3.5	1.2
Ne/CO_2 50/50	1023	1	14.99	101.1	115.2	1.6	3.5	1.0
CO_2 100	1023	1	13.55	72.8	80.0	1.6	3.5	0.8

11.3 Broken Timepix Events

If one creates a histogram of the total collected charge per event compared to the charge per pixel per event for runs with Timepix as readout ASIC, a distribution as in Figure 11.2(a) is obtained. An elliptical preferred region is visible that represents the overlap of the peak of the gas gain distribution that represents the x-axis and the peak of the charge spectrum that represents the y-axis. Additionally, a diagonal preferred region is visible in the measured data which can neither be explained by the gas gain distribution, nor by the charge spectrum. In a comparison with data from a Timepix3-based detector this is not visible (see Figure 11.2(b)). This indicates that for some events there is a linear dependence of the total charge on the charge per pixel. To investigate this, several events of the two regions were plotted (see Figure 11.3). While events in the elliptical region look like expected events with a random charge distribution along the track and most charges at the end of the track based on the expected Bragg peak, the events in the diagonal region show a clear charge gradient along the track.

This difference can be explained by the working principle of the Timepix and the setup of the measurement: For the measurement, no trigger was present, and the chip was operated with a clock-based shutter mode. In this mode the shutter opens and closes periodically for the readout. So, after a given time of an open shutter, it was closed for the readout and then opened again. At the same time, the beam was continuous and thus the events were evenly distributed over time. This means that it is possible that a photon arrives in the detector and deposits charges in the pixels before the shutter is opened and also that a photon arrives shortly before the shutter is closed. This spoils the charge measurement of the corresponding events as the ToT clock only runs when the shutter is opened. Thus, events that are detected close to the opening or closing of the shutter are not fully recorded and thus the charge measurement gets biased. This also explains why this behaviour is not visible in Timepix3 data: the Timepix3 operates in a shutter-less data-driven readout mode (Section 5.2) which prevents this effect.

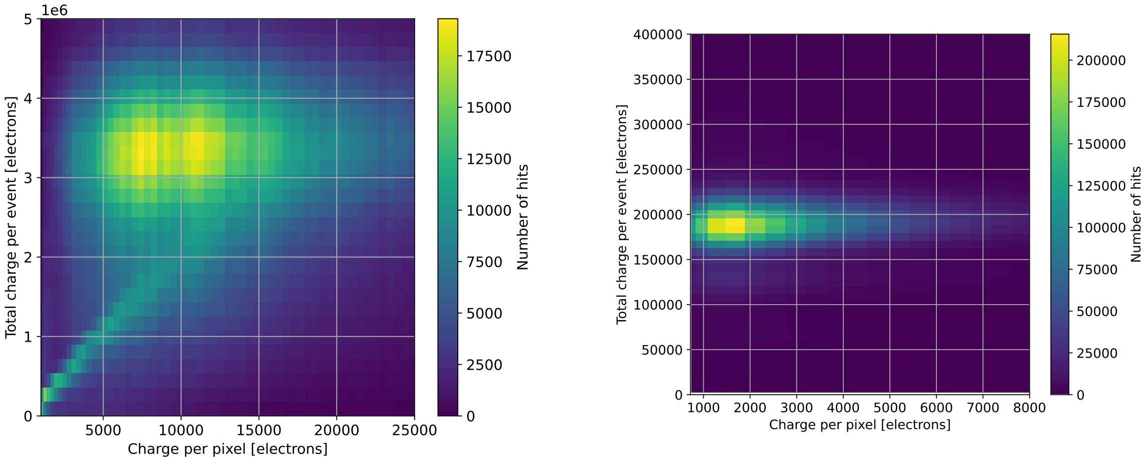

(a) Correlation of total charge and gain

(b) Correlation of total charge and gain

Figure 11.2: Correlation of the total charge per event and the charge per pixel for Timepix (a) and Timepix3 (b). While the Timepix data shows in the bottom left a region with a linear dependence between total charge and charge per pixel, this is not present for data that was recorded with a Timepix3-based detector.

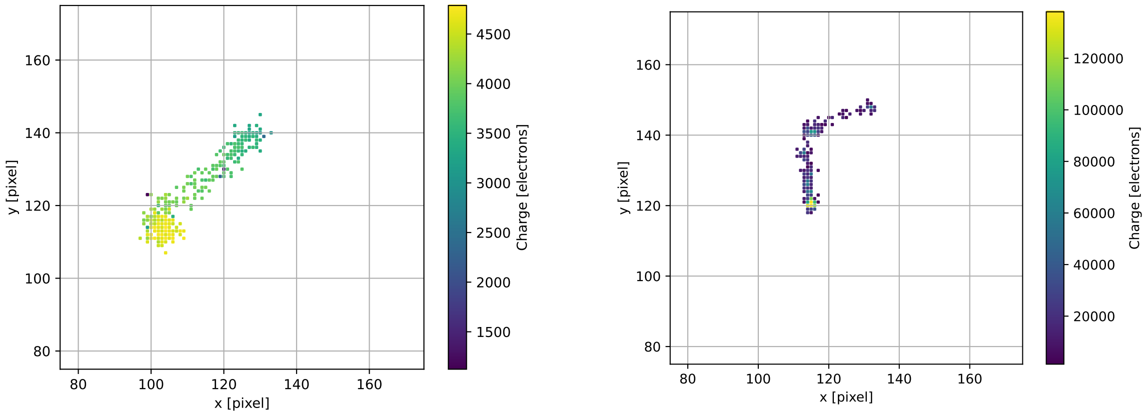

(a) Incomplete ToT measurement

(b) Complete ToT measurement

Figure 11.3: Example events from a Timepix-based detector. In (a) the event was detected shortly before the shutter of the Timepix closed and thus the measurement of the ToT was interrupted leading to a gradient of the ToT along the track. (b) shows a normal event with completed ToT measurement.

As in such events the ToT does not represent the charge but just the time until the shutter closed, the reconstruction does not work as expected, as it requires the charge information to differentiate between start and end of the track. To deal with this, a cut for the Timepix data was introduced: as this effect biases the charge distribution within an event it is expected that the root-mean-square (RMS) of the ToT distribution deviates from fully detected events. So, a cut on the ToT RMS per event should be able to get rid of them. Therefore, the ToT RMS distribution is plotted and fitted with a Gaussian distribution. The cut is then based on 2σ around the mean of the fit. Such a distribution is presented in Figure 11.4(a). Applying this cut to the data and plotting again the same histogram as in Figure 11.2(a), leads to the histogram in Figure 11.4(b). Here one can see, that the additional branch vanishes and only the expected region based on the peak in the charge spectrum and the gas gain distribution remains. Therefore, this cut is used for all runs with the Timepix-based detector. For the overall efficiency of the detector this means that some photon events must be discarded and thus the number of available events is reduced. The efficiency of this cut strongly depends on the gas gain and its distribution, the photon rate, and the shutter time. With this cut for all runs with the Timepix-based detector about 25 % of the events were discarded. This gives an additional limit on the photon rate that can be detected with the detector, besides the limitations due to the dead time and the possible frame rates, as it drastically reduces the number of usable events and shows a major advantage of a Timepix3-based detector.

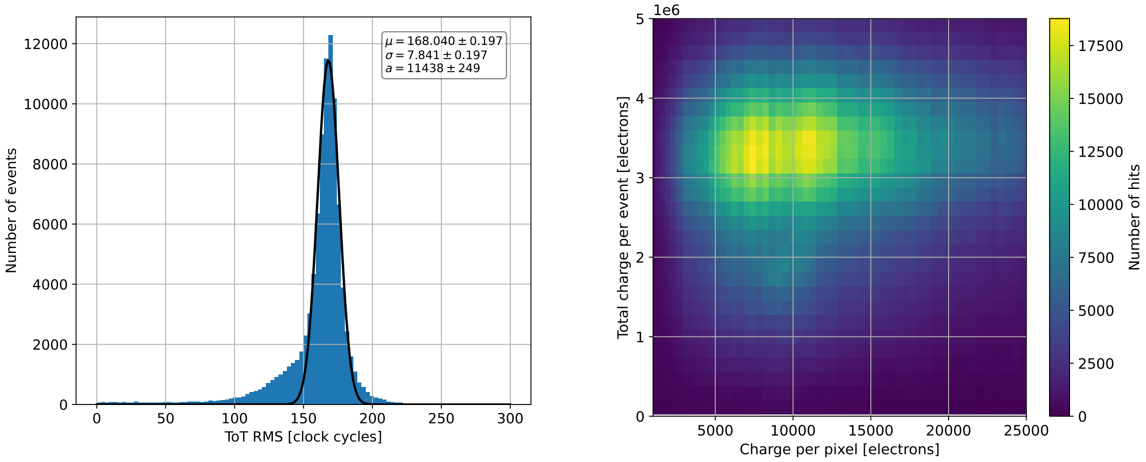

(a) ToT RMS distribution

(b) Correlation of total charge and gain

Figure 11.4: Distribution of the ToT RMS for Timepix (a) and the result of a cut on this on the correlation of total charge and charge per pixel (b). To the ToT RMS distribution, a fit of a Gaussian with the scaling a was applied and with its result a $\pm 2\sigma$ cut on the ToT RMS was applied. With this cut, the region that showed a linear correlation between the total charge and the charge per pixel vanishes and only the expected peak due to the photo peak in the charge spectrum and the gas gain distribution remains.

11.4 Energy Resolution

To determine the energy resolution, two types of energy spectra that were presented in Section 9.6 can be studied: the energy based on active pixels per event and the energy based on total collected charge per event. Both types of spectra were extracted from the data that was taken with the Timepix and the Timepix3 detectors. A comparison between the two types of spectra is displayed in Figure 11.5 for a data set with an ^{55}Fe source and a mixture of Argon and CO_2. The comparison shows the effects that were discussed when these two energy spectra were introduced. One can see that the resolution in the charge-based spectrum is better than in the hit-based spectrum. For example, in the charge-based spectrum in Figure 11.5(b) a peak with a smaller amplitude is visible at lower energies while in the hit-based spectrum it only appears at a shoulder of the main peak. The higher peak is the photo peak for the ^{55}Fe source that was used for this measurement and the lower peak is the Argon escape peak. The lower resolution in the pixel spectrum is caused by the low diffusion, which is needed for tracking the photoelectrons. Because of this, a lot of hits are based on multiple electrons, thus biasing the measurement. For the charge-based spectrum all of these electrons still cause avalanches below the grid of the GridPix and thus contribute to the spectrum. Therefore, the charge-based spectrum was used for the energy determination and thus defined the energy resolution.

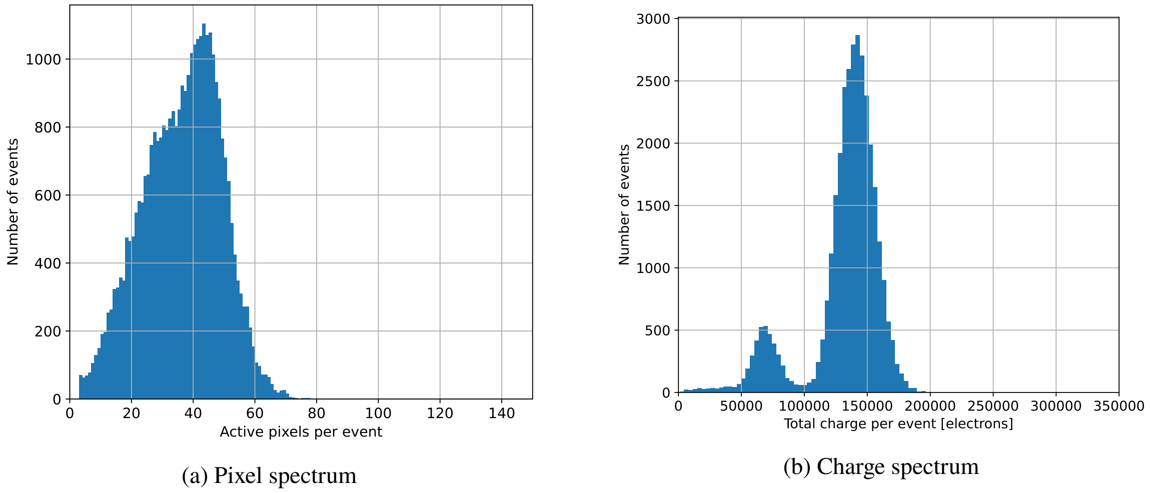

(a) Pixel spectrum

(b) Charge spectrum

Figure 11.5: Comparison of the pixel spectrum (a) and the charge spectrum (b) for the same run. The data was taken with an ^{55}Fe source, a 1 cm drift cylinder and Ar/CO_2 in a mixing ratio of 50 %/50 % at normal pressure with the Timepix3-based detector. While the photo peak at higher energies and the Argon escape peak at lower energies are clearly separated in the charge spectrum, the Argon escape peak only occurs as a shoulder of the photo peak in the pixel spectrum, indicating the lower energy resolution of this approach.

The full width half max (FWHM) energy resolution is defined as:

$$E_{\mathrm{res}} = \frac{\sigma_{\mathrm{FWHM}}}{\mu} \,. \tag{11.1}$$

Based on a Gaussian fit of the spectrum with the mean μ and the width σ the σ_{FWHM} can be calculated with:

$$\sigma_{\mathrm{FWHM}} = \sigma \cdot 2\sqrt{2\log(2)} \,. \tag{11.2}$$

As an alternative the energy resolution can be also calculated by just dividing σ by μ, but for comparability with the results of the gas pixel detectors for IXPE the definition via the FWHM was chosen.

Based on the previous description, the data was fitted and the energy resolution determined. Figure 11.6 shows the results for all data of the Timepix-based and the Timepix3-based detectors. Both detectors reached energy resolutions up to 20 % (at 11 keV for the Timepix-based detector and at 6.4 keV for the Timepix3-based detector) which gets close to the resolution of 17.5 % that the gas pixel detectors for IXPE achieved at 5.9 keV [20], although it is not directly comparable as these detectors operated with pure DME at 0.8 bar with a drift length of 1 cm. For a direct comparison, a measurement with the same parameters would be needed as they influence the number of primary electrons, the diffusion, and the avalanches, all of which have an influence on the energy resolution. Furthermore, it is possible that the resolution of the Timepix3-based detector can be improved with an optimisation of the DAC settings of the Timepix3 leading to a lower threshold and thus an increase in the detection efficiency. Further analysis of the results show that shorter drift cylinders tend to show better energy resolutions. This points into the direction that the detection efficiency plays an important role, because with a shorter drift, there is less diffusion and thus more pixels that detect multiple avalanches. Thus, there is a lower probability that hits are below the threshold and are not counted for the overall charge of the event. This is also a plausible explanation for the trend of worse resolutions towards lower energies. As there are less electrons for lower energies, there is also a lower probability for multiple avalanches that are detected by the same pixel and thus a higher probability for hits below the threshold. This could be improved by lowering the threshold, but both detectors were already operated close to the noise level. Thus, lowering the threshold comes at the cost of additional noise or again, via an optimisation of the DAC settings of the chips and the selection of chips with an intrinsically low noise level. Another possibility is, to increase the gas gain, as this increases the chance that avalanches contain enough charge to cross the threshold. However, this broadens the gain distribution which also broadens the charge distribution and also lowers the resolution. Hence, the optimum must be scanned for a particular detector and application, with the consideration of the threshold of the chip, the gas gain, and the gas parameters.

Based on the fits of the spectra, also an additional energy cut for the data can be introduced. There might be multiple energies from the source due to higher harmonics but also background events like X-ray fluorescence of for example the copper of the cathode. Thus, the cut is used such that only the response of the detector to the source and its specific energies is tested. For all following analysis such a cut was performed with a 3σ distance around the mean of the Gaussian fit.

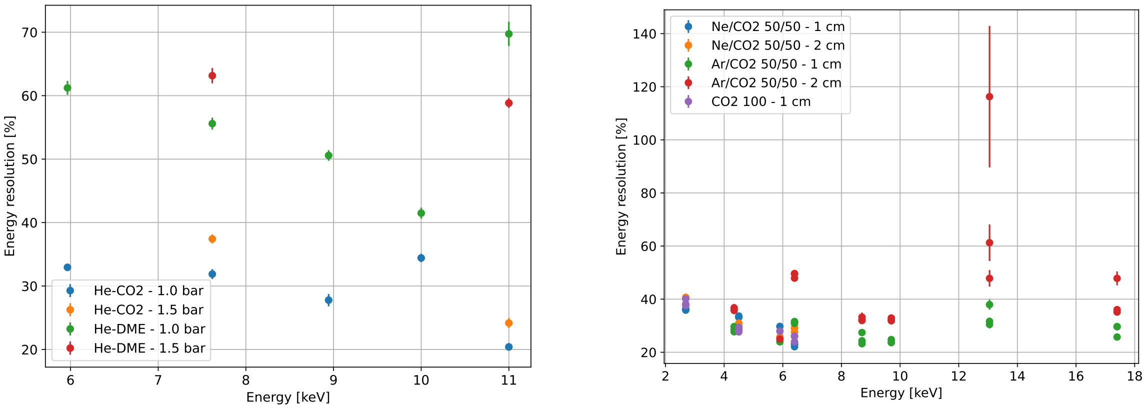

(a) Timepix-based detector

(b) Timepix3-based detector

Figure 11.6: Energy resolutions for the Timepix-based (a) and the Timepix3-based (b) detectors. The full width half maximum energy resolution is displayed for all combinations of gases, drift lengths and pressures. For all Timepix-based data a 2 cm drift cylinder was used and for all Timepix3-based data normal pressure was used. Multiple measurement points for the same gas, energy and drift length originate from the measurements with different polarisation planes.

11.5 Gas Gain Studies

The gain in the combination with the threshold of the ASIC influences how many of the electrons that enter the amplification region of the GridPix create a sufficient avalanche to cross the threshold and thus be detected. In this regard, a low efficiency of hit detection would mainly influence the start of photoelectron tracks as there are less hits and thus less pixels that detect multiple primary electrons. This could influence the polarisation reconstruction efficiency. Therefore, sets of runs with a polarised beam for different grid voltages were taken. For this purpose, the Timepix-based detector was operated at the P09 beam line at PETRA III (see Section 11.1) with a polarised beam at 11 keV. The detector was filled with a mixture of Helium and DME in ratios of 80 % and 20 % at normal pressure. While the grid voltage was changed, the other voltages of the detector were changed accordingly such that the drift field was constant and thus, only the amplification field changed. The upper limit of the voltage range was given by discharges such that a stable operation of the detector was no longer possible. The data collected with the settings described above, allows to investigate how the number of pixels per event changes with the amount of collected charge per event. While the former should get constant at a certain grid voltage and thus gas gain, the latter should rise exponentially with the grid voltage. This is the case because the number of expected ionisation electrons depends on the gas mixture and the photon energy, which were both constant. Additionally, the number of multiple electrons going into the same grid hole and being detected in the same pixel should not change if the drift field and thus the diffusion are constant. Therefore, the number of active pixels should rise with the gas gain until a constant is reached. This is the case because at lower gas gains some electrons lead to avalanches that are not sufficient to cross the threshold, while with higher gas gains the efficiency of this process should rise until everything is detected. This is different for the number of total collected charge per event because with higher gas gains the number of deposited charges by avalanches will also rise. The results for the hits per cluster and the total charge per cluster are presented in Figure 11.7.

Here one can see the expected effects: the number of hits rises with the grid voltage and saturates at about 430 V, while the total collected charge per event rises exponentially with it. Continuing with this data, the energy resolution and the resulting modulation factors from the polarisation reconstruction can be investigated. The result for the energy resolution is presented in Figure 11.8(a). Comparing it with Figure 11.7(a) shows, that the energy resolution reaches its optimum when the number of hits saturates. This shows, that at this point the effect of losing information due to signals below the threshold is minimised and thus its statistical influence on the resolution is small. The results can then be used to cut on the photo peak in the charge-based spectrum to analyse only these events for the angular reconstruction. As the data was taken with the Timepix-based detector, also the cut on the RMS of the ToT must be performed to exclude events with incomplete ToT (see Section 11.3). Applying these cuts to the data and limiting all runs to the same amount events led to the modulation factors that are presented in Figure 11.8(b). One can see that the modulation is the highest, when the energy resolution is the best and thus, when the efficiency for the hit detection is the highest. This is expected, as lower efficiencies would mainly influence the important start of the track and thus spoil the angular reconstruction. These results show that a too low gas gain or a too high threshold can have a significant impact on the polarisation and energy measurement. Thus, the gain must be tuned to the optimal value depending on the application.

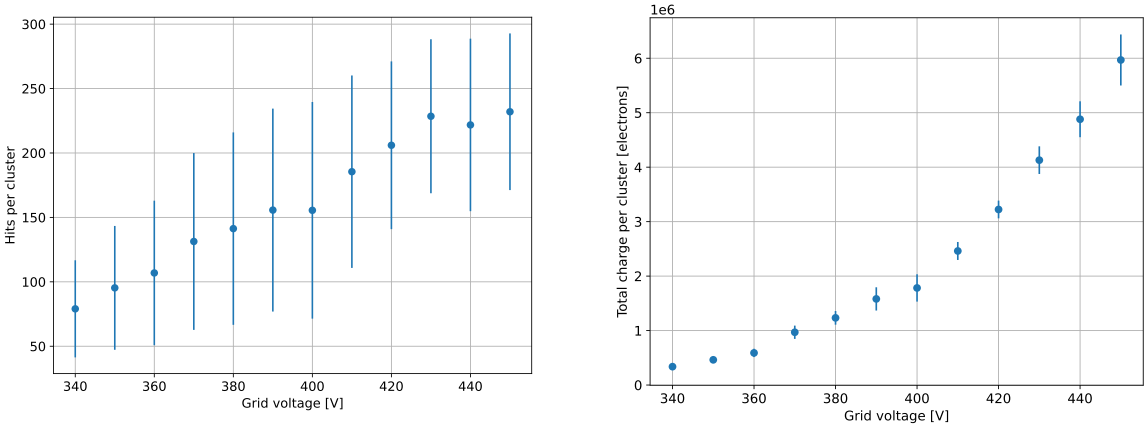

(a) Hits per cluster

(b) Total charge per cluster

Figure 11.7: Influence of the grid voltage on the hits (a) and the charge per cluster (b). Error bars for the total charge are enhanced by a factor of 10. The data was taken with a Timepix-based detector, filled with He/DME 80/20 at normal pressure and with an 11 keV polarised photon beam at the P09 beamline at PETRA III.

11.6 Measured Position Resolution

For the measurements at the P09 beamline at PETRA III a focused beam was available, and it was used to study the resolution of the reconstruction of the photon absorption point. For this, several measurement runs with He/CO_2 with a mixing ratio of 80 %/ 20 % were taken with the focused beam. The weight-based reconstruction, with the simulation-based optimal parameters, was used for the reconstruction of the absorption point. Two cuts were applied to the data: a cut on the ToT RMS to avoid events with incomplete ToT measurements (see Section 11.3), and a cut on the charge spectrum

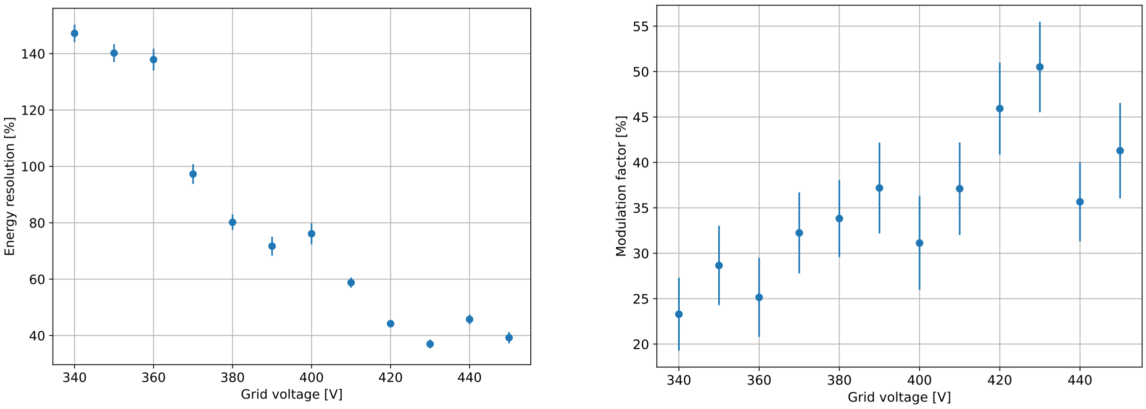

(a) Energy resolution

(b) Modulation factor

Figure 11.8: Influence of the grid voltage on the energy resolution (a) and the measured modulation factor (b). The data was taken with a Timepix-based detector, filled with He/DME 80/20 at normal pressure and with an 11 keV polarised photon beam at the P09 beamline at PETRA III.

to select only events within the photo peak (see Section 11.4). To reconstruct the beam spot for each run, the x- and y-positions of all hits in the run were accumulated in histograms and fit with Gaussians. The means of these two fits served as the reference position. The result of the resolution in x-direction, which was the polarisation direction is presented in Figure 11.9. It is based on a Gaussian fit to the distance between the reconstructed point and the reference point and the standard deviation of this fit is interpreted as the position resolution. The plot contains the resolutions based on the measurements but also based on simulations for the same gas, beam, and detector parameters. Comparing the measured results to the simulated results shows that their qualitative behaviour is similar. The resolution gets worse with higher energies but improves with an increase of the pressure of the gas. These results are expected, as a higher energy and a lower pressure led to longer tracks and thus an easier bias of the absorption point along the track.

Comparing the absolute values shows better resolutions for the simulation than for the measurements. One possible reason for this is that the beam in the simulation is perfectly focused and hits always exactly the same spot. In reality there is always some beam profile which adds an additional statistical distribution to the measurement. This can be estimated by the width of the two Gaussians that were used to get the beam spot. For all runs it was in the order of 30 µm. So, it definitely lowers the position resolution, but it is not the dominant effect. Another possible reason is that the simulation did not simulate the gas amplification and thus the charge distribution along a measured track and a simulated track are different. Furthermore, if threshold effects are considered this could especially lead to hits at the start of the tracks, that create a signal below the threshold and thus are not detected. As these are the important pixels for the polarisation reconstruction and thus, also for the absorption point reconstruction, these effects have a significant influence on the measurement. Therefore, only a qualitative comparison is possible.

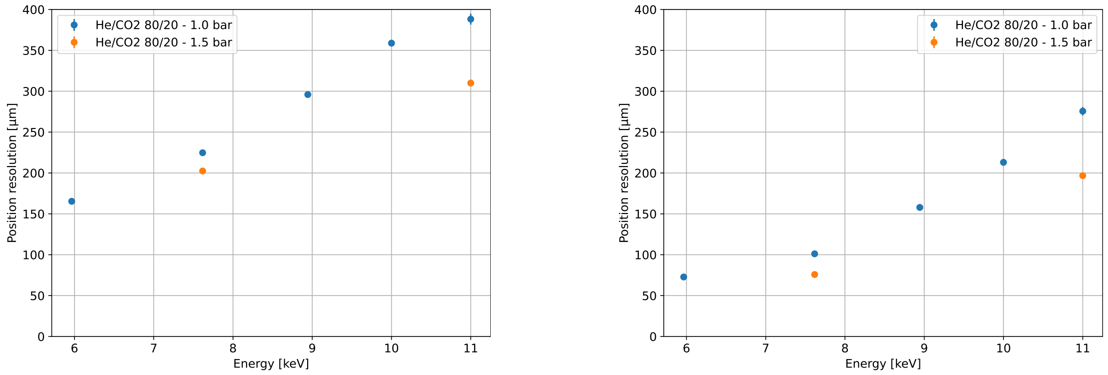

(a) Measured

(b) Simulated

Figure 11.9: Position resolution of the absorption point for the Timepix-based detector. (a) shows the resolution based on a measurement and (b) shows the simulated resolution.

11.7 Rate Capability of the Timepix3-based Detector

Based on the design of the Timepix3 (see Section 5.2 and [37]), it is expected that a Timepix3-based detector can achieve a much higher event rate than a Timepix-based detector. The main reason for this is that the Timepix with the Timepix readout system has a dead time in the order of 25 ms, resulting in a maximum event rate of 40 Hz. However, the Timepix3 can operate quasi dead-time free up to rates of 40 MHits $s^{-1}cm^{-2}$ [37]. Below this rate the only dead time occurs in active pixels due to the collection of ToT information and the pixel readout. It is 18 Clock cycles + ToT with a clock cycle being 25 ns. Additionally, the simultaneous measurement of the ToA to the ToT helps to increase the hit rate, as this information can be used to separate events in time. With the Timepix-based detector the only time information is the frame in which pixels were active. Thus, if multiple events occurred within one frame they could be only differentiated if they were well separated spatially. Otherwise, it is ambiguous to determine which pixels corresponds to which event. Therefore, the Timepix-based detector was often operated with a lower event rate than the possible 40 Hz to increase the possibility for individual events in a frame at the cost of several empty frames between events.

To test the rate capability of the Timepix3 detector several runs at INAF-IAPS were performed with increasing currents of the X-ray tube, leading to an increase in the X-ray photon rates. Figure 11.10 shows how the gas gain and the energy resolution changed with the rate of the beam. One can see that with a higher rate, the gas gain drops, and at the same time also the energy resolution gets worse. This is likely caused by a charge-up of the protective layer of the GridPix (see Section 7.1). As it is non-conductive, charges that are deposited on it by the avalanches can only dissipate slowly and thus lead to a build-up of a negative potential on the layer. This effectively lowers the electric field in the amplification gap. As the gas gain rises with the electric field, this effect leads to a decrease in gas gain with an accumulation of charges on the protective layer. In addition, with a higher X-ray rate, the rate of avalanches increases which increases the amount of charge that is collected on the protective layer. Thus, the charge-up worsens the energy resolution, as more avalanches create signals below the threshold. Furhtermore, the charge-up is not uniformly distributed over the chip, but mainly present in regions where most avalanches are detected. As this introduces additional systematics into the charge measurement, the resolution is negatively influenced.

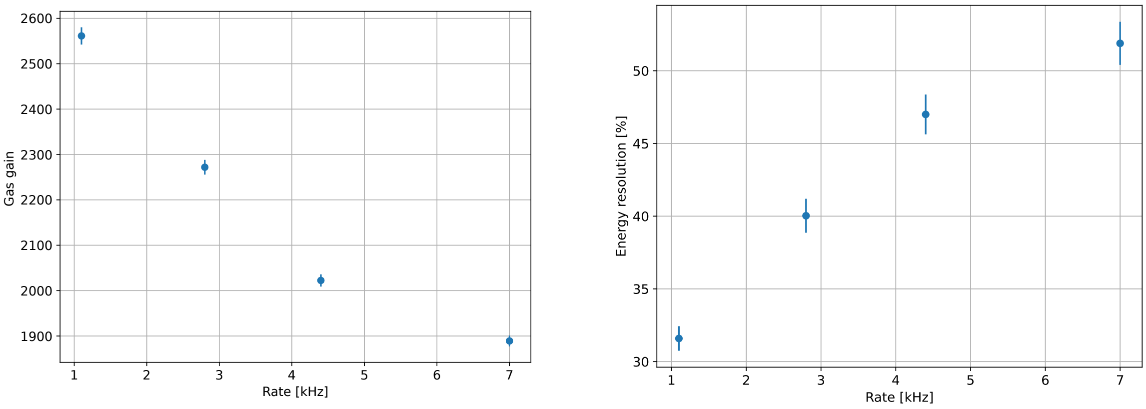

(a) Gas gain

(b) Energy resolution

Figure 11.10: Influence of the photon rate on the gas gain (a) and the energy resolution (b). Error bars for the gain, which result from a fit, are enhanced by a factor of 10. Due to charge up of the protective layer of the GridPix the gas gain gets lower with higher photon rates, and this causes a worse energy resolution.

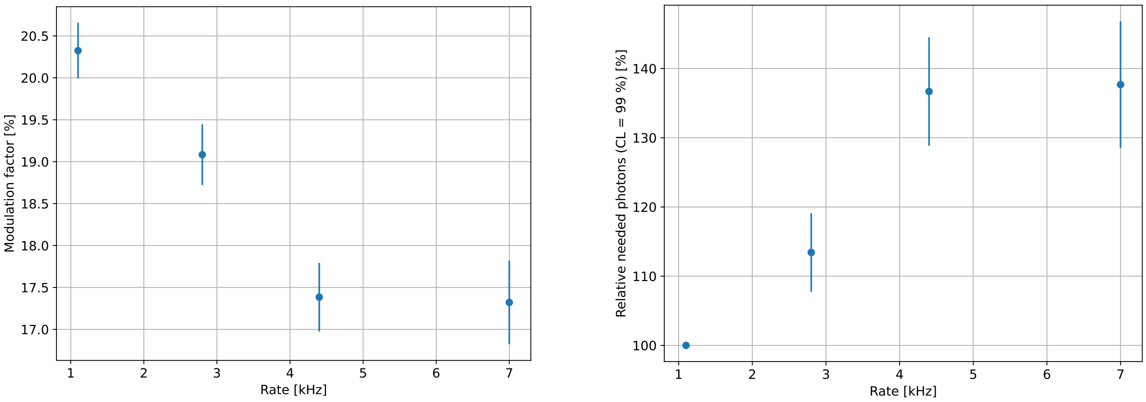

(a) Modulation factor

(b) Relative needed photons

Figure 11.11: Influence of the photon rate on the modulation factor (a) and the needed photons to measure the polarisation of a source with a confidence level of 99 % (b). The values in plot (b) are normalised to the number of needed photons for the lowest rate. As the modulation factor decreases with the photon rate, the number of photons rises based on the definition of the minimal detectable polarisation.

Using the runs with different X-ray rates to reconstruct the angles and get the modulation factor shows, that it also decreases with increasing rates (see Figure 11.11(a)). One possible reason for this is that due to the lower gain, it is likelier that avalanches do not contain sufficient charge to cross the threshold, and thus the hit detection efficiency is lowered. In these conditions, the more isolated primary electrons from the initial part of the photoelectron track have a higher chance to not be detected. As a result, the performance of the angular reconstruction is reduced. Based on the results for the modulation factor, it can be calculated via the minimal detectable polarisation if this effect is relevant. For lower modulations, a higher number of electrons is needed to get to the same confidence level of a polarisation measurement. But because of the higher rate it is possible that this number is collected in a shorter amount of time. The result of this calculation is presented in Figure 11.11(b). Here the minimal detectable polarisation was used to calculate how many more photons are needed for higher rates in relation to the lowest of the four rates. One can see that at about twice the rate roughly 15 % more photons are necessary to get to the same confidence level and for about four times and seven times the rate, roughly 38 % more photons are necessary. This shows that higher rates, in this case up to 7 kHz are beneficial in terms of measurement time as the gain though the higher rate is much larger than the loss due to the lower modulation factor. Therefore, if the source is capable of providing such rates, it should be used with the Timepix3-based detector. For even higher rates than this, it must be considered that the charge-up effect is expected to get stronger. Furthermore, at some point the much slower ions in the amplification region will get relevant, as they additionally shield the electric field and reduce the gas gain. Thus, it is expected that there will be an upper limit to the possible rate which also depends on the gas mixture and its parameters. This is the case, as the rate influences the gas gain and thus the number of ionisations and the drift velocity of the ions. A study of charge-up effects in GridPix X-ray detectors can be found in [54].

11.8 Modulation Factor

With the reconstruction parameters that are based on simulation (see Section 11.2), the cut on the ToT-RMS for the Timepix-based detector (see Section 11.3), and the cut on the energy (see Section 11.4), all data was reconstructed to study the modulation factor. For the data taken with the Timepix-based detector the weight-based and the cut-based reconstruction were used in 2D. For the data taken with the Timepix3-based detector, both reconstructions were used with the full 2D, the full 3D, and the 3D-2D approaches. As some runs differed in run time and especially in the detection efficiency due to the gas mixture and the photon energy, the number of available events also differed in the runs. For a comparison of the results without a statistical bias all Timepix-based runs were limited to the same number of events after the cuts via a random selection. The same was done for all Timepix3-based runs. After the reconstruction, the angular distributions were fit with a $\cos^2$-distribution, and the modulation factor was extracted. An example of such a distribution can be found in Figure 11.12 for a Timepix-based run and in Figure 11.13 for a Timepix3-based run. Figure 11.13 presents the modulation curve for three different rotations of the detector and thus three different polarisation directions: parallel to the x-axis, parallel to the y-axis and a 45 ° diagonal to the x-axis.

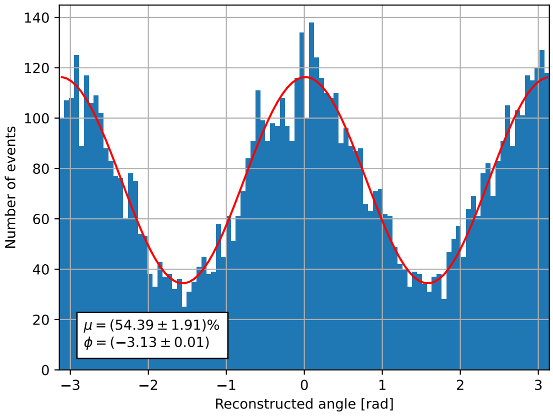

Figure 11.12: Angular distribution with the Timepix-based detector.

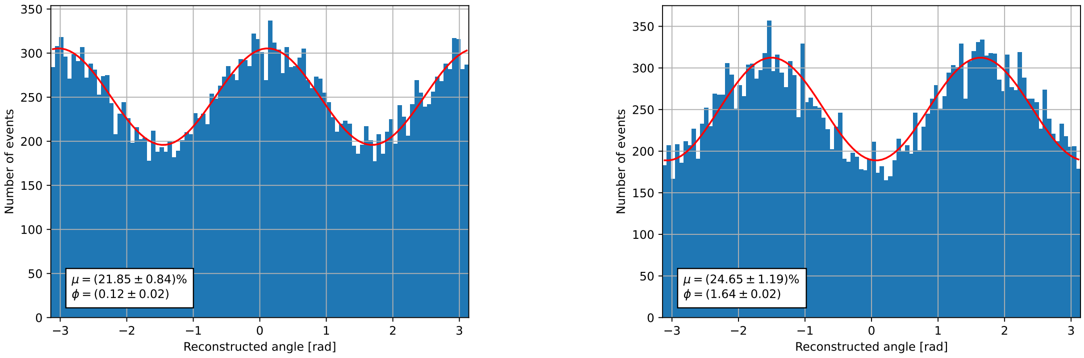

(a) Polarisation in x-direction

(b) Polarisation in y-direction

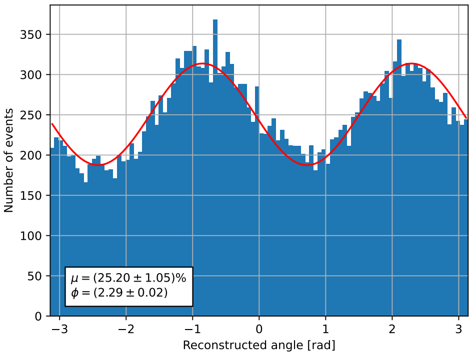

(c) Diagonal polarisation

Figure 11.13: Angular distributions with the Timepix3-based detector for three polarisation directions.

In these plots one can see that the distribution points in the expected direction and especially one can see that this direction rotates when the polarisation axis is rotated, as it was done for the Timepix3-based runs. One can see that the modulation factors slightly differ between the two rotations indicating a slight preference towards the y-direction and thus, presence of spurious modulation. This will be further discussed in Section 11.9. Using the modulation factor of all runs, one gets the results that are presented in Figure 11.14 and Figure 11.15. These plots also include the modulation factors based on simulation data. Runs for which the reconstructed polarisation direction did not point into the expected direction are excluded from this plot. This happened for the Timepix3-based detector for most runs with Ar/CO_2 and with a 2 cm drift cylinder but also for the lowest energies with Ne/CO_2 with 1 cm and 2 cm drift cylinders. One possible reason why the reconstruction fails, can be the presence of spurious modulation, which is higher in magnitude than the modulation of the beam. In such a case the resulting polarisation angle would be dominated by spurious modulation and not represent the polarisation of the beam. This effect is more prominent at low X-ray energies because the expected modulation is quite low and thus, spurious modulation can have a significant influence on the reconstruction. At higher energies, the photoelectron tracks get longer and thus it is easier, that the tracking is influenced by edge effects on the chip (see Section 11.9). Furthermore, the beam spot changed from run to run. This was especially for the Timepix3-based detector the case, as it was rotated, but the rotation axis of the setup was off-centre and thus for each run a new beam spot had to be found, that would not interfere with the copper strong back of the X-ray window. As a result, some beam sports were placed closer to the edge of the chip than others. This induced the edge effects and lead to the patterns that were discussed in Section 10.4.

Comparing the measured and simulated results shows the same qualitative behaviour: for example, the modulation rises with the energy and decreases with an increase in the pressure and the drift length. Furthermore, for the Timepix detector the mixture with CO_2 performed better than the mixture with DME in both, measurement, and simulation, but with a bigger measured advantage of the CO_2-based mixture than expected based on the simulation. One reason for this is the much worse energy resolution of the DME-based mixture compared to the CO_2-based mixture (see Section 11.4). Thus, the same cut on the energy via the charge-based spectrum of $\pm 3\sigma$ results in a much broader energy region that is kept for the angular reconstruction. Thus, there is a higher probability for polarised background in the data for example from X-ray fluorescence of the detector cathode. In terms of the gas choice for the Timepix3-based detector, pure CO_2 showed the best performance for low energies, as it did in the simulation. It is followed by the Neon-based mixtures and then finally, the Argon-based mixtures are better suited for higher energies. Comparing the absolute results of the modulation factors of simulations and measurements shows that there are some differences. For the Timepix-based detector, the measured modulation factors are higher than the simulated while for the Timepix3 detector they are for most data points roughly similar with slight variations. One possible reason for the better measured performance of the Timepix-based detector could be that the ToT RMS cut is only applied to the data. It is not applied to the simulation as it does not contain the amplification process. It could be that the cut improves the reconstruction as it not just cuts events that have a low RMS due to an incomplete ToT but maybe also events that are hard to reconstruct. For example, for events that scattered so much that the Bragg peak of the track is at the same position as another part of the track, it would be hard to reconstruct the event, as it is harder to differentiate start and end of the track. But because this would also lead to more multi hits in the region of the Bragg peak, this would also shift the RMS of the ToT. Thus, it could be that this cut discards some events that are hard to reconstruct and thus would lower the modulation.

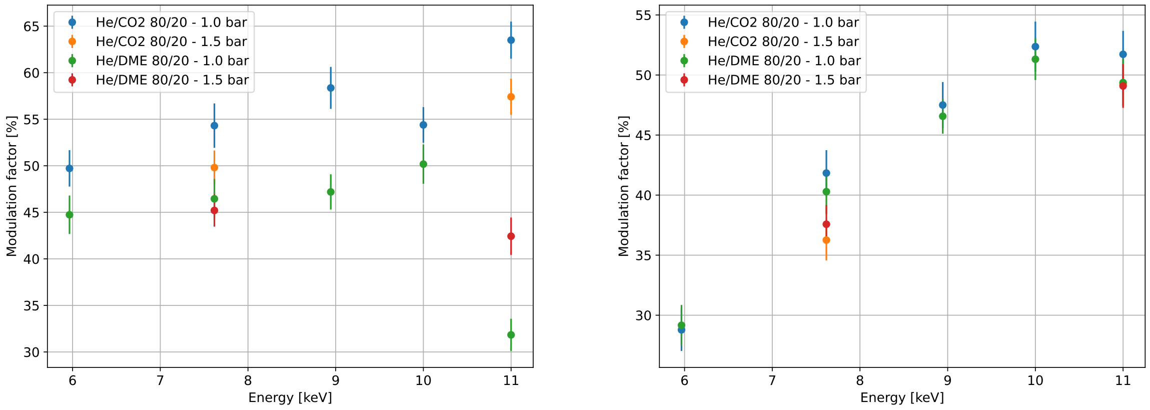

(a) Measurement

(b) Simulation

Figure 11.14: Modulation factors for the Timepix-based detector. (a) shows the modulation factors based on a measurement and (b) shows the simulated modulation factors.

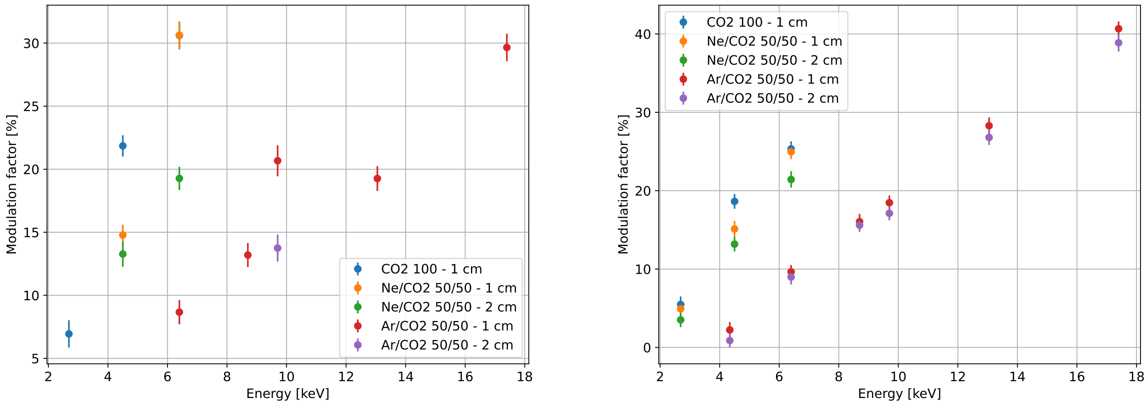

(a) Measurement

(b) Simulation

Figure 11.15: Modulation factors for the Timepix-based detector. (a) shows the modulation factors based on a measurement and (b) shows the simulated modulation factors. Data points for which the reconstructed polarisation angle did not point into the expected direction were excluded from the measurement plot, as they do not represent the modulation of the polarisation measurement. The excluded points are from the measurement with Ar/CO_2 50/50 with a 2 cm drift cylinder and also for the lowest energy the data point for Ne/CO_2 50/50 with both drift lengths.

The measurements can also be used to check the performance of the different reconstruction approaches. Therefore, Figure 11.16(a) shows the resulting modulation factors for the Timepix-based detector in a comparison of the cut-based and the weight-based reconstruction. Figure 11.16(b) shows the modulation factors for the Timepix3-based detector in a comparison for the weight-based reconstruction with the full 2D and the 3D-2D approaches. Similar to the results in Section 10.1, the weight-based reconstruction shows a much better performance than the cut-based reconstruction. Also, the 3D-2D approach shows for the dataset in the plot a significantly higher modulation than for the full 2D approach. Depending on the detector parameters the gain due to the 3D data varies and for some data point the full 2D approach has a slight advantage. This was also visible in the simulation data, as the gain of the 3D data varied depending on the detector parameters and the beam energy. The comparison of the approaches in measurement and simulation are consistent in terms of the magnitude of the gain.

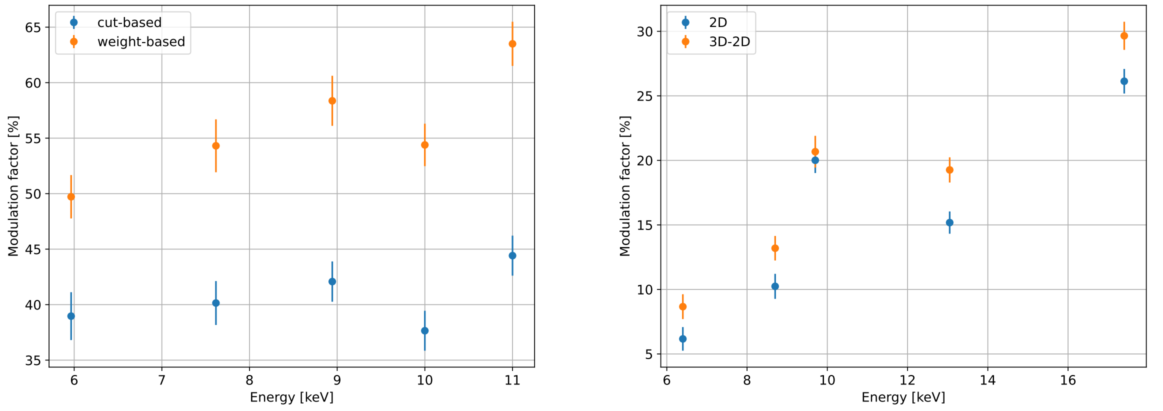

(a) Comparison of cut-based and weight-based reconstruction

(b) Comparison of full 2D and 3D-2D weight-based reconstruction

Figure 11.16: Measured modulation factors for different reconstruction approaches. (a) compares the cut-based and the weight-based reconstruction measured with the Timepix-based detector for He/CO_2 80/20 at normal pressure. (b) compares the full 2D and the 3D-2D reconstruction with the weight-based approach measured with the Timepix3-based detector with Ar/CO_2 50/50 and a 1 cm drift cylinder.

11.9 Spurious Modulation

Spurious modulation means modulation that even occurs without a polarised source and thus introduces a bias in the modulation measurement. Potential sources for this could be the design of the detector that would lead to a preferential detection direction or a bias due to the reconstruction algorithm. To use the reconstructed modulation of a measurement to calculate the degree of polarisation and the Stokes parameters (see Section 2.2), the spurious modulation must be studied such that it scan be subtracted from the measurement.

The spurious modulation was studied via a simulation of unpolarised beams to test if any kind of modulation occurs in the data with an idealised detector. With this, it was tested if modulation occurs after the angular reconstruction. Figure 11.17 shows that even with an unpolarised beam a modulation of about 2.2 % is reconstructed and it points in the direction of the diagonal of the ASIC. With this, it can be assumed that the square pattern of the pixel matrix leads to preferential reconstruction in the diagonal direction. This could be explained because of the different distance of pixels in this direction due to the square shape and thus a diagonal track would look different than an orthogonal or a parallel track. To test this, the pixel matrix was rotated in the simulation and the resulting modulation curve and especially the resulting direction was studied. These are the different rotations on the x-axes in the two plots in Figure 11.17. One can see that the modulation is not changed by the rotation of the pixel matrix, but the reconstructed direction rotates with it, such that the reconstructed angle is always in the direction of the diagonal of the matrix. Thus, it seems plausible that there is a spurious modulation of about 2.2 % in the diagonal direction due to the shape of the pixel matrix.

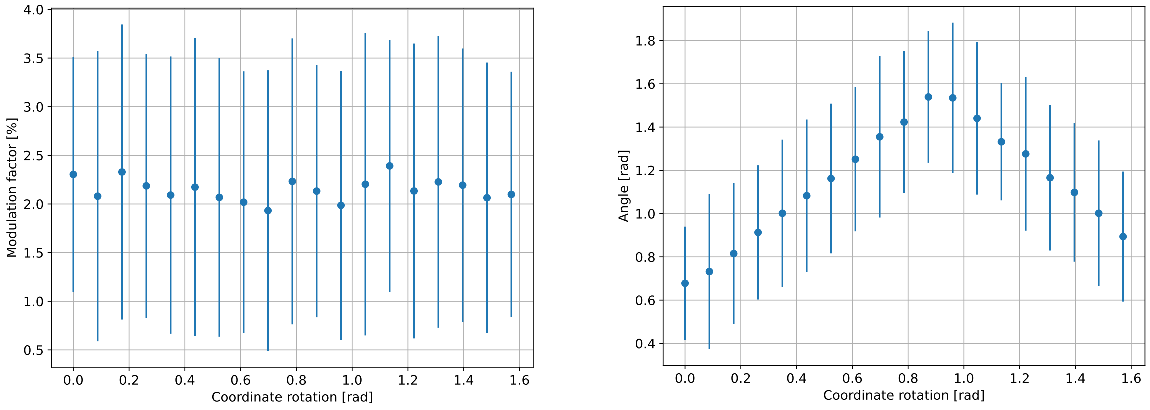

(a) Modulation factor

(b) Reconstructed angle

Figure 11.17: Simulated modulation factor (a) and reconstructed angle (b) for an unpolarised beam and different coordinate rotations.

To test if the detector itself shows spurious modulation, an ^{55}Fe source can be used. It decays via electron capture into an exited state of ^{55}Fe that then de-excites. This happens via the emission of an X-ray photon of either 5.90 keV or 6.49 keV depending on the origin shell of the electron. The empty spot in the K-shell is filled by this electron after the de-excitation [27]. The X-rays emitted by the source are unpolarised such that the polarisation response of the detector to this can be tested. Modulation that occurs in such a measurement setup is then spurious modulation. Figure 11.18 shows the modulation curves based on such a measurement for the Timepix-based detector and the Timepix3-based detector. One can see that for both detectors a spurious modulation in y-direction occurs, but it is more prominent for the Timepix3-based detector. As the reconstruction algorithm was checked and did not introduce spurious modulation and the simulation showed a weaker spurious modulation in the diagonal direction based on the square pattern if the pixel matrix, the observed modulation must originate from the detector or internal features of the ASICs.

Within the ToT calibration and the time walk calibration (see Section 6.5) of several Timepix3 ASICs it was observed that even after the equalisation of the ASIC some pattern in the ToT distribution of the pixels for the injection of test pulses was present. An example is shown in Figure 11.19(a). One can see that despite the equalisation, pixels show up to a 50 % difference in their recorded ToT for the same test pulse amplitude. Furthermore, this behaviour is not randomly distributed but shows a clear pattern. While the response along the vertical axis is rather uniform, there are several gradients occurring along the horizontal axis.

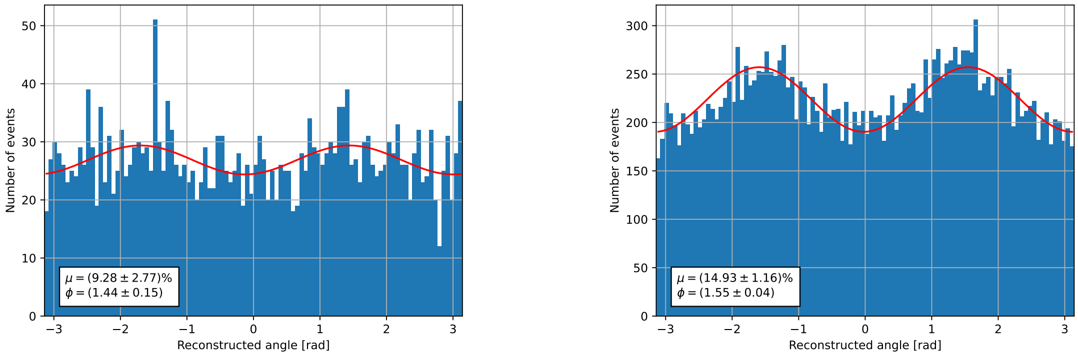

(a) Timepix-based detector

(b) Timepix3-based detector

Figure 11.18: Modulation of the Timepix-based (a) and the Timepix3-based (b) detectors with an unpolarised ^{55}Fe source. As the source is unpolarised, ideally no modulation should occur. Thus, the measured modulation is spurious modulation introduced by the detector.

A plausible reason for this could be that this is a general feature of the Timepix3 at low input charges and thus low Krummenacher [35] currents. This explanation would fit that this behaviour was observed with several Timepix3 at these DAC settings. A second explanation would be a systematic effect by the scan procedure, but this seems unlikely because for the scan all active pixels have the same distance to each other and for each step always the same number of pixels is active (see Section 6.5). So, one would expect the behaviour to change if a different number of mask steps per DAC step is used but this is not the case. The third possibility would be that there was a production issue that created this behaviour, but this also seems unlikely because the tested Timepix3s originated from different wafers.

The source of this behaviour needs to be studied in the future. To do this, the masking could be changed and even a test to the extreme with only one active pixel per mask step can be performed. Furthermore, it could be tested if the same behaviour occurs with external test pulses instead of the internal ones that were so far used for the scans. This test could show if the charge distribution is just a problem of the internal test pulses that influences the scans or a general problem. Additionally, a pulsing of the grid to induce charge into the pixels or X-ray measurements illuminating the whole grid for a flat field measurement could be performed. For these two measurements it must be considered that this will not only show the ToT collection effect of the pixels but also effects of the grid of the GridPix because for example sagging of the grid between pillars leads to a smaller distance. This increases locally the electrical field and thus, increases the gas gain. But as it is unlikely that the pattern in the grid exactly reassemble the observed ToT pattern, an observation of the same pattern in this measurement, points strongly in the direction of an internal chip effect. Such a flat field measurement was performed with the Timepix3-based detector and the result is presented in Figure 11.19(b). In this plot, for each 8 by 8 pixel bin the mean charge of all hits was calculated and is displayed by the colour. Comparing this to the pattern that was observed in the ToT scan of the same Timepix3 shows roughly the same pattern and thus indicates an intrinsic effect of the chip.

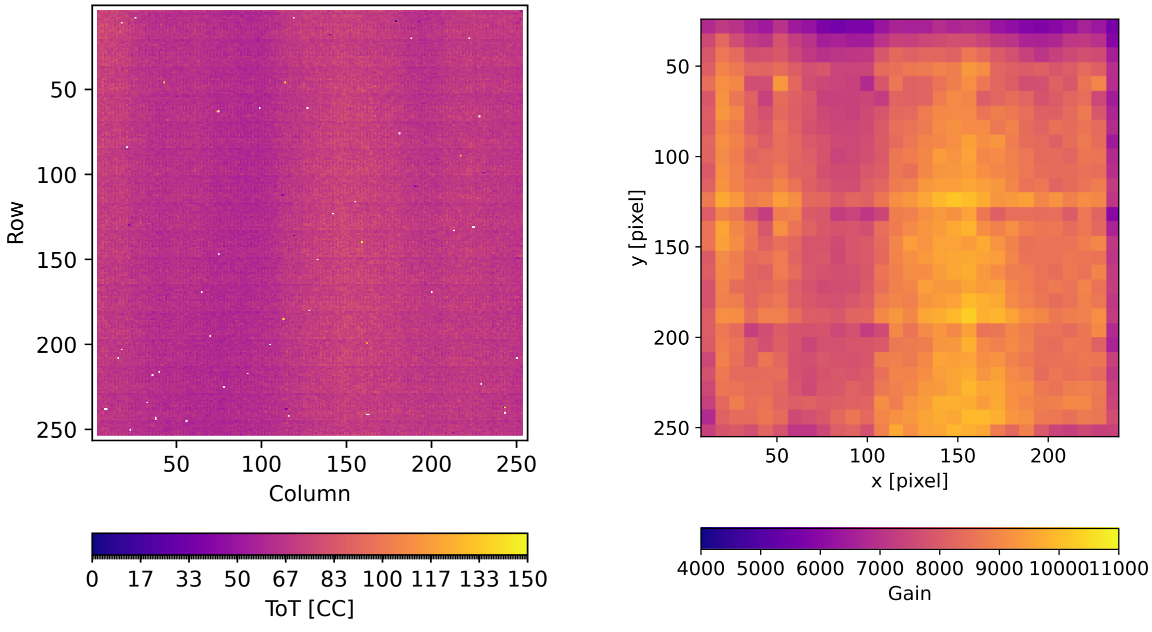

(a) ToT distribution

(b) Gain distribution

Figure 11.19: Pixel map of the measured ToT in GridPix W15-G6 for the injection of 375 mV test pulses (a) and map of the gain in 8 by 8 pixel bins based on a flat field measurement with the same GridPix. Both shows roughly the same pattern with gradients along the horizontal axis.

As the observed effect was present on the used Timepix3-based GridPix with its settings, it must be studied how this influences the measurements and if this could lead to spurious modulation. This is expected, because with such a behaviour in the ToT measurement events that start in the centre and then develop horizontally get a different weight to later charges than for events that develop vertically. To test this, the ToT distribution of such a scan was extracted and normalised to the mean ToT. This was then used as a map of weights for all pixels for an unpolarised simulation run. Figure 11.20(b) shows the angular distributions with the $\cos^2$-fits before and after applying this weight map to the hits. One can see, that while the modulation without it is compatible with 0 %, adding it leads to a modulation of about 5 % roughly in y-direction. To test how this influences the measurements, the inverse of the individual pixel weights was applied to an ^{55}Fe run that showed spurious modulation. Figure 11.21 shows a comparison of the angular distribution of this with and without these weights. One can see that the influence of the weights is minor. Thus, it can be followed that the distribution of the charge measurement can induce spurious modulation as it was shown with simulation data but for the measured data it does not seem to be the main source as its influence on the data was minimal.

Another source of spurious modulation are inhomogeneities in the electric field. Based on the rather small size of the GridPix in comparison to the anode and the cathode, and field simulations (see [42]), it is expected that the electric field between cathode and anode is rather homogeneous. But it is expected that there are some inhomogeneities between the anode and the grid, because the GridPix is glued by hand onto the carrier boards. This means that small rotations of the GridPix around the beam axis are possible and that the GridPix is not necessarily parallel to the carrier board. Furthermore, the anode partially covers the wire bonds which leads to different lateral distances of grid and anode

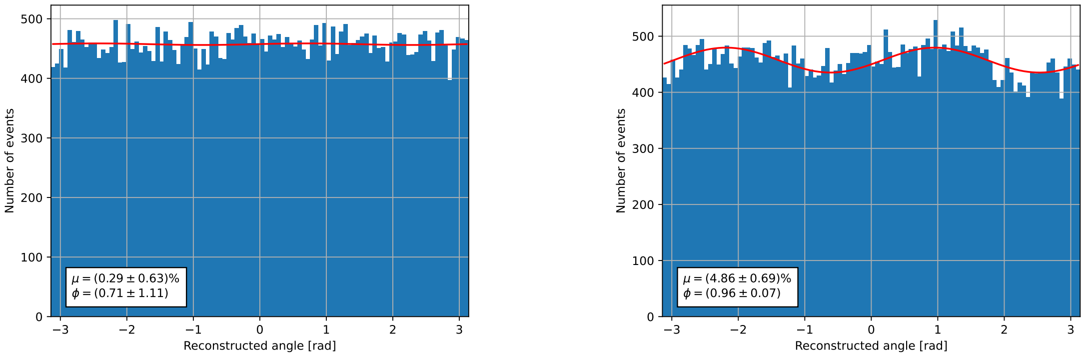

(a) Without weights

(b) With weights

Figure 11.20: Influence of the ToT measurement distribution of the Timepix3 on the spurious modulation in simulation. (a) shows the modulation curve for an unpolarised run without applying charge weights to the pixels, while (b) shows it for the same run with weights based on a ToT calibration of a Timepix3.

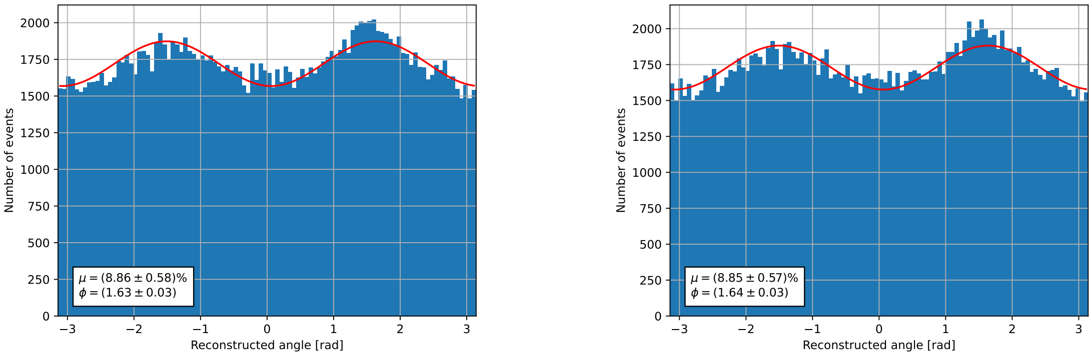

(a) Without weights

(b) With weights

Figure 11.21: Influence of the ToT measurement distribution of the Timepix3 on the spurious modulation in a measurement. (a) shows the modulation curve for an unpolarised ^{55}Fe run without applying charge weights to the pixels, while (b) shows it for the same run with weights based on a ToT calibration of the Timepix3. Compared to the simulation the weights are inverted.

for different edges. Such a geometry also creates inhomogeneous electric fields. To get an insight of possible effects, the hits per pixel can be integrated for a flat field measurement. This was done for the plot in Figure 11.19(b). One can see a square pattern across the chip which is caused by the strong back of the X-ray window within the cathode, as this effectively creates a shadow of the X-ray beam. On the edges one can see that there are in fact differences in the illuminated area, which are caused by the anode covering the GridPix. Here one can also see that the parallel lines of the strong back are bend towards the edges of the GridPix, indicating an inhomogeneous electric field. Furthermore, by comparing the plot to a picture of the anode of the detector in Figure 11.22(b), one can see that the cut-out for the GridPix is not perfectly rectangular and thus causing further field effects that are for example well visible in the bottom left corner of the occupancy plot. As these field effects also disturb the direction of the photoelectron tracks, this is a major cause of spurious modulation. This is the case especially for long tracks, as they have a higher probability of getting towards the edge of the chip and also if the beam spot is close to the edge of the chip. For future applications, the anode of the detector should be improved and then a flat field measurement should be done in advance such that the information can be used for the selection of the beam spot and as a reference for correcting the spurious modulation during reconstruction.

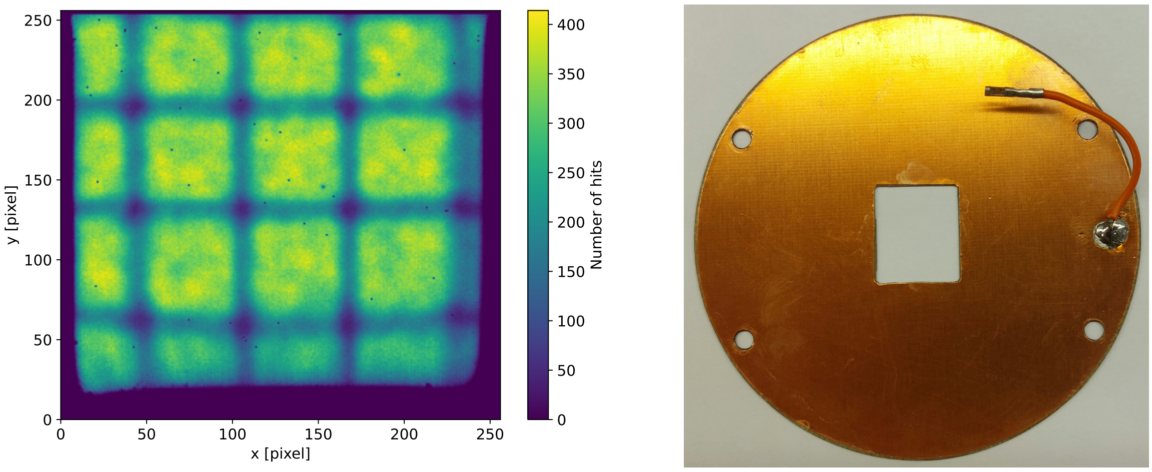

(a) Flat field occupancy

(b) Timepix3 detector anode

Figure 11.22: Occupancy of a flat field measurement and picture of the anode of the Timepix3 detector.

11.10 Comparison of Timepix- and Timepix3-based Detectors

Based on the results presented in the previous sections, the performance of a Timepix-based detector and a Timepix3-based detector can be compared. It leads to the following results:

- **Rate capability**: Timepix3-based detectors can be successfully operated at considerably higher photon rates compared to Timepix-based detectors due to their data-driven readout and the resulting lower dead-time. It is also important to note that the Timepix3 offers a mode with simultaneous charge and time measurement (ToT and ToA) while for the Timepix either charge or time is recorded. That enables the possibility for Timepix3 to separate events not just based on space coordinates, like for Timepix, but also based on the timing. In Section 11.7 it was shown that the Timepix3-detector could be operated successfully at an effective photon rate of 7 kHz. Compared to this, the Timepix-based detector can be read out at a maximum of 40 Hz at which there is still a high probability for multiple photons being recorded within in the same frame. Avoiding this leads to rates in the range of 5 Hz to 10 Hz. Therefore, the Timepix3 can reduce the measurement time to get to a given confidence level for a polarisation detection by about three orders of magnitude.

- **Event integrity**: Due to the data-driven readout of the Timepix3, the charge measurement of an event cannot be interrupted as for the Timepix (see Section 11.3), as there is no shutter during the readout. For the measurements presented in this thesis this effect reduced the effective photon rate of the Timepix-based detector by an additional 25 %.

- **Event reconstruction**: Based on the simultaneous time and charge measurement, it is possible to reconstruct events in 3D without losing the charge information. Even though there is a timing mode for the Timepix, it is not useful for this kind of detector as it cannot be triggered externally and thus most hits would measure an overflow in the timestamp. Furthermore, a time-walk calibration needs the time and charge information per hit and thus is only possible with Timepix3 on an individual hit basis. Simulations have shown that the additional information can reduce the number of necessary photons for the same confidence level by about 10 %. Measurements with the Timepix3-based detector also showed that depending on the detector parameters and the beam energy, a significant improvement of the modulation factor is possible due to the three-dimensional data, and thus an increase of the confidence level with the same dataset or a further reduction of the measurement time with the Timepix3-based detector can be achieved. The gain of the measured data was compatible with the simulation.

- **Background rejection**: The additional ToA information of the Timepix3 adds an additional observable that can be used for background rejection. The possibility of a muon background rejection based on this was shown in [42]. For polarimeters it could be especially interesting in environments with a lot of background radiation and a small photon flux like for example for a satellite-based polarimeter.

CHAPTER 12

Conclusion and Outlook

Over the course of this thesis several advancements towards using GridPix-based detectors as X-ray polarisation sensitive devices were made. For this, a new readout system of the Timepix3 ASIC was developed, implemented and tested that allows to enable the operation of Timepix3-based GridPixes. This readout system was not only developed specifically for X-ray polarimetry, but also with modularity and scalability in mind to support a wide range of possible detectors and applications.

In addition to the readout system, an end-to-end simulation for GridPix X-ray detectors was developed based on the existing simulation framework Garfield++ and the simulation tools Magboltz and Degrad. This simulation starts with a set of user-defined detector and beam parameters and generates the same data output as the readout system of the Timepix and the newly developed readout system of the Timepix3 in addition to the storage of internal data of the simulations to compare simulation results to expectations. The described end-to-end simulation enabled the verification of analysis tools and a direct comparison of the separated parts of the analysis chain for Timepix-based and Timepix3-based data. Furthermore, with the simulation it was possible to directly test the influence of advantages of the Timepix3 over the Timepix. One of the most important advantages is that the Timepix3 can record charge and time of each hit simultaneously while the Timepix can only record one of them. This made it possible to improve the reconstruction of the polarisation based on the additional data per hit.

Using the simulation data, two different reconstruction approaches for the polarisation were implemented. A simple approach that uses the charge distribution along the photo electron track to decide which part is the start and which part is the end of the track. It uses the fact that at the end of the photoelectron track the so-called Bragg peak occurs, leading to a higher charge disposition. The hits that were considered as part of the end of the track were discarded and the remaining pixels were fitted via the maximisation of the second moment of the charge distribution. The second reconstruction approach refines this by adding first two simulation-based parameters that define circles around the centre of charge of the track. Then the absorption point is reconstructed via the centre of charge of the pixels that are between the outer and the inner circle and also within the part that is considered as the start of the track. With this absorption point then the second moment of the charge distribution is maximised for all hits, but their charge is weighted based on the distance to the absorption point. Therefore, hits closest to the absorption point have the biggest influence on the reconstructed angle.

These two approaches were tested against each other via simulation data. It was shown that the second approach performs significantly better, being able to extract higher modulation factors. It was able to reconstruct the polarisation for setup parameters and especially lower beam energies for which the first approach failed. For both approaches also the possibility to use the three-dimensional data of the Timepix3 was implemented, considering the drift velocity of the gas. With this it was possible to perform each reconstruction fully in 2D, fully in 3D and with the first step in 3D and the second step in 2D. It was shown that the reconstruction fully in 3D had the worst performance and that the reconstruction with the first step in 3D and the second step in 2D had a slight advantage over the fully two-dimensional reconstruction. This was explained by the purposes and the goals of the two steps: the first step should differentiate the start and the end of the track such that only the start is considered for the second step. In this case, the additional data of the third dimension helps to differentiate the two, especially in cases where the start and the end of a track are close together in the two-dimensional projection due to scattering but can be well separated in three dimensions. The goal of the second step is to reconstruct the angle of the event in two dimensions, thus the addition of data from the third dimension negatively influenced it.

Furthermore, the simulation was used to test the influence of detector parameters like the length of the drift cylinder, the pressure of the gas and the mixing ratio of the gases. It was shown that they do not affect the radii of the weight-based reconstruction but require different values for the weight parameter. These reconstruction parameters were used to study the influence of the detector parameters on the modulation factor and the necessary number of photons to detect the X-ray polarisation of a source with a given confidence level. It was also shown that the reconstruction with different beam spots spread over the active area of the readout ASIC works well. However, at higher energies the modulation factor at the edges is decreased and in the corners of the active area the direction of the polarisation could not be reconstructed correctly.

The measurements performed, using the presented detectors, have shown that these detectors can be successfully operated as devices to measure the polarisation of an X-ray source. The data was used to verify the qualitative results of the simulation and showed quantitatively results in the same order of magnitude with some differences. The cause of these differences was the missing simulation of the gas gain and further idealisations of the simulation. The data also reinforced the result that the weight-based reconstruction performs significantly better than the cut-based reconstruction and that using the 3D data of the Timepix3 for the first step of the reconstruction can significantly improve the modulation factor. This showed that a reduction of the necessary photons for measuring a polarisation with a confidence level of 99 % by about 10 % is possible with 3D data. Furthermore, it was demonstrated that energy resolutions of 20 % (FWHM) could be achieved, bringing the detector close to the best energy resolutions that were achieved with the gas pixel detectors for IXPE.

The analysis of the data showed a significant spurious modulation, especially for the Timepix3 detector. Investigations with the simulation, calibration data of the ASIC via the readout system, and measurement data showed three potential sources of spurious modulation. The simulation showed that based on the setup of the pixels in a quadratic matrix, diagonal directions are slightly preferred by the reconstruction over horizontal and vertical directions, creating a modulation of about 2 %. The calibration of the ASIC showed that for the injection of test pulses with the same amplitude there is a systematic variation of the measured charge across the chip, effectively applying a position dependent weight to detected hits. Based on a flat field measurement with the detector it could be shown that there are some inhomogeneities in the electric field that cause lensing effects for the drifting electrons and thus, can induce spurious modulation. It was concluded that these effects mainly occur in the transfer field between the anode and grid due to potential tilts of these surfaces with respect to each other and due to non-uniformities in the cutout of the anode for the grid.

Besides the higher spurious modulation for the Timepix3-based detector than for the Timepix-based detector, several improvements due to the change from Timepix to Timepix3 were shown. One is the higher rate capability and the lower dead time of the Timepix3. These changes allow to get from photon detection rates in the order of Hz for Timepix to rates in the order of kHz with the Timepix3. Thus, if the higher rate is available by the source, the measurement time to reach the same confidence level of the polarisation detection can be drastically reduced. This was demonstrated with tests of different photon rates with the Timepix3-based detector, and it could be successfully operated at 7 kHz. Additionally advantages due to the simultaneous measurement of charge and time with the Timepix3 were shown. This helped to increase the rate capability of the detector as the timestamps of the hits can be used to separate events that would otherwise overlap if no time information were available.

There are several aspects of the detector and the tools for it, that can and should be improved. Most importantly, there is the aspect of spurious modulation which is more prominent for the Timepix3 detector. As there is a strong influence of the non-uniformity of the charge measurement of the Timepix3 that leads to spurious modulation, this should be further investigated. It should be tested if this behaviour changes with different settings of the Krummenacher current that is responsible to discharge the capacitances in the pixels and thus has a direct influence on the dynamic range and the resolution of the charge measurement. To get a reasonable charge resolution, its corresponding DAC value had to be set close to the lower end of its range and it cannot be excluded that this has an influence on the uniformity. However, this only helps to understand the problem but not to solve it. An additional possibility is to check an equalisation of the Timepix3 and change it from a threshold-based equalisation to a ToT-based equalisation. This could lead to an increased noise level as then the threshold distribution of the pixels is broader, but it could be worth it if the spurious modulation vanishes in result. Furthermore, on the side of the detector, a new anode should be manufactured as the results pointed into the direction that it could have induced some field inhomogeneities and thus spurious modulation. Based on the results of this thesis, there is work ongoing to prepare GridPix-based X-ray polarimeters as detectors for material science at PETRA III and as a possible successor of the gas pixel detectors (GPDs) on future X-ray astronomy satellites.

As already presented in the context of the detectors, an interesting concept for the future would be a detector in which the beam is parallel to the readout and not orthogonal as for the detectors that were tested and simulated during this thesis. Such a detector would have several advantages. For example, a decoupling of the photon absorption distribution from the electron drift length and thus, the diffusion leading to a higher independence of the detector performance on the energy of the photons. This design could enable GridPix-based X-ray polarimeters that work for a broader energy band. Such a detector is possible due to the implementation of the Timepix3, as it enables three-dimensional reconstruction of events which is crucial for the more complex reconstruction in such a detector compared to an orthogonal detector.

APPENDIX A

Appendix

A.1 Software Versions

For reproducibility of the results presented in this thesis, all developed software was uploaded to GitHub. In general, all public repositories of the working group can be found here: `https://github.com/GasDet-Bonn` Table A.1 contains a list of developed and used software and the versions that were used to achieve the results of this thesis.

Table A.1: List of software and versions

Software	Link	Version
GridPix simulation	`https://github.com/GasDet-Bonn/GridPix_xray_simulation`	$92bf7e9$
Tpx3 DAQ	`https://github.com/GasDet-Bonn/tpx3-daq`	$afd6b56$
Tpx3 interpretation	`https://github.com/GasDet-Bonn/tpx3_interpretation`	$1a7f5f1$
Xray pol reco	`https://github.com/GasDet-Bonn/Xray_pol_reco`	$d4242f5$
Xray pol plotting	`https://github.com/GasDet-Bonn/Xray_pol_plotting`	$e11f4f4$
TimepixAnalysis	`https://github.com/Vindaar/TimepixAnalysis`	$7a3a20a$

Bibliography

[1] S. Fabiani and F. Muleri, *Astronomical X-Ray Polarimetry*, 2014 (cit. on pp. 3–8, 11, 14, 18–20, 88, 92).

[2] T. E. Strohmayer and T. R. Kallman, *On the Statistical Analysis Of X-ray Polarization Measurements*, The Astrophysical Journal **773** (2013) 103 (cit. on pp. 6, 8).

[3] J. E. Vaillancourt, *Placing Confidence Limits on Polarization Measurements*, Publications of the Astronomical Society of the Pacific **118** (2006) 1340, ISSN: 1538-3873 (cit. on p. 8).

[4] M. C. Weisskopf, R. F. Elsner and S. L. O'Dell, "On understanding the figures of merit for detection and measurement of x-ray polarization", *Space Telescopes and Instrumentation 2010: Ultraviolet to Gamma Ray*, ed. by M. Arnaud, S. S. Murray and T. Takahashi, vol. 7732, International Society for Optics and Photonics, SPIE, 2010 77320E (cit. on pp. 8, 9).

[5] W. Demtröder, *Experimentalphysik 3: Atome, Moleküle und Festkörper*, Springer-Verlag, 2016 (cit. on pp. 10, 11).

[6] R. Novick, M. Weisskopf, R. Berthelsdorf, R. Linke and R. Wolff, *Detection of X-ray polarization of the Crab Nebula*, Astrophysical Journal, vol. 174, p. L1 **174** (1972) L1 (cit. on p. 13).

[7] M. Weisskopf et al., "The X-ray polarization experiment on the OSO-8", *X-ray binaries, Proceedings of a Symposium held at NASA's Goddard Space Flight Center, Greenbelt, Maryland, October 20-22, 1975, and associated with a coordinated campaign (IAU Commissions 42 and 44) to observe X-ray binaries, p. 81-96 (SEE N76-26056 16-90)*, vol. 389, 1976 81 (cit. on p. 13).

[8] M. Weisskopf, H. Kestenbaum, K. Long, R. Novick and E. Silver, *An upper limit to the linear X-ray polarization of Scorpius X-1*, Astrophysical Journal, Part 2-Letters to the Editor, vol. 221, Apr. 1, 1978, p. L13-L16. **221** (1978) L13 (cit. on p. 13).

[9] M. Weisskopf, E. Silver, H. Kestenbaum, K. Long and R. Novick, *A precision measurement of the X-ray polarization of the Crab Nebula without pulsar contamination*, Astrophysical Journal, Part 2-Letters to the Editor, vol. 220, Mar. 15, 1978, p. L117-L121. **220** (1978) L117 (cit. on p. 13).

[10] C. Kennel and F. Coroniti, *Confinement of the Crab pulsar's wind by its supernova remnant*, Astrophysical Journal, Part 1 (ISSN 0004-637X), vol. 283, Aug. 15, 1984, p. 694-709. **283** (1984) 694 (cit. on p. 14).

[11] C. Kennel and F. Coroniti, *Magnetohydrodynamic model of Crab nebula radiation*, Astrophysical Journal, Part 1 (ISSN 0004-637X), vol. 283, Aug. 15, 1984, p. 710-730. **283** (1984) 710 (cit. on p. 14).

[12] M. C. Weisskopf et al., *Discovery of spatial and spectral structure in the X-ray emission from the Crab Nebula*, The Astrophysical Journal **536** (2000) L81 (cit. on p. 14).

[13] S. Bogovalov and D. V. Khangoulian, *On the origin of the torus and jet-like structures in the centre of the Crab Nebula*, Monthly Notices of the Royal Astronomical Society **336** (2002) L53 (cit. on p. 14).

[14] S. Shibata, H. Tomatsuri, M. Shimanuki, K. Saito and K. Mori, *On the X-ray image of the Crab nebula: comparison with Chandra observations*, Monthly Notices of the Royal Astronomical Society **346** (2003) 841 (cit. on p. 14).

[15] Y. E. Lyubarsky, *On the structure of the inner Crab Nebula*, Monthly Notices of the Royal Astronomical Society **329** (2002) L34 (cit. on p. 14).

[16] S. Komissarov and Y. E. Lyubarsky, *The origin of peculiar jet-torus structure in the Crab nebula*, Monthly Notices of the Royal Astronomical Society **344** (2003) L93 (cit. on p. 14).

[17] N. Bucciantini, L. Del Zanna, E. Amato and D. Volpi, *Polarization in the inner region of pulsar wind nebulae*, Astronomy & Astrophysics **443** (2005) 519 (cit. on p. 14).

[18] D. Volpi, L. Del Zanna, E. Amato and N. Bucciantini, *Polarization in Pulsar Wind Nebulae*, arXiv preprint arXiv:0903.4120 (2009) (cit. on p. 14).

[19] M. C. Weisskopf et al., *The imaging x-ray polarimetry explorer (IXPE)*, Results in Physics **6** (2016) 1179 (cit. on pp. 14, 15, 127).

[20] L. Baldini et al., *Design, construction, and test of the Gas Pixel Detectors for the IXPE mission*, Astroparticle Physics **133** (2021) 102628 (cit. on pp. 14, 88, 92, 133).

[21] W. Demtröder, *Experimentalphysik 4: Kern-, Teilchen-und Astrophysik*, Springer-Verlag, 2017 (cit. on p. 15).

[22] W. B. Peatman, *Gratings, mirrors and slits: beamline design for soft X-ray synchrotron radiation sources*, Routledge, 2018 (cit. on p. 15).

[23] J. Strempfer et al., *Resonant scattering and diffraction beamline P09 at PETRA III*, Journal of synchrotron radiation **20** (2013) 541 (cit. on pp. 16, 127).

[24] L. Spieß, H. Behnken, C. Genzel, R. Schwarzer and G. Teichert, *Moderne röntgenbeugung*, vol. 2, Springer, 2009 (cit. on p. 16).

[25] L. Rolandi, W. Riegler and W. Blum, *Particle Detection with Drift Chambers*, Springer Berlin, Heidelberg, 2008, ISBN: 9783540766834 (cit. on pp. 17, 21–26, 95).

[26] H. Kolanoski and N. Wermes, *Particle Detectors: Fundamentals and Applications*, Oxford University Press, 2020, ISBN: 9780198858362 (cit. on pp. 17–22, 24).

[27] S. Navas et al., *Review of particle physics*, Phys. Rev. D **110** (2024) 030001 (cit. on pp. 20, 144).

[28] M. S. Longair and M. S. Longair, *High energy astrophysics: volume 1, particles, photons and their detection*, vol. 1, Cambridge University Press, 1992 (cit. on p. 20).

[29] E. Kobetich and R. Katz, *Energy deposition by electron beams and δ rays*, Physical review **170** (1968) 391 (cit. on p. 21).

[30] E. Wagner, F. Davis and G. Hurst, *Time-of-Flight Investigations of Electron Transport in Some Atomic and Molecular Gases*, The Journal of Chemical Physics **47** (1967) 3138 (cit. on p. 23).

[31] W. Legler, *Die Statistik der Elektronenlawinen in elektronegativen Gasen, bei hohen Feldstärken und bei großer Gasverstärkung*, Zeitschrift für Naturforschung A **16** (1961) 253 (cit. on pp. 25, 96).

[32] G. Alkhazov, *Statistics of electron avalanches and ultimate resolution of proportional counters*, Nuclear Instruments and Methods **89** (1970) 155 (cit. on p. 25).

[33] W. Legler, *The influence of the relaxation of the electron energy distribution on the statistics of electron avalanches*, British Journal of Applied Physics **18** (1967) 1275 (cit. on p. 25).

[34] X. Llopart, R. Ballabriga, M. Campbell, L. Tlustos and W. Wong, *Timepix, a 65k programmable pixel readout chip for arrival time, energy and/or photon counting measurements*, Nuclear Instruments and Methods in Physics Research Section A: Accelerators, Spectrometers, Detectors and Associated Equipment **581** (2007) 485, VCI 2007, ISSN: 0168-9002 (cit. on p. 27).

[35] F. Krummenacher, *Pixel detectors with local intelligence: an IC designer point of view*, Nuclear Instruments and Methods in Physics Research Section A: Accelerators, Spectrometers, Detectors and Associated Equipment **305** (1991) 527 (cit. on pp. 27, 145).

[36] X. Llopart, *Timepix3 v1.0*, 2006 (cit. on p. 28).

[37] T. Poikela et al., *Timepix3: a 65K channel hybrid pixel readout chip with simultaneous ToA/ToT and sparse readout*, Journal of Instrumentation **9** (2014) C05013 (cit. on pp. 29, 50, 51, 63, 65, 137).

[38] X. Llopart and T. Poikela, *Timepix3 Manual v1.9*, 2014 (cit. on pp. 29, 31, 32).

[39] M. Lupberger, K. Desch and J. Kaminski, *Implementation of the timepix ASIC in the scalable readout system*, Nuclear Instruments and Methods in Physics Research Section A: Accelerators, Spectrometers, Detectors and Associated Equipment **830** (2016) 75 (cit. on pp. 33, 34).

[40] M. Lupberger, *The Pixel-TPC: A feasibility study*, PhD thesis: Universität Bonn, 2015 (cit. on pp. 33, 34).

[41] J. Toledo et al., *The Front-End Concentrator card for the RD51 Scalable Readout System*, Journal of Instrumentation **6** (2011) C11028 (cit. on p. 34).

[42] T. Schiffer, *Detector development towards axion searches with BabyIAXO*, PhD thesis: Universität Bonn, 2025 (cit. on pp. 35, 59, 60, 72, 74, 77, 82, 146, 149).

[43] I. Rubinskiy et al., *An EUDET/AIDA pixel beam telescope for detector development*, Physics Procedia **37** (2012) 923 (cit. on p. 38).

[44] Y. Bilevych, private communication (cit. on p. 70).

[45] M. Chefdeville, *Development of Micromegas-like gaseous detectors using a pixel readout chip as collecting anode*, PhD thesis: University of Amsterdam, 2009 (cit. on p. 69).

[46] W. Koppert et al., *GridPix detectors: Production and beam test results*, Nuclear Instruments and Methods in Physics Research Section A: Accelerators, Spectrometers, Detectors and Associated Equipment **732** (2013) 245 (cit. on p. 69).

[47] M. Lupberger et al., *InGrid: Pixelated Micromegas detectors for a pixel-TPC*, PoS TIPP2014 **225** (2014) (cit. on p. 69).

[48] L. Scharenberg, *Studies on the Thermal Behaviour of GridPix-Based Detectors*, Master's thesis: Universität Bonn, 2019 (cit. on p. 69).

[49] C. Krieger, *Search for solar chameleons with an InGrid based X-ray detector at the CAST experiment*, PhD thesis: Universität Bonn, 2018 (cit. on pp. 71, 73, 95).

[50] S. M. Schmidt, *Search for solar axions using a 7-GridPix IAXO prototype detector at CAST*, PhD thesis: Universität Bonn, 2024 (cit. on pp. 71, 85, 87).

[51] S. Biagi, *Degrad - transport of electrons in gas mixtures*, 2024 (cit. on p. 77).

[52] H. Schindler and R. Veenhof, *Garfield++—simulation of ionisation based tracking detectors*, 2024 (cit. on p. 77).

[53] S. Biagi, *Magboltz - transport of electrons in gas mixtures*, 2024 (cit. on p. 77).

[54] M. Gruber, *Study of ionisation and amplification processes in GridPix detectors*, Master's thesis: Universität Bonn, 2018 (cit. on pp. 81, 82, 139).

[55] L. Richarz, *Studien zur Entwicklung eines GridPix-basierten Röntgenpolarimeters*, Bachelor's thesis: Universität Bonn, 2019 (cit. on p. 88).

[56] M. Gruber, K. Desch, J. Kaminski and L. Richarz, "Development of a GridPix X-ray polarimeter", *Journal of Physics: Conference Series*, vol. 2374, 1, IOP Publishing, 2022 012148 (cit. on p. 88).

[57] B. L. Henke, E. M. Gullikson and J. C. Davis, *X-ray interactions: photoabsorption, scattering, transmission, and reflection at E= 50-30,000 eV, Z= 1-92*, Atomic data and nuclear data tables **54** (1993) 181 (cit. on p. 108).

List of Figures

List of Tables

Acknowledgements

First, I want to thank Klaus Desch for the opportunity to do this work in your working group but additionally, for all the support during the long time from my Bachelor thesis until this thesis that I spent in your group. I also want to thank Jochen Kaminski for the support during this time.

I would like to thank the whole working group for the enjoyable time and the productive work environment. I always enjoyed spending time with you, especially during the Jamborees and our regular group lunches. In particular, I want to thank my current and former colleagues Tobias Schiffer, Lucian Scharenberg, Sebastian Schmidt, Christoph Krieger, and Vladislavs Plesanovs for the great time that we always had. It was a great fun and always a pleasure to work with you and I will always look back on it with joy.

A special thanks also to the team at INAF-IAPS and especially to Paolo Soffitta, for the support and for the opportunity to do measurements at your facility. It was very helpful to learn from your experience in X-ray polarimetry and from the great discussions that we had during the measurements and our regular meetings.

I would like to thank Prof. Dr. Jochen Dingfelder, Prof. Dr. Carsten Urbach, and Prof. Dr. Matthias Hullin for accepting to be part of the review committee.

I acknowledge DESY (Hamburg, Germany), a member of the Helmholtz Association HGF, for the provision of experimental facilities. Parts of this research were carried out at PETRA III and I would like to thank Dr. Sonia Francoual and Dr. Jose R. Linares Mardegan for assistance in using P09. Beamtime was allocated for proposal I-20200649. I also acknowledge the user travel reimbursement for this proposal.

I especially want to thank my family for all the support throughout my PHD and my entire studies. You were always on my side and without you, I could not have accomplished this.